BRNO UNIVERSITY OF TECHNOLOGY

VYSOKÉ UČENÍ TECHNICKÉ V BRNĚ

FACULTY OF ELECTRICAL ENGINEERING AND COMMUNICATION

FAKULTA ELEKTROTECHNIKY A KOMUNIKAČNÍCH TECHNOLOGIÍ

DEPARTMENT OF PHYSICS

ÚSTAV FYZIKY

ADVANCED METHODS AND MATERIALS FOR RESEARCH AND DEVELOPMENT OF FIELD EMISSION EMITTERS

POKROČILÉ METODY A MATERIÁLY PRO VÝVOJ A VÝZKUM AUTOEMISNÍCH KATOD

HABILITATION THESIS

HABILITAČNÍ PRÁCE

AUTHOR Ing. Alexandr Knápek, Ph.D.

AUTOR PRÁCE

BRNO 2021

Abstract

This habilitation thesis focuses on advanced methods for the preparation and characterization of field emission cathodes operating at room temperature and acting as a source of free electrons to the vacuum. Since the preparation and characterization of the field emission sources is a highly multidisciplinary field, combining knowledge from solid-state physics, particle physics, physical statistics, inorganic chemistry and of course the electrical engineering, several technological and analytical methods need to be covered, which is the goal of this work. The habilitation thesis is presented as a commentary on a set of scientific papers published in peer-reviewed impacted journals, three indexed conference papers and one utility model, which represents an overview of significant results achieved in this field since 2013.

Field emission of electrons refers to the phenomenon in which electrons of high beam density are emitted. When a strong electric field is applied to the sharp tip of a cathode located in an ultra-high vacuum, the increased electric field strength at the source surface results in the curvature of the surface barrier, thus enabling the quantum tunneling phenomenon itself. At room temperature, an electron beam can thus be obtained that is approximately a thousand times denser than a conventional thermal emission electron source based on an annealed tungsten filament. Because of the reduced operating temperature of the source, which is the source of undesirable noise and fluctuation phenomena of the total emission current, and because of the requirement for ultra-high vacuum, the deployment of pure cold field emission is considerably more complicated, both technologically and technically.

Although the tunnel effect has been known for more than a century, there is still no widespread electron source that is built purely on the influence of the electric field and is sufficiently stable. The publications annotated in this paper cover the solution of partial problems associated with the development and characterization of new types of field emission sources, at several levels. First and foremost is a repeatable technical method for forming a sharp tip from polycrystalline tungsten, which forms the substrate for historically older coated cathodes. However, these are still relevant due to the increasing portfolio of thin films. Furthermore, a methodology for the optimization and preparation of a new lithographic structure, intended to work with a nanotube-based cathode, is proposed. As an alternative to conventional carbon nanotubes, a newly developed tungsten oxide-based nanotube was also

used in this work. In the next part of the thesis, the study of new materials moves from tungsten to carbon allotropes; to graphite, or so-called polymer graphite, which appears to be a very interesting alternative to the currently very popular graphene. In this research, the field emission properties from a single crystal sample of highly oriented pyrolytic graphite, which was used as a reference material, were described for the first time. The research continues to polymer graphite where three different methods of sharp tip preparation were developed. Depending on the specific method, a sharp tip can be produced whose field emission properties are like those of carbon nanotubes or, conversely, a tip with a larger radius whose surface contains several suitably oriented graphite flakes that form a stochastically distributed array of sources, and hence one can speak of a disordered array of field emission sources.

Following this research, a methodology for preparing a polymer graphite probe that can be used as a cheap and effective substitute for tungsten or platinum-iridium probes for scanning probe microscopy has also been developed.

The final part of the thesis is devoted to characterization field emission microscope compatible methods focusing on the characterization (and partly also for diagnosis) of field emission sources based on total emission current measurements. This involves noise spectroscopy, which was first applied at the level of noise measurement not only of the cathode, but also of the whole electron-optical system of a scanning electron microscope, as well as the method of analysis of the total emission current based on orthodox testing, which can be implemented to field emission microscope or any existing device utilizing focused electron beam and thus to extend its function by a sort of self-diagnostic function.

Abstrakt

Tato habilitační práce se věnuje pokročilým metodám přípravy a charakterizace autoemisních katod, pracujících za pokojové teploty a sloužících jako zdroj volných elektronů do vakua. Jelikož příprava a charakterizace autoemisních zdrojů je vysoce multioborová záležitost, která slučuje poznatky z oborů jako jsou fyzika pevné fáze, fyzika částic, fyzikální statistika, anorganická chemie a samozřejmě elektrotechnika, je zapotřebí pokrýt řadu technologických a analytických metod, což si klade za cíl tato práce. Habilitační práce je předkládána jako komentář k souboru vědeckých prací publikovaných v recenzovaných impaktovaných časopisech, tří konferenčních příspěvků a jednoho užitného vzoru, což představuje přehled významných výsledků dosažených v tomto oborou od roku 2013.

Vlastní emise neboli autoemise elektronů označuje jev, při kterém jsou emitovány elektrony o vysoké hustotě svazku. Pokud je na ostrý hrot katody, v podmínkách ultra-vysokého vakua, přivedeno silné elektrické pole, zvýšená intenzita elektrického pole na povrchu zdroje má za následek zakřivení povrchové bariéry, což umožňuje samotný kvantový tunelovací jev. Při pokojové teplotě je takto možno získat elektronový svazek, který je přibližně tisíckrát hustší než konvenční termoemisní elektronový zdroj založený na žhaveném wolframovém vlákně. Právě kvůli snížené pracovní teplotě zdroje, která je zdrojem nežádoucího šumu a fluktuačních jevů proudu totální emise a také kvůli požadavku na ultra-vysoké vakuum, je nasazení čistě studené autoemise podstatně více komplikované, a to jak technologicky, tak technicky.

Přestože tunelový jev je známý déle než sto let, dosud neexistuje rozšířený zdroj elektronů, který by byl postavený čistě na vlivu elektrického pole a byl dostatečně stabilní. Publikace komentované v této práci pokrývají řešení dílčích problémů spjatých s vývojem a charakteristikou nových druhů autoemisních zdrojů, a to na několika úrovních. V prvé řadě se jedná o opakovatelnou technickou metodu formování ostrého hrotu z polykrystalického wolframu, který tvoří substrát pro historicky starší povlakované katody. Ty jsou však díky zvětšujícímu se portfoliu tenkých vrstev stále aktuální. Dále se jedná o návrh metodiky optimalizace a přípravy nové litografické struktury, určené pro práci s katodou na bázi nanotrubky. Jako alternativa ke klasickým uhlíkovým nanotrubkám je v této práci využita i nově vyvinutá nanotrubka na bázi oxidů wolframu. V další části práce se studium nových materiálů přesouvá od wolframu k alotropům uhlíku. Konkrétně se jedná o grafit, resp. polymerní grafit, který se jeví jako velmi zajímavá alternativa k dnes velmi populárnímu grafénu. V rámci tohoto výzkumu byly poprvé popsány autoemisní vlastnosti ze vzorku

monokrystalu vysoce orientovaného pyrolytického grafitu, který byl použit jako referenční materiál. Výzkum dále pokračoval na polymerním grafitu, kde byly vyvinuty tři různé metody přípravy hrotů. V návaznosti na konkrétní metodu lze vyrobit ostrý hrot, jehož autoemisní vlastnosti jsou podobné vlastnostem uhlíkových nanotrubiček nebo naopak hrot s větším poloměrem, jehož povrch obsahuje řadu vhodně orientovaných grafitových vloček, které utváří stochasticky distribuované pole zdrojů, a tedy se dá hovořit o neuspořádaném poli autoemisních zdrojů.

V návaznosti na tento výzkum byla také vyvinuta metodika přípravy sondy z polymerního grafitu, kterou lze použít jako levnou a efektivní náhražku wolframové či platino-iridiové sondy pro mikroskopii skenující sondou.

Závěrečná část práce se věnuje metodikám charakterizace kompatibilním s autoemisním (projekčním) mikroskopem zaměřujíce se na charakteristiku (a částečně i na diagnostiku) autoemisních zdrojů na základně měření proudu totální emise. Jedná se o šumovou spektroskopii, která byla poprvé aplikovaná na úrovni měření šumu nejen katody, ale i celého elektronově optického systému rastrovacího elektronového mikroskopu a dále na metodě analýzy proudu totální emise na bázi ortodoxního testování, kterou lze implementovat do autoemisního (projekčního) mikroskopu nebo jakéhokoli stávajícího zařízení, které využívá fokusovaný elektronový svazek a rozšířit tak jeho funkcionalitu o vhodnou autodiagnostickou funkci.

Keywords

field emission of electrons, field emission emitters, polymer graphite, noise spectroscopy, orthodoxy testing

Klíčová slova

vlastní emise elektronů, autoemisní zdroje elektronů, polymerní grafit, šumová spektroskopie, orthodoxní testování

Acknowledgments

Many thanks to my colleagues from the Institute of Scientific Instruments of CAS, especially to Mr. Pavel Klein and late prof. Armin Delong, who introduced me to cold emission research years ago and supported me in my research.

Furthermore, I would like to thank my colleagues at the University of Technology, especially Prof. Lubomír Grmela, long-time head of the Department of Physics at the FEEC BUT and the former supervisor of my PhD thesis for motivation and support during the pursuit of this work. I would also like to thank Dr. Dinara Sobola for her motivation and help with the technology-oriented part of the research, to Prof. Josef Šikula for his help with noise spectroscopy, and to Dr. Pavel Škarvada for his help when regarding the electronics design of the updated automated etching device.

Finally, I would like to thank my family for their support and patience, namely to my wife Michaela and our daughter Kateřina.

CONTENTS

LIST OF SYMBOLS AND ABBREVIATIONS **8**

LIST OF FIGURES **11**

LIST OF TABLES **13**

INTRODUCTION **14**

1. ADVANCED METHODS OF PRODUCTION OF COLD FIELD EMITTERS **16**

1.1 REPRODUCIBLE ELECTROCHEMICAL TIP FORMATION METHOD 17
1.1.1 The programmable etching set-up *17*
1.1.2 The implementation of the etching method *18*
1.1.3 FE and STM tip performance *20*
1.2 DESIGN AND FABRICATION OF NANOTUBE-BASED STRUCTURES 22
1.2.1 Fabrication method for a gate structure based on electron beam lithography *22*
1.2.2 Simulation and optimization of optical properties of gated CNT source *25*

2. NOVEL MATERIALS FOR COLD FIELD EMITTERS **27**

2.1 COLD FIELD EMISSION FROM GRAPHITE SURFACE 27
2.2 COLD FIELD EMISSION FROM TUNGSTEN OXIDES 29
2.2.1 Material analysis of the W_5O_{14} and $W_{18}O_{49}$ nanowires *29*
2.2.2 Field emission testing of W_5O_{14} and $W_{18}O_{49}$ NWs in microscopic regime *31*
2.2.1 Field emission testing of $W_{18}O_{49}$ and W_5O_{14} NW in macroscopic regime *32*
2.3 COLD FIELD EMISSION FROM POLYMER GRAPHITE 34
2.3.1 Material properties of the polymer graphite *35*
2.3.2 Polymer graphite tips made by focused ion beam *36*
2.3.3 Polymer graphite tips formed by mechanical grinding *37*
2.3.4 Polymer graphite tips electrochemical etching *38*
2.3.5 Application of polymer graphite tips as probes for STM *40*

3. NOVEL METHODS OF ELECTRON EMITTER CHARACTERIZATION **42**

3.1 NOISE SPECTROSCOPY IMPLEMENTED IN FIELD EMISSION MICROSCOPE 42
3.1.1 Application of the noise spectroscopy method for FE sources *42*
3.1.2 Analysis of complex electron optical systems *45*
3.2 ORTHODOX TESTING IMPLEMENTED IN FIELD EMISSION MICROSCOPE 49
3.2.1 Introduction to the field electron emission analysis *49*
3.2.2 Introducing the field electron emission analysis plots *51*
3.2.3 The field emission orthodoxy testing *51*
3.2.4 Implementation of the orthodoxy test *53*

4. CONCLUSIONS **54**

SELECTED PUBLICATIONS OF THE AUTHOR **57**

REFERENCES **58**

LIST OF APPENDICES. **62**

LIST OF SYMBOLS AND ABBREVIATIONS

Symbols:

ϕ	local work function	[eV]
I_{eb}	electron beam current (total emission current)	[A]
s	Scanning speed	[a.u.]
S_u	Voltage noise spectral density	[V^2/Hz]
f_c	Cut-off frequency	[Hz]
F_L	Local electrostatic field	[V/m]
F_C	Characteristic electrostatic field	[V/m]
F_R	Reference electrostatic field	[V/m]
v_F	is the value of $v(x)$ applies to the SN barrier defined by ϕ and F_L	[a.u.]
c_s	Schottky constant	[eV $V^{-1/2}$ $m^{1/2}$]
a	First Fowler-Nordheim constant	[A eV V^{-2}]
b	Second Fowler-Nordheim constant	[$eV^{-3/2}$ V m^{-1}]
A_n	The notional area	[m^2]
A_f^{SN}	The formal emission area	[m^2]
I_m	Measured total emission current	[A]
$J(F)$	Current density as a function of field	[A/m^2]
V_m	Measured voltage	[V]
V_{mR}	Reference measured voltage	[V]
κ	Exponential factor for Murphy-Good plots	[a.u.]
η	Scaled parameter	[a.u.]
θ	Scaled parameter	[A/m^2]
S_{FN}^{fit}	Slope of fitted line to Fowler-Nordheim plot	[Np V^2]
S_{MG}^{fit}	Slope of fitted line to Murphy-Good plot	[Np V^2]
S_{ML}^{fit}	Slope of fitted line to Millikan-Lauritsen plot	[Np V^2]
Np	ln(current . voltage ^{number})	[ln(A V^{number})]
S_I	Current noise spectral density	[A^2/Hz]
R_{FN}^{fit}	Exponent of the vertical axis intercept for a fitted line to Fowler-Nordheim plot	[A V^{-2}]
R_{FN}^{fit}	Exponent of the vertical axis intercept for a fitted line to Murphy-Good plot	[A $V^{-\kappa}$]
R	Electrical resistance	[Ω]
U	Electrical voltage	[V]
s_t	Slope correction factor	[a.u.]
r_t	Vertical axis intercept correction factor	[a.u.]

Abbreviations:

AFM	Atomic force microscopy
AXS	X-ray strain
BKH	Burgess-Kroemer-Houston (sci. group)
BN	Background noise
BUT	Brno University of Technology
CAS	Czech Academy of Sciences
CF_4	Tetrafluoromethane
CFE	Cold field emission
CI	Coulomb interactions
CNT	Carbon nanotube
DC	Direct current
DLC	Diamond-like carbon
EDX	Electron diffraction spectroscopy
FE	Field emission
FEE	Field electron emission
FEEC	Faculty of Electrical Engineering
FEM	Field emission microscope
FIB	Focused ion beam
FN plot	Fowler-Nordheim plot
GPIB	General Purpose Interface Bus (IEEE-488)
GR	Generation-recombination
HOPG	Highly ordered pyrolytic graphite
CHF_3	Fluoroform
IML	Intermediate lens
KOH	Potassium hydroxide
KPFM	Kelvin probe force microscopy
LAFE	Large area field emitter
MC	Monte Carlo
MG	Murphy-Good
ML	Milikan-Lauritsen
NaOH	Sodium hydroxide
NT-MDT	NT-MDT Spectrum Instruments (company)
NW	Nanowire
PECVD	Plasma Enhanced Chemical Vapor Deposition
PG	Polymer graphite
PMMA	Poly(methyl methacrylate)
PSD	Power spectral density
SE	Schottky emission
SFE	Single field emitter
SEM	Scanning electron microscopy
SF_6	Sulfur hexafluoride

SiO_2	Silicon dioxide
SLEEM	Scanning low energy electron microscopy
SN	Schottky-Nordheim
SNOM	Near-field scanning optical microscopy
SPM	Scanning probe microscopy
STFE	Single tip field emitters
STM	Scanning tunneling microscopy
TE	Thermal emission
TFE	Thermal-field emission
UHV	Ultra-high vacuum
WF	Work function
XPS	Photoelectron Spectroscopy
XRD	X-ray powder diffraction
YAG:Ce	Cerium-doped Yttrium Aluminum Garnet
ZYA	The highest quality HOPG; ZYA is intended for instrument calibration

LIST OF FIGURES

Figure 1.1 Historical development of the configuration of emission cathodes [3]. 16
Figure 1.2 A model of the mechanical holder which is driven by a precise micro-stepper motor. Electrical schematic of the etching set-up is included [A2]. 18
Figure 1.3 A flowchart representing the control software, in particular: (left) one-step method, (left and right) two-step method [A2]..19
Figure 1.4 An example of a produced nano tip, made of a polycrystalline tungsten tip created by the preprogrammed two-step method (left), and the geometrical parameters of interest including commonly used approximations (right) [A2]. 20
Figure 1.5 Stacked plot of Fowler-Nordheim plot slopes (10 samples) as an indicator of tip manufacture reproducibility [A2]...21
Figure 1.6 An example of image obtained by the produced nano tip, made of a polycrystalline tungsten showing surface of a compact disc [A2]. 21
Figure 1.7 Fabricated gate structure after the PECVD process including an example of wiring [A3]. 22
Figure 1.8 Fabrication technology of the gate structure: the fifteen basic steps (a-o) [A3]. 23
Figure 1.9 Profile measurement of an example gate structure created by electron beam lithography; the overall image (left) and the 3D image of the structure (right) [A4]. 23
Figure 1.10 Profile Measurement results: a) 1.480 µm; b) 0.396 µm; c) 0.628 µm [A4]..........................24
Figure 1.11 SEM image obtained by magnifying the structure 10,000x illustrating the side view of the Pt nanorod embedded gate structure (A) and the top view (B) [A4]. 24
Figure 1.12 Potential in the vicinity of the cathode (left) for a system with a bore diameter of 250 µm computed as a function of the extraction voltage for several bore diameters (right) [A3]. 25
Figure 1.13 The emission energy width – FW50 (left) and the axial reduced brightness (right) with respect to the emission current for several bore radii [A3]...26
Figure 1.14 Linear electron density around the optical axis for several bore radii and the emission current 1 µA (left), energy width of the beam in planes perpendicular to the optical axis for several bore radii and emission current 1 µA (right) [A3]..26
Figure 2.1 Experimental setup; the HOPG sample is connected to the negative dc source and the YAG scintillator is grounded, serving as an anode [A5]. 27
Figure 2.2 HOPG FE measurements: I-V characteristics of the emission current as a function of applied voltage (left); corresponding FN plot for the I-V characteristics (right) [A5]..................................28
Figure 2.3 (A) SEM image of the HOPG surface. (B) AFM topography image of the HOPG surface showing the height of sample: a typical example of ridge-like morphological structures on the surface; (C) peak-like structures [A5]..28
Figure 2.4 SEM images of a) W_5O_{14} and b) $W_{18}O_{49}$ nanowires [A6]. 30
Figure 2.5 The XRD spectra of a) W_5O_{14} nanowires; b) $W_{18}O_{49}$ wires [A6]...30
Figure 2.6 I–V curves and corresponding F–N plots: (a, b): W_5O_{14} NW; (c, d) $W_{18}O_{49}$ wire. The first tests are labelled with A, and the second with B. The measurements were performed at 2 µm [A6]. 32
Figure 2.7 FE testing of a $W_{18}O_{49}$ NW at two distances (600 µm and 800 µm): a) I–V characteristics; b) The corresponding F–N plots with linear fits [A6]..33
Figure 2.8 FE properties of a single W_5O_{14} NW in subsequent tests: a) the first test; b) the second test; c) the third test; d) F–N plot of the first test [A6]. 34
Figure 2.9 Stacked Raman spectra of each sample: Pentel Hi-Polymer E (blue), KOH-I-NOOR (red) and STAEDTLER (black) [A9]. 35
Figure 2.10 SEM image of the produced by FIB milling (left) and tip surface detail (right) showing graphite flakes from top before milling. Material used for this tip is STAEDTLER 0.3 HB [A9]. 37

Figure 2.11 SEM image of the tip produced by mechanical sharping from the Hi-Polymer rod (left); by the mechanical sharping from KOH-I-NOOR rod (middle) and the mechanical sharping from Staedtler rod (right) [A9]. 37
Figure 2.12 Etching current of a polymer graphite rod using two various etchants [A8]. 38
Figure 2.13 SEM image of the produced tip by electrochemical etching (left) and the tip surface detail (right) showing graphite flakes. Material used for this tip is Staedtler 0.3 HB [A8]. 39
Figure 2.14 FE analysis of the electrochemically etched tip: the I–V Characteristics for the 5 measurement cycles (let) and the corresponding MG plots (right) [A8]. 39
Figure 2.15 SPM image of the reference sample obtained by PG tip: (left) the surface of a compact disc and (right), the surface of a HOPG [A9]. 41
Figure 2.16 SPM image of the special calibration grid showing tip performance and spatial resolution: (left) 10µm grid, (middle) 5µm grid and (right) 2.5 (left) 10 µm grid [A9]. 41
Figure 3.1 Noise measurement implementation into FEM showing the connection of the electron gun and the noise measurement system located within a Faraday cage. The tip to extraction cathode distance is usually between 0.75–1 mm [A7]. 42
Figure 3.2 The current-voltage characteristics obtained from measurement in FEM (left); The Fowler-Nordheim plot showing F-N slope and field enhancement factor (right) [A7]. 43
Figure 3.3 Noise power spectral density for the total emission current measured at V_{ext} = 325 V (left) and for V_{ext} = 525 V. Both measurements were done at constant pressure and electron energy [A7]. 44
Figure 3.4 Schematic representation of the cathode and optical elements of the scanning electron microscope Tescan Vega v1, where left are distances in mm [A10]. 45
Figure 3.5 The initial voltage noise spectral density for long-time stored cathode that was coated by tungsten oxide; marked as SEM1-1 [A10]. 46
Figure 3.6 Influence of the accelerating voltage: the measured current noise spectral density S_I at anode voltage 5 to 20 kV (left) and the current noise spectral density vs. electron beams current (right) [A10]. 47
Figure 3.7 Influence of the scanning speed: voltage noise spectral density for measured for s=0 (left) and s=12 (right) [A10]. 48
Figure 3.8 Simulated current-voltage characteristics. 50
Figure 3.9 Comparison for the three types of analysis [A12]. 51

LIST OF TABLES

Table 2.1 Properties of analyzed pencil leads, Raman I_D/I_G intensity ratio, calculated crystallite size, relative atomic concentration derived from XPS measurements [A9]. 36
Table 3.1 The mathematical assumptions of the extraction procedure for the scaled field values and the emitter's characterization parameters. 52
Table 3.2 Field emission Orthodoxy Test general criteria. 53
Table 3.3 The extracted scaled field range limits as a function of the local work function. 53

INTRODUCTION

Field emission, also called as *Cold Field Emission* is a discharge of electrons to escape through a surface of a given material subjected to a strong electric field. The material surface acts here as a *barrier* to electron passage. In the mathematical form, the Field electron emission (FEE) process was introduced for the first time by R. H. Fowler and L. W. Nordheim, when they supposed that the nature of FEE is a *deep quantum tunneling* process from an exact triangular potential energy barrier. These assumptions were later modified by Nordheim who considered the existence of the image potential energy for the electrons, which changed the shape of the potential barrier yielding approximately triangular potential energy barrier, often called the *Schottky-Nordheim barrier* [1],[2]. This effect is utilized in the field-emission electron microscope (FEM), which in some instances achieves resolution of atomic dimensions [3].

This is how simple the issue of cold field emission can be described in a textbook, however; the physical and technical reality is much more complicated. Research on the phenomenon of field electron emission and especially the implementation of this phenomenon in the subject of field emission sources of free electrons from solids to vacuum is an *interdisciplinary problem* that can be addressed at many levels. From the experimental development of emitters using modern micro- and nanotechnologies, through the modification of the surface of emitters using thin film physics and chemical sciences, to the latest technologies in electronics and computing, which are used to evaluate and analyze these sources. A separate chapter is devoted to the basic research and theory of cold field emission, which is developed using precise experimental data.

From my point of view, as a researcher who has been involved in the development and fabrication of field emission sources for more than 10 years, I came to the decision that significant part of my work can be improved by inventing and implementing several special methods and instruments intended for preparation and testing of field emission sources yielding effective tools this way. One of the main benefits of the existence of these methods and instruments is a relatively fast way how to obtain a structure for further experiments without the need for a highly erudite coworker. These methods are therefore relatively *easy to control* even and to provide repeatable outputs even for students who have almost no previous experience with the technology. Another benefit is that the methods are developed in relation to a particular hardware or concurrently, so after laboratory testing, they are in fact ready to be transferred to the industrial area or to be offered to another field emission related (FE) laboratory for the purpose of joint research.

The methods presented in this thesis map the results of my work in the field of cold field emission and can be broadly divided into *production methods* and *characterization methods*. The first group of the methods deals with laboratory preparation of the field emission structures using classical approach which is based on electrochemical formation of a sharp tip from a metal wire. I was led to develop the first method, mentioned above, by the daily need

for sharp tips, which are used as a carrier for special thin (activation) layers through which the field emitted electrons pass. Lately, the set-up proved itself that helpful and interesting that we decided to develop even the commercial version, that will go to the beta testing by the start of 2021. The first group of methods mentioned also includes an up-to-date approach which incorporates a combination of state-of-the-art *lithography techniques* and modern *nanotechnologies* to fabricate nanotube-based emitter embedded in a gated structure.

A special attention is paid to seek out for a new cathode material, which can be used to advantage in both approaches. I was particularly interested in modern *nanomaterials* and *nanocomposites*; specifically, I focused on tungsten oxide-based nanowires and polymer graphite. While researching the properties of polymer graphite, I made a unique discovery where I also used the obtained tips as a probe for scanning probe microscopy and thus achieved a significant reduction in cost of operation.

Second group of methods is based on *in-situ testing* and *characterization*. The *in-situ* condition is a fundamental requirement, because in common daily practice it is not possible to remove the emitter out of the vacuum chamber to do for example scanning electron microscopy (SEM), atomic force microscopy (AFM), electron dispersive spectroscopy (EDX), and then return the cathode back into vacuum, with respect to the high sensitivity of the surface. For these reasons, the methods presented in this thesis concentrate on measurement of current-voltage analysis which provide the required information about cathode function. Both methods therefore work with magnitude of *recorded total emission current* collected by faraday cage or by coated scintillator, relative to the extraction and/or acceleration voltage. The first analytical method is based on the application of *noise spectroscopy*, where the noise and fluctuations of the total emission current are monitored. Based on the slope of the power noise spectrum, the specific physical processes taking place in the system are identified. The method has been applied not only to evaluate the operation of an individual emitter, but also to the operation of the entire electron-optical device like scanning electron microscope.

The second of the analytical methods is based on the evaluation of the slope of the recalculated current-voltage characteristics, such as the *Fowler-Nordheim* plot, *Milikan-Lauritsen* plot or the *Murphy-Good* plot. Based on these measurements we obtain several parameters and thus provide quality-related information about performance of the emitter. Based on the existing theoretical apparatus, a computer-based implementation was developed and made public to extract the necessary parameters from a set of experimental data.

The two groups of methods presented form the necessary basis for the experimental development and characterization of cold emission emitters. The methods provide advanced solutions and implement latest technologies in areas where standard solutions do not exist or are very complicated. The methods thus contribute to the search for an ultimate electron source with high beam current density, high electron beam brightness and narrow energy bandwidth.

1. ADVANCED METHODS OF PRODUCTION OF COLD FIELD EMITTERS

To create a cathode or structure with the desired field emission parameters , it is first necessary to select a suitable cathode material. The criteria necessary to ensure its functionality are high melting point, low work function, high mechanical strength, and low chemical affinity.

Currently, a single-crystalline tungsten remains the widely used cathode material precisely because it meets all these criteria except for work function [1],[4]. The average work function of tungsten ($\phi = 4.5$ eV) is slightly higher than that of other transition metals that generally appear to be suitable as well (e.g., Tantalum with a work function of $\phi = 4.31\, eV$ or Hafnium with $\phi = 3.9$ eV). Work function of a metal, which is the primary parameter affecting the ability of the electron to tunnel from the surface to the vacuum, can be affected by coating it with a thin layer, that is usually oxide-based or dielectric-based [A1]. Secondly, it is necessary to ensure a suitable shape of the cathode itself, and to ensure a suitable arrangement of the cathode relative to the extraction electrode (for a triode configuration) or directly relative to the anode (for a diode configuration, e.g. scanning tunneling microscopy (STM) mode) [3],[5],[8].

The shape of the cathode tip is related to the electric field distribution on the cathode surface, where a sufficient current gradient needs to be obtained [6]. The evolution of field emission cathode tips is illustrated in Figure 1.1, which illustrates various configurations that are most often used in setup intended for electron microscopes [1]. Figure 1.1.a shows a classic thermoemission cathode made of bent wire, called a hairpin-filament cathode and its modification improved by sharpening the bending of the wire as illustrated in Figure 1.1.b. This kind of cathodes are based on pure thermal emission (TE). When a sharp wire is spot-welded to the filament (tip diameter is 150 nm – 1 µm) as it is illustrated in Figure 1.1.c., the cathode may operate in thermal-field emission (TFE) mode or in Schottky mode (SE) Figure 1.1.d, based on the temperature and electric field that is applied on a tip apex. However, the sharpness of the tip is not sufficient to get proper field gradient on the tip apex and to operate in a pure cold field emission mode.

Finally, Figure 1.1.d. shows field emission cathode mounted on the classic hairpin-filament, with extra sharp wire (5 nm – 150 nm), which is suitable to work in cold field emission (CFE) mode.

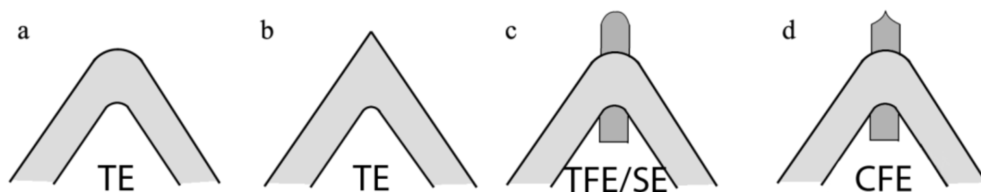

Figure 1.1 Historical development of the configuration of emission cathodes [3].

The novel technical method of automatic tip forming using electrochemical etching will be presented in a subsection 1.1 [A2] including the effect of a dielectric coating on the surface of a field emission cathode, which also proved to be effective solution [A1].

Another way to obtain a novel field emissive cathode with a very low diameter is to use a suitably oriented nanotube [A6],[A3],[8]. Nanotube-based cathodes began to appear after year 2000, which was enabled by technological progress in the field of carbon allotrope research, especially research on single- and multi-wall carbon nanotubes and research on graphene. Although the work function from these materials is comparatively higher than that of tungsten, this is compensated by a higher electric field obtaining a beam with the same or higher current density than by the classical tip-shaped cathode [6].

The development has not stayed with carbon itself, and several other materials suitable for thin nanotube deposition with metal-like conductivity properties have emerged. One of these new materials, the nanowires W_5O_{14} and $W_{18}O_{49}$ were developed as part of the research [A6] and will be presented in subsection 2.2. The design of a lithographic structure in a triode arrangement with an implemented nanotube is discussed in the subsection 1.2. In addition to the fabrication technology, calculations for the optimization of the cathode function within the designed structure are also discussed here.

1.1 Reproducible electrochemical tip formation method

1.1.1 The programmable etching set-up

The most widely used method of forming an extra sharp tip is based on anodic dissolution [A1], [6], [7]. Although the anodic dissolution is an elementary chemical concept, the method of preparing the sharp tip is rather more complicated and there is no standardized, generally available instrumentation for which this theory can be fine-tuned. The individual technical solutions used by companies (e.g., Denka, Japan) are highly classified and there is no automated system for the end user or for laboratory or R&D personnel.

The situation is even more complicated when polycrystalline wire is used instead of single-crystalline wire, which is a highly desirable material for research development and laboratory work, due to lower price of the material [A1], [6]. For this purpose, a computer-driven tip etching method has been proposed to achieve mainly the good repeatability and to keep the ease of use [A2]. In connection with the publication, a utility model was created, which is part of the appendix of this thesis [A13].

The programmable etching set-up described in [A2] is illustrated in Figure 1.2 consisting of three mutually connected blocks that are supplemented by standard GPIB instruments, namely the waveform generator, the DC source, and the multimeter. The instruments are connected directly to the computer providing quick response and data monitoring almost in real time. The mechanical holder provides movement and setting of the wire during the etching. The latter is equipped with a precise micro-stepper motor enabling fine movement which allows a precise setting of the wire on the electrolyte surface during the multiphase etch

process. The mechanical holder that was invented especially for this set-up illustrated in Figure 1.2 consists of: (a) an adjustment screw allowing for a fine manual setting of the wires position by directly rotating the motor's shaft (b). A single step is equal to 2.7 degree of arc, which is transferred to a vertical movement of 1.2 micrometers.

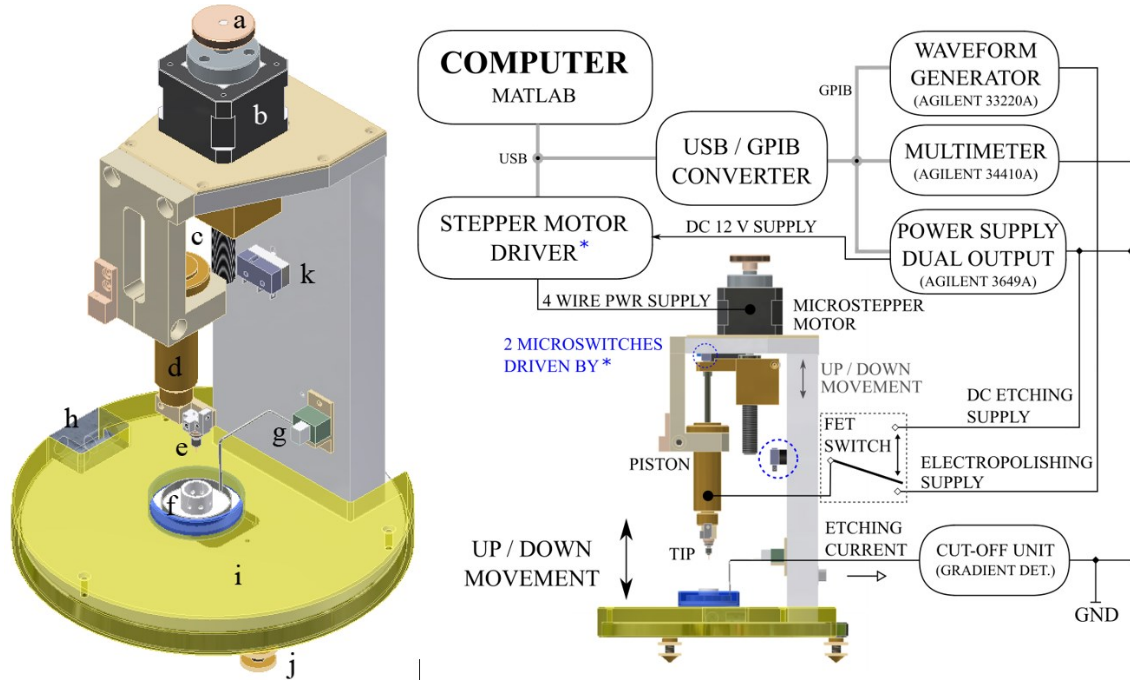

Figure 1.2 A model of the mechanical holder which is driven by a precise micro-stepper motor. Electrical schematic of the etching set-up is included [A2].

The electrical set-up is illustrated in Figure 1.2 and consist of the three main parts. The first part consists of the controlling computer equipped with a self-standing Matlab software prototype that communicates with instruments and evaluates the current-voltage measurements obtained nearly in real time. The second part is the micro-stepper driver unit and the last part consist of three instruments: (1) a multi-meter Agilent 34410A measuring the etching current and voltage, (2) a waveform generator Agilent 33220A providing the alternating current for the electro-polishing and (3) a dual DC source Agilent E3641A providing the etching voltage and supplying the micro-stepper motor driver. The presented configuration is used for the prototype to evaluate the quality of the output of such a designed device.

1.1.2 The implementation of the etching method

The implemented etching method is based on a principle of anodic dissolution of a metal electrode (wire) in liquid electrolyte with voltage applied. For the clamps which were developed be used both in our FEM and etching holder, it possible to use 0.1 up to 0.4 wire diameters, however, the preferred diameter is 0.3 mm. Within the set-up, it is possible to work both with single crystalline and polycrystalline wire. To obtain a sharp tip of a radius of curvature as small as possible, it is necessary to set a proper etching voltage in combination

with a properly concentrated NaOH solution. For our tips, 8–10% solution is used. The etching voltage is set to 6.9 Volts with current limit of 20 mA for both the one-step and two-step method.

The newly invented block illustrated in Figure 1.2, the so-called gradient detector is of highest importance. Its purpose is to instantly disconnect the etching current and thus prevent the tip blunting that may appear. As shown in Figure 1.3 which describes the control algorithm of the production method, the cut-off algorithm is implemented at the end of the two-step method based on the calculation of the second differentiation in real-time.

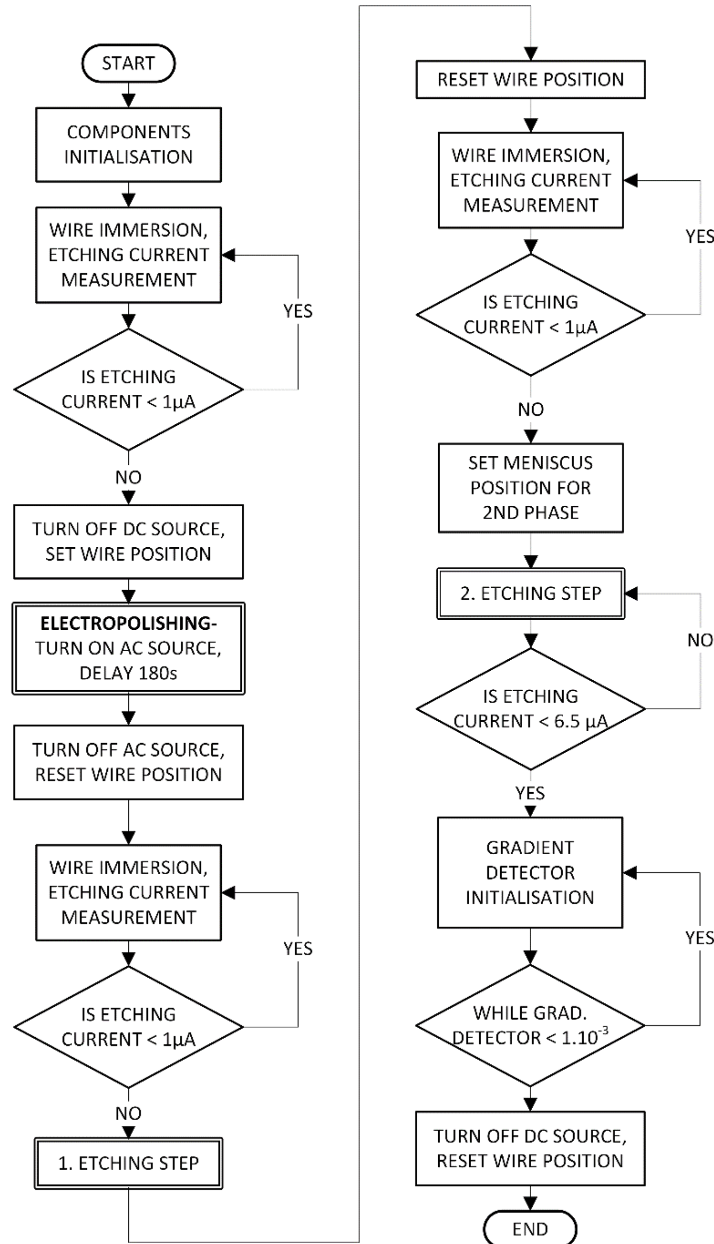

Figure 1.3 A flowchart representing the control software, in particular: (left) one-step method, (left and right) two-step method [A2].

Because of the delay that is caused by the time lag of connected instruments (i.e., a period between two related actions), the detector is implemented directly to the hardware level by creating a self-standing device based on an analogue differentiator circuit, which allows to respond in approx. 25 ns.

For a polycrystalline tip illustrated in Figure 1.4, the tip reproducibility is rather high, which is illustrated by relatively low variance of the taper angle that is equal to 0.05 for our testing set of 100 tips. For single crystalline tips, due to homogenous etching rate caused by uniform crystalline orientation, the variance of the taper angle is even lower allowing to achieve an almost 100% reproducible tip. Despite the higher reproducibility for the single crystalline tips, it still makes sense to keep preparing tips from a polycrystalline W-wire because of its lower price. Moreover, most polycrystalline W-wires are partially oriented due to the pulling process since the grains are often several mm long. For this reason, the crystalline orientation at the tip is uniform allowing to obtain a homogeneous work function at the active area of the tip surface, which is required for stable field-emission based cathodes. The previously mentioned utility model [A13] protects the technical solution developed to implement this methodology.

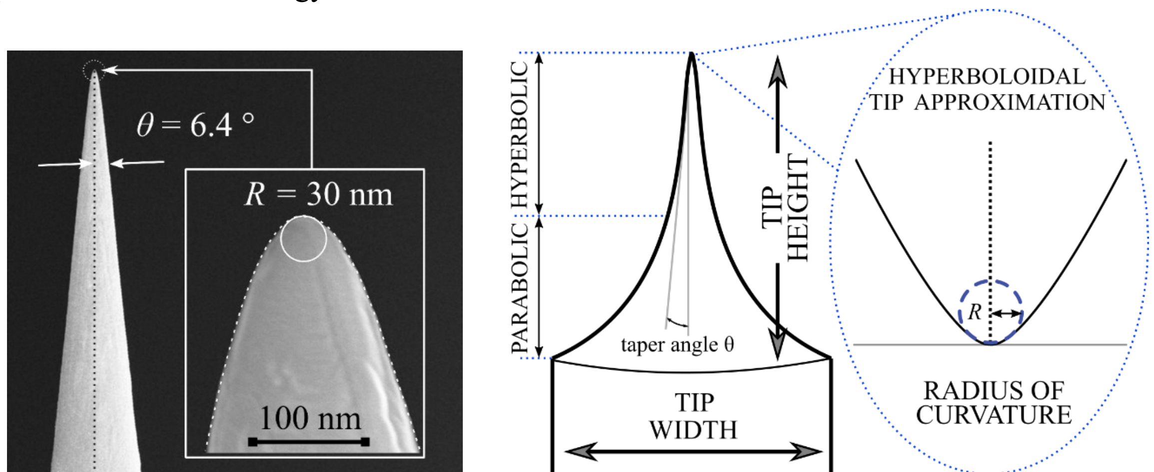

Figure 1.4 An example of a produced nano tip, made of a polycrystalline tungsten tip created by the preprogrammed two-step method (left), and the geometrical parameters of interest including commonly used approximations (right) [A2].

1.1.3 FE and STM tip performance

The tip STM performance and field emission performance, proving its ability to provide a tunneling current is evaluated by the Fowler-Nordheim analysis in the paper [A2]. The tip-testing set-up is generally based on the field emission microscope (FEM), operating in ultra-high vacuum conditions. The original FEM was invented by E. W. Müller in 1936 [9]. Its function can be explained in a very simple way: an applied extractor voltage emits electrons, and the cathode voltage accelerates them towards the grounded anode. Within the frame of our work, the current-voltage measurements have been done for each tip of the testing set and converted to a Fowler-Nordheim plots in which a slope is yielded from each plot. A physical interpretation of the FN plot will be provided in detain in Section 3.2. For now, we state that

the line-shaped plot is consistent with the presence of quantum tunneling, which is the main feature of a field emission emitter. The slope of the FN chart can also be used to compare production output and thus became a basic indicator of the tip reproducibility. An example of slope comparison is represented by a stacked FN-plot of the reduced set of ten samples, as illustrated in in Figure 1.5.

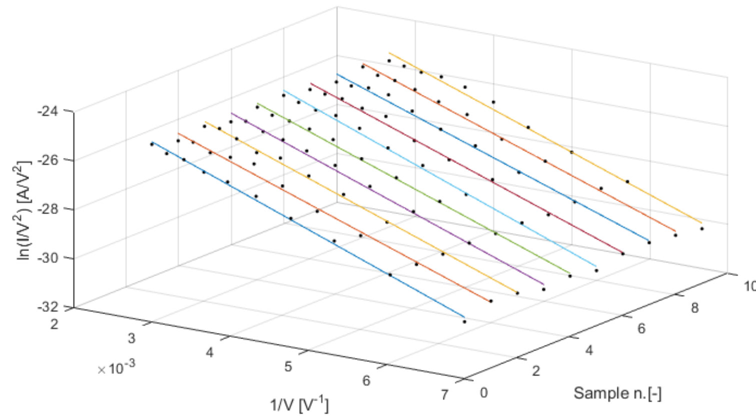

Figure 1.5 Stacked plot of Fowler-Nordheim plot slopes (10 samples) as an indicator of tip manufacture reproducibility [A2].

The STM performance of the prepared tip was tested using NT-MDT Solver Nano, which is a STM device operating at atmospheric pressure (Figure 1.6). Since we are not working in vacuum conditions, it is not possible to maintain perfect surface cleanness of the tip like in comparison to vacuum conditions in the field-emission regime.

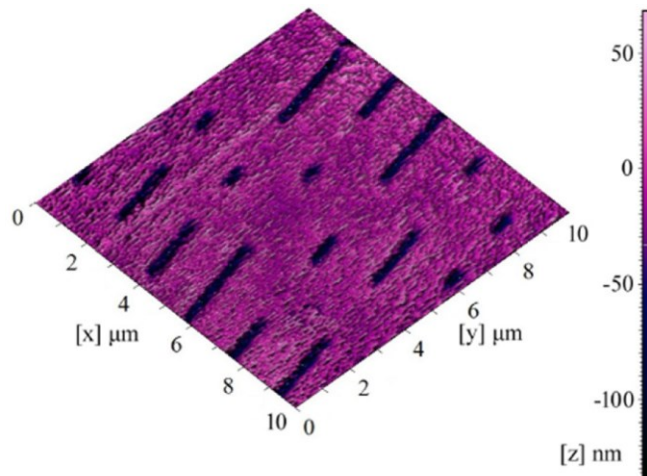

Figure 1.6 An example of image obtained by the produced nano tip, made of a polycrystalline tungsten showing surface of a compact disc [A2].

Thus, the tip gets covered by tungsten trioxide during the operation increasing its radius of curvature and blunting the tip. An oxide layer forms over the tungsten tip due to reactivity with air, further measurements of tunnel current only support the tip degradation. Nevertheless, large area images of conductive materials could be studied by prepared tips at room temperatures [A2].

1.2 Design and fabrication of nanotube-based structures

Carbon nanotubes (CNT) are a quasi-one-dimensional, non-metal structure meeting many of the requirements of field-emission (FE) applications that are unavailable in traditional emitter materials [A3]. In the beginning of the 21st century, it has been anticipated that a carbon nanotube electron source will replace the Schottky emitter for devices such as scanning electron microscopes, but still Schottky emitters are generally considered to be the most reliable field-emission-based electrons sources to be used within existing electron optical devices. In this paper, we have proposed a methodology for fabrication and optimization of a Plasma-enhanced chemical vapor deposition (PECVD) deposited carbon nanotube inside a gate structure [A3]. The novelty of this structure lies in its versatility. It can be used for a variety of nanotubes with respect to the type of precipitate that is placed at the bottom of the gating structure. In this chapter we have demonstrated the growth of platinum nanotubes, but it is also possible to use the tungsten oxide-based nanotubes (W_5O_{14} and $W_{18}O_{49}$) demonstrated in a chapter 2.2 of this thesis.

1.2.1 Fabrication method for a gate structure based on electron beam lithography

The designed system is based on a triode configuration incorporating an extractor enabling the field strength on the tip to be easily changed as illustrated in Figure 1.7.

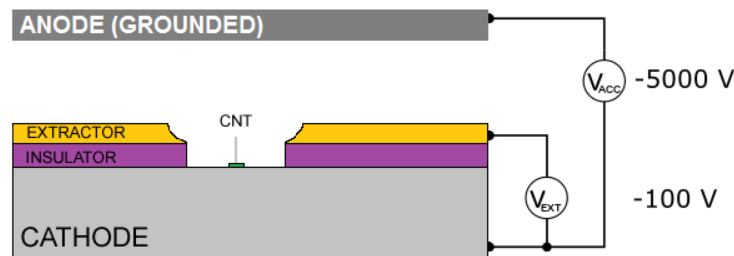

Figure 1.7 Fabricated gate structure after the PECVD process including an example of wiring [A3].

As a feature of this structure, the extraction voltage can be adjusted within a range from zero to approx. 1 kV. The acceleration voltage can be set to as high as 5 kV. The radius of the CNT cathode is influenced mainly by the size of the iron particle from which it grows. The described gate structure is prepared using electron beam lithography and reactive ion-etching that are suitable for this task [A3],[10],[11]. The method consists of the following fifteen technological steps as it is illustrated in Figure 1.8. Firstly, a 300 nm layer of SiO_2 is evaporated in a vacuum onto the surface of a silicon wafer of a (100) orientation. Secondly, a molybdenum layer that is to be used as the extractor is magnetron-sputtered on the oxide layer. The next step incorporates a 300 nm layer of Poly(methyl methacrylate), abbreviated to PMMA, using the spin-coating technique. As the PMMA layer is prepared, it is possible to exposure a pattern using a 100 keV electron beam writer. After the chemical development of the exposed pattern, the plasma developing of resist residues is performed by oxygen plasma. The molybdenum electrode is then etched by a mixture of SF_6 and O_2, followed by removal

of the resist layer. At this moment, it is possible to etch the SiO_2 layer to prepare a space for CNT cathode growth. This is done using reactive ion etching of CF_4/CHF_3 mixture [A3].

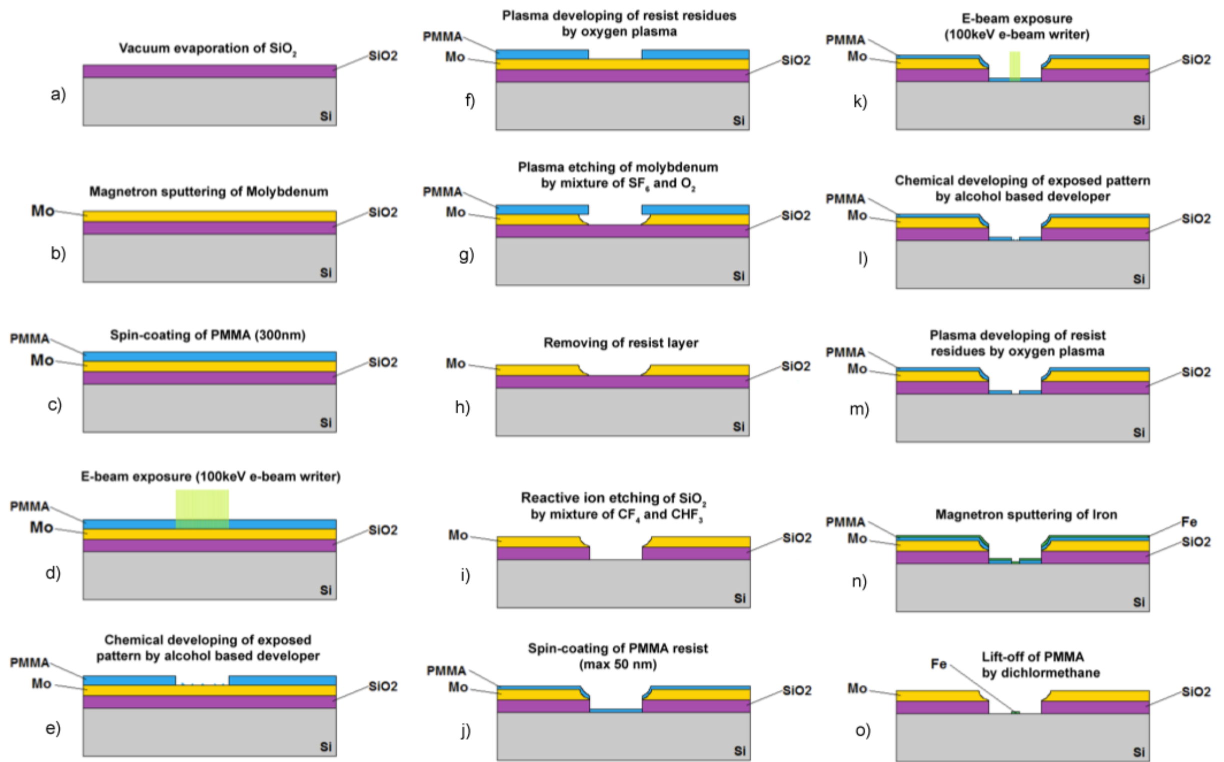

Figure 1.8 Fabrication technology of the gate structure: the fifteen basic steps (a-o) [A3].

The usual lithography steps are performed to prepare the layer of catalytic iron particles: Spin-coating of PMMA resist, E-beam exposure of the pattern and its chemical developing by an alcohol-based developer, followed by plasma developing of resist residues using oxygen plasma. A thin layer of catalytic particles is sputtered after the residues are developed, followed by the lift-off of the PMMA and the PECVD process used for CNT growth.

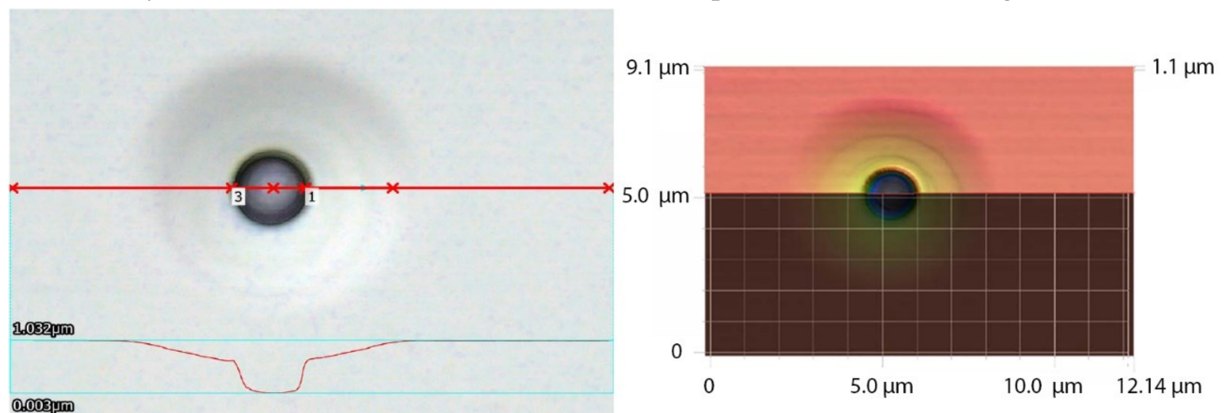

Figure 1.9 Profile measurement of an example gate structure created by electron beam lithography; the overall image (left) and the 3D image of the structure (right) [A4].

An example of a fabricated gated structure is illustrated in Figure 1.9 along with its profile measurements in Figure 1.10. The imaging was performed using a confocal microscope branded Keyence VK-X series [A4].

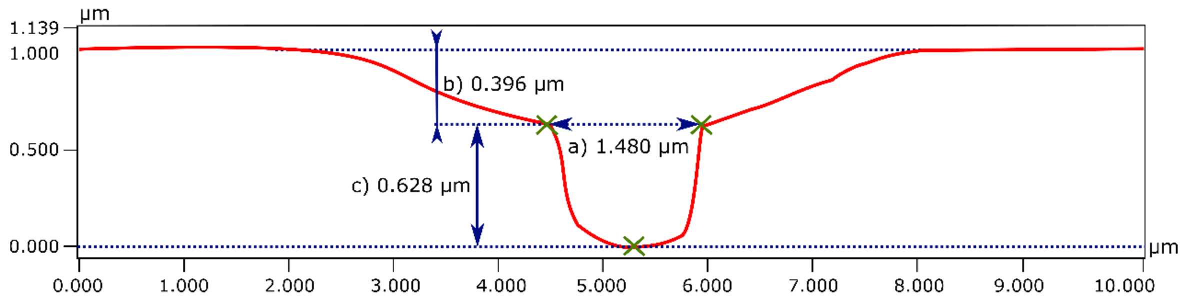

Figure 1.10 Profile Measurement results: a) 1.480 µm; b) 0.396 µm; c) 0.628 µm [A4].

The bore in the SiO_2 substrate bounds the region where the catalytic iron particles react during the plasmatic growth of the CNT. The length of the tube, determined by the PECVD process, will be higher than 0.5 µm to achieve a strong field at the tip of an order of magnitude of units of V/nm which is necessary for the field emission. As the molybdenum used for the extractor electrode has good chemical resistivity [12], it is possible to functionalize the CNT's surface using plasmatic or chemical methods. The bore diameter in the extractor is calculated based on a method by Radlicka [13]. As mentioned at the beginning of the chapter, the structure can also be embedded with another nanotube that is not carbon-based.

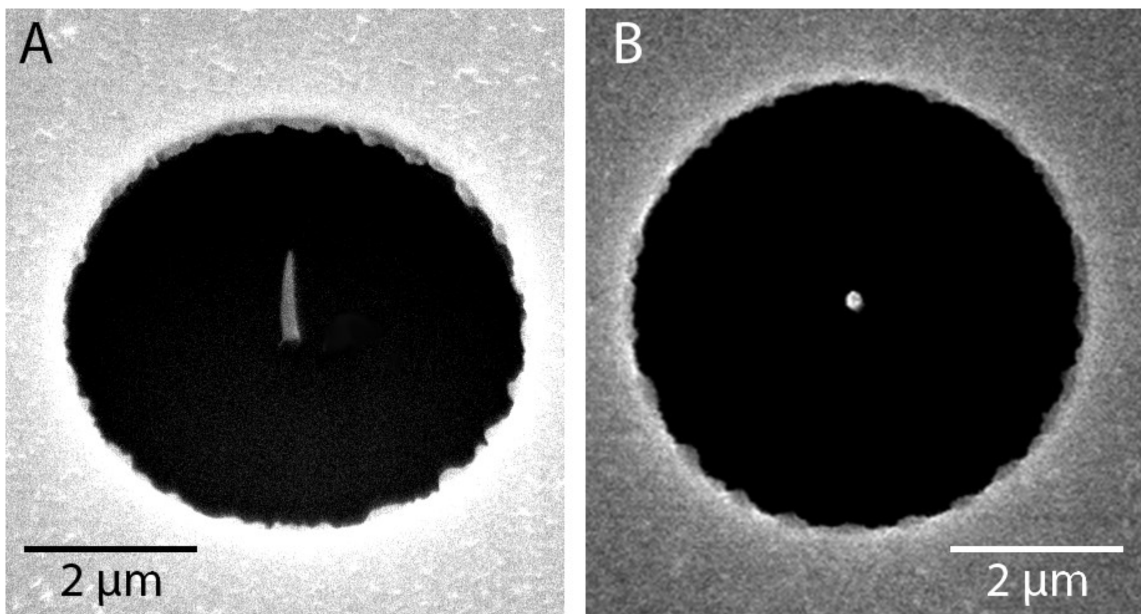

Figure 1.11 SEM image obtained by magnifying the structure 10,000x illustrating the side view of the Pt nanorod embedded gate structure (A) and the top view (B) [A4].

Figure 1.11 illustrates an identically made structure with an aperture size of 5 µm, which is fitted with a platinum nanorod fabricated using electron beam assisted deposition [A4],[14]. The imaging was performed using a scanning electron microscopy branded JEOL JSM-7001F.

1.2.2 Simulation and optimization of optical properties of gated CNT source

The CNT sources work at room temperature and a high field, so the emission is well described by the thermal-field emission model [13] which is a generalization of the standard cold field emission model (or Fowler-Nordheim model that is discussed in bigger detail within the chapter 3.2 [A3].

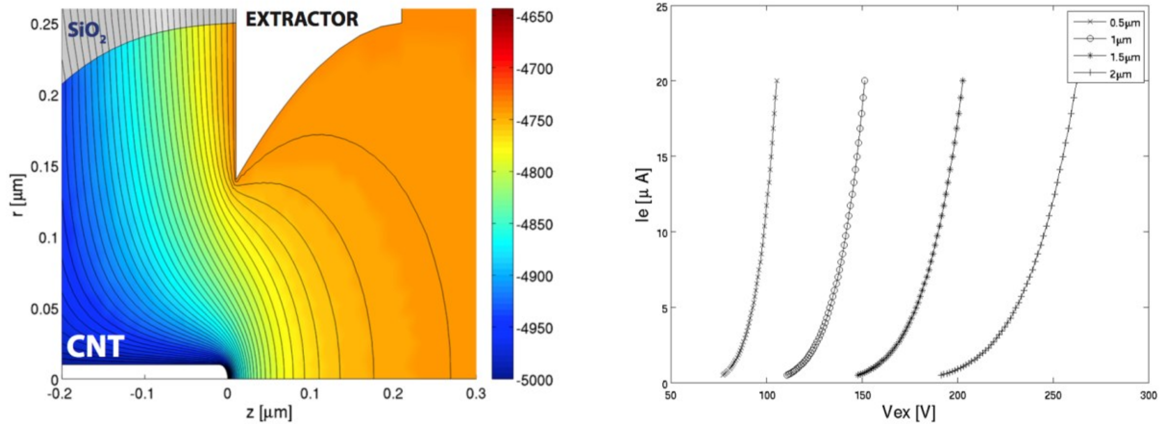

Figure 1.12 Potential in the vicinity of the cathode (left) for a system with a bore diameter of 250 µm computed as a function of the extraction voltage for several bore diameters (right) [A3].

The electrostatic field in the system was computed using the first order finite element method (FEM). We used a triangular mesh which is sufficiently dense in the vicinity of the CNT with a tip diameter of 20 nm, and which expands in other parts of the system. The field calculation took about five minutes with a mesh consisting of about a million triangular elements. The emission was studied for several extractor bore diameters within a range from 0.5 to 2 µm. The typical potential in the vicinity of the cathode is plotted in Figure 1.12 (left). The emission current can be computed as a function of the extraction voltage using a thermal field emission model; Figure 1.12 (right).

As the size of the CNT source is very small the energy distribution and brightness are strongly influenced by the stochastic Coulomb interactions (CI) in the beam. Their effect on the energy distribution was simulated using a Monte-Carlo simulation presented in [13] yielding the emission energy width of the beam (Figure 1.13, left) and the axial reduced brightness (Figure 1.13, right). The effect of the bore diameter in the extractor was analyzed using another MC simulation: (a) The initial conditions of emitted electrons were randomly generated to fulfill the theoretically computed current density j_{TF} and the energy distribution in the thermal field emission regime [A3]. (b) The electrons were traced through the system field including the effect of the stochastic CI.

We simulated a beam consisting of 20,000 electrons. For high efficiency, the beam was separated into sub-beams of 400 electrons bordered by 100 electrons on both ends to eliminate the effect of beam separation.

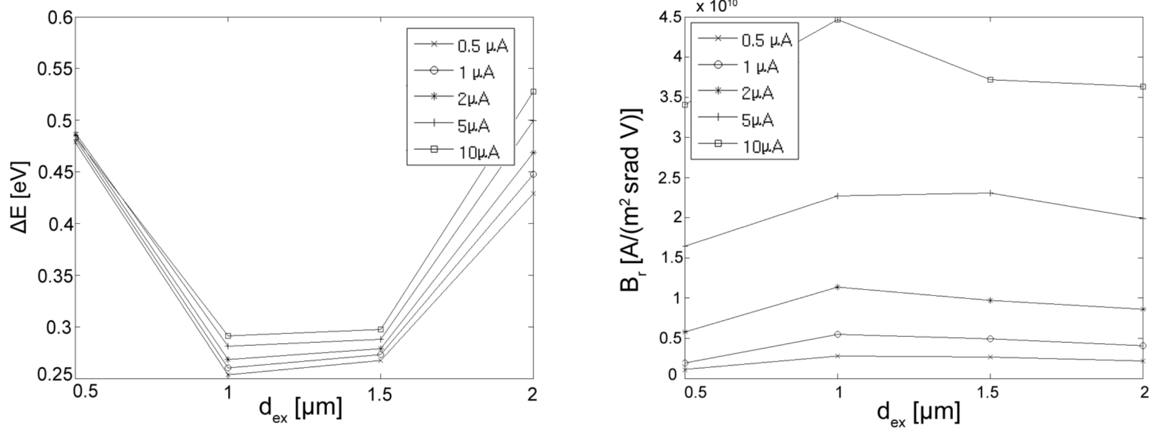

Figure 1.13 The emission energy width – FW50 (left) and the axial reduced brightness (right) with respect to the emission current for several bore radii [A3].

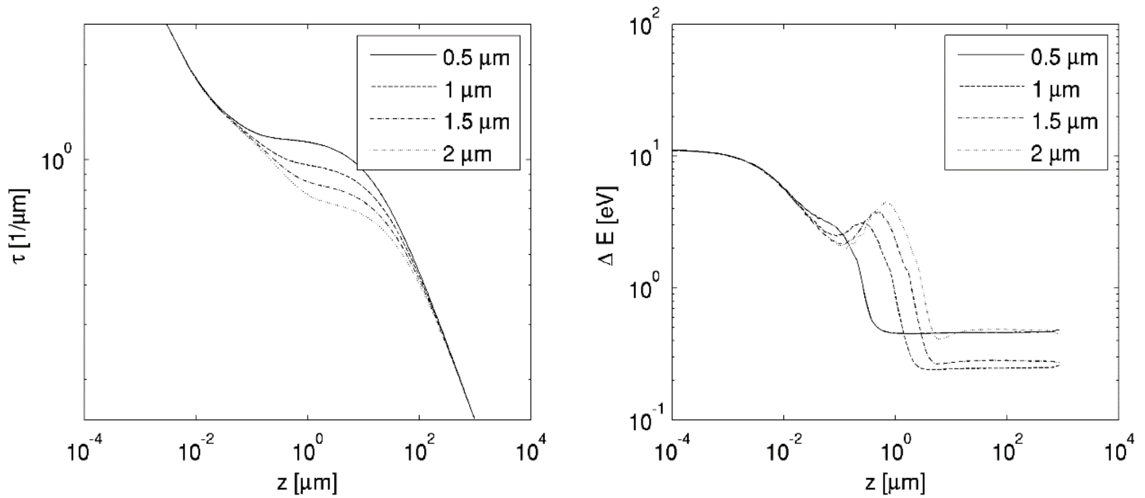

Figure 1.14 Linear electron density around the optical axis for several bore radii and the emission current 1 µA (left), energy width of the beam in planes perpendicular to the optical axis for several bore radii and emission current 1 µA (right) [A3].

The influence of the beam current on the global electrostatic field was ignored. (c) The resulting energy width and the reduced brightness were computed from the beam properties in the anode plane. The effect of the stochastic CI is proportional to the electron density in the vicinity of the cathode which decreases with increasing bore diameter; Figure 1.14 (left). On the other hand, the equipotential lines are more curved with increasing bore radius which leads to higher energy width in each plane perpendicular to the axis; Figure 1.14 (right). In the region close to the extractor plane the particles that are further from the axis are accelerated by different potential differences than particles near the axis. This increases the effect of the stochastic CI. The results presented in Figure 1.13 show that the optimal value of the bore diameter is between 1 and 1.5 micrometers, where the maximal brightness and the minimal energy width were achieved for all emission currents.

2. NOVEL MATERIALS FOR COLD FIELD EMITTERS

2.1 Cold field emission from graphite surface

In the paper [A5], we were the first to measure and describe the field emission behavior from the surface of exfoliated highly ordered pyrolytic graphite (HOPG) correlating it with the sample's topography that was obtained using SEM and AFM. Therefore, after CNT, graphite is meant to be another suitable allotrope of carbon applicable for fabrication of field emission structures.

A sample of single-crystalline HOPG of a ZYA grade, was used for the experiment. The upper layers of HOPG were mechanically exfoliated using 3M adhesive tape and the freshly prepared sample was immediately placed via a vacuum feedthrough into a high vacuum chamber with a residual gas pressure of 10^{-7} Pa. The chamber allows for sample cleaning using electron bombardment heating and/or argon ion sputtering prior to electron microscopy observation in the adjacent ultra-high vacuum (10^{-8} Pa) chamber [A5]. To remove any possible contaminants that may have stuck to the surface, the HOPG slab was annealed to 900 degrees Celsius for 20 minutes by means of electron bombardment heating. After the cleaning procedure, the sample was moved via a feedthrough to the ultra-high vacuum chamber equipped for scanning low energy electron microscopy (SLEEM) [15]. There, the sample was connected to a negative DC source providing the necessary extraction voltage. The emitted electrons were collected by a cerium-doped Yttrium Aluminum Garnet (YAG:Ce) scintillator, allowing to measure the emitted current. A schematic arrangement is illustrated in Figure 2.1 [A5].

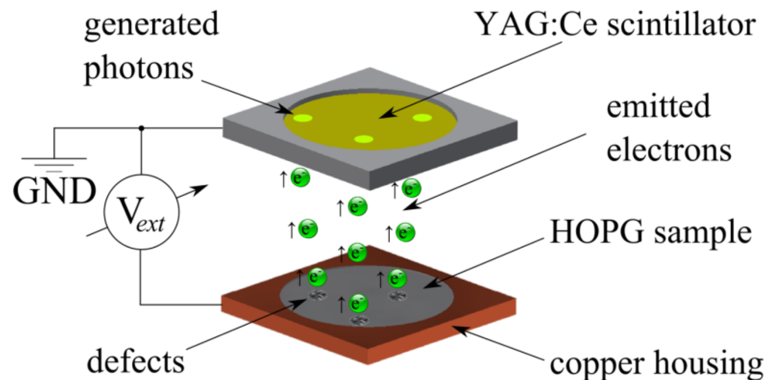

Figure 2.1 Experimental setup; the HOPG sample is connected to the negative dc source and the YAG scintillator is grounded, serving as an anode [A5].

The effect of field emission occurs only at disrupted surface, i.e., surface containing ripped and warped shreds of the uppermost layers of graphite. These deformations provide the necessary field gradients which are required for measuring tunneling current caused by field electron emission. Results of the field emission measurements were correlated with other surface characterization methods such as scanning electron microscopy (SEM), scanning

near-field optical microscopy (SNOM) or atomic force microscopy (AFM) [A5]. Figure 2.2 (left) illustrates the I-V characteristics showing a nearly exponential increase of the current, where $I\ [A]\ =\ 2 \cdot 10^{-12}\exp(0.0036 \cdot \mathrm{V_e})$. Also, the Fowler-Nordheim plot (FN) Figure 2.2 (right) confirmed the presence of electron tunneling because of the nearly linear plot.

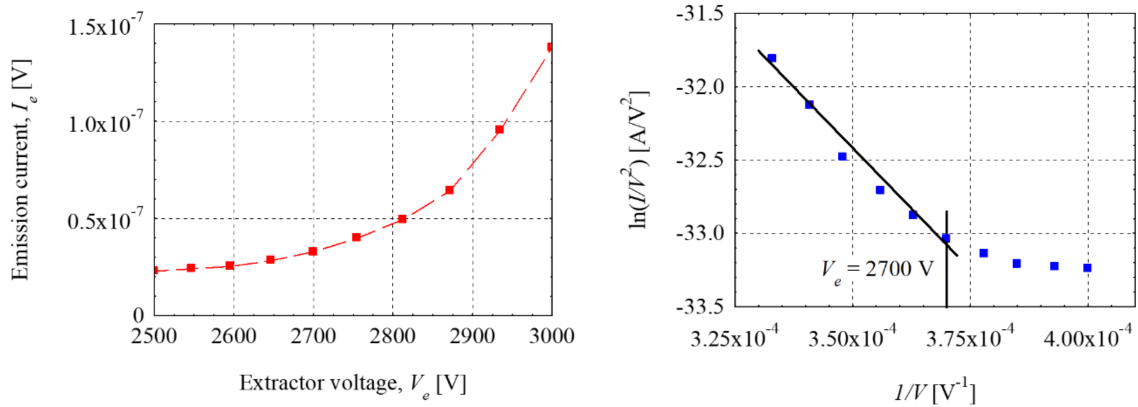

Figure 2.2 HOPG FE measurements: I-V characteristics of the emission current as a function of applied voltage (left); corresponding FN plot for the I-V characteristics (right) [A5].

As shown in Figure 2.2 (right) the non-linear behavior starts to appear at $\mathrm{V_e}\ =\ 2700\ \mathrm{V}$ suggesting the current contribution of larger defects, i.e., defects with lower field gradient. The nonlinearity of the plot can be explained by the presence of multiple microscopic electron sources. As each of them has a different geometry, the field gradient also differs, and with it the voltage necessary for the onset of field emission. This caused a gradual activation of individual sources making the I-V plot non-exponential [A5].

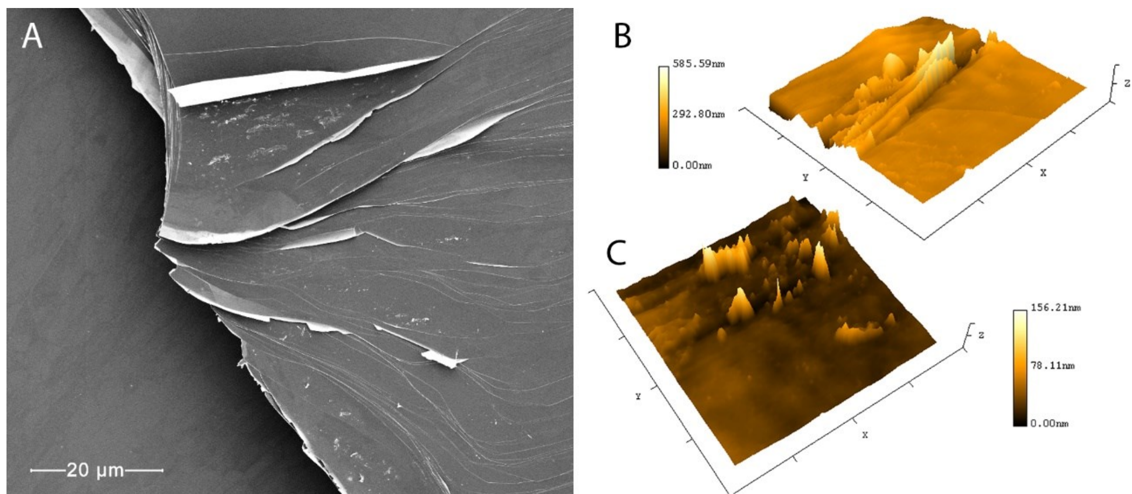

Figure 2.3 (A) SEM image of the HOPG surface. (B) AFM topography image of the HOPG surface showing the height of sample: a typical example of ridge-like morphological structures on the surface; (C) peak-like structures [A5].

The morphology of the shred was characterized by AFM and SEM. Typical shreds found on the sample surface are shown in Figure 2.3 (A) and (B). The SEM image shows an

otherwise smooth HOPG surface with some partly exfoliated shreds. The shreds exhibit a layered structure with folds and corrugations. The results obtained in this paper became the basis for further experimental work on the polymer graphite described in Subsection 2.3.

2.2 Cold field emission from tungsten oxides

2.2.1 Material analysis of the W_5O_{14} and $W_{18}O_{49}$ nanowires

Metal oxides have been often used to create so-called activation layer for a cold- or thermionic field emission cathode. For this reason, it makes good sense to try to create a nanotube (or generally a nanowire) from an oxide-based material and take advantage of its favorable material properties as they are introduced in the following paragraph.

Among the metal oxides, one of the most important are tungsten oxides which belongs to a family of transition metal oxides, and have currently various applications in photocatalysis [16], electrochemistry and energy conversion [17], gas sensors [18], and as recently found also in phototherapy [19]. Besides stoichiometric WO_3, which exists at different temperatures in several structures, such as monoclinic, triclinic, tetragonal, orthorhombic, cubic, and hexagonal [20], oxygen reduced WO_{3-x} phases are also known, where tungsten oxidation state for some atoms changes from W^{6+} to W^{5+}. Among these phases, $W_{18}O_{49}$ is the most reduced stable phase. Less reduced W_5O_{14} crystals in needle like shape were reported as a homogeneous phase using iron in 1978 [21] and nickel in 2007 [22] as growth promoters. Oxygen vacancies in these sub-stoichiometric WO_{3-x} phases create donor states and strongly improve the electrical conductivity. In contrary with the stoichiometric WO_3 semiconductor with a band gap in the range of 2.5–3.2 eV [23] and electrical conductance from 10 to 10^4 Ωcm [24],[25]; the reduced W_5O_{14} phase growing as nanowires, revealed metallic conductivity with an electrical resistance of 25 μΩcm [22]. For comparison, electrical resistance of the most reduced $W_{18}O_{49}$ wires is 2750 μΩcm [25], i.e., more than two orders of magnitude larger with respect to W_5O_{14}.

In our paper [A6], we reported a comparative study of surface and field emission properties of W_5O_{14} and $W_{18}O_{49}$ nanowires (NWs) synthesized by a modified method using WO_3 and elemental tungsten as starting materials in the iodine transport method using nickel as a growth promotor. The method is in detail described here [22].

The crystalline structure of the NWs was examined by XRD at room temperature with D4 Endeavor diffractometer (Bruker AXS) using a quartz monochromatic Cu Kα1 radiation source ($\lambda = 0.1541\ nm$) and a Sol-X dispersive detector. Morphology, surface structure and work functions of W_5O_{14} and $W_{18}O_{49}$ NWs were measured by scanning electron microscope (SEM) Supra 36 V P, Carl Zeiss, scanning tunneling microscope (STM), atomic force microscope (AFM), and Kelvin probe operating in ultra-high vacuum (Omicron VT-AFM) [A6].

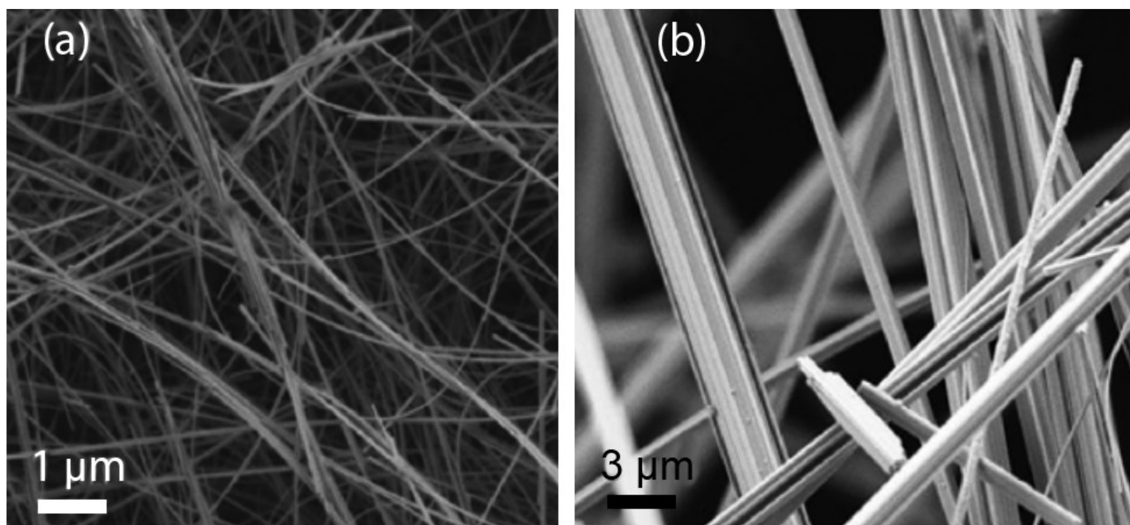

Figure 2.4 SEM images of a) W_5O_{14} and b) $W_{18}O_{49}$ nanowires [A6].

Electron microscopy images (Figure 2.4) of (a) W_5O_{14} and (b) $W_{18}O_{49}$ wires show that the length of both types of NWs exceeds several ten μm. The nanowires are very rigid and have a homogeneous diameter along their length. The mean diameter of the W_5O_{14} NWs is in the range of 100–200 nm, while majority of the $W_{18}O_{49}$ wires are thicker (up to 3 μm) with rare thinner ones.

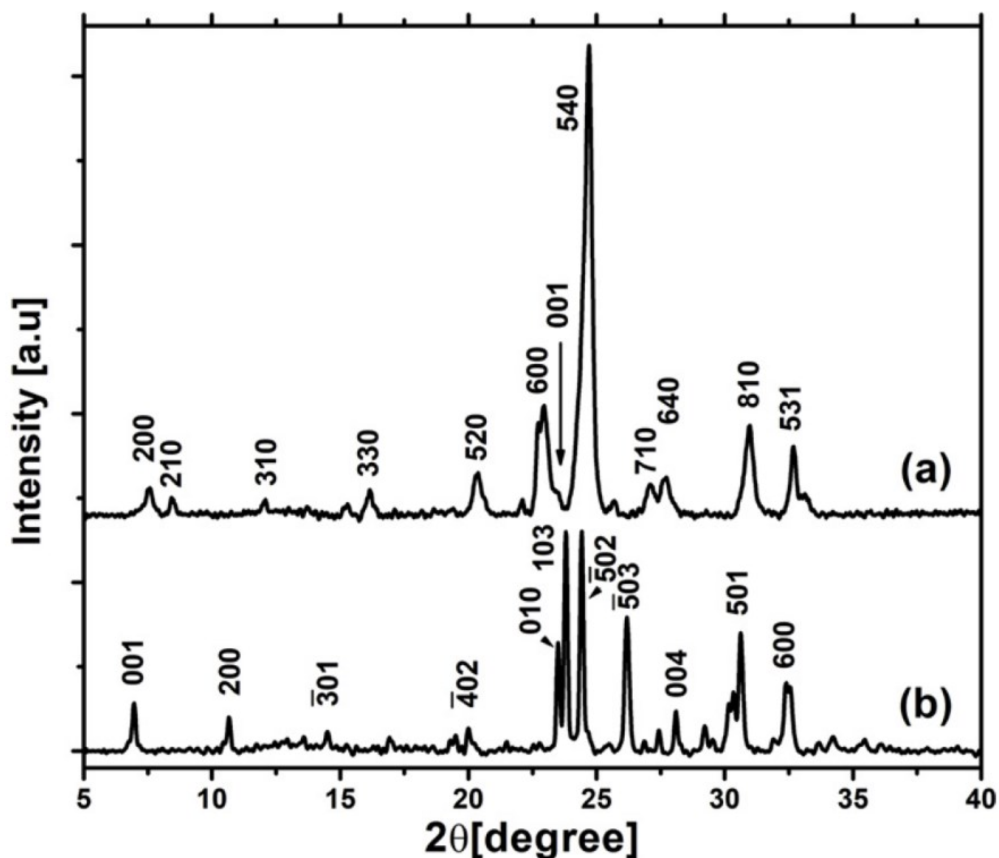

Figure 2.5 The XRD spectra of a) W_5O_{14} nanowires; b) $W_{18}O_{49}$ wires [A6].

The X-ray diffraction (XRD) spectra (Figure 2.5) of (a) W_5O_{14} and (b) $W_{18}O_{49}$ match the tetragonal W_5O_{14} structure (JCPDS 71-0292) with lattice parameter: a=23.33 Å and c=3.78 Å, and monoclinic W18O49 phase with lattice parameters: a=18.32 Å, b=3.78 Å, c=14.03 Å and β=115.20° (JCPDS 036-0101) [27], respectively. There are no indications of any other WO_{3-x} phase in the samples. The sharps peaks in the XRD pattern are clear evidence of high crystallinity of the materials.

STM was used to study the surface corrugation of the NWs, and structure of their longitudinal ends showing surface corrugations on a W_5O_{14} NW that are typically several nm deep and have a periodicity of 20–30 nm in comparison to W_5O_{14}, therefore the corrugations in $W_{18}O_{49}$ wires are shallower with a typical periodicity of around 10 nm [A6].

Kelvin probe force microscopy (KPFM) was used to measure the work functions of the wires at the nanoscale. The WF values obtained on W_5O_{14} single NW were from 4.20 to 4.34 eV (which is slightly lower than polycrystalline pure tungsten i.e., 4.53 eV) and on $W_{18}O_{49}$ the WF values were from 4.55 eV to 4.57 eV. The method of measurement is in detail described in [A6].

2.2.2 Field emission testing of W_5O_{14} and $W_{18}O_{49}$ NWs in microscopic regime

FE measurements with both kinds of wires were carried out in the STM chamber at the same distance ($2 \pm 0.2\,\mu m$) between a wire's apex and HOPG, which was used as an electron collector. The threshold voltages (onset voltages) for FE were determined from the minima of the corresponding Fowler–Nordheim (F–N) plots. After comparative testing, FE from a W_5O_{14} NW was studied also at distance of 4 and 5 μm [A6].

The comparative FE studies were performed on two wires with very different diameters in the same FE configuration. A W_5O_{14} NW, 14 μm long and 109 nm in diameter, was attached on a tungsten wire using FIB. The $W_{18}O_{49}$ wire, 247 μm in length and 4 μm in diameter, was attached on a Pt/Ir wire with silver epoxy paste. Then both tips were transferred into the UHV-STM chamber (7×10^{-10} mbar) and tested without any cleaning or annealing [A6].

Firstly, the so-called activation process was studied, in which the FE tips were cleaned of adsorbents and/or impurities. Figure 2.6 shows current-voltage (I–V) characteristics of the first (A) and the second (B) consecutive test and their corresponding F–N plots: a-b: W_5O_{14} NW, c-d: $W_{18}O_{49}$ wire. Firstly (A), the so-called activation process was studied, in which the FE tips were cleaned of adsorbents and/or impurities. Significant changes have been noticed in the onset voltages in two consecutive FE measurements, which dropped for both wires in the second test. A possible reason is the removal of adsorbates from the top end of the wires. Also, the knees in the F–N plots of the first tests can be explained with desorption of adsorbates under high electric fields [28].

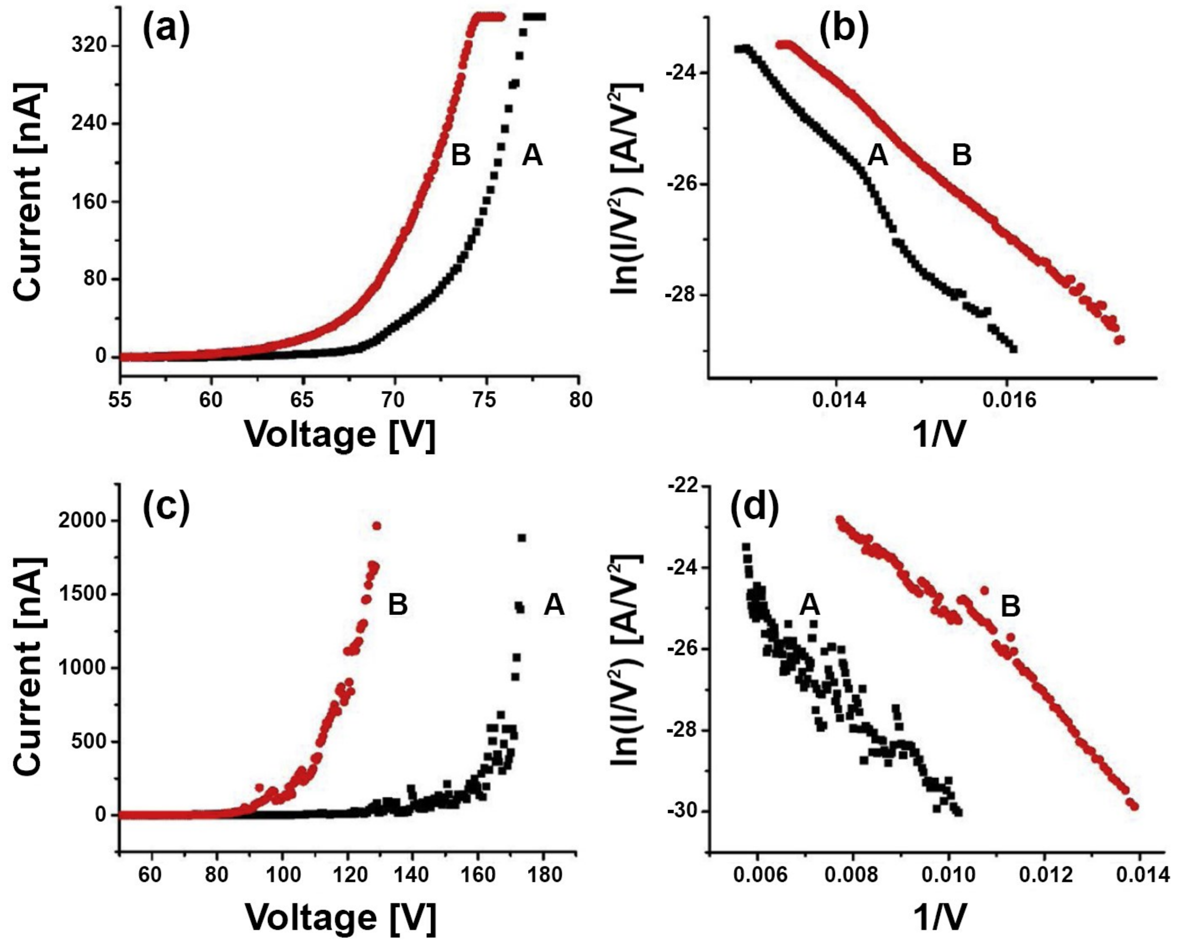

Figure 2.6 I–V curves and corresponding F–N plots: (a, b): W_5O_{14} NW; (c, d) $W_{18}O_{49}$ wire. The first tests are labelled with A, and the second with B. The measurements were performed at 2 µm [A6].

2.2.1 Field emission testing of $W_{18}O_{49}$ and W_5O_{14} NW in macroscopic regime

The FE experiments at macroscopic distances (≈ 1 mm) were performed in two configurations: the $W_{18}O_{49}$ NW in a negatively biased cathode and grounded anode configuration, and W_5O_{14} NW in a positively biased electron extractor configuration.

For the $W_{18}O_{49}$ NW, a 10 µm long and 180 nm in diameter, was attached on a tungsten electrochemically etched tip using FIB. The tip was annealed by the electron bombardment procedure for 15–20 min and flashed for 20 s. Thereafter, FE measurements of the $W_{18}O_{49}$ NW were carried out at two distances: 600 µm and 800 µm from the Si wafer which served as a collection electrode.

Figure 2.7 shows the FE I–V characteristics for both distances and their corresponding F–N plots. At each position, FE experiments were performed three times to confirm repeatability. The FE currents were limited to 45 nA with the aim to prevent damage of the nanowire. The onset voltage of FE was 322 ± 1 V at 600 µm and 354 ± 1 V at 800 µm. The limit current was reached at 433 V and at 463 V, respectively (Figure 2.7.a). No significant differences were detected when the voltage was ramped up or down. In the F–N plots (Figure

2.7.b), the straight lines indicate the standard barrier-tunneling mechanism of the field electron emission. No degradation was observed. The field enhancement factors were determined using FN formalism incorporating the value of work function (i.e., 4.56 eV) experimentally obtained by KPFM. The field enhancement factors were 5050 ± 30 and 6450 ± 30 for 600 and 800 μm, respectively.

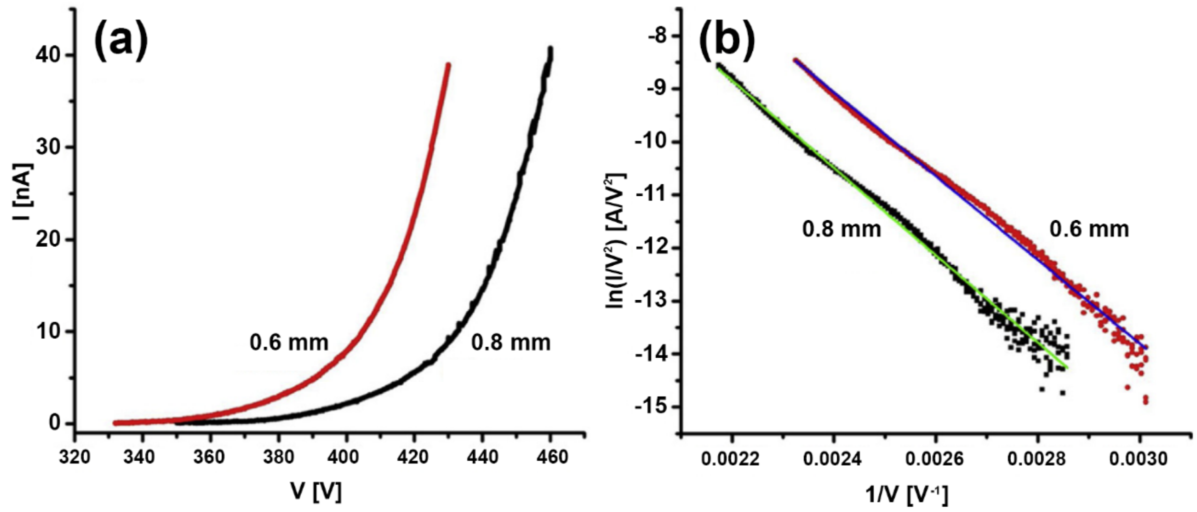

Figure 2.7 FE testing of a $W_{18}O_{49}$ NW at two distances (600 μm and 800 μm): a) I–V characteristics; b) The corresponding F–N plots with linear fits [A6].

The W_5O_{14} NW used in the macroscopic FE regime measurement was 5 μm long, 148 nm in diameter and mounted on an electrochemically etched tungsten wire by FIB. The experiment took place in an UHV chamber at 2×10^{-9} mbar with a separation of 1060 μm between the NW apex and the extractor plate. Three FE tests were performed. The voltage was manually increased step by step in 5 min intervals for the current to stabilize.

In the *first test*, the voltage was increased to 990 V and the corresponding FE current reached 183 nA. The I–V curve (Figure 2.8.a) is exponential and relatively smooth. The *second test* revealed the maximum FE current of 1.2 μA at 890 V, while at higher voltages the current started to decrease. The FE current (990 nA) at 990 V was more than 5 times larger (Figure 2.8.b) than in the first test. In the *third test*, the maximum current of 1.063 μA was obtained at a higher voltage as in the second test, i.e., at 1063 V, while at 990 V the current was 1008 nA, i.e., again larger than in both previous tests (Figure 2.8.c).

The explanation of the increase of FE current relate to the absence of cleaning of the emitters before FE testing. The subsequent tests gradually removed adsorbates from the NW, and the FE current consequently increased. Relatively high currents, which could cause diffusion of tungsten atoms and structural changes of the nanowire, could be the origin of degradation of the FE tip. Field enhancement factor from the F–N plot corresponding to the first test (Figure 2.8.d) was ≈ 17.000, while using the Eq. 3, it is 7 ± 0.5. The onset fields for three subsequent tests were 3.3 ± 0.3 V/μm, 3.4 ± 0.3 V/μ, and 3.5 ± 0.3 V/μm.

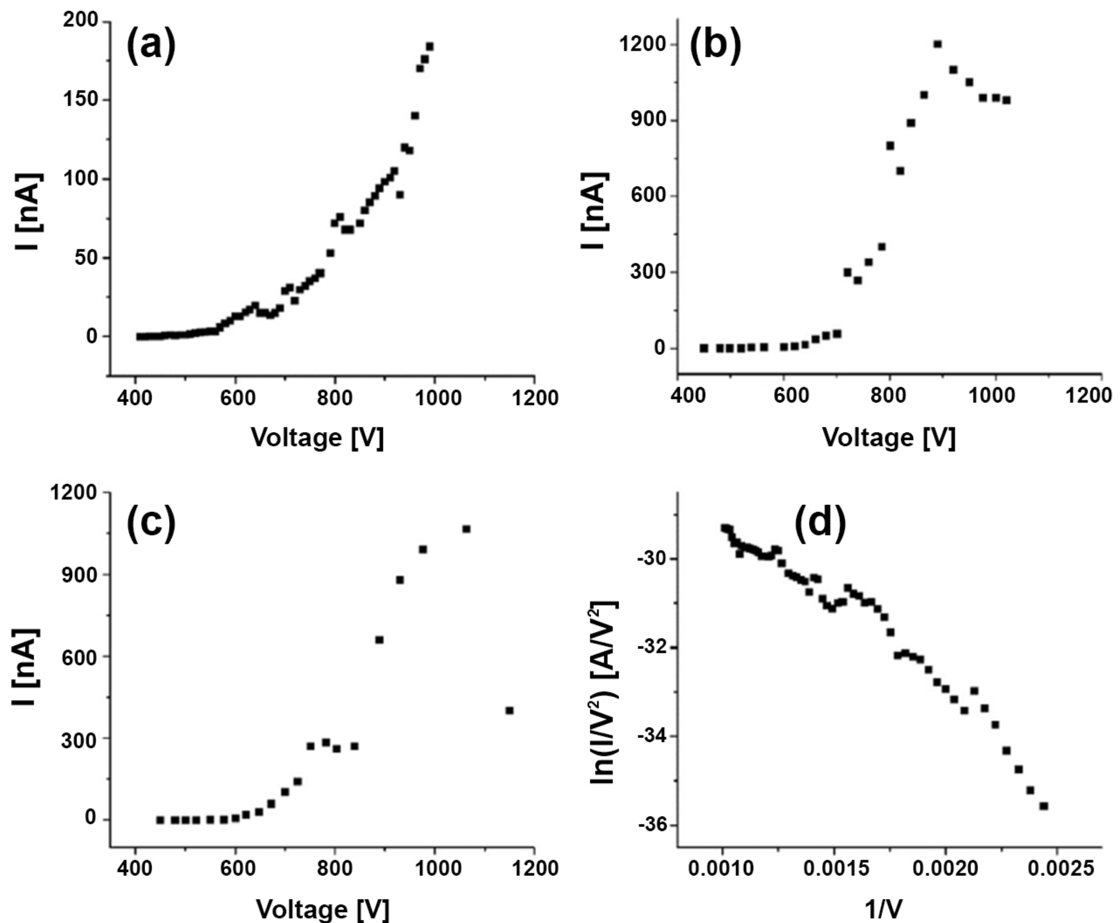

Figure 2.8 FE properties of a single W_5O_{14} NW in subsequent tests: a) the first test; b) the second test; c) the third test; d) F–N plot of the first test [A6].

In comparison to the $W_{18}O_{49}$ NW, the W_5O_{14} NW was found to be a more efficient field emitter because of its lower work function and lower onset voltage. The obtained results open several perspectives in utilization of tungsten oxide nanowires as a source of low-energy electrons in different devices. In particular, the W_5O_{14} NWs are promising with larger electric conductance and typically smaller diameter than $W_{18}O_{49}$ NWs, as well as due to relatively high field enhancement factors they can be activated at relatively low electric fields [A6].

2.3 Cold field emission from polymer graphite

Polymer graphite (PG) is a relatively young nanocomposite material that was invented mainly for micro-pencil refills containing a polymer-based binding agent and graphite flakes [A7],[A8],[A9]. Following the research on field emission from the HOPG surface presented in Chapter 2.1 and considering the favorable properties of graphite, it was logical to continue investigating this special composite form of Graphite, which pleasantly surprised us not only with its FE properties.

The PG has high conductivity and immunity against surface contamination, with a low price, which make it seem a highly suitable material for electrode manufacture in general

[29],[30],[31]. Such pointed graphite rods may find various applications in analytical methods; for example, they can be used as a source of free electrons [A7],[A8] or they can operate with a tunneling current in Scanning Probe Microscopy (SPM) conductive modes [A9]. During our research, we described the material properties of polymer graphite from several manufacturers and presented 3 methods of tip formation, each of which is suitable for a different application.

2.3.1 Material properties of the polymer graphite

The graphite pencil rods have generally two main constituents: graphite itself and various clay minerals or rocks, which are finely ground (small amounts of wax or polymers are also present to serve as a binder) [31]. In the paper, it was also reported that polymer graphite contains usually from 30% up to 80% of sp^3 hybridized carbon which may shift its properties more toward those of diamond-like carbon (DLC) structures. The macroscopic hardness of polymer graphite rod is determined by the graphite–clay ratio. An increase in the amount of clay will result in a harder rod that is therefore less smudgy when used on paper, whereas by reducing the amount of clay, a softer, more graphite-rich rod may be produced [A8]. The market of pencil leads consists of several popular brands of mechanical pencils (e.g., Pilot, Erich Krause, Proff, Parker, KOH-I-NOOR, Stabilo, Pentel, Staedtler, Faber-Castell, Rotring, Bic, Conte, Index, Lamy, Constructor, and many others). Each product is based on a special fabrication technology. For our experiments, we have used three different brands of polymer graphite rod, in particular: KOH-I-NOOR, Staedtler, and Pentel Hi-polymer E [A9].

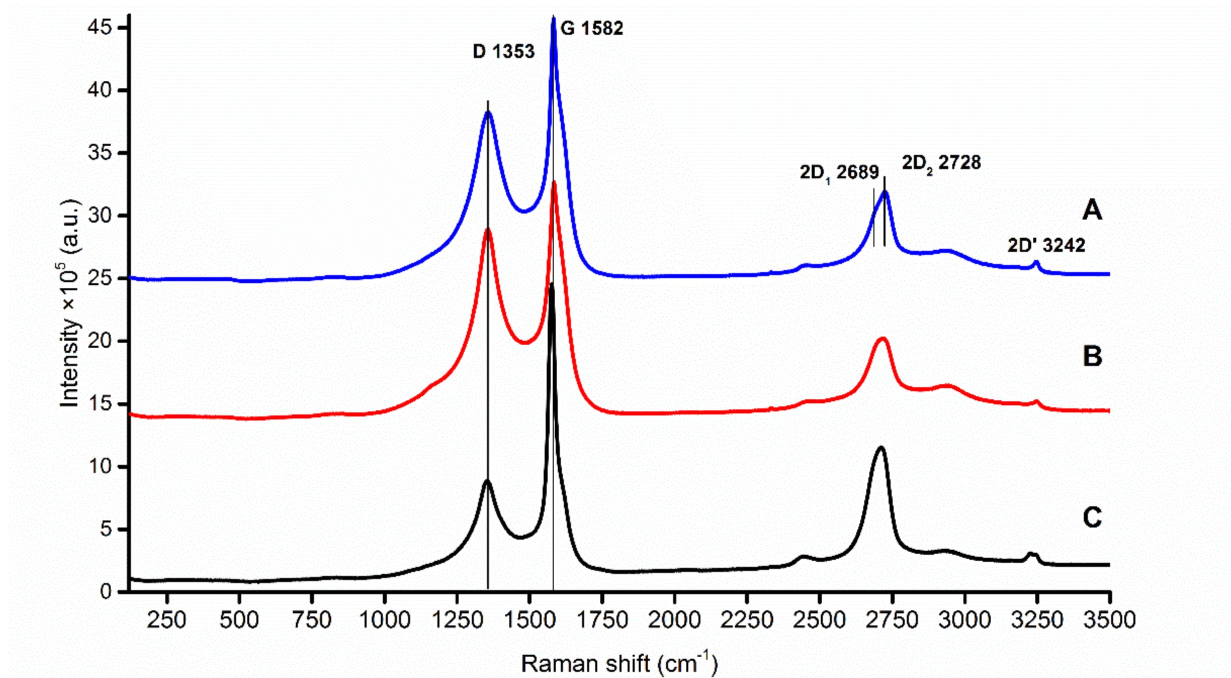

Figure 2.9 Stacked Raman spectra of each sample: Pentel Hi-Polymer E (blue), KOH-I-NOOR (red) and STAEDTLER (black) [A9].

The Raman spectra of pencil leads show peaks common in polycrystalline graphite, the G peak observed at 1580 cm^{-1}, which arises from the bond stretching of all pairs of sp^2 hybridized atoms, the D peak at around 1360 cm^{-1}, which becomes visible in relation with the defects in sp^2 graphite sheets, in polycrystalline graphite and graphite like materials with crystalline defects, D peak overtone called 2D peak is observed at around 2690 cm^{-1} and on polycrystalline graphite samples splits into two components $2D_1$ and $2D_2$ [33]. The above-mentioned measurements are illustrated in Figure 2.9 [A9].

D/G and $2D_1/2D_2$ intensity ratios [33] gives information about the estimated size and turbostraticity of layers of polycrystalline graphite flakes, which may play a significant role in the fabrication of sharp STM tip. The pencil leads were also thoroughly investigated using EDX and XPS with the aim to obtain complex information about both the surface and the bulk properties. Compositional analysis of different carbon leads was presented originally by Navratil et al. in [31] and Kariuki in [34].

Table 2.1 Properties of analyzed pencil leads, Raman I_D/I_G intensity ratio, calculated crystallite size, relative atomic concentration derived from XPS measurements [A9].

	Raman		EDX Contaminants		XPS [atomic %]				
Sample	I_D/I_G	Crystallite Size [nm]	Side surface	Spot at the rod axis	C	O	Si	Fe	F
Pentel	0.60	63	O, Na, Si, P, Fe	O, Na, Si, P, Zn	65.3	23.4	8.8	0.6	1.3
KOH-I-NOOR	0.36	101	O, Na, Mg, Al, Si, P, S, Cl, K, Ca, Fe	O, Na, Mg, Al, Si, P, S, Cl, K, Ca, Fe	67.2	23.9	8.0	0.7	-
Staedtler	0.35	102	O, Na, Mg, Al, Si, S, Cl, Ca	O, Na, Si, S, Cl, Ca	48.2	24.1	15.6	0.8	1.3

Properties of analyzed pencil leads incl. Raman ID/IG intensity ratio, calculated crystallite size and relative atomic concentration (derived from XPS measurements) are illustrated in Table 2.1.

2.3.2 Polymer graphite tips made by focused ion beam

The probes were prepared by FIB at microscope Helios (FEI production). The advantage of this microscope is possibility to automatization of tips sharpening and preparation of tip with desired shape. FIB processing provides control of shape and sharpness of the probes. The setback of this process is high price of the final product. A sample of the produced tip is illustrated in Figure 2.1.

We used preliminarily mechanically sharped probes to decrease the time of milling [A9]. The tip apex diameter can go down to tens of nanometers, which is usually smaller than the size of a graphite flake. This is the uniqueness of this method, as it produces a compact tip whose FE parameters are practically identical to those of the metal. These findings are described in [A7]. Another disadvantage of a tip made in this way, and the main difference from the conductive behavior of metals, is the presence of impurities in the volume. Based on noise spectroscopy presented in [A7], it was found that the presence of these impurities causes

quasiperiodic trapping and releasing of conduction electrons. Thus, the impurities behave as electron traps and contribute to the current fluctuations of the charge carriers [A7].

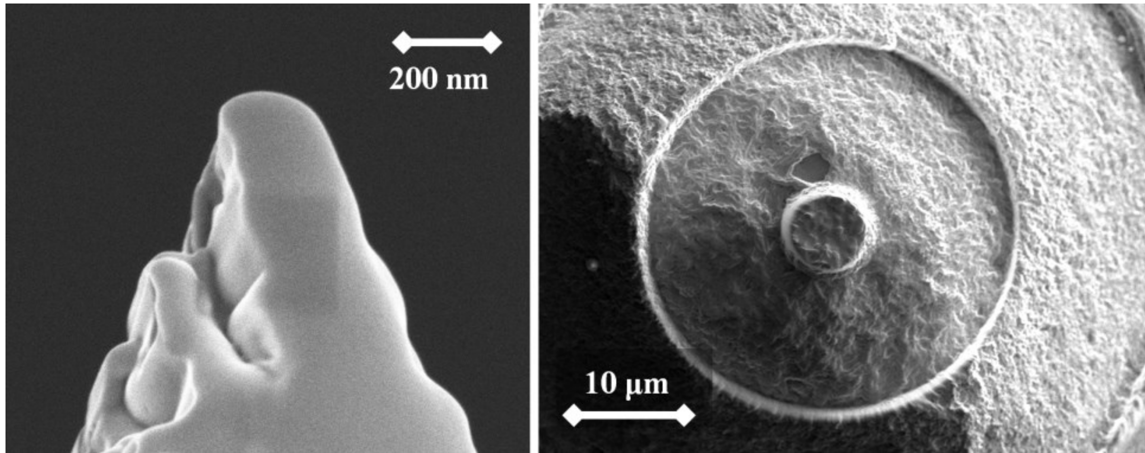

Figure 2.10 SEM image of the produced by FIB milling (left) and tip surface detail (right) showing graphite flakes from top before milling. Material used for this tip is STAEDTLER 0.3 HB [A9].

2.3.3 Polymer graphite tips formed by mechanical grinding

Mechanical grinding achieved by a sanding is the simplest method how to form a sharp tip on a PG rod. The only disadvantage is the low reproducibility of the probe's shape and absence of a sharping control-mechanism of the tip. The sharping could be carried out by grinding, for example, on a sandpaper or by forming with a sharpener [A9].

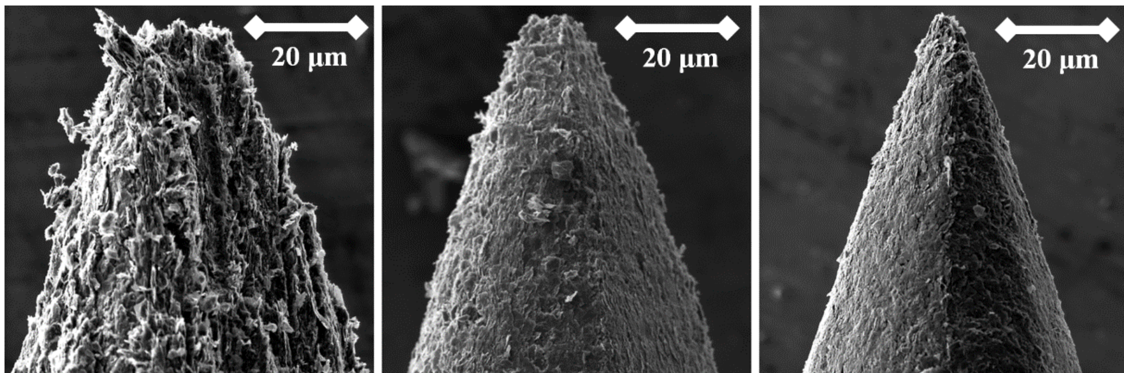

Figure 2.11 SEM image of the tip produced by mechanical sharping from the Hi-Polymer rod (left); by the mechanical sharping from KOH-I-NOOR rod (middle) and the mechanical sharping from Staedtler rod (right) [A9].

Apparently, the diameter of the tip prepared in this way is many times larger than conventional tips that are suitable for field emission of electrons; however, the presence of perpendicularly oriented flakes (with respect to the surface) allows this tip to be used as a large area field emitter (LAFE), with individual flakes serving as partial electron sources. Emitters based on mechanically ground tips are still under investigation. This phenomenon will be described in detail in the subsection 2.3.4.

2.3.4 Polymer graphite tips electrochemical etching

Basic method that has been tested for preparation of the graphite sharp tip is based on an electrochemical etching, as it was published earlier [A2]. This method is well known and used for field-emission microscopes production. Electrochemical method of tip preparation and sharpening provides good reproducibility of the tip shape and sharpness [A2]. Type and concentration of hydroxide (NaOH, KOH) along with the kind and voltage of an etching current allows controlling of tip etching rate and thus about the tip quality.

The bulk of the graphite is most likely remained unreacted and precipitates on the metal ring in the form of flakes. The gas generation is illustrated in Figure 2.12 by etching current waveforms. There are two different waveforms for two different solutions etched by the same etching voltage (5V) showing quasiperiodic occurrence of peaks that are connected to the generation of bubbles. When a bubble is generated near the etched tip, the surface that is in connection with the etchant starts to be reduced and hence, the etching current starts decreasing. When the equilibrium between air pressure and the surface tension of the bubble is broken, the bubble pops whilst increasing the wetted area of the etched rod and in this way increases the etching current. This effect appears in quasiperiodic order as it was mentioned above. The slope of the etching is usually linear depending on the conductivity of the bulk.

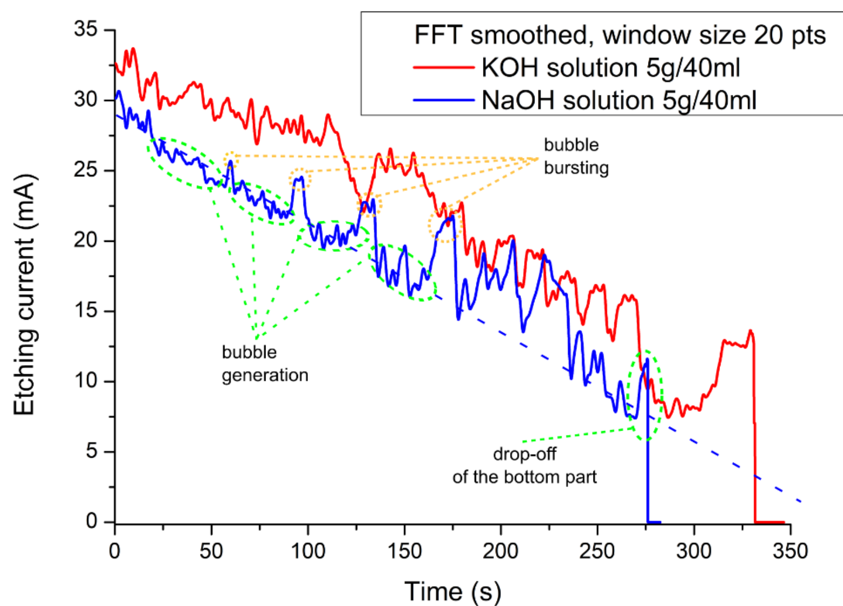

Figure 2.12 Etching current of a polymer graphite rod using two various etchants [A8].

The initial material-analysis of the polymer graphite tip, providing basic tip geometry and structure, was obtained by classical SEM. Those observations showed that the surface of electrochemically etched tip looks similar like the mechanically grinded tip and that also here, there are multiple graphite flakes oriented in various directions towards to the surface. Some of the flakes may have sufficient field gradient when connected to the negative power supply in the vacuum chamber of the FEM and act as a partial electron source. For these reasons, also this kind of tip is considered more like a field emission array of non-homogeneously

distributed tips of different sharpness and hence different field enhancement. In the left part of the Figure 2.13, the overall view done by SEM on to the tip is shown. The surface detail is illustrated in a right part of figure Figure 2.13 showing the tip surface.

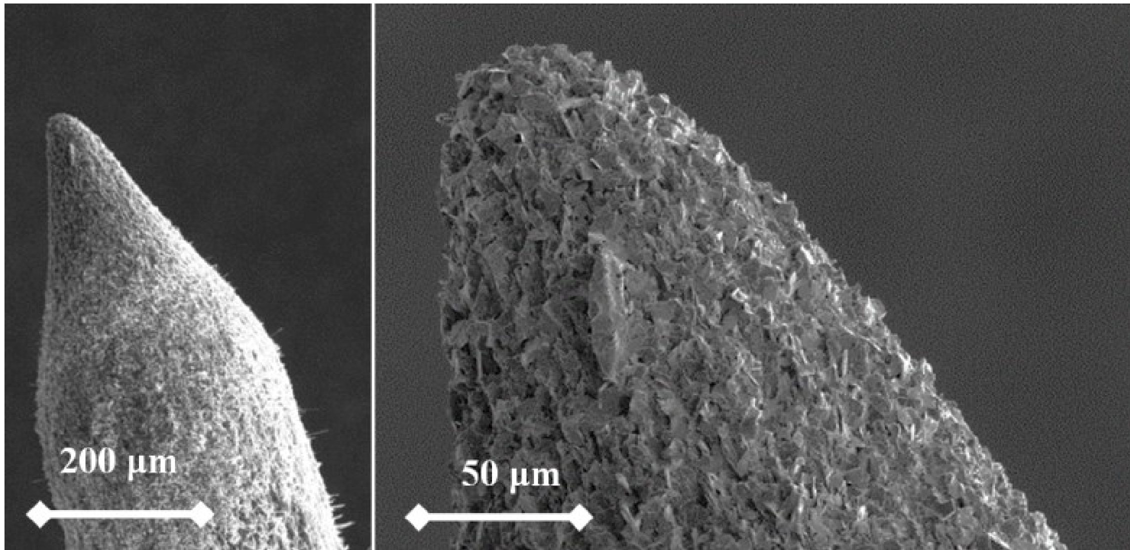

Figure 2.13 SEM image of the produced tip by electrochemical etching (left) and the tip surface detail (right) showing graphite flakes. Material used for this tip is Staedtler 0.3 HB [A8].

As it will be discussed in more detail in section 3.2, to do the complete analysis of the surface of the a Large Area Field Emitter (LAFE) we need to extract two important characterization parameters which are the Macroscopic Field Enhancement Factor M – FEF (γ_M) and the Formal Area Efficiency (α_f^{SN}) for Schottky – Nordheim (SN) like potential barrier. To do these analyses the Murphy – Good plots were used to analyze the obtained data and to extract the characterization parameters for the emitter.

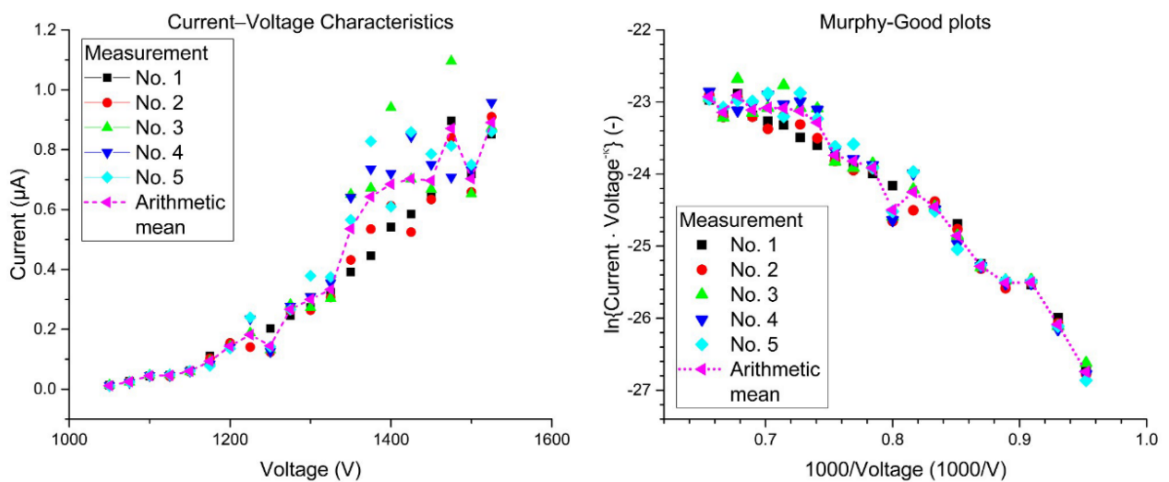

Figure 2.14 FE analysis of the electrochemically etched tip: the I–V Characteristics for the 5 measurement cycles (let) and the corresponding MG plots (right) [A8].

Figure 2.14 (left) presents the I-V characteristics of polymer graphite electron emitter in diode configuration that was measured in the field electron microscope and Figure 2.14 (right) presents the analysis plots for the 5 periods for the tested tip [A8]. Based on the result, this analysis also implied existence if multiple sources (sharp tips) that are sufficiently sharp to achieve field gradient strong enough to provide field emission current. This is in perfect agreement with the topographical analysis provided by the SEM showing multiple flakes oriented perpendicularly towards to the tip surface. Latter arrangement behaves similarly like general LAFE providing extended tunneling capabilities even for a tip of a relatively blunt diameter [A8]. More detailed explanation of the MG formalism will be given in the chapter 3.2.

2.3.5 Application of polymer graphite tips as probes for STM

Based on the convenient material properties that allow electron tunneling from polymer graphite, an application has been proposed where the polymer graphite is used as a material to fabricate low-cost probes for SPM. The idea behind this is related to the replacement of PtIr alloy and tungsten, which are most used to produce SPM probes. Main characteristics of polymer graphite which could be found to be one of the most convenient for usage in scanning probe microscopy (SPM) are heat resistance, considerable durability, resistance to mechanical and hydraulic stress, and finally, the corrosion resistance [A9].

To test the functionality, three types of probes for SPM measurements were used: the tips prepared by electrochemical etching as described in section 2.3.4, the tips prepared by mechanical grinding as described in section 2.3.3 and the tips prepared by FIB milling as described in section 2.3.2.

Each of the tip was successfully used for SPM images acquisition. The sharpness of all our tips proved to be sufficient; however, the sharpness depended strongly on the mark of the chosen pencil lead. The lowest sharpness was obtained by Pentel HiPolymer rod. KOH-I-NOOR and Stadler allows preparation of tip with small cultivate radius. FIB processing and chemical etching of the tips ensure reliable obtaining of the tips with demanded geometry. Nevertheless, even the mechanical sharping proved to sufficient during STM in air when sub-nanometer resolution is not demanded. The probes are also stable against oxidation and can be repeatedly sharped for continuous measurement by simple sharping procedure. The shape of the tip apex is usually created by a single flake of a graphite and determines the output quality of SPM while the precise shape of the tip does not play a significant role [A9].

To demonstrate the simplicity of working with PG probes, all the results presented were made by mechanically sharped tips that can be prepared almost effortlessly just by sharpening a PG rod by a sandpaper of high granularity (> 1600 grains/cm^2). The probes were tested within SPM NT-MDT Nanoeducator II. As a reference sample for estimation of our probes, a surface of a compact disc and highly oriented pyrolytic graphite (HOPG) were chosen (Figure 2.15, left). The HOPG surface (Figure 2.15, right) was used as reference sample for different types of electrical characterization in probe microscopy.

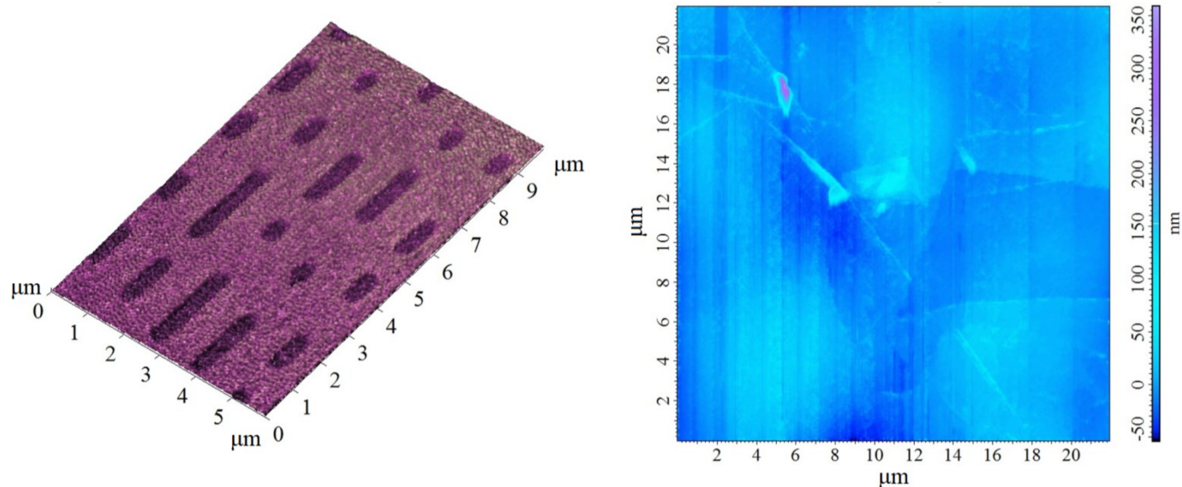

Figure 2.15 SPM image of the reference sample obtained by PG tip: (left) the surface of a compact disc and (right), the surface of a HOPG [A9].

Tip's performance was demonstrated on a SEM calibration standard. The standard contains grids of various sizes. For our measurements, we have used 10µm, 5µm and 2.5µm grid to demonstrate tip's resolution.

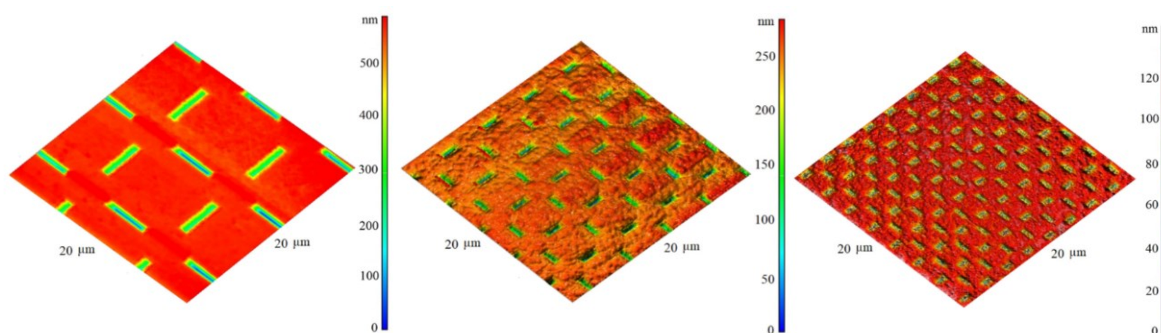

Figure 2.16 SPM image of the special calibration grid showing tip performance and spatial resolution: (left) 10µm grid, (middle) 5µm grid and (right) 2.5 (left) 10 µm grid [A9].

The results of the measurements are illustrated by figure Figure 2.16 showing three various grid sizes presented above. It can be seen, that in all the grids used a probe was able to follow the surface details precisely and to cover broader area without a change of the spatial sensitivity. By the results presented above, it has been demonstrated that mechanically polished pencil leads are suitable for fast and low-resolution SPM measurements. These probes proved to be reliable for routine characterization of the samples by SPM in air with low resolution of surface features. Cost-effective easy preparations make them useful at education process at laboratory classes of SPM. Generally, a tip made of PG can find an application during education process to scanning probe microscopy techniques or for estimation of topography of conductive samples with high roughness at low resolution of texture details.

3. Novel methods of electron emitter characterization

3.1 Noise spectroscopy implemented in field emission microscope

The noise spectroscopy method is one of the non-destructive evaluation methods used especially in semiconductor science and technology [35],[36]. The principle of the method is based on the identification of the main noise components in time- and frequency domain and their assignment to physical phenomena occurring in the system. The most common noise components are 1/*f* noise, generation-recombination (GR) noise, thermal noise and shot noise [36],[37],[38]. Based on our previous findings [39],[40], it can be used not only to characterize the electron emitter, but also to evaluate the function of the entire electron-optical system since the unwanted fluctuations and noises have adverse effect on the electron aberrations and on a detection system in general [41].

The longtime goal of my research is this to fully implement this method for use in a field emission microscope, which is in fact the simplest electron projection system used now mostly for analyzing emission sources [A7]. This chapter also includes a demonstration of the utilization of this method to a more complex system, which is a scanning electron microscope [A10].

3.1.1 Application of the noise spectroscopy method for FE sources

In this chapter, the noise spectroscopy method was implemented into field emission microscope to describe the noise and fluctuations of electron beam that is being collected by a coated scintillating crystal inside an ultra-high vacuum chamber [A7].

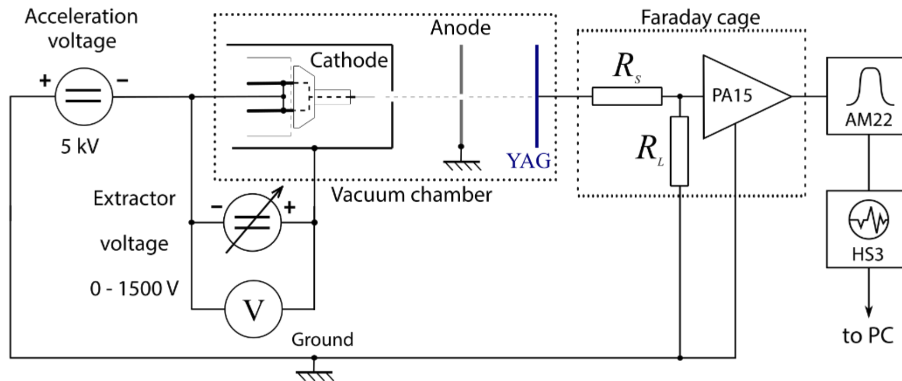

Figure 3.1 Noise measurement implementation into FEM showing the connection of the electron gun and the noise measurement system located within a Faraday cage. The tip to extraction cathode distance is usually between 0.75–1 mm [A7].

A field emission cathode is placed within an extractor electrode embedded within a vacuum chamber (P~10^{-7} Pa) aiming towards an anode which accelerates electrons by high voltage (5 keV). The accelerated electrons are collected on the scintillator electrode made of

Cerium doped Yttrium Aluminum Garnet coated with a conductive layer (20nm Al layer), which allows to display an emission pattern, and to conduct the impinging primary electrons. The measurement part of the set-up is placed outside the vacuum chamber within a Faraday cage shielding the measurement resistors R_S (491 kΩ), R_L (492 kΩ) and the preamplifier PA15 (20 dB) made by 3S Sedlak. The measurement amplifier AM22 is dynamically set based on the output signal level. The AM22 also serves as a filter providing a proper signal for the HS3 oscilloscopic card which samples the signal to the computer [A7].

As it was mentioned in chapter 2.3.2, the polymer graphite cathode made by FIB behaves like metal emitter, which is further supported by a I-V and FN plots illustrated in Figure 3.2.

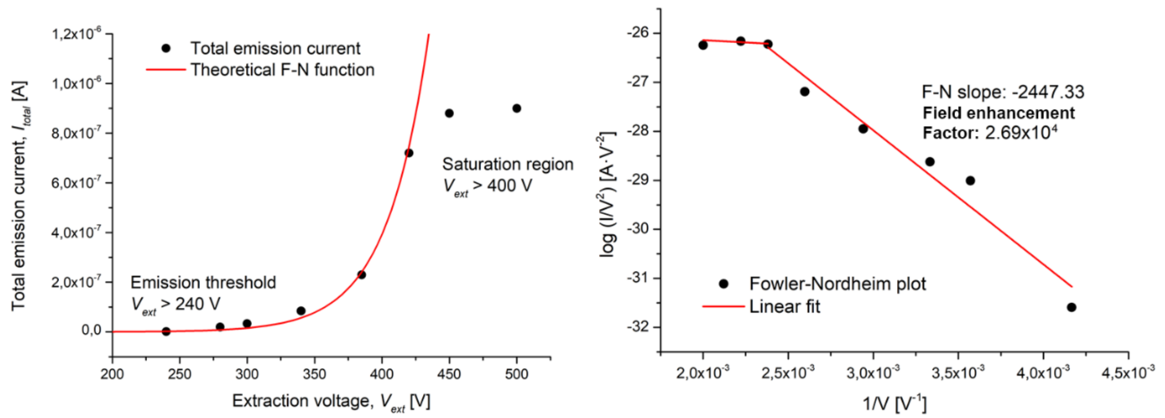

Figure 3.2 The current-voltage characteristics obtained from measurement in FEM (left); The Fowler-Nordheim plot showing F-N slope and field enhancement factor (right) [A7].

Those measurements provide us with some important information about the FE behavior like for example it confirms the quantum tunneling and determines the position of the saturation region, however; for this experimental cathode, we miss information about the charge carrier transport, which is always a critical information for non-homogeneous materials.

The current that is measured on the YAG scintillator in the time domain is transformed into a spectral domain and further analyzed. The noise measurements were obtained using two different extraction voltages representing two determining states of the field emission illustrated in Figure 3.3 (left; V_{ext} = 325 V) and Figure 3.3, (right; V_{ext} = 525 V). According to Figure 3.3 (left), each voltage represents a different operation mode. For V_{ext} = 325, our cathode operates in a regular, unsaturated state and for V_{ext} = 525 V, the cathode operates in a saturation state, which means that for the increased extraction voltage, the emission current does not increase anymore. For both extraction voltages, the thermal noise level is calculated, and its value is given by 4kTR, where T is temperature, R is resistance and k is Boltzmann constant [35]. For our measurement, the 4kTR equals 4.07×10^{-15} V^2s (or V^2/Hz) [A7].

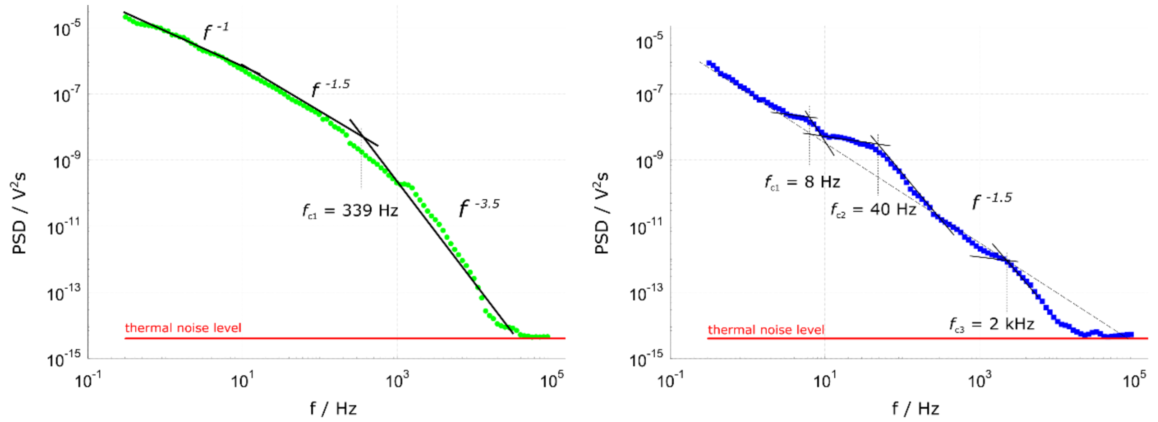

Figure 3.3 Noise power spectral density for the total emission current measured at V_{ext} = 325 V (left) and for V_{ext} = 525 V. Both measurements were done at constant pressure and electron energy [A7].

For V_{ext} = 325 V as illustrated in Figure 3.3 (left), the $1/f$ noise, dominates up to the cut-off frequency f_{c1} = 339 Hz. The $1/f$ noise is a process with a frequency spectrum such that the power spectral density is proportional to the reciprocal of the frequency and has been already studied in numerous papers [37],[38]. As for the lower part of the spectrum where the $1/f^{\,n}$ noise, where the n parameter is in the range $1.0 \leq n \leq 1.5$ [A7]. The exact value of n is determined by the nature of the recombination, the lifetime probability density function, and by the trap density function. It has been already shown that the trap densities close to the conduction and valence band lead to higher values of n [42]. The cutting frequency is located near the region where the spectrum becomes steeper, which is caused by a superposition of the particular $1/f$ and generation-recombination (GR) processes. Such an effect may be explained by adsorption and desorption of various atoms present with some residual gas in the vacuum chamber, which happens on the tip surface [40]. In the bulk, a volume diffusion (i.e., a diffusion within a single graphite flake) plays a more significant role, especially in the direct vicinity of the emission tip, where the temperature is increased due to electron tunneling. For V_{ext} = 525 V, the spectrum slope shows such an influence, which is probably caused by the increased temperature induced by a higher emission current. The diffusion again takes place along with a GR process caused by particle movement in the bulk towards the tip. The defects contained within the bulk which are probably the polymer particles behave like particle traps with an exponential energy distribution function. There are several cut-off frequencies connected to the particular GR noise components; in particular: 8 Hz, 40 Hz, and 2 kHz [A7].

Based on the presented data, the polymer pencil graphite may be used as a material for preparation of field emission cathodes when operating in a particular voltage regime. It has been shown that the bulk defects, behave like particle traps creating significant generation-recombination noise and hence the volume and surface diffusion which directly affects the number of emitted electrons.

3.1.2 Analysis of complex electron optical systems

In this subsection, the author applies noise spectroscopy methodology at the level of a complex electron-optical system, for which we have chosen an older scanning electron microscope (Tescan Vega v1). This microscope was selected because it can be very easily disassembled and contacted through existing set of feedthroughs. As the electron source for this microscope operates in a purely thermoemission mode, it was not possible to fully assess the effect of electrical noise and fluctuations on the stability of the applied field, however, this was not the focus of the investigation. The aim was to test the method on a complex electron-optical device and to assess the main sources of noise on the operation of the whole system [A10].

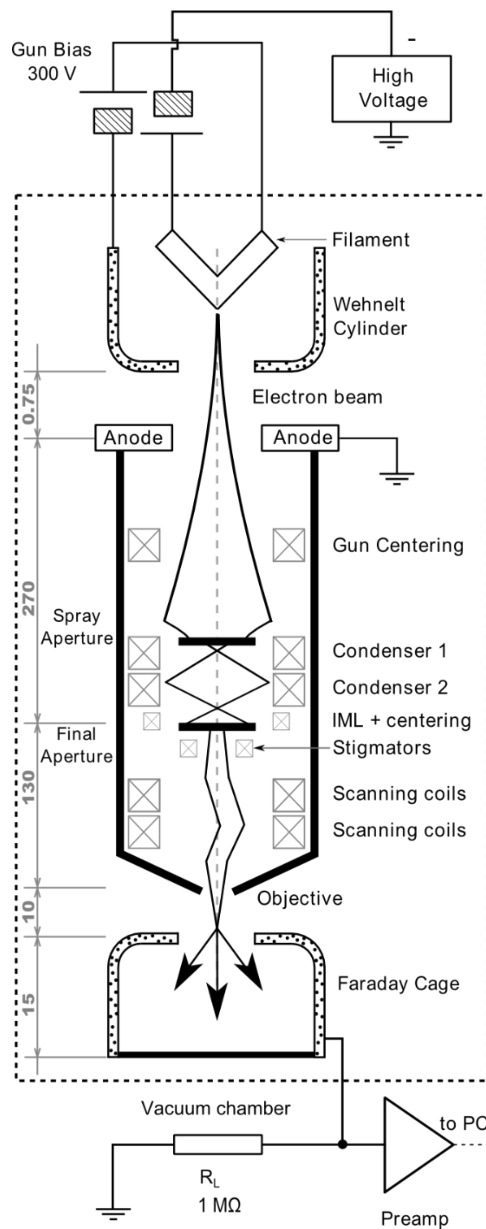

Figure 3.4 Schematic representation of the cathode and optical elements of the scanning electron microscope Tescan Vega v1, where left are distances in mm [A10].

Emitted current goes through a column consisting of two condenser lenses, the auxiliary centering lenses and stigmators and a pair of scanning coils. The beam then continues through objective out of the column as illustrated in Figure 3.4. There were two apertures cropping the electron beam and reducing the total emission current approximately thousand times. The electron beam was focused into a Faraday cage through narrow aperture on the top of the cage that was placed under the objective collecting all impinging electrons within [A10].

To reduce a deflection of the beam, the following configuration was set: the beam has been focused to the edge of the Faraday cage and then magnified inside the cage to obtain as smallest field of view. At the highest magnification the area of scanning was minimized to a square covering 5 nm^2, which almost suppressed the beam scanning. By reducing the scanning speed (s) to level s=12, the dwell time (i.e., the period that a beam remains in a same position) for a single pixel is equal to 2.36 ms, therefore, the area of 5 nm^2 (17 squared pixels) is scanned periodically every 0.68 s obtaining continual output current. Output current of the Faraday cage has been grounded through a 1MΩ resistor on which the voltage fluctuations have been measured. After the voltage on the load resistor stabilizes, the voltage was measured, sampled, and recorded [A10]. The paper describes 3 basic experiments + one additional that are commented on below.

The first measurement was performed on a cathode that was stored for a longtime at the room temperature. In this case the cathode surface was initially covered by thin film of tungsten trioxide that is created during cathode cooling from previous operation. Voltage noise spectral density S_u as a function of frequency is shown in Figure 3.5. The measurement resistor R operates at room temperature T=300 K yielding background noise level (BN) equal to 4kTR, as it is plotted in Figure 3.5.

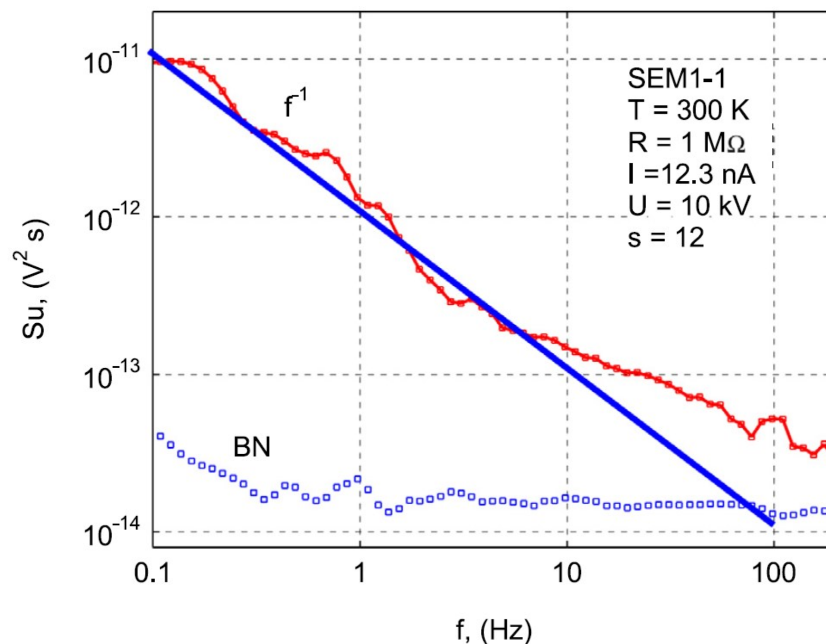

Figure 3.5 The initial voltage noise spectral density for long-time stored cathode that was coated by tungsten oxide; marked as SEM1-1 [A10].

At the frequency range from 0.1 up to 10 Hz is noise spectral density $1/f$ type. The change of the low frequency component is described further in the text. For electron beam with a current of $I_{eb} = 9.8$ nA, the current noise spectral density $S_i = 3.14 \cdot 10^{-27}$ A^2/Hz because of the shot noise was found. Shot noise may be dominant when the finite number of charged carriers is sufficiently small so that uncertainties due to the Poisson distribution, which describes the occurrence of independent random events, are of significance. In our measurements, the shot noise component is about one order below the mean the obtained current noise spectral and for this reason, the effects of a shot noise were neglected [A10].

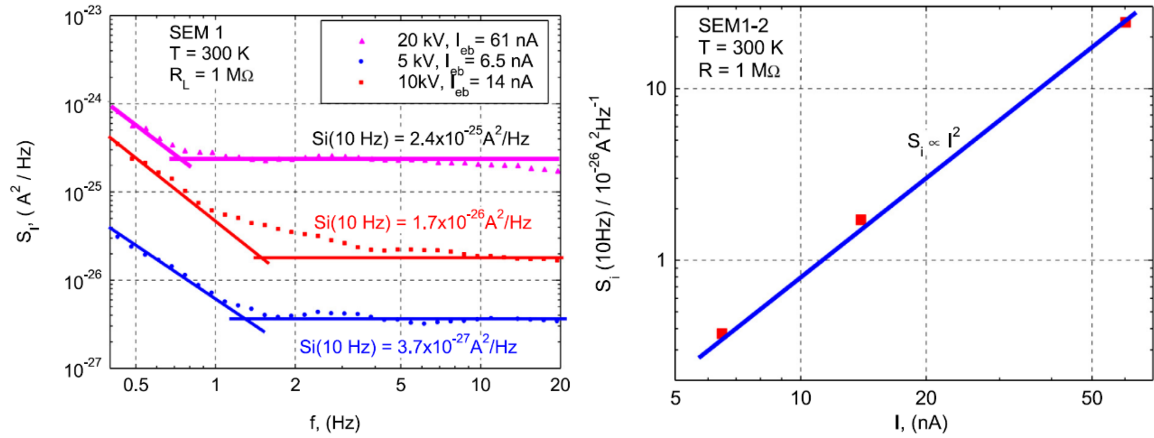

Figure 3.6 Influence of the accelerating voltage: the measured current noise spectral density S_I at anode voltage 5 to 20 kV (left) and the current noise spectral density vs. electron beams current (right) [A10].

The second experiment described in the paper [A10] was performed with various accelerating voltages starting from 5 to 20 kV as it is illustrated in Figure 3.6. Low frequency noise measured was in scale from 0.3 to 1 Hz and was of $1/f^n$ type where n varies from 1 to 2. Low frequency component is changed from $1/f$ spectrum to $1/f^2$ due to a progressive accumulation of emitted carriers near the cathode surface. These carriers don't have sufficient energy to leave the surface and move towards the anode. For the period of t =1000 s the voltage noise spectral density is decreasing as is shown in Figure 3.6 [A10]. This phenomenon was explained in a previous paper published along with Sergeev [40], where we suppose that the one part of that the generation-recombination noise results from the electron movement which takes place near the surface of the cathode. Presuming, that one part of electrons is being evaporated out of the cathode surface, the second part is being attracted and caught back on the surface. Considering these interactions between two reservoirs, a model of adsorption-desorption noise was formulated based on the Kolmogorov equation [40].

From the measurement illustrated in Figure 3.6 (left), it has been concluded that the current noise spectral density at frequency 10 Hz increased with increasing electron beam current as it is shown in Figure 3.6 (tight). The current noise spectral density increased with a square of current also confirming a supposition that the noise is of a GR type [A10],[40].

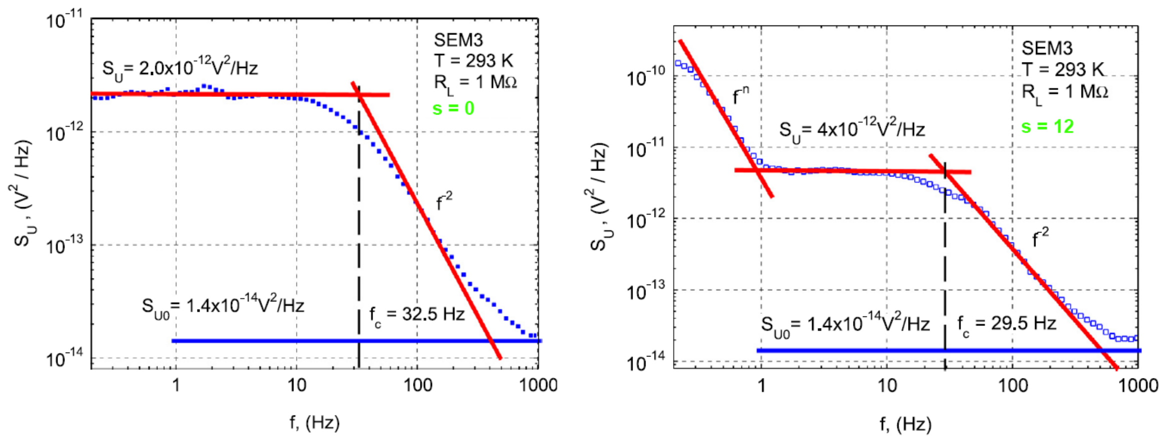

Figure 3.7 Influence of the scanning speed: voltage noise spectral density for measured for *s*=0 (left) and *s*=12 (right) [A10].

The third experiment was performed with accelerating voltage 30 kV and special values of voltages on condensers and stigmators. This configuration is described by Figure 3.4. Measured voltage noise spectral density for scanning speed *s*=0 is GR type as is shown in Figure 3.7 (left). The cut-off frequency in this case is f_c=32.5 Hz and voltage noise spectral density at 1 Hz S_u equal to 2×10^{-12} V^2/Hz, as it is illustrated by Figure 3.7 (left). It is supposed that this GR noise component originates from the electron optics and relates to the electric field distribution among anode, condensers, stigmators and objective as it is illustrated in Figure 3.4. Beam deflectors which are used to scan the electron beam across the specimen consist basically of two scanning coils: one is for horizontals deflection and second one for vertical deflection. Since both operate on frequencies whose overall speed may be set by end-user, the effect of beam deflection has been considered as a possible source of unwanted fluctuations and was further examined. Effect of scanning frequency is shown in Figure 3.7 (right) where f_c=29.5 Hz, which is slightly lower than for the scanning frequency where *s*=0. Moreover, in the frequency band below 1 Hz, a new source of noise appears. This noise component is related to the electric field distribution between anode and objective and is dependent on the scanning frequency [A10].

The additional experiment dealt with the influence of the filament heating as it is illustrated in in Figure 3.4. The level of the filament heating can be simply chosen from four different presets which are marked as: “weak”, “middle”, “strong” and “extra” offering four levels of a cathode heating. The increase of the heating intensity also increases the total emission current. For each heating level, two spectral measurements were done, which was illustrated in fig. 9 of [A10]. From the spectral density measurements, it was determined that the heat increase is not directly proportional to the mean value and to the shape of the spectral curve (or spectral components distribution) is not constant.

The explanation is rather straightforward and may be explained in by that the cathode works most smoothly when the “extra heat” option is selected. In this case, the cathode working point is in the region of current saturation, which means that all the available electrons are

used for charge transport and any current increase would not increase the emission. This also positively influences the electron emission probability, which means that vast part of electrons emitted has sufficient momentum energy to leave the surface and move towards the anode, hence, the effect of superposed generation-recombination noise is rather minor.

3.2 Orthodox testing implemented in field emission microscope

3.2.1 Introduction to the field electron emission analysis

The orthodox testing methodology based on the updated Fowler-Nordheim theory proved to be another suitable and completely non-destructive method for implementation in focused electron beam devices [43]. The general idea is to implement an automated method whereby a device (such as an electron microscope or electron lithograph) tests the cathode before or after the operation and uses the extracted data to determine cathode parameters related to cathode lifetime and performance. We have recently presented the online implementation in several common papers with Forbes [A11], [A12] and offered it to the public for free use in the form of a website[1]. Version 0.9 is currently available and offers extended functionality implementing features such as: scaling parameters calculator, macroscopic field analysis, macroscopic current density, and current density-field analysis for single tip emitters (SFE) and large area field emission emitters (LAFE). In the future, an implementation tied to a specific type of electron-optical device will be developed to provide continuous information about the emitter state using orthodox testing, which is presented in more detail in the following subsections.

To explain the theoretical background of the method, we must return to 1953, when Burgess, Kroemer and Houston (BKH) found a physical mistake in Fowler-Nordheim thinking, and a related mathematical mistake in the 1928 work of Nordheim. In one of the mathematical functions, the definition was not correct [43]. In 1956, E. L. Murphy and R. H. Good used the BKH results to introduce a modified form for the Fowler-Nordheim equation [44]. In 2019, after a series of well-known work of modifying the Fowler-Nordheim equation, R. G. Forbes introduced the most recent form of this series of equations, which he called the *Extended Murphy-Good equation* that connects the local emission current density to the local electrostatic field, which is the basis of our common work [45]. The mathematical form of this equation is given by:

$$J(F) = \lambda a \phi^{-1} F_{\mathrm{L}}^{2} \exp\left(\frac{-\mathrm{v}_{\mathrm{F}}\, b\phi^{3/2}}{F_{\mathrm{L}}}\right) \quad 3.1$$

In equation 3.1, a and b are the first and second Fowler-Nordheim constants, ϕ is the local work function value, F_{L} is the local electrostatic field at the tip of the emitter, and λ is a local pre-exponential correction factor of unknown exact functional dependence or value [45]. Another important parameter in the theory of FEE can be introduced by considering that

[1] The public implementation can be found on: **https://fieldemissionanalysis.weebly.com/**

emission process takes place at a characteristic point on the tip apex, where $F_{\mathrm{L}} = F_{\mathrm{C}}$ (the Fc is a characteristic electrostatic field), and by introducing the reference electrostatic field $F_{\mathrm{R}} = c_{\mathrm{S}}^2 \phi^{-2}$ to be the field that is required to pull the top of the Schottky-Nordheim barrier to the Fermi level, where c_{S} is the Schottky constant, this parameter is the characteristic scaled field $f_{\mathrm{C}} = F_{\mathrm{C}}/F_{\mathrm{R}}$ [46]. Using the definition of f_{C}, $\mathrm{v_F} \equiv \mathrm{v}(f_{\mathrm{C}}) \cong 1 - f_{\mathrm{C}} + f_{\mathrm{C}} \ln(f_{\mathrm{C}})$ is a special mathematical function in the theory of Murphy-Good equation [46]. Parameter A_{n} is considered to be the notional area, which is related to the real geometrical shape of the tip. With $A_{\mathrm{f}}^{\mathrm{SN}} = \lambda A_{\mathrm{n}}$, which is the formal emission area from a Schottky-Nordheim barrier, the value can be found by analyzing experimental FEE data [45] and therefore the measured emission current $I_{\mathrm{m}}[= J(F) A_{\mathrm{n}}]$ can be expressed using the scaled extended Murphy-Good equation [46]:

$$I_{\mathrm{m}}(f_{\mathrm{C}}) = A_{\mathrm{f}}^{\mathrm{SN}}\, a\phi^3 c_{\mathrm{S}}^{-4}\, f_{\mathrm{C}}^2 \exp\left(\frac{-\mathrm{v_F}\, b c_{\mathrm{S}}^2 \phi^{-1/2}}{F_{\mathrm{L}}}\right) \quad 3.2$$

Followingly, considering $\theta(\phi) = a\phi^3 c_{\mathrm{S}}^{-4}$ and $\eta(\phi) = b c_{\mathrm{S}}^2 \phi^{-1/2}$ to be scaled parameters, and defining the characteristic voltage conversion length ζ_{C} to be a mathematical parameter connecting $F_{\mathrm{C}} = V_{\mathrm{m}}/\zeta_{\mathrm{C}}$ to the measured/applied voltage $V_{\mathrm{m}}[= f V_{\mathrm{mR}}]$, the V_{mR} is the reference measured voltage. Thus, the measured current can be expressed as a function of the measured voltage using:

$$I_{\mathrm{m}}(V_{\mathrm{m}}) = A_{\mathrm{f}}^{\mathrm{SN}}\, \theta V_{\mathrm{mR}}^{-2}\, V_{\mathrm{m}}^2 \exp\left(\frac{-\mathrm{v_F} \eta V_{\mathrm{mR}}}{V_{\mathrm{m}}}\right) \quad 3.3$$

Equation 3.3 provides the well-known behavior of the current-voltage characteristics $I_{\mathrm{m}}(V_{\mathrm{m}})$ for FEE experiment and is presented in Figure 3.8, the simulation is set for ϕ =4.5 eV, ζ_{C} =200 nm and $A_{\mathrm{f}}^{\mathrm{SN}}$ =100 nm^2.

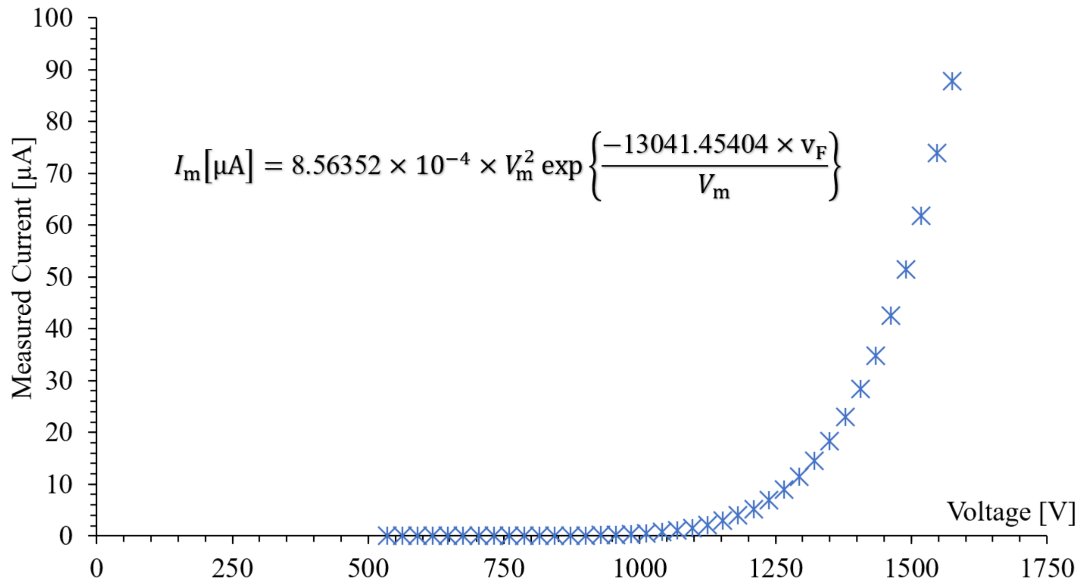

Figure 3.8 Simulated current-voltage characteristics.

3.2.2 Introducing the field electron emission analysis plots

In 1928, the first straight line relation was introduced by R. A. Millikan and C. C. Lauritsen, which is now well known as the Millikan-Lauritsen (ML) plots [47], this type of plots takes the form of $\ln(I_{\mathrm{m}})$ vs V_{m}^{-1}. In 1929, a second straight-line relation has been found by T. E. Stern, B. S. Gossling and R. H. Fowler that takes the form of $\ln(I_{\mathrm{m}}/V_{\mathrm{m}}^{2})$ vs V_{m}^{-1}, this is well known as the Fowler-Nordheim (FN) plots [48].

The most modern form of these analysis plots is introduced in 2019 by R. G. Forbes when he introduced the extended Murphy-Good (MG) plots, this is expressed as $\ln(I_{\mathrm{m}}/V_{\mathrm{m}}^{\kappa})$ vs V_{m}^{-1}, where $\kappa = 2 - \eta/6$ [A11]. Murphy-Good plots theory provides the most nearly exact straight-line form of the analysis plots and is characterized by the absence of the correction factors. For these two reasons, it is more advised to used Murphy-Good method to test and analyze FEE experiments data. In what follows, and for simplicity, $\kappa = 2 - \eta/6$ for MG plots, $\kappa = 2$ for FN plots and $\kappa = 0$ for ML plots. Figure 3.9 presents simulated analysis plots of each type.

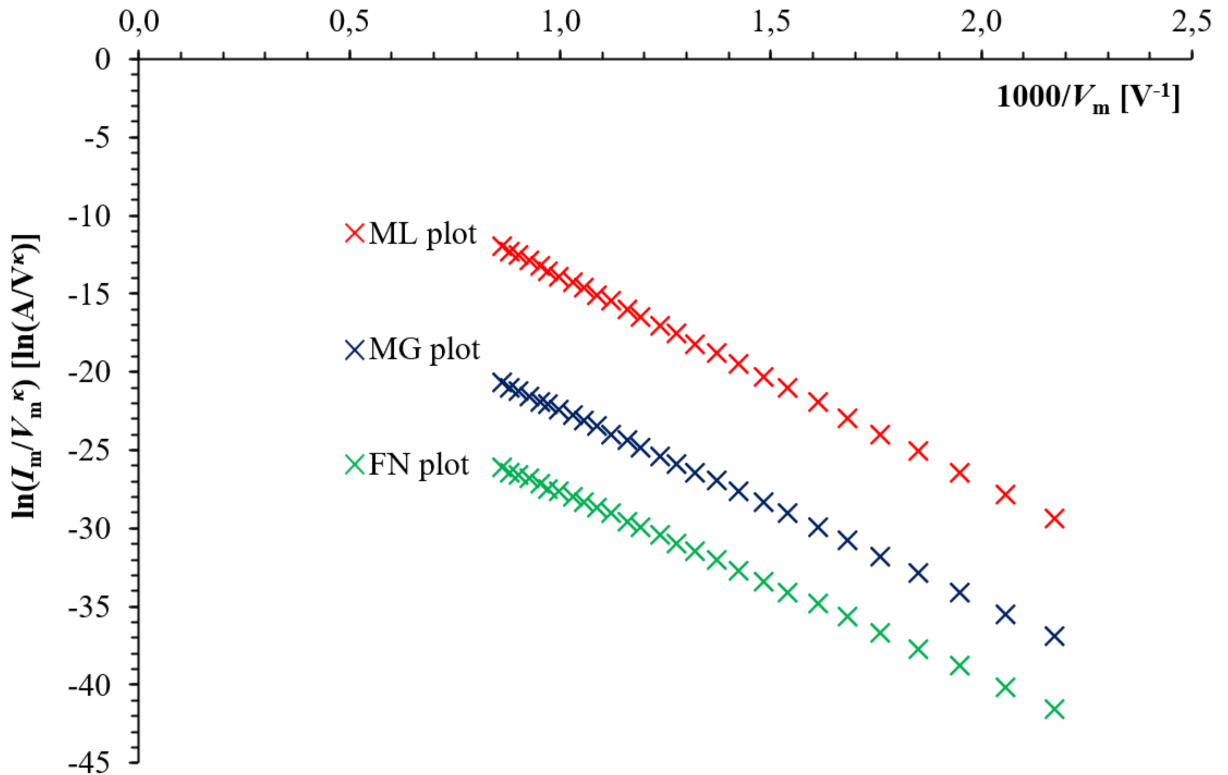

Figure 3.9 Comparison for the three types of analysis [A12].

3.2.3 The field emission orthodoxy testing

The field emission orthodoxy test is a quantitative test aims to check for the validity and the preciseness of the analysis results. The test uses (commonly trusted) reference data achieved between 1926 to 1972 serving for comparison with the tested data. The procedure includes extracting of the characterization parameters for the test-pass emitters. The

characterization parameters that can be extracted from field electron emission current-voltage characteristics are mainly [A12]:

1. *The voltage conversion length* ζ_{C} , is a mathematical parameter that is used to connect the voltage difference to the corresponding electrostatic field, which give us an information about the change of the curvature of the tip. It can be defined as the distance from the surface of the metal where the local electrostatic field remains uniform. The potential difference across a distance ζ will be equals to $V = E\zeta$.
2. *The field enhancement factor* γ_{C}, is a mathematical parameter that is used to connect the local electrostatic field to the applied external electrostatic field and can be defined also as the ratio between the local field to the applied field. The physical meaning of γ can be described by its value, since it is used to enhance the E_{M} so that quantum tunneling through the metal potential barrier for the electrons becomes possible.
3. *The formal emission area* $A_{\mathrm{f}}^{\mathrm{SN}}$, is a mathematical parameter related to the real geometrical/notional area of the emission process. It does not represent the real geometrical emission area, but it can be connected to $A_{\mathrm{n}} = (A_{\mathrm{f}}/\lambda)$ using an uncertainty factor $0.005 \leq \lambda \leq 14$. In a simple word, it is the area where the electrons leave the surface of the metal to the vacuum. Its value can be less than, larger or equal to A_{n}.
4. *The formal area efficiency* $\alpha_{\mathrm{f}}^{\mathrm{SN}}$, is the ratio between the formal emission area to the total geometrical macroscopic area of the surface of the emitter of the effective emission area to the total geometrical area $\alpha_{\mathrm{f}} = (A_{\mathrm{f}}/A_{\mathrm{M}})$. Its physical meaning is clear, the ratio of the contributed area in the emission process.

The characteristic voltage conversion length and the related characteristic field enhancement factor for either single tip field emitters (STFE) or large area field emitters (LAFE).

The mathematical assumptions of the extraction procedure from FN and MG analysis plots are described in Table 3.1. Note that the superscript *extr* is related to an extracted value from any type of the analysis plots. Also, it should be noted that the extraction of the scaled field values from ML plots is connected to the extraction procedure from FN plots, however, there is still no valid theory to extract the formal emission area from this type of plots.

Table 3.1 The mathematical assumptions of the extraction procedure for the scaled field values and the emitter's characterization parameters.

Plot type	k	slope	Vertical axis intercept	$f_{\mathrm{C}}^{\mathrm{extr}}$	$\zeta_{\mathrm{C}}^{\mathrm{extr}}$	$\{A_{\mathrm{f}}^{\mathrm{SN}}\}^{\mathrm{extr}}$
FN	2	$\frac{-\mathrm{s}_{\mathrm{t}}\eta V_{\mathrm{mR}}}{V_{\mathrm{m}}}$	$\ln\left(r_{\mathrm{t}} A_{\mathrm{f}}^{\mathrm{SN}} \theta V_{\mathrm{mR}}^{-2}\right)$	$\frac{\mathrm{s}_{\mathrm{t}}\eta}{\lvert S_{\mathrm{FN}}^{\mathrm{fit}}\rvert\, V_{\mathrm{m}}^{-1}}$	$\frac{\lvert S_{\mathrm{FN}}^{\mathrm{fit}}\rvert}{\mathrm{s}_{\mathrm{t}}\, b\phi^{3/2}}$	$\frac{R_{\mathrm{FN}}^{\mathrm{fit}}\,\left(S_{\mathrm{FN}}^{\mathrm{fit}}\right)^{2}}{\mathrm{r}_{\mathrm{t}}\mathrm{s}_{\mathrm{t}}^{2}\, ab^{2}\phi^{2}}$
MG	2-*h*/6	$\frac{-\eta V_{\mathrm{mR}}}{V_{\mathrm{m}}}$	$\ln\left(A_{\mathrm{f}}^{\mathrm{SN}} \theta \exp(\eta)\, V_{\mathrm{mR}}^{-\kappa}\right)$	$\frac{\eta}{\lvert S_{\mathrm{MG}}^{\mathrm{fit}}\rvert\, V_{\mathrm{m}}^{-1}}$	$\frac{\lvert S_{\mathrm{MG}}^{\mathrm{fit}}\rvert}{b\phi^{3/2}}$	$\frac{R_{\mathrm{MG}}^{\mathrm{fit}}\,\lvert S_{\mathrm{MG}}^{\mathrm{fit}}\rvert^{\kappa}}{\exp\{\eta\}\,\eta^{\kappa-2}\, ab^{2}\phi^{2}}$

3.2.4 Implementation of the orthodoxy test

The orthodoxy testing is based on the presented theory and was originally suggested by Forbes in 2013 based on experimental results provided in generally trusted publications since 1926. The general idea of the concept is to extract the scaled field values from experimental FEE-$I_{\mathrm{m}}(V_{\mathrm{m}})$ data and compare it to a set of the existing experimental scaled field values. The test results are then used to determine whether the extracted characterization parameters for the used emitter are precise or less precise. Converting the function to a computer function, we have reached the very first practical implementation in the previously mentioned papers prepared along with Forbes [A11], [A12]. The implemented function operates based on extraction of the scaled field values for the upper and lower limits (of an analysis plot) and there apply the test general criteria, to the limits presented in Table 3.2. Followingly, the $f_{\mathrm{low}}^{\mathrm{A}}$ and $f_{\mathrm{low}}^{\mathrm{NA}}$ are the lower allowed/not allowed limits $f_{\mathrm{C}}^{\mathrm{extr}}$, and $f_{\mathrm{up}}^{\mathrm{A}}$ and $f_{\mathrm{up}}^{\mathrm{NA}}$ are the upper allowed/not allowed limits when compared to $f_{\mathrm{C}}^{\mathrm{extr}}$. The extracted scaled field range limits as a function of the local work function are listed in Table 3.3.

Table 3.2 Field emission Orthodoxy Test general criteria.

General conditions	Test result	Description
$f_{\mathrm{low}}^{\mathrm{A}} \leq f_{\mathrm{C}}^{\mathrm{extr}} \leq f_{\mathrm{up}}^{\mathrm{A}}$	Pass	The extracted parameters are precise and valid to consider
$f_{\mathrm{C}}^{\mathrm{extr}} \leq f_{\mathrm{low}}^{\mathrm{NA}}$ OR $f_{\mathrm{C}}^{\mathrm{extr}} \geq f_{\mathrm{up}}^{\mathrm{NA}}$	Fail	The extracted parameters are not precise and not valid to consider
$f_{\mathrm{low}}^{\mathrm{NA}} < f_{\mathrm{C}}^{\mathrm{extr}} < f_{\mathrm{low}}^{\mathrm{A}}$ OR $f_{\mathrm{up}}^{\mathrm{A}} < f_{\mathrm{C}}^{\mathrm{extr}} < f_{\mathrm{up}}^{\mathrm{NA}}$	Inconclusive	More study and analysis are needed

Table 3.3 The extracted scaled field range limits as a function of the local work function.

Work Function List [eV]	$f_{\mathrm{low}}^{\mathrm{NA}}$	$f_{\mathrm{low}}^{\mathrm{A}}$	$f_{\mathrm{up}}^{\mathrm{A}}$	$f_{\mathrm{up}}^{\mathrm{NA}}$
5.5	0.09	0.14	0.41	0.69
5.0	0.10	0.14	0.43	0.71
4.5	0.10	0.15	0.45	0.75
4.0	0.11	0.16	0.48	0.79
3.5	0.11	0.17	0.51	0.85
3.0	0.12	0.18	0.54	0.91
2.5	0.13	0.20	0.59	0.98

To conclude, the field emission orthodoxy test can be used to check for the status of the used field emitter in various instruments utilizing focused electron beam [A12]. This can be done by monitoring the status of the characterization parameters and the test results. We find this very useful for cathodes that are continuously placed in vacuum and their removal from the vacuum chamber would not be possible due to contamination of the emitter surface. The future goal is to simplify the output interpreting the fourth extracted parameters by a single function providing relative output in precents that is directly corelated to the lifetime and performance of the FE emitter.

4. CONCLUSIONS

This habilitation thesis is presented in the form of an annotated list of publications that deal with new methods and materials for research on field emission electron emitters. These publications which were produced between 2013 and 2021 dealing with a common topic, which are novel methods leading to the creation of field emission sources. The research topic is loosely related to and further extends the topic I addressed within the frame of my PhD thesis in 2008-2013.

The publications listed were produced within the framework of partial projects carried out at the Institute of Scientific Instruments of CAS (mainly Technology Agency of Czech Republic, Grant Agency of Czech Republic and SIMDALEE2 project funded by the European Commission) participating within several working groups, which allowed to establish international and interdisciplinary cooperation and therefore to extend the topic beyond the usual disciplinary focus on physics and electrical engineering. Thus, the publications that the author comments on in this thesis are mainly peer-reviewed impacted articles from international journals [A2],[A5],[A6],[A7],[A8],[A9],[A10],[A11], from the peer-reviewed indexed article [A1] and from international conferences [A3],[A4],[A12]. A practical output in a form of a utility model which further extends the paper [A2] is attached to the list [A13].

As mentioned before, the topic is very broad and multidisciplinary, and therefore the primary focus of this thesis has been on methods that are applicable in experimental development and allowing us to obtain samples of functional cathodes, on which the further material research and characterization has been carried out. The method for the fabrication of the cathode and the functional nanotube-based structure is discussed in Chapter 1. Special attention is paid to introduce cathodes with ultra-sharp tips, which are coated with a thin layer of dielectric [A1]. This issue was previously the essence of my PhD thesis and yielded many findings which I lately reinterpreted and correlated with the research results of our Jordanian colleagues, namely Prof. Mousa's laboratory at Mu'tah University in Al-Karak [A1].

In the first chapter, the focus is given to improved methodology for the preparation of classical field-emission tips, which we upgraded to a modern and fully automated way. In the commented paper [A2], a new method of etching is described increasing the repeatability and quality of the obtained tips even from polycrystalline tungsten. This output is of great interest for companies and a commercial prototype is currently being prepared.

In the second part of the first chapter, the lithographic formation of a gate structure for an arbitrary nanotube is described and the growth of a platinum nanotube in this structure is demonstrated as an example [A4]. The design also includes the optimization of the gate structure in terms of electron-optical parameters, which will allow the optimum total emission current and the narrowest possible energy spectrum of the emitted beam [A3].

The second chapter of this thesis deals with new materials that have the potential to be used in the fabrication of field emission cathodes. In the beginning of this chapter, the field emission properties are measured on defects of highly oriented pyrolytic graphite providing promising results despite the relatively high work function of the material [A5]. With these basic results, we have extended the research to polymer graphite, which is a modern composite form of graphite used mainly to produce refills for micro-pencils, but also to produce very efficient electrodes for voltametric measurements [A7],[A8]. Polymer graphite is a very affordable and easy to process material that offers several possible applications in relation to the method by which it is processed. It can work as a classical single-point electron source with metal-like properties. Furthermore, it can function as a multipoint electron source, due to the large number of suitably oriented flakes of graphite from which the emission takes place. Lastly, it can serve as a probe for SPM microscopy techniques, where it scans over the surface of the sample as a probe [A9]. These outputs have been documented as functional samples and subsequently published in impacted publications.

The second chapter also includes the development and characterization of tungsten oxide-based nanotubes, specifically the W_5O_{14} and $W_{18}O_{49}$ phases [A6]. The development of these nanotubes was carried out as part of a large EU project in international scientific cooperation with Slovenia and Switzerland. The author was supervising the measurements for the Czech side and was responsible for the preparation and characterization of the functional samples in microscopic and macroscopic modes. The results of measurements on the obtained nanotube samples demonstrated suitable field emission properties of these materials [A6].

A minor overlap with fundamental research is related to the characterization methodology, which is the subject of the final chapter. This consists of two parts; noise spectroscopy [A7],[A10] and an orthodox testing methodology based on the Murphy-Good formalism [A11], [A12]. The noise spectroscopy method builds on preliminary measurement done within the last chapter of my PhD dissertation where it was first time used for non-destructive characterization of FE tips. Within the papers [A7] and [A10], the method has

been further studied and successfully implemented both on a cathode sample (in this thesis we demonstrate its use on a polymer graphite cathode) and within a complex electron-optical system (electron microscope). The research was carried out in the framework of a long-term collaboration with the Czech Noise Research Laboratory led by Professor Šikula at FEEC BUT.

The second method, which is also based on the measurement and analysis of electrical quantities, is being investigated in collaboration with the University of Surrey, specifically with a pioneer in the field, Dr. Richard Forbes. As part of this research, a comprehensive method of testing experimental data has been proposed yielding four essential parameters characterizing the field emitter *in situ*. The very first implementation has been done on a web platform to be available for the professional community [A11], [A12]. In a near future, the implementation should be implemented directly into the control software of an electron microscopy, which should provide a cathode health rating related directly to the four parameters presented and thus inform user when the cathode reaches the end phase of its lifetime.

To conclude, both methods are very suitable as non-destructive, *in situ* methods for diagnosing the function of field emission cathodes, where the cathode does not need to be removed from the vacuum chamber and studied in a complicated manner by other methods.

SELECTED PUBLICATIONS OF THE AUTHOR

[A1] MOUSA, M. S.; KNÁPEK, A.; GRMELA, L. Similarities and Differences between Two Researches in Field Emission of Electrons: A Way to Develop More Powerful Electron Source. *Jordan Journal of Physics*, 2020, 13.2: 171-179, 10.47011/13.2.9.

[A2] KNÁPEK, A. et al. Programmable set-up for electrochemical preparation of STM tips and ultra-sharp field emission cathodes. *Microelectronic Engineering*, 2017, 173: 42-47, 10.1016/j.mee.2017.04.002.

[A3] KNÁPEK, A.; RADLIČKA, T.; KRÁTKÝ, S. Simulation and Optimization of a Carbon Nanotube Electron Source. *Microscopy and Microanalysis*, 2015, 21.S4: 60-65, 10.1017/S1431927615013148.

[A4] BURDA, D.; KNÁPEK, A. Lithographic method of preparing a gating structure for a nanotube-based field mission source. In: *6th IMAPS Flash Conference. Book of Abstracts*. Brno: Brno University of Technology, 2021, ***(in submission/in press)***.

[A5] KNÁPEK, A., et al. Field emission from the surface of highly ordered pyrolytic graphite. *Applied Surface Science*, 2017,395:157-161, 10.1016/j.apsusc.2016.05.002.

[A6] SAQIB, M.; DE PIETRO, L.; KNÁPEK, A. et al. Field emission properties of single crystalline W_5O_{14} and $W_{18}O_{49}$ nanowires. *Journal of Electron Spectroscopy and Related Phenomena*, 2020, 241: 146837, 10.1016/j.elspec.2019.03.005.

[A7] KNÁPEK, A., et al. Preparation and noise analysis of polymer graphite cathode. *Metrology and Measurement Systems*, 2018, 25.3. 10.24425/123895

[A8] KNÁPEK, A., et al. Field emission properties of polymer graphite tips prepared by membrane electrochemical etching. *Nanomaterials*, 2020, 10.7: 1294, 10.3390/nano10071294

[A9] KNÁPEK, A., et al. Polymer graphite pencil lead as a cheap alternative for classic conductive SPM probes. *Nanomaterials*, 2019, 9.12: 1756. 10.3390/nano9121756

[A10] KNÁPEK, A.; ŠIKULA, J.; BARTLOVÁ, M. Fluctuations of focused el. beam in a conventional SEM. *Ultramicroscopy*, 2019, 204: 49-54, 10.1016/j.ultramic.2019.05.008

[A11] ALLAHAM, M. M.; FORBES, R. G.; KNÁPEK, A.; MOUSA, M. S. Implementation of the orthodoxy test as a validity check on experimental field emission data. *Journal of Electrical Engineering* 71, no.1 (2020): 37-42, 10.2478/jee-2020-0005

[A12] ALLAHAM, M. M.; KNÁPEK, A.; MOUSA, M. S.; FORBES, R. G. User-friendly method for testing field electron emission data: Technical report. In: Proceedings of 34th International Vacuum Nanoelectronics Conference (IVNC2021), 2021: 138-139.

[A13] ÚSTAV PŘÍSTROJOVÉ TECHNIKY AV ČR, V. V. I. Zařízení pro opakovatelnou výrobu ostrých hrotů [Device for repeatable production of sharp points]. Originators: Alexandr KNÁPEK, Pavel KLEIN, Armin DELONG.
Czech Republic. Užitný vzor [Utility model] CZ 33278 U1.7.10.2019.

REFERENCES

[1] FOWLER, R. H.; NORDHEIM, L. W. Electron emission in intense electric fields. *Proceedings of the Royal Society of London. Series A*, Containing Papers of a Mathematical and Physical Character, 1928, 119.781: 173-181.

[2] NORDHEIM, L. W. The effect of the image force on the emission and reflexion of electrons by metals. *Proceedings of the Royal Society of London. Series A, Containing Papers of a Mathematical and Physical Character*, 1928, 121.788: 626-639.

[3] ECKERTOVÁ, L.; FRANK, L. Metody analýzy povrchů: elektronová mikroskopie a difrakce [Methods of surface analysis: electron microscopy and diffraction]. 1. ed. Prague: Academia, 1996, 379 p. ISBN 80-200-0329-0.

[4] MELMED, A. J. The art and science and other aspects of making sharp tips. *Journal of Vacuum Science & Technology B*: Microelectronics and Nanometer Structures Processing, Measurement, and Phenomena, 1991, 9.2: 601-608.

[5] IBE, J. P., et al. On the electrochemical etching of tips for scanning tunneling microscopy. *Journal of Vacuum Science & Technology A*: Vacuum, Surfaces, and Films, 1990, 8.4: 3570-3575.

[6] EKVALL, I., et al. Preparation and characterization of electrochemically etched W tips for STM. *Measurement Science and Technology*, 1999, 10.1: 11.

[7] YU, Z. Q., et al. Reproducible tip fabrication and cleaning for UHV STM. *Ultramicroscopy*, 2008, 108.9: 873-877.

[8] FRANSEN, M. F. *Towards high-brightness, monochromatic electron sources*. TU Delft, Delft University of Technology, 1999.

[9] MÜLLER, E. W. Work function of tungsten single crystal planes measured by the field emission microscope. *Journal of Applied Physics*, 1955, 26.6: 732-737.

[10] CUI, Z. Nanofabrication: Principles, Capabilities and Limits: Second. DOI: 10: 978-3.

[11] RAI-CHOUDHURY, P. *Handbook of Microlithography, Micromachining, and Microfabrication: Micromachining and Microfabrication*. SPIE Press, 1997.

[12] BALASUBRAMANIAN, K.; BURGHARD, M. Electrochemically functionalized carbon nanotubes for device applications. *Journal of Materials Chemistry*, 2008, 18.26: 3071-3083.

[13] RADLIČKA, T.; LENCOVÁ, B. Coulomb interactions in Ga LMIS. *Ultramicroscopy*, 2008, 108.5: 445-454.

[14] DE TERESA, J. M., et al. Origin of the difference in the resistivity of as-grown focused-ion-and focused-electron-beam-induced Pt nanodeposits. *Journal of Nanomaterials*, 2009.

[15] MÜLLEROVÁ, I.; FRANK, L. Scanning low-energy electron microscopy. *Advances in imaging and electron physics*, 2003, 128: 310-445.

[16] GESHEVA, K., et al. Technologies for deposition of transition metal oxide thin films: application as functional layers in “Smart windows” and photocatalytic systems. In: *Journal of Physics: Conference Series*. IOP Publishing, 2016. p. 012011.

[17] GAVANIER, B.; MICHALAK, F. M.; OWEN, J. R. Electrochemistry of WO_3 based smart windows: Beliefs and facts. *Ionics*, 1997, 3.3: 265-269.
[18] LADOUCEUR, M., et al. Plasma-sprayed semiconductor electrodes: photoelectrochemical characterization and ammonia photoproduction by substoichiometric tungsten oxides. *Journal of Physical Chemistry*, 1990, 94.11: 4579-4587.
[19] HUANG, Z., et al. Tungsten oxides for photocatalysis, electrochemistry, and phototherapy. *Advanced Materials*, 2015, 27.36: 5309-5327.
[20] LOCHERER, K. R.; SWAINSON, I. P.; SALJE, E. K. H. Phase transitions in tungsten trioxide at high temperatures-a new look. *Journal of Physics: Condensed Matter*, 1999, 11.35: 6737.
[21] MCCOLM, I. J.; STEADMAN, R.; WILSON, S. J. Iron-promoted phases in the tungsten-oxygen system. *Journal of Solid State Chemistry*, 1978, 23.1-2: 33-42.
[22] REMŠKAR, M., et al. W5O14 Nanowires. Advanced Functional Materials, 2007, 17.12: 1974-1978.
[23] WANG, F.; DI VALENTIN, C.; PACCHIONI, G.. Electronic and structural properties of WO3: a systematic hybrid DFT study. *The Journal of Physical Chemistry C*, 2011, 115.16: 8345-8353.Hirose
[24] HIROSE, T.; KAWANO, I.; NIINO, M. Electrical conductivity of tungsten trioxide (WO_3). *Journal of the Physical Society of Japan*, 1972, 33.1: 272-272.
[25] HU, Z., et al. K-enriched WO_3 nanobundles: high electrical conductivity and photocurrent with controlled polarity. *ACS applied materials & interfaces*, 2013, 5.11: 4731-4738.
[26] VISWANATHAN, K.; BRANDT, K.; SALJE, E. Crystal structure and charge carrier concentration of $W_{18}O_{49}$. *Journal of Solid State Chemistry*, 1981, 36.1: 45-51.
[27] BOOTH, J., et al. Notes on phases occurring in the binary tungsten-oxygen system. *Journal of Solid State Chemistry*, 1982, 41.3: 293-307.
[28] DEAN, K. A.; CHALAMALA, B. R. Current saturation mechanisms in carbon nanotube field emitters. *Applied Physics Letters*, 2000, 76.3: 375-377.
[29] PURUSHOTHAMA, H. T.; NAYAKA, Y. Arthoba. Pencil graphite electrode based electrochemical system for the investigation of antihypertensive drug hydrochlorothiazide: An electrochemical study. *Chemical Physics Letters*, 2019, 734: 136718.
[30] RIMAN, D., et al. Low-cost pencil graphite-based electrochemical detector for HPLC with near-coulometric efficiency. *Sensors and Actuators B: Chemical*, 2019, 296: 126618.
[31] NAVRATIL, R., et al. Polymer lead pencil graphite as electrode material: Voltammetric, XPS and Raman study. *Journal of Electroanalytical Chemistry*, 2016, 783: 152-160.
[32] KIM, Y., et al. Measurement of hardness and friction properties of pencil leads for quantification of pencil hardness test. *Advances in Applied Ceramics*, 2016, 115.8: 443-448.

[33] FERRARI, A. C. Raman spectroscopy of graphene and graphite: Disorder, electron–phonon coupling, doping and nonadiabatic effects. *Solid state communications*, 2007, 143.1-2: 47-57.

[34] KARIUKI, J. K. An electrochemical and spectroscopic characterization of pencil graphite electrodes. *Journal of the Electrochemical Society*, 2012, 159.9: H747.

[35] SIKULA, J. and M. LEVINSHTEIN. *Advanced experimental methods for noise research in nanoscale electronic devices*. Boston: Kluwer Academic Publishers, 2004. ISBN 14-020-2170-4.

[36] VASILESCU, G. *Electronic noise and interfering signals: principles and applications*. New York: Springer-Verlag, c2005, xviii, 709 p. ISBN 35-404-0741-3.

[37] DUTTA, P. and P. HORN. *Low-frequency fluctuations in solids: 1/f noise. Reviews of Modern Physics*. 1981, vol. 53, iss. 3, p. 497-516. ISSN 0034-6861. DOI: 10.1103/RevModPhys.53.497.

[38] HANDEL, P. Quantum approach to 1/f noise. *Physical Review A*. 1980, vol. 22, iss. 2, p. 745-757. ISSN 0556-2791. DOI: 10.1103/PhysRevA.22.745.

[39] KNÁPEK, Alexandr, et al. Cold field-emission cathode noise analysis. *Metrology and Measurement Systems*, 2012, 19.2: 417-422.

[40] SERGEEV, E., et al. Noise diagnostic method of experimental cold field-emission cathodes. In: *2013 22nd International Conference on Noise and Fluctuations (ICNF)*. IEEE, 2013. p. 1-4.

[41] HAWKES, P.W. and E. KASPER. *Electron optics. 2*. Engl. ed., rev. Oxford: Pergamon Pr, 1972. ISBN 978-008-0162-287.

[42] MOHAMMADI, S.; PAVLIDIS, D. A nonfundamental theory of low-frequency noise in semiconductor devices. *IEEE Trans. on Electron Devices*, 2000, 47.11: 2009-2017.

[43] BURGESS, R. E.; KROEMER, H.; HOUSTON, J. M. Corrected values of Fowler-Nordheim field emission functions v (y) and s (y). *Physical Review*, 1953, 90.4: 515.

[44] MURPHY, E. L.; GOOD JR, R. H. Thermionic emission, field emission, and the transition region. *Physical review*, 1956, 102.6: 1464

[45] FORBES, R. G. The Murphy–Good plot: A better method of analysing field emission data. *Royal Society open science*, 2019, 6.12: 190912.

[46] FORBES, R. G. Development of a simple quantitative test for lack of field emission orthodoxy. *Proceedings of the Royal Society A: Mathematical, Physical and Engineering Sciences*, 2013, 469.2158: 20130271.

[47] MILLIKAN, R. A.; LAURITSEN, C. C. Relations of field-currents to thermionic-currents. *Proceedings of the National Academy of Sciences of the United States of America*, 1928, 14.1: 45.

[48] STERN, T. E.; GOSSLING, B. S.; FOWLER, Ralph Howard. Further studies in the emission of electrons from cold metals. *Proceedings of the Royal Society of London. Series A, Containing Papers of a Mathematical and Physical Character*, 1929, 124.795: 699-723.

[49] ALLAHAM, M. M.; FORBES, R. G.; MOUSA, M. S. (2020), Applying the Field Emission Orthodoxy Test to Murphy-Good Plots. *Jordan journal of Physics*, Volume 13, Number 2. pp. 101-111.

[50] ALLAHAM, M. M.; MOUSA, M. S.; FORBES, R. G. Comparing the performance of Fowler-Nordheim plots and Murphy-Good plots. In: *2020 33rd International Vacuum Nanoelectronics Conference (IVNC)*. IEEE, 2020. p. 1-2.

LIST OF APPENDICES.

A. **pp. 63 - 71**
MOUSA, M. S.; KNÁPEK, A.; GRMELA, L. Similarities and Differences between Two Researches in Field Emission of Electrons: A Way to Develop More Powerful Electron Source. *Jordan Journal of Physics*, 2020, 13.2: 171-179.

B. **pp. 72 - 77**
KNÁPEK, A. et al. Programmable set-up for electrochemical preparation of STM tips and ultra-sharp field emission cathodes. *Microelectronic Engineering*, 2017, 173: 42-47.

C. **pp. 78 - 79**
KNÁPEK, A.; RADLIČKA, T.; KRÁTKÝ, S. Simulation and Optimization of a Carbon Nanotube Elect. Source. *Microscopy and Microanalysis*, 2015, 21.S4: 60-65.

D. **pp. 80 - 84**
BURDA, D.; KNÁPEK, A. Lithographic method of preparing a gating structure for a nanotube-based field mission source. In: *6th IMAPS Flash Conference. Book of Abstracts*. Brno: Brno University of Technology, 2021, (in press).

E. **pp. 85 - 94**
KNÁPEK, A., et al. Field emission from the surface of highly ordered pyrolytic graphite. *Applied Surface Science*, 2017, 395: 157-161.

F. **pp. 95 - 107**
SAQIB, M.; DE PIETRO, L.; KNÁPEK, A. et al. Field emission properties of single crystalline W_5O_{14} and $W_{18}O_{49}$ nanowires. *Journal of Electron Spectroscopy and Related Phenomena*, 2020, 241: 146837.

G. **pp. 108 - 115**
KNÁPEK, A., et al. Preparation and noise analysis of polymer graphite cathode. *Metrology and Measurement Systems*, 2018, 25.3.

H. **pp. 116 - 127**
KNÁPEK, A., et al. Field emission properties of polymer graphite tips prepared by membrane electrochemical etching. *Nanomaterials*, 2020, 10.7: 1294.

I. **pp. 128 - 133**
KNÁPEK, A., et al. Polymer graphite pencil lead as a cheap alternative for classic conductive SPM probes. *Nanomaterials*, 2019, 9.12: 1756.

J. **pp. 134 - 139**
KNÁPEK, A.; ŠIKULA, J.; BARTLOVÁ, M. Fluctuations of focused electron beam in a conventional SEM. *Ultramicroscopy*, 2019, 204: 49-54.

K. **pp. 140 - 149**
ALLAHAM, M. M.; FORBES, R. G.; KNÁPEK, A.; MOUSA, M. S. Implementation of the orthodoxy test as a validity check on experimental field emission data. *Journal of Electrical Engineering* 71, no.1 (2020): 37-42.

L. **pp. 150 - 151**
ALLAHAM, M. M.; KNÁPEK, A.; MOUSA, M. S.; FORBES, R. G. User-friendly method for testing field electron emission data: Technical report. In: *Proceedings of 34th International Vacuum Nanoelectronics Conference (IVNC2021)*, 2021: 138-139.

M. **pp. 152 - 158**
ÚSTAV PŘÍSTROJOVÉ TECHNIKY AV ČR, V. V. I. Zařízení pro opakovatelnou výrobu ostrých hrotů [Device for repeatable production of sharp points]. Originators: Alexandr KNÁPEK, Pavel KLEIN, Armin DELONG. Czech Republic. Užitný vzor [Utility model] CZ 33278 U1. 7.10.2019.

Volume 13, Number 2, 2020. pp. 171-179

Jordan Journal of Physics

ARTICLE

Similarities and Differences between Two Researches in Field Electron Emission: A Way to Develop a More Powerful Electron Source

M. S. Mousa[a], **A. Knápek**[b] and **L. Grmela**[c]

[a] *Department of Physics, Mu'tah University, Al-Karak 61710, Jordan.*

[b] *Institute of Scientific Instruments of the CAS, Královopolská 147, Brno 61264, Czech Republic.*

[c] *Department of Physics, Brno University of Technology, Technická 8, Brno 61600, Czech Republic.*

Received on: 28/11/2019; *Accepted on: 20/2/2020*

Abstract: This paper discusses the similarities and differences between two studies that deal with resin-coated field-emission cathodes. The two works that are compared within this paper are entitled: *Hot Electron Emission from Composite-Insulator Micropoint Cathodes* and *Methods of Preparation and Characterization of Experimental Field-Emission Cathodes*. Within the text, both studies are reviewed and put into context, pointing out and commenting the advantageous features of this type of cathodes. The comparison focuses mainly on the method of preparation including deposition of a thin film on the cathode tip and the characterization of the coating itself. The effect of the coating on the field emission is discussed as well.

Keywords: Cold field emission, Epoxylite 478, Epoxylite EPR-4.

Introduction

At present, field electron emission from a metal through a dielectric layer is a subject of considerable interest. Its importance is caused mainly by electron devices utilizing a focused electron beam which requires a high-quality source of free electrons that is sufficiently bright and able to provide high current density and work in low-quality vacuum conditions [1, 2]. This paper discusses and further compares two experimental emitters appearing in two separate projects, implying a single way to develop the ultimate electron source.

An experimental field-emission emitter based on tungsten ultra-sharp emitter with a metal-oxide-dielectric structure proved to be the ideal candidate based on the conditions stated above. Regarding the advantages of cold field-emission sources, it should be emphasized that only slight demagnification is required to obtain a 1nm-diameter probe, because of the small virtual source starting from 2 up to 5 nm [2]. Secondly, there is only a very small energy spread, which enables operation at low accelerating voltages. This, in turn, enables to obtain a very sharp, high-contrast image without major radiation damage, especially when working with biological specimens (e.g. tissues or single cells). Lastly, thanks the epoxy layer, it is possible to work in relatively low-quality vacuum (less than 10^{-6} Pa), preventing the ion-bombardment and chemi/physisorption of residuals on the surface of the tip. The preservation of the lower vacuum also enables faster manipulation with the sample and a generally lower price compared to devices working with UHV exceeding 10^{-7} Pa [2].

Corresponding Author: Marwan. S. Mousa **Email**: mmousa@mutah.edu.jo

The need for a better understanding of high-voltage phenomena and development of theories of field electric emission from epoxy-coated tips represents the motivation to study further the behavior of composite tips [1-4]. In general, field electron emission occurs after switch-on voltage is applied to the tip, which has been introduced in previous papers [5-8]. This produces an emission current at considerably lower voltage compared to pure (virgin) tungsten cathodes. Cycling of the voltage provides reproducible I-V characteristics [7,8] with an improved stability [9,10] and a brighter spot [11].

The summary that is presented in this paper concerns our investigations carried out under high vacuum following the pressure 10^{-6} Pa and baking the system at 150–200 °C. In this work, all the experiments were carried out using a high-purity single/polycrystalline tungsten wire, due to its favorable properties, such as: high melting point, high hardness, high work function and significant heat resistance at high temperatures [1-4].

Methods of Preparing Cathodes

Ultra-sharp tips used as a metallic substrate of epoxy-coated emitters were prepared by the same method based on electrolytic etching in both cases [1, 2]. For the electrolyte, a solution of 2–2.5 molar sodium hydroxide was used. After applying the two-phase etching method [4], the samples were cleaned by HF and ethylene (or isopropyl alcohol) in the first step. In the second step, the samples were further cleaned in water for a few minutes using ultrasonic bath in order to get rid of the contaminants originating from the electrochemical etching that are discussed further in the text. The composition of a typical cathode is obtained by Energy Dispersive X-ray spectroscopy (EDS), as illustrated in Fig. 1.

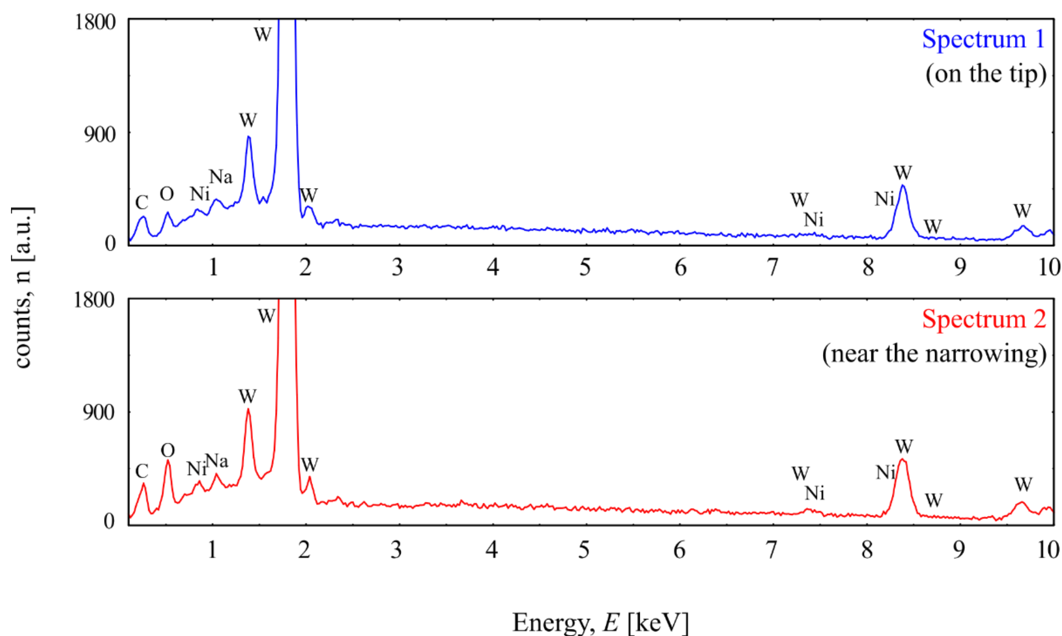

FIG. 1. The spectra of the SEM-EDS analysis for a sample coated by (*478 Epoxy resin*) a) EDS on the tip (blue). b) EDS in the area of wire narrowing (red).

From the results of the EDS analysis of the second emitter, it can be seen that even though tungsten predominates, there is a certain amount of contaminants present. The EDS spectrum was measured twice: on the coated surface (blue) and on the narrowing (uncoated area). Both measurements are comparable and show only a limited influence of the epoxy thin film on the chemical composition. Contaminants, such as Nickel (Ni) and Sodium (Na), originate from a grounded electrode (cathode) that releases some of the components from its surface during the etching process.

These contaminants move from the cathode towards the etched tip and attach to the surface of the etched tip. Despite the fact that this analysis was performed only in the second study, it can be concluded that it goes also for the first study, since it depends on the chemical composition of the etched wire (that was pure tungsten in both cases) and on the composition

of the grounded electrode (that was steel in both cases as well).

After the final etching step, the tip was in both cases coated by epoxy resin: in the first paper, commercially available resin branded *Epoxylite UPR-4* is used, whereas in the second paper, the *Epoxylite 478* is used. In both cases, resins are cured in an electric furnace at two different phases, each at a different temperature. The first phase, where the temperature is usually about 100 °C, serves for degassing of the epoxy. The second phase serves for reaching the glass transition temperature. Fig. 2 shows the emitters coated by using transmission electron microscopy (TEM) and scanning electron microscopy (SEM). The TEM shows a slight difference of the contrast between the dielectric layer and the metallic core. The SEM, on the other hand, shows surface contrast and hence the part of the tip that has been coated. Both methods are complementary and provide different information about coating. The coating method itself in both cases is based on dipping the tip in the epoxy and covering the very top of the tip by a homogeneous layer.

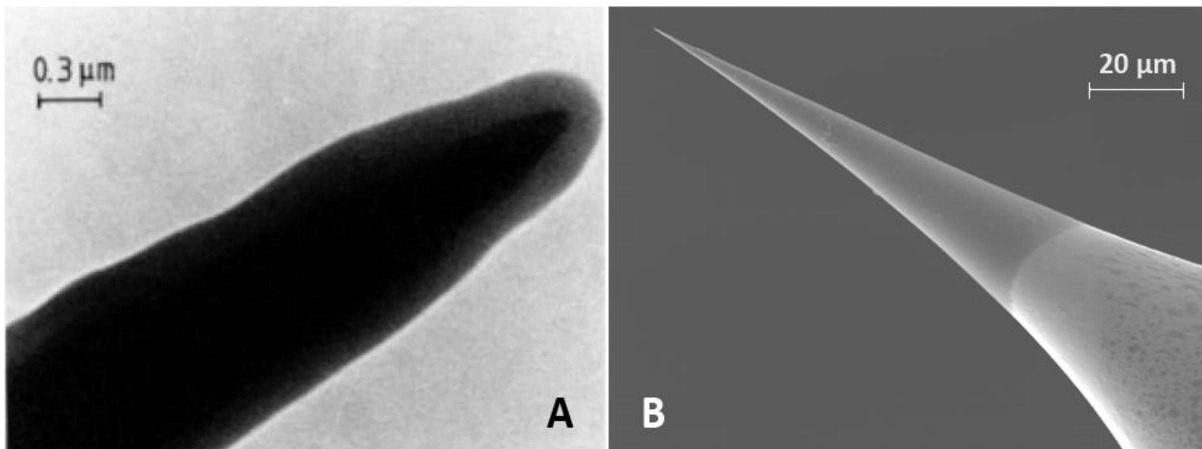

FIG. 2. a) TEM micrograph of W-tip coated by *Epoxylite UPR-4* with a diameter of approx. 200 nm; b) SEM micrograph of W-tip coated by *Epoxylite 478* with a diameter of approx. 20–30 nm.

In the first case, the tip is dipped twelve times into the Epoxylite UPR-4 epoxy, where the concentration ratio of the A and B components was 1:1. The single dip creates a layer that is approximately 15 nm thick. The ultra-sharp tips used as a metallic substrate of the epoxy-coated emitters were prepared by using the same method based on electrolytic etching in both cases [1, 2]. The layer thickness is approximately 200 nm. In the second case, the tip is dipped only once into the Epoxylite 478 which is a single component epoxy resin creating a layer of 20–30nm thickness. Both epoxy resins are based on a *Bisphenol A diglycidyl ether* which is a colorless solid that melts slightly above room temperature. The UPR-4 is a two-component epoxy, whilst the 478 is a single-component epoxy. The difference in thickness amongst the two epoxy resins is caused mainly by different densities of the epoxy resins. In both cases, the tip is then subjected to a curing cycle. In the first case, the tip is baked directly in the vacuum chamber during the degassing procedure, whilst in the second case, the tip is cured in the electric oven. The first part of the curing procedure takes thirty minutes at 100 °C to expel the solvents, followed by thirty minutes at 160 °C to complete the curing of the resin [2, 3]. In both cases, the epoxy resin undergoes glass transition and becomes a hard and relatively brittle “glassy” matter.

Comparison of the Experimental Results

In this part, the experimental results obtained by several methods are described and compared in more detail. Those methods are, in particular:

a) Current-voltage (I-V) characterization and Fowler-Nordheim (F-N) analysis of the I-V data,

b) Analysis of the switch-on phenomena and the emission patterns,

c) Energy and noise spectral analysis of the electron beam.

a. Current-Voltage Characterization and Fowler-Nordheim Analysis

The I-V curve is used to determine basic parameters of the field-emission cathode and to model its behavior during operation. In Fig. 3, curve A shows the I-V characteristics for an uncoated tungsten emitter with a 30nm tip apex connected in a simple diode configuration. Compared to curve A, curve B represents the characteristics of a coated tip by 200 nm of Epoxylite UPR-4 resin. It can be seen that the threshold voltage V_{th} decreased and an additional hysteresis appeared, slightly moving the characteristics toward higher current values when the applied voltage is increased in contrary to the opposite way. These effects have been already described and discussed in several papers [1, 5, 7].

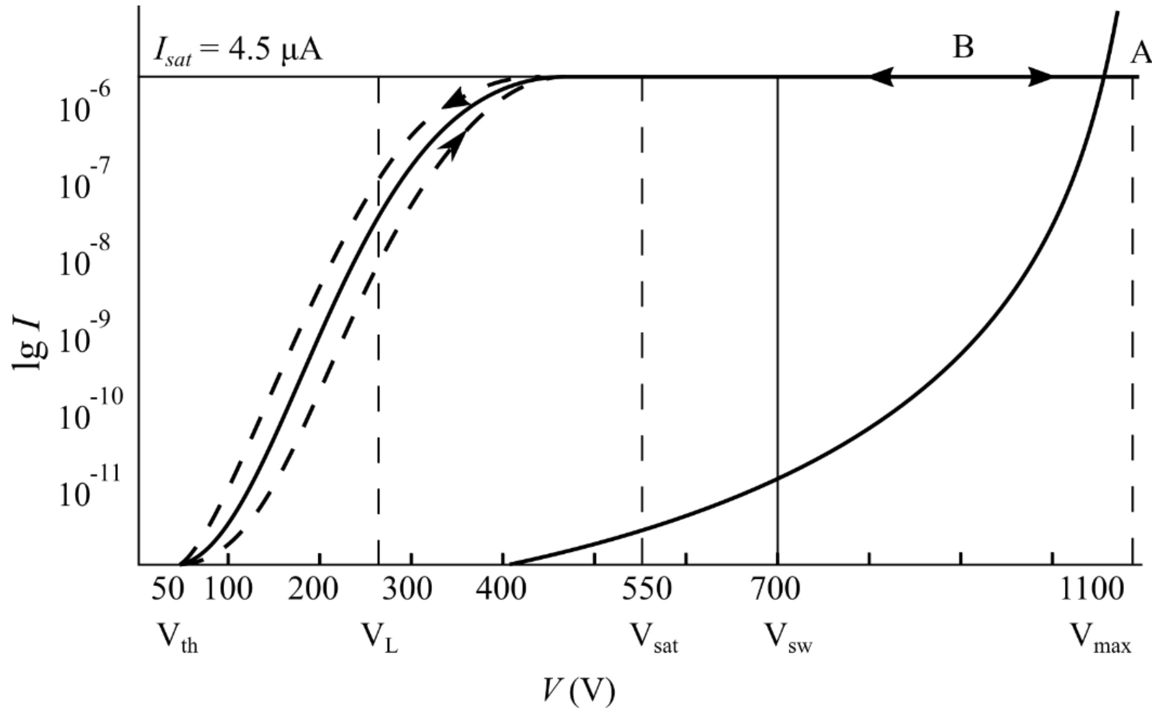

FIG. 3. A comparison of I-V characteristics of an uncoated (A) *vs*. coated (B) W-emitter of a tip radius of 30 nm and an epoxy coating of approx. 200 nm (*UPR-4 Epoxylite resin*).

Fig.4 shows the Fowler-Nordheim plots of the uncoated (curve A) and the resin-coated (Epoxylite UPR-4) sharp tip. The Fowler-Nordheim plot is the most common method of analyzing the I-V characteristics and it is used to graphically interpret and analyze data obtained from the theoretical equation derived by Fowler-Nordheim [11]. The original idea was to obtain an exact straight line of slope S_{FN}, which would be a ratio related to the parameters appearing in the exponent of a Fowler-Nordheim-type equation of I-V form by: $S_{FN} = -b\varphi^{3/2}/\beta$; and therefore the knowledge of the work-function φ would enable the determination of field enhancement factor β and *vice versa*. From Fig. 4, a certain difference between slopes of lines representing uncoated (A) and coated (B) emitters can be seen. A decrease in the slope of the F-N plots of the coated cathode at room temperature is obtained with a factor β of 3 to 4. This also results in a decrease in the work function φ with respect to that of the uncoated W-tip of 4.52 eV [5].

In Fig. 5, the left curve shows the I-V characteristic for a sample coated with (478 Epoxylite resin) [4, 8]. The cathode was measured in the triode mode incorporating an additional anode called *the extractor* electrode which is located close (approx. 0.75 mm) to the field emission tip. This configuration is used mostly for devices utilizing a focused electron beam, where it is possible to change the size of the cross-over simply by changing the ratio between voltages applied. The extractor electrode makes the electrons leave the surface and the additional (acceleration) energy is provided by the anode which serves as the main acceleration electrode here. The particular set-up

and the precise measurement method is described in more detail by Knápek [4].

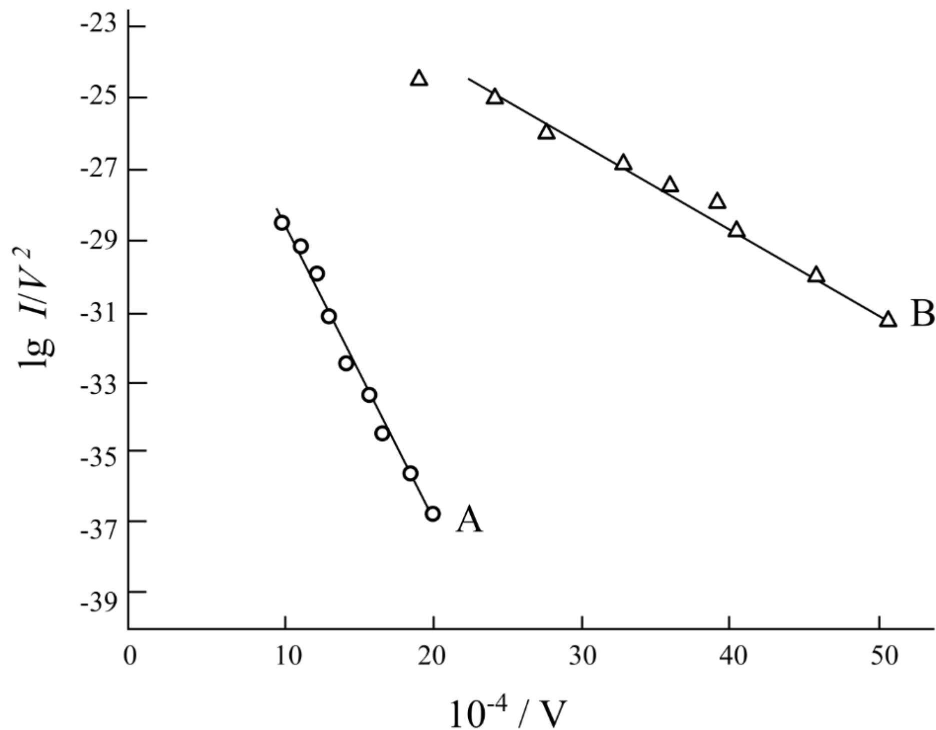

FIG. 4. The Fowler-Nordheim plots of the uncoated (curve A) and *Epoxylite UPR-4* coated tip (curve B).

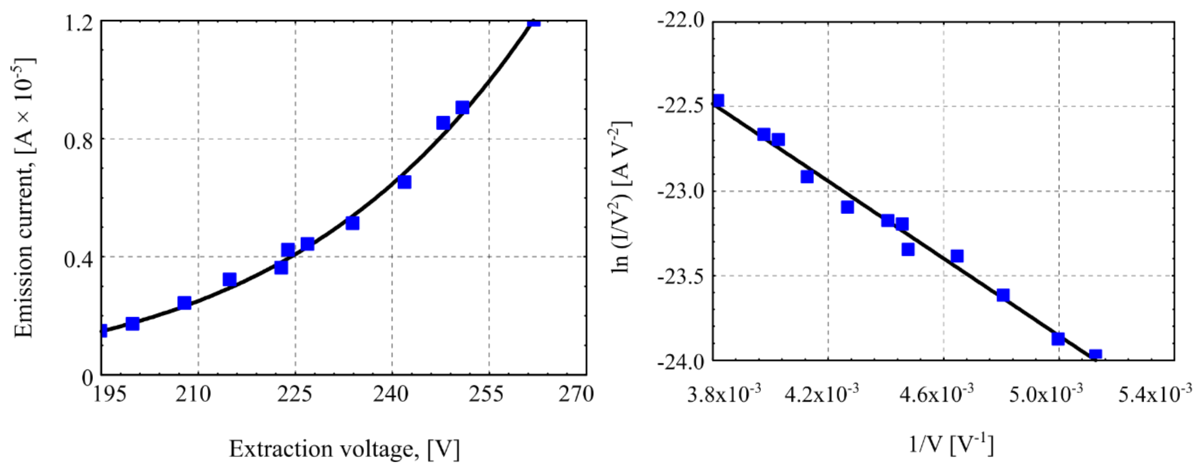

FIG. 5. Electrical characteristics of the tip coated by *Epoxylite 478*. Left: I-V characteristics of the emission current based on extraction voltage following exponential function. Right: calculated Fowler-Nordheim plot following linear slope.

The current-voltage measurements of the second sample are represented by Fig. 5 left (I-V characteristics) and right (F-N plot). Even though the I-V characteristics curve covers just a limited range of extraction voltages (195–270 V), it implies that the current there follows the same exponential function as the previous coated sample illustrated in Fig. 3. B. The difference of the nominal current is caused mainly by a different operation mode (the triode mode *vs*. the diode mode), by a different detection method (the Al-coated scintillation crystal *vs*. phosphorus screen in the previous case) and by different coating where both layer thickness and different chemical structure affect the emission. In the F-N plot illustrated in the right part of Fig. 5, it can be seen that there is a certain similarity to the previous sample implying the same effect on the field emission. This effect was explained in more detail by Mousa [12].

The ideal thickness of the Epoxylite 478 coating whose relative permittivity ε_r = 4 has

been theoretically calculated (based on WKB approximation) and found to be around 5 nm [2]. To conclude this part, the typical slope of a coated emitter is ≈ 1/4 that of the uncoated tungsten emitter. The maximum voltage that may be applied for stable emission is typically twice the voltage required for saturated emission [1, 6, 8].

b. Analysis of Switch-on Phenomena and Emission Patterns

The initiation of the field emission is observed after a “switch-on” voltage has been applied to the tip. This produces a saturated emission current that can then be maintained at much lower voltages. A summary of the most important results was reviewed in a paper published by Mousa [5]. The projection images that appear on the screen are also referred to as emission patterns due to their geometric arrangement for single-crystalline emitters. In each of the studies, the analysis of the emission pattern is made from a different point of view. For the first paper, the difference between virgin (uncoated) and coated emitters is analyzed, whilst for the second, the effect of the extractor voltage is analyzed for the coated emitter.

The field emission pattern displays the projected work function map of the emitter surface. The closely packed faces {110}, {100}, and {211} have higher work functions than atomically rough regions and they thus appear in the image as dark spots on the brighter background (see Fig. 6. A). In the right part of the figure, the effect of epoxy coating can be seen creating a single emission region in the position of the facet {110}. This is one of the most important and interesting features of using the epoxy coating.

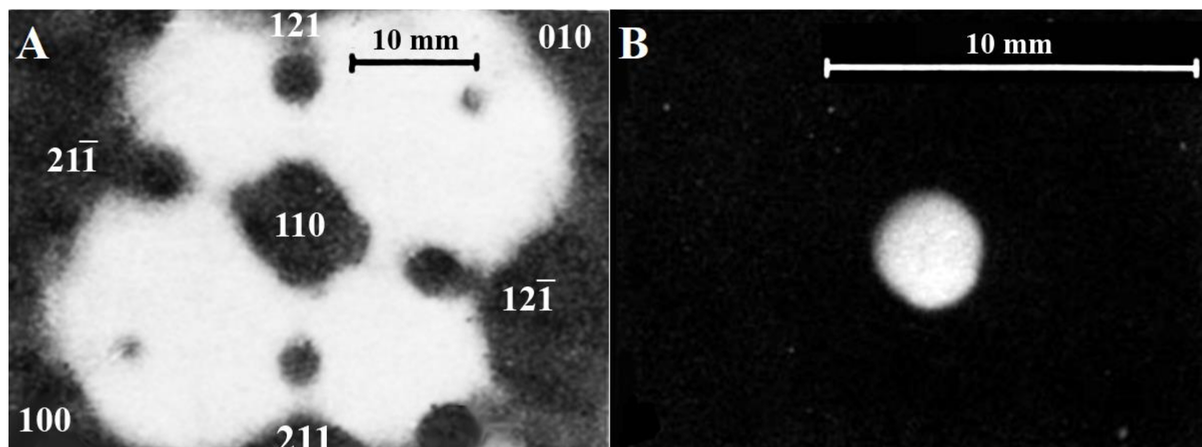

FIG. 6. Emission pattern obtained from a) the clean tungsten emitter and from b) the emitter that was coated by a 150nm layer of *Epoxylite UPR-4* resin. Both images were recorded with the same tip-to-screen separation and the same emission current of 4.5 pA [1, 6].

For the tips that were coated by Epoxylite 478 in the second work, it has been experimented with an increasing extractor voltage and its effect on the shape of the field-emission-active area. Instead of the phosphorus screen used in the previous case, in this case, a Cerium-doped Yttrium Aluminium garnet was used to display the emission pattern and to conduct a constant part of the electron beam that has been used for analysis. The measurement is illustrated in Fig. 7, showing 4 extracting V_{ex} voltages and the corresponding spot size d. It has been found out that the intensity of the spot size is equally distributed and the shape is equidistant in respect to the optical axis. Another pursued parameter is the relative light intensity that is a parameter based on the number of photons impinging on the surface of the CCD chip of a camera used to record the image, which is expressed in percents. Authors have found out that the relative light intensity L follows the linear function [2].

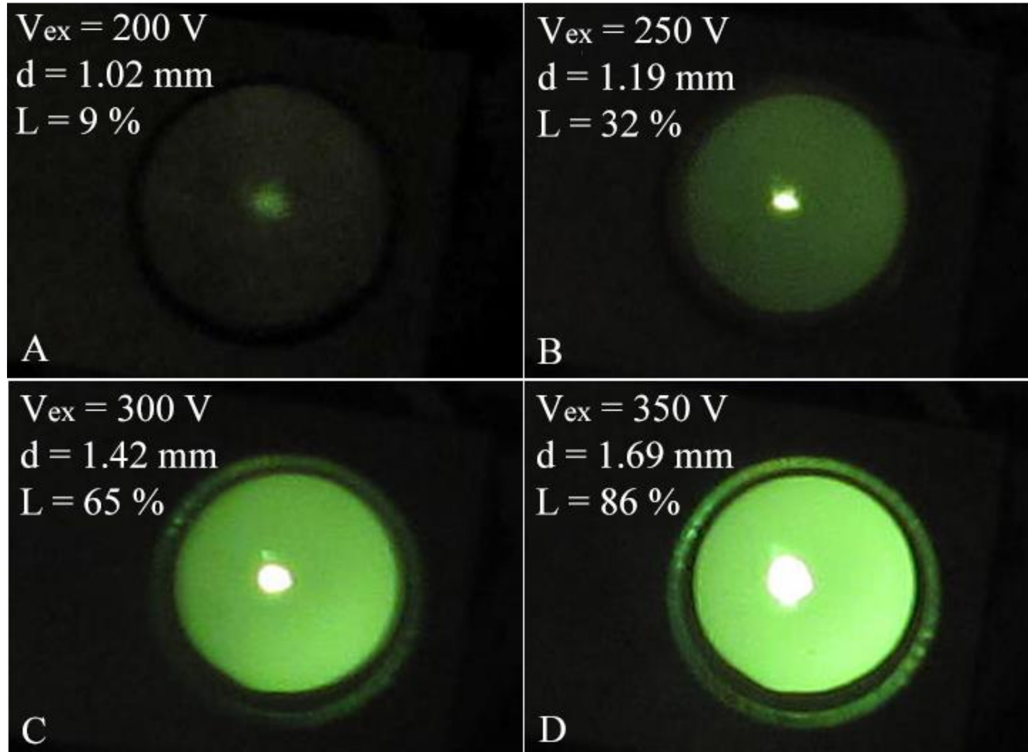

FIG. 7. The emission patterns *vs*. the extraction voltage for the sample coated by *Epoxylite 478* resin [8].

c. Energy and Noise Spectral Analysis of the Electron Beam

The electron spectra were measured only for the cathodes coated by Epoxylite UPR-4 to provide important information on the emission mechanism associated with the composite regimes. The measurements were performed using a well-known retarding potential analyzer design of Van Oostrom (1966), but incorporating fully automated electronically controlled drive and detection systems [1]. In particular, a lock-in amplifier technique was used to obtain a direct differential spectral output providing an output that is comparable to the more widely used hemispherical type of analyzer [1].

Fig. 8 illustrates and compares the energy spectra obtained from a tungsten emitter before (A) and after (B) coating with a 200nm thick layer of the Epoxylite UPR-4 resin. In both cases, the emission currents were equal to 4 pA.

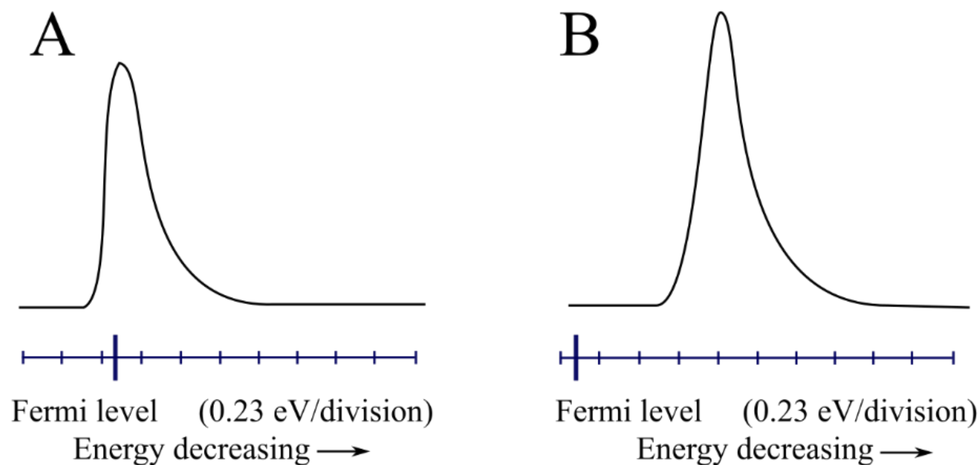

FIG. 8. A comparison of the energy spectra obtained from the tungsten emitter (a) before and (b) after coating with a 150 nm thick layer of resin at identical emission currents of 4 pA.

These results have shown that with respect to the Fermi level, the spectrum obtained in the metal cathode is displaced towards lower energies by approx. 0.7 eV and that the composite emitter has a significantly larger full width at half-maximum compared to the uncoated one. Last, but not least, the measurements showed that the spectrum of the composite emitter is more symmetrical compared to the clean tungsten tip [1, 5].

In the second case, for the Epoxylite 478-coated tip, the electron beam was analyzed using a method that is based on evaluating the slope of the power noise spectral density spectrum of the total emission current. This method is mostly used for semiconductor analysis and it is obtained by performing the Fourier transformation on the sampled emission current. From the slope of the spectrum at particular frequency bands, it is possible to identify processes responsible for particular events that are responsible for the noise at the quantum level. The precise method was described by Knápek [10].

From the measurements shown in Fig. 9, it is evident that the power spectral density of whole spectra is being slowly increased in time and that the slope is staying constant. From the slope, which is constantly about 1.5, it is evident that the measured noise has characteristics of the so-called $1/f$ (flickering) noise. The $1/f$ noise is a process with a frequency spectrum, such that the power spectral density is proportional to the reciprocal of the frequency. We can see that, for the red curve, the parameters changed to $a = 1.5\times10^{-4}$, the slope $n = -1.3$ and the time constant remains the same, $b = 1\times10^{-3}$ s. In conclusion, the period τ between each hop to the different energy level is computed as 1.59×10^{-4} s. The cutting frequency is located near 1000 Hz. The $1/f^{\,n}$ noise (where $n > 1$) originates from the superposition of particular $1/f$ and generation-recombination (G-R) processes which originate from adsorption and desorption of various atoms present with some residual gas in the vacuum chamber.

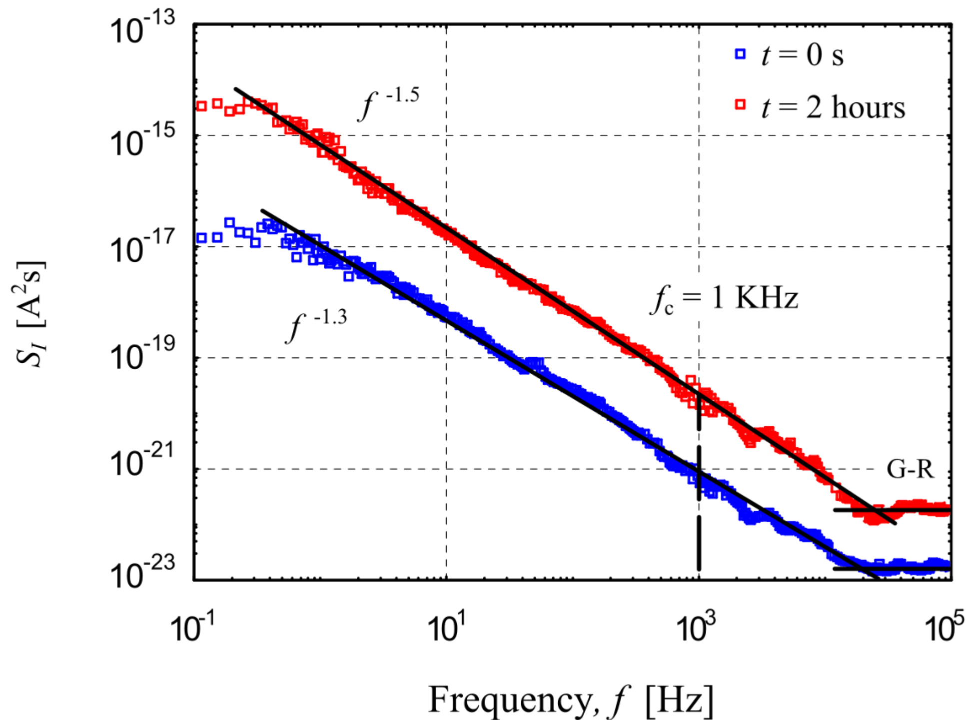

FIG. 9. A comparison of long-time noise power spectrum density measured at $V_{ex} = 200$ V, from $t = 0$s (blue) to $t = 120$ min (red).

The results suggest that the ions which are bombarding the cathode's surface can be observed from the noise measurement as well. They prove themselves by random *burst noise*. The bombardment reduces the epoxy layer, which leads to its unavoidable damage. The noise spectral density (where the $1/f$ noise prevails) changes to $1/f^{\,n}$, where n is located between 1 and 2. In general, the $1/f^{\,n}$ noise originates from the superposition of particular $1/f$ and generation-recombination (G-R) processes. Therefore, the higher the n, the more significant

the G-R. Generation-recombination is caused mostly by the chemisorption of the ion residuals present in the chamber. These effects of chemisorption are unavoidable, since only the surface on the tip is protected by the epoxy layer.

Conclusions

In this paper, two similar studies have been compared with the emphasis on similar features, confirming the excellent field emission behavior of the dielectric-coated emitter tip. This is a prospective candidate for a future advanced electron field emitter.

Amongst the most suitable attributes, the most interesting are the low operating voltages and the high current densities. The resin coating protects the surface of the emission plane from unwanted chemical or physical sorption of ions which are attracted backwards towards the cathode and cause a massive bombardment of the tip. This protection enables the cathode to work at lower vacuum than for classical field emission. The coating also slightly reduces the emission current, making the energy more symmetrically distributed compared to the distribution of the uncoated emitter. The epoxy influence of the coating thickness on emission stability will be discussed later in a follow-up publication. For now, it can be concluded that the coating is very thin. Epoxy coating also causes a decrease in the beam energy spectrum which is lower by ≈ 0.7 eV with respect to the Fermi level of the metallic cathode, as we can see in the electron spectra.

Acknowledgements

From the Czech part: The research was supported by the Ministry of Industry and Trade of the Czech Republic, MPO-TRIO project FV10618. The research infrastructure was funded by the Czech Academy of Sciences (project RVO:68081731).

References

[1] Mousa, M.S. and Latham, R.V., Le Journal de Physique Colloques, 47 (C7) (1986) C7-139.

[2] Knápek, A. and Grmela, L., "Methods of Preparation and Characterisation of Experimental Field-Emission Cathodes", (Brno University of Technology, Brno, Czech Republic, 2013).

[3] Knápek, A. and Grmela, L., Chemické Listy, 107 (7) (2013) 545.

[4] Knápek, A. et al., Microelectronic Engineering, 173 (2017) 42.

[5] Mousa, M.S., Karpowicz, A. and Surma, S., Vacuum, 45 (2-3) (1994) 249.

[6] Al-Qudah, A.A., Mousa, M.S. and Fischer, A., IOP Conference Series: Materials Science and Engineering, 92 (2015) 012021.

[7] Mousa, M.S., Surface Science, 231 (1-2) (1990) 142.

[8] Mousa, M.S., Surface and Interface Analysis, 39 (2-3) (2007) 102.

[9] Latham, R.V. and Salim, M.A., Journal of Physics E: Scientific Instruments, 20 (2) (1987) 181.

[10] Knápek, A. et al., Metrology and Measurement Systems, 19 (2) (2012) 417.

[11] Forbes, R.G. et al., Journal of Vacuum Science & Technology B: Microelectronics and Nanometer Structures Processing, Measurement and Phenomena, 22 (3) (2004) 1222.

[12] Mousa, M.S., Le Journal de Physique Colloques, 48 (C6) (1987) C6-115.

Microelectronic Engineering 173 (2017) 42–47

Contents lists available at ScienceDirect

Microelectronic Engineering

journal homepage: www.elsevier.com/locate/mee

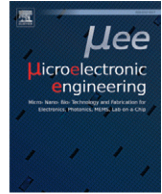

Research paper

Programmable set-up for electrochemical preparation of STM tips and ultra-sharp field emission cathodes

Alexandr Knápek [a,*], Jiří Sýkora [a], Jana Chlumská [a], Dinara Sobola [b]

[a] Institute of Scientific Instruments of the ASCR, v.v.i., Královopolská 147, Brno, Czech Republic
[b] Department of Physics, FEEC, Brno University of Technology, Technická 8, Brno, Czech Republic

ARTICLE INFO

Article history:
Received 31 January 2017
Received in revised form 27 March 2017
Accepted 1 April 2017
Available online 5 April 2017

Keywords:
Field emission cathode
STM tip
Electrochemical etching

ABSTRACT

This paper describes a newly designed set-up which is intended for automated preparation both for STM tips and for ultra-sharp field emission cathodes made of polycrystalline and single crystal tungsten in laboratory conditions. The newly designed set-up incorporates electrochemical etching of a wire in the surface layer of an electrolyte and also the so called drop-off method which consists of two steps and requires more precise wire and current setting. Additionally, the method was extended for polycrystalline wires of tungsten using a special cut-off algorithm, which deals with variable etching speed for various crystallographic orientation of the current grain. Produced tips are examined using scanning low energy electron microscopy as for the surface and by the occurrence of electron field-emission as for the geometry based on the Fowler-Nordheim analysis. STM performance of the produced tip is discussed and examined as well.

© 2017 Elsevier B.V. All rights reserved.

1. Introduction

In this paper, a relatively simple and effective set-up designed for sharp tip preparation is presented. The set-up may be useful especially for smaller laboratories requiring reproducible and affordable way for the sharp tip preparation. Despite the fact that the topic of sharp tip making has been discussed many times and from many points of view in the past, there is still room for improvement due to the progress enabled by computers and quite a few applications which motivate us to pursue this topic. A partial review on the sharp tip preparation was made by Melmed in 1991 who literally “counted the ways” and presented suitable techniques and methods for sharp tip making including the electrochemical polishing/etching method, which was mainly discussed in his paper [1]. It should not be omitted that Melmed's article attracted serious attention since, until then, the problem was imbedded for the most part in papers which were not specifically devoted to the tip preparation as the primary issue. Hence the paper inspired others to contribute, both from the point of view of the etching technique and the etching set-up improvement [2–7].

Sharp tips are essential for the scanning tunnelling microscopy (STM). The tip quality is a major parameter which influences the performance of the STM. Among the most important are the tip size, tip shape and surface cleanliness which are very important for the resolution [3,4]. Tips that are used in the ultra-high vacuum (UHV) conditions are mostly made of tungsten because of its high melting temperature, high mechanical strength and because of the relatively simple preparation allowed by the electrochemical etching technique [4]. As reported by Watanabe [2], rhenium polycrystalline tips seem to be suitable for STM as well. Sharp tips with low apex radius are also important for cathodes based on field emission (FE) of electrons. The need for them arose in the early days of electron microscopy, especially in connection with field electron emission microscopy (FEEM). Nowadays, the ultra-sharp tips with diameters lower than 100 nm are mostly used for electron guns with cathodes operating at a room temperature. This kind of free electron source has proven to have the highest source brightness accompanied with the lowest energy spread compared to common ZrO/W emitters. The apex radius of curvature is rather small in order to achieve a sufficiently large electric field. In order to keep the highest possible stability of the emitted current, it is necessary to work in UHV conditions and to choose proper material with high melting point and high mechanical strength. For these reasons, tungsten seems to be still one of the most suitable materials, although there are some other metals (Mo, Cr, Nb) that are suitable for the field emission [8].

Since there are many common parameters and requirements, it seems reasonable to operate one single set-up which would be able to prepare both STM tips and FE tips from commonly used metals just by using different electrolyte and pre-programmed procedure. In order to achieve good reproducibility, the control software along with the mechanical adjustment during the etching plays a significant role and will be discussed in this paper as well. Last but not least, the presented set-up is ready to be used for a Method of Electrochemical Etching of Tungsten Tips with Controllable Profiles presented by Chang [5] allowing obtaining custom tip profile.

* Corresponding author.
E-mail address: knapek@isibrno.cz (A. Knápek).

http://dx.doi.org/10.1016/j.mee.2017.04.002
0167-9317/© 2017 Elsevier B.V. All rights reserved.

2. The etching set-up

The programmable etching set-up consists of three mutually connected parts that are supplemented by standard Agilent instruments, namely the Waveform generator, the DC source, and the multimeter. The mentioned instruments are connected using IEEE 488 (GPIB) bus through the USB/GPIB convertor directly to the computer providing quick response and data monitoring almost in real time. The cut-off unit is a self-standing device based on fast analogue circuit which is connected between the etched wire and the source of etching current as illustrated in Fig. 2. Its function will be discussed in part 4 of the paper.

The mechanical holder provides movement and setting of the wire during the etching. The latter is equipped with a precise micro-stepper motor enabling fine movement which allows a precise setting of the wire on the electrolyte surface during the multiphase etch process. The mechanical holder illustrated in Fig. 1 consists of: (a) an adjustment screw allowing for a fine manual setting of the wires position by rotating directly the motor's shaft (b). A single step is equal to 2.7 degree of arc, which is transferred to a vertical movement of 1.2 μm.

The rotary movement of the shaft is transferred to a piston (d) that carries out the up and down movement and also holds the removable wire clamp (e). The piston also acts as a centring device to keep the movement strictly axial. The piston movement is delimited by a couple of micro switches that send signals directly to the microcontroller of the stepper motor driver. The lower one is labelled (k) in Fig. 1. The cathode clamp (e) that contains the etched wire (up to 0.4 mm of diameter) is then immersed into a cylinder that is filled with an electrolyte (f). The glass cylinder is also equipped with a Teflon protection grid preventing bubbles originating from the cathode from affecting the surface etching of the wire (anode). The cylinder therefore co-creates the cathode along with the Teflon grid and Pt plate that are connected to the terminal strip (g) using a platinum wire. Platinum was used since it is chemically inert, transferring just the charge without any unwanted chemical contamination. The part (i) is a transparent table under the cylinder that transmits light originating from a small LED panel placed under the table, which is advantageous when using a visible light microscope to observe a tip shape during the etching. The parts (h) and (j) are intended for fine mechanical adjustment of the table: there are three feet forming a triangle (i) which serve to set the horizontal plane of the table complemented with a water level (h).

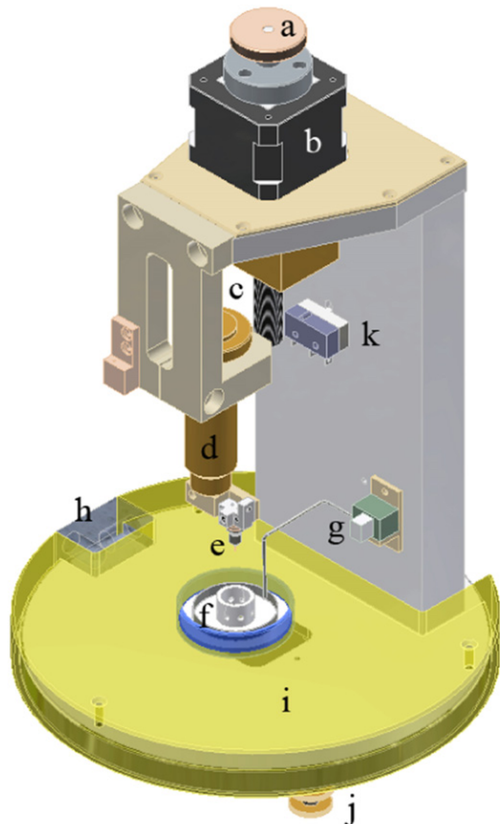

Fig. 1. A model of the mechanical holder which is driven by a precise micro-stepper motor. Individual components are marked with Latin letters.

The electrical set-up is illustrated in Fig. 2 and can be in principle divided into three main parts. The first part consists of the controlling computer equipped with a self-standing Matlab programme that communicates with instruments and evaluates the current-voltage measurements obtained nearly in real time.

The second part is the micro-stepper driver unit (see Fig. 3). It is equipped with a programmable microprocessor Atmel AT Mega 32/L (8bit RISC with 8 Kbyte of programmable memory) driven at 16 MHz that communicates with the computer over a universal serial bus (USB) using FT232.

The last part consist of three instruments: (1) a multi-meter Agilent 34410A measuring the etching current and voltage, (2) a waveform generator Agilent 33220A providing the alternating current for the electro-polishing and (3) a dual DC source Agilent E3641A providing the etching voltage and supplying the micro-stepper motor driver. The group of instruments is connected through Agilent USB/GPIB interface 82,357 to the computer and served by the Instrument Control Toolbox™ developed by MathWorks.

3. Preparation method

The implemented method is based on a principle of anodic dissolution of a metal electrode (wire) in liquid electrolyte with voltage applied [1]. The heightened pressure at the electrolyte surface increases the etching speed and hence shapes the tip. For our clamps, it possible to use 0.1 to 0.4 wire diameters, however, the preferred diameter is 0.3 mm.

Within our set-up, sodium hydroxide is used as the electrolyte to etch tungsten wires. It is possible to work both with single crystalline or polycrystalline wire. Based on the etched material the process differs in terms of etching speed and selectivity that is a typical attribute of polycrystalline materials. Also the initial immersion depth is different: for single crystals, it is possible to use a single step method (Fig. 4a) and etch the shape at the surface level of the electrolyte. For

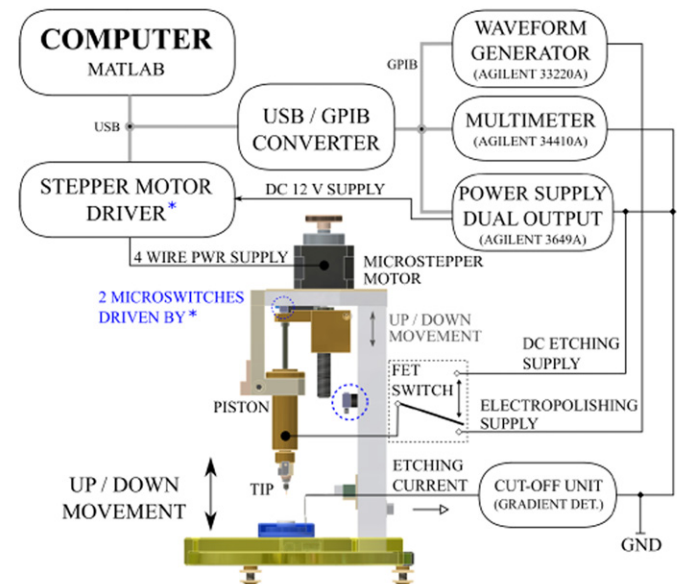

Fig. 2. An electrical schematic of the etching set-up.

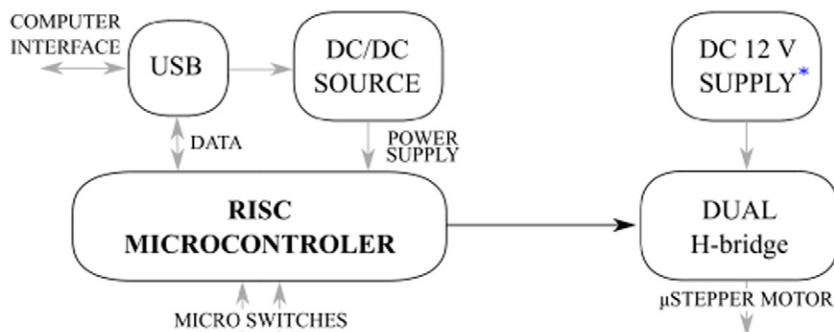

Fig. 3. An electrical schematic of the electronic driver unit.

polycrystalline materials, it is desirable to use a two-step method (Fig. 4b) in order to shape the tip properly (Fig. 6). The two-step method involves the creation of meniscus and dropping of its bottom part, which gave a name to the method (*drop-off*) [1]. For etching tungsten tips, the cathode is made of platinum, preventing thus unwanted contamination which may occur for example in the case of a stainless steel electrode. From the chemical point of view, the following reactions are taking place, in particular [7]:

Cathode:

$$6H_2O + 6e - \rightarrow 3H_2(g) + 6OH^- \quad (1)$$

Anode:

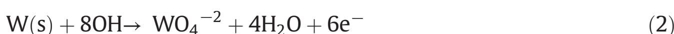

$$W(s) + 8OH \rightarrow \; {WO_4}^{-2} + 4H_2O + 6e^- \quad (2)$$

Overall reaction:

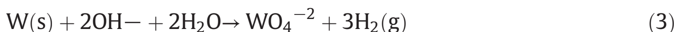

$$W(s) + 2OH- + 2H_2O \rightarrow {WO_4}^{-2} + 3H_2(g) \quad (3)$$

In order to obtain a sharp tip of a radius of curvature as small as possible (illustrated in Fig. 6, right), it is necessary to set a proper etching voltage in combination with a properly concentrated NaOH solution. For our tips, 8–10% solution is used. The etching voltage is set to 6.9 V with current limit of 20 mA for both the one-step and two-step method. For the two-step method, a slightly less concentrated electrolyte may be used in the second step in order to slow down the etching process and prevent any tip blunting that could be caused by a delayed DC supply disconnecting.

The pre-programmed procedure is also responsible for an automated detection of electrolyte's surface based on the current measurement during the tip movement towards the electrolyte. When the current is measured ($I > 1$ μA), the edge of the wire has touched the surface and can be immersed further by required length into the solution. This is mostly 0.5 mm for the single-step method and 1 mm for the two-step method. Deeper immersions would create a heavier bottom part which might release excess elastic energy and thus deform the etched tip.

4. Control algorithm

As mentioned before, the control software was developed especially for use with the presented set-up. A simplified software function is illustrated by a flowchart in Fig. 5. The main application that is written in Matlab® controls instruments connected via GPIB and evaluates their outputs (current/voltage). It also controls the self-standing Stepper Motor Driver unit which is equipped with a CPU controlling the movement of the micro-stepper motor.

The gradient detector is one of the critical parts of the proposed algorithm, since the cut-off rate is considered to have significant influence on to the final tip shape. As shown in Fig. 6, the cut-off algorithm is implemented at the end of the two-step method based on the calculation of the second differentiation in real-time. For this reason it has been named the Gradient Detector. Because of the delay that is caused by the time lag of connected instruments (i.e. a period of time between two related actions), the detector has been recently transferred from computer procedure to the hardware level by creating a self-standing device based on an analogue differentiator circuit (see Fig. 2), which allows to respond in approx. 25 ns.

5. Experimental tip description and evaluation

A schematic diagram of the tip profile is illustrated in Fig. 6. based on Chang [5], the tip profile includes length, radius of curvature at apex and taper angle. Based on the statistical data, the average taper angle

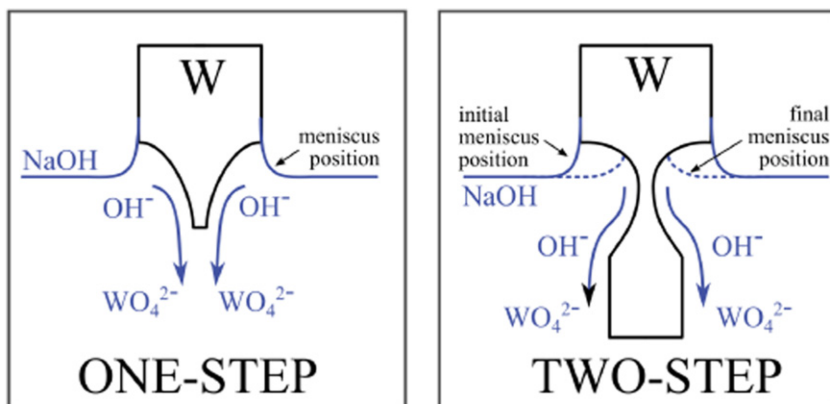

Fig. 4. Tip formation diagrams for Tungsten: (a) one-step method used for single crystalline materials and (b) two-step *drop-off* method used for polycrystalline materials.

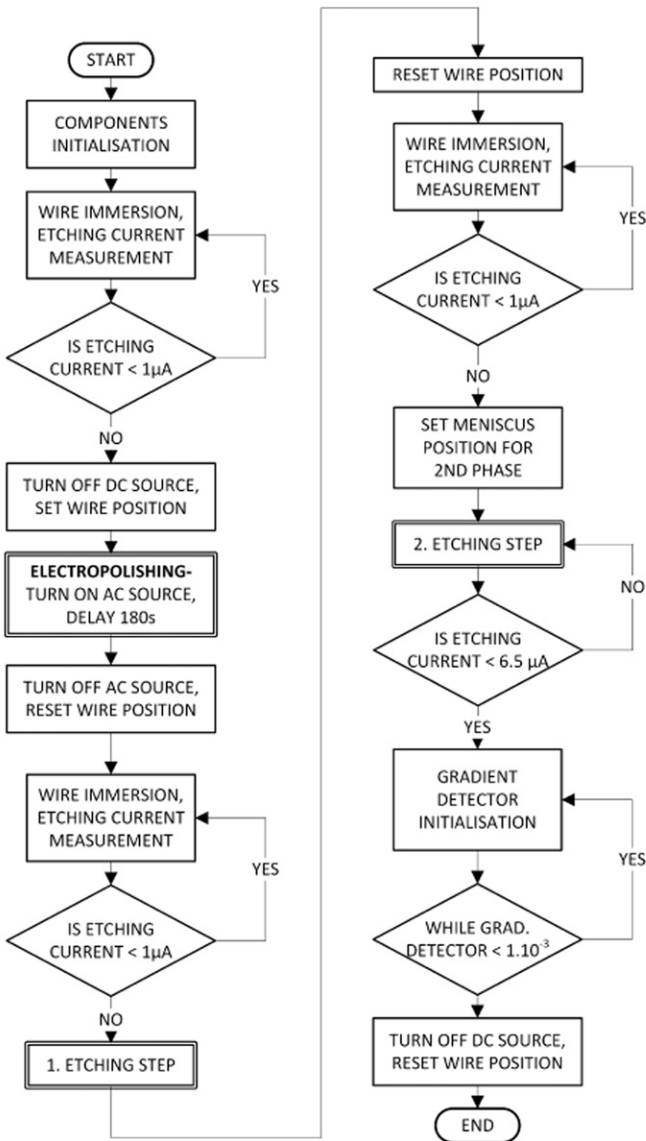

Fig. 5. A flowchart representing the control software, in particular: (left) one-step method, (left + right) two-step method.

reached was 6.4° for a testing set of ten tips. An example of produced nano tip is given in Fig. 7.

The tip height/weight (H/W) ratio is approximately equal to 1; the lower the ratio is, the higher electric field gradient at the tip is obtained.

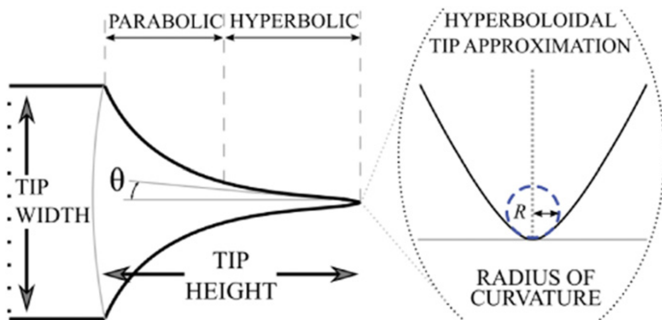

Fig. 6. (left) The shape of the created tip characterized by the tip height/width ratio and taper angle θ. (right) Hyperbolic approximation of the tip incorporating radius of curvature *R*.

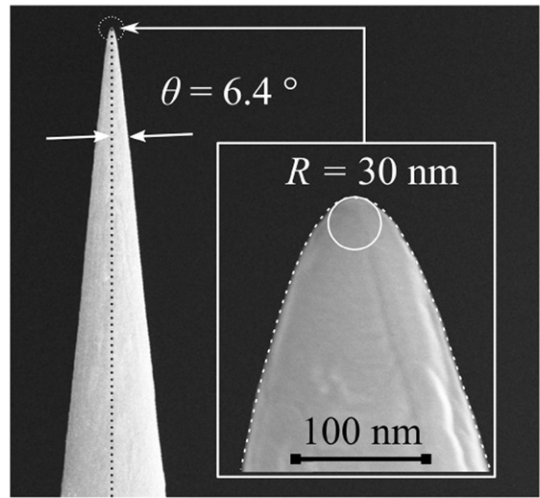

Fig. 7. An example of a produced nano tip, made of a polycrystalline tungsten tip created by the preprogrammed two-step method.

The Tip height can be set by altering wire position in the first step of the two-step method as illustrated in Fig. 5. The radius of curvature *R* of the tip can be calculated using hyperboloidal emitter model proposed by Yuasa et al. in order to provide preliminary information about the tip geometry. The Yuasa hyperboloidal linear model is similar to the Fowler-Nordheim model and defines the radius of curvature as [8]:

$$\boldsymbol{R} = \boldsymbol{a}\frac{\sin^2 \boldsymbol{u}_0}{\cos \boldsymbol{u}_0} = \boldsymbol{L}\tan^2 \boldsymbol{u}_0, \tag{4}$$

where parameters a and u_0 are related to the distance between emitter and collector (anode) calculated as $L = a\cos u_0$. Hence, the parameter u_0 is the parameter which characterizes the sharpness of the emitter. It should not be omitted that this parameter is not contained within the ordinary Fowler-Nordheim theory which is based on the planar emitter model [8].

For the polycrystalline tips the tip reproducibility is rather high, which is illustrated by relatively low variance of the taper angle that is equal to 0.05 for our testing set. Among the taper angle and the radius of curvature, which are the parameters determining geometrical parameters and hence the proportions of a yielded tip, the slope of F—N function can be considered to be a good indicator of reproducibility as will be shown below.

For single crystalline tips, due to homogenous etching rate caused by uniform crystalline orientation, the variance of the taper angle is even lower allowing to achieve an almost 100% reproducible tip. Despite the higher reproducibility for the single crystalline tips, it still makes sense to keep preparing tips from a polycrystalline W-wire because of its lower price. Moreover, most polycrystalline W-wires are partially oriented due to the pulling process since the grains are often several mm long. For this reason, the crystalline orientation at the tip is uniform allowing to obtain a homogenous work function at the active area of the tip surface, which is required for stable field-emission based cathodes.

The tip performance and its ability to provide a tunnelling current is evaluated by the Fowler-Nordheim analysis [7] that is based on measuring the emission current when a strong electric field is applied. For a typical field-emission, it is necessary to achieve a field strength of $E = 10^{10}$ V/m, which requires either an application of a very high voltage (kilovolts) or working with a significant field enhancement factor. The latter can be achieved by a high field gradient on the tip which depends on the tip geometry and mainly on the tip diameter [7]. The tip is

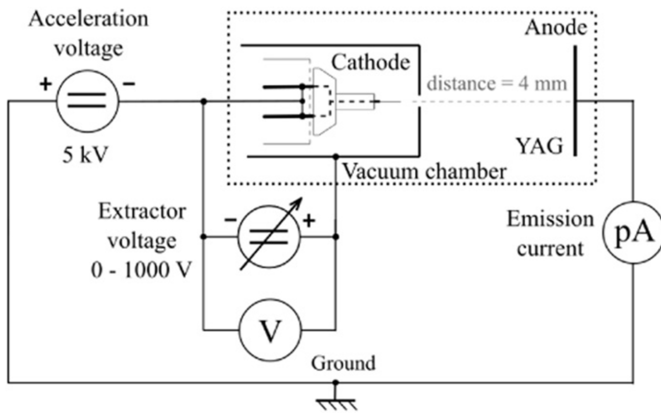

Fig. 8. Schematic drawing of our measurement set-up.

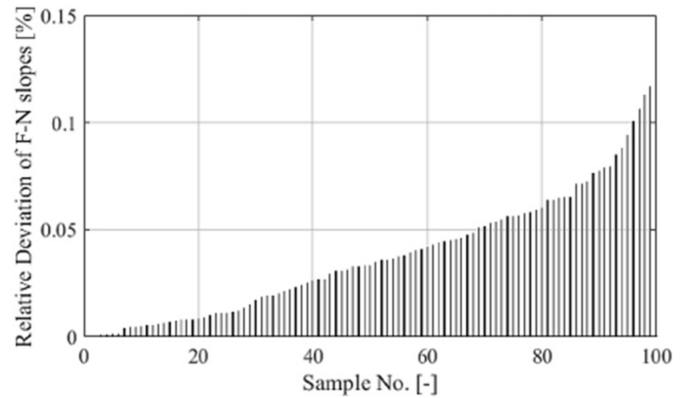

Fig. 10. Relative deviation of the testing set correlating Fowler-Nordheim slopes against a mean value of the set which is represented by the X axis.

therefore moved to the vacuum chamber (UHV is desirable) where a triode connection is used.

Our tip-testing set-up (see fig. 8.) is generally based on the field emission microscope (FEM) invented by E. W. Müller in 1936 [9]. It's function and mainly its contribution to the surface analysis has been published many times. Our method incorporates a FEM based technique which is intended for tip characterisation and comparison as published by Lucier et al. [10].

The applied extractor voltage emits electrons and the cathode voltage accelerates them towards the grounded anode. The current-voltage measurements have been done for each tip of the testing set and converted to a Fowler-Nordheim plots in which a slope is yielded from each plot. As mentioned above, a nearly identical slope of the plot is considered to be a good indicator of the tip reproducibility. An example of slope comparison is represented by a stacked FN-plot of the reduced set of ten samples in Fig. 9. Statistical evaluation for the whole set is illustrated in Fig. 10 using F—N slopes relative deviation against a mean value of the set which is represented by the zero on the X axis. The relative deviation is given by $\boldsymbol{\Delta u_i}/\overline{\boldsymbol{u}}$, where $\boldsymbol{\Delta u_i}$ denotes the mean of a set of quantities $\overline{\boldsymbol{u}}$. The coefficient of variation v_x for the whole set is equal to -4.85%.

Apart from the geometrical shape, the surface cleanness is important for the performance of both STM tips and FE cathodes. Contaminants that are present on the surface of the tip, such as metal oxides (in our case tungsten trioxide) act as additional tunnelling barriers. The latter causes tunnel current fluctuations as well as electrical noise, which might reduce the resolution of both microscopy techniques [11]. For STM technique, the small gap voltages could even lead to tip crashing and cause damage to the sample and the tip [3].

For this reason, it is necessary to add an additional surface-cleaning step. For cleaning tungsten tips, the annealing temperature is 1300 K. Annealing in vacuum leads to an atomically clean surface, which was further verified by Auger spectroscopy [12]. A tip that is prepared this way and overall cleaned is prepared to be used both as a field-emission cathode or an STM tip. The STM performance of the prepared tip was tested using NT-MDT Solver Nano (Fig. 11).

Since this STM device is intended to operate at atmospheric pressure, it is not possible to maintain perfect surface cleanness of the tip, comparing to vacuum conditions in the field-emission regime. Therefore, the tip which has been previously cleaned in HF is covered by tungsten trioxide during the operation in STM, which increases the radius of curvature and blunts the tip. An oxide layer forms over the tungsten tip due to reactivity with air, further measurements of tunnel current only support the tip degradation. Nevertheless, large area images of conductive materials could be studied by prepared tips at room temperatures. The usage of tungsten probes for such measurements is supported by some producers (e.g. Bruker).

6. Conclusions

The programmable etching set-up for Electrochemical Preparation of STM tips and Ultra-Sharp Field Emission Cathodes is outlined. The set-up allows the preparation of various sharp tips from single-crystalline and polycrystalline wires based on a pre-programmed routine. The programming allows for increasing the reproducibility of the preparation and improves the quality of the preparation process. The prepared tips were characterized in electron microscope using

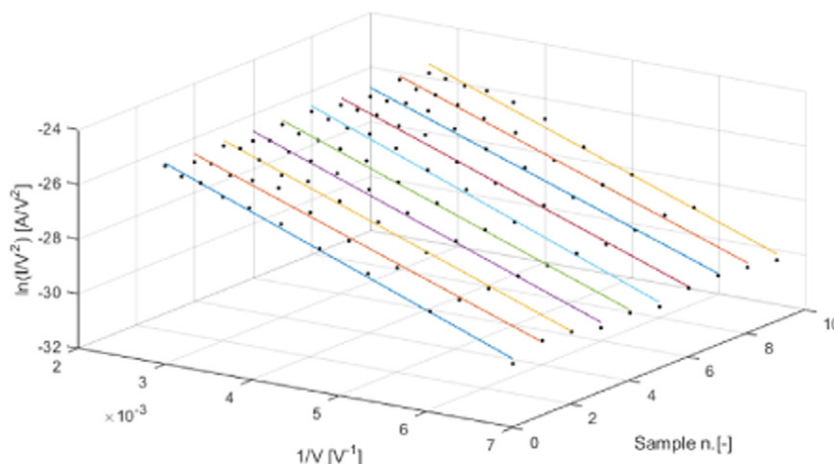

Fig. 9. Stacked plot of Fowler-Nordheim plot slopes (10 samples) as an indicator of tip manufacture reproducibility.

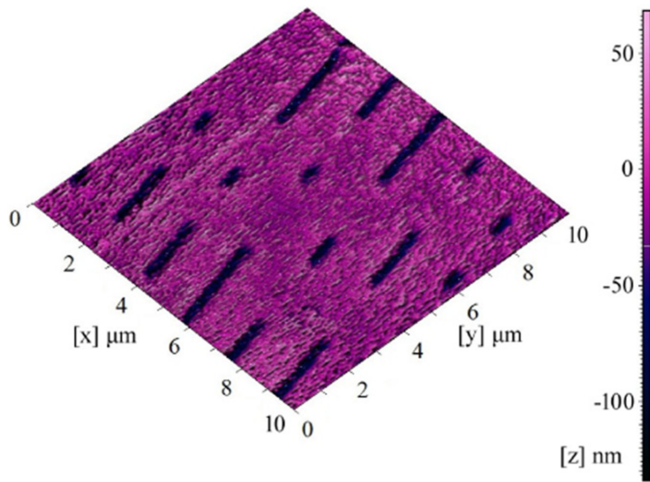

Fig. 11. An example of image obtained by the produced nano tip, made of a polycrystalline tungsten showing surface of a compact disc.

fundamental tip profile parameters such as the H/W ratio and the curvature diameter. The surface cleanness was discussed as well, including the influence of the surface oxide in relation to the performance of the STM technique and the field emission based microscopy. The tip was tested using two methods: the observing of Fowler-Nordheim slope and the evaluation of the function in STM where the tip is used to obtain the surface image. The results were discussed and the statistical ratio of tip production reproducibility using our set-up was determined.

Acknowledgment

The results of this project (LO1212) were obtained with the financial support of the Ministry of Education, Youth and Sports under the targeted support of the "National Programme for Sustainability I.

References

[1] A.J. Melmed, The art and science and other aspects of making sharp tips, J. Vac. Sci. Technol. B Microelectron. Nanom. Struct. 9 (1991) 601, http://dx.doi.org/10.1116/1.585467.
[2] M.O. Watanabe, T. Kinno, Preparation and characterization of electrochemically etched Re tips for STM, Appl. Surf. Sci. 76-77 (1994) 353–358, http://dx.doi.org/10.1016/0169-4332(94)90367-0.
[3] I. Ekvall, et al., Preparation and characterization of electrochemically etched W tips for STM, Meas. Sci. Technol. 10 (1999) 11–18 (PII: S0957-0233(99)97203-X).
[4] Z.Q. Yu, C.M. Wang, Y. Du, S. Thevuthasan, I. Lyubinetsky, Reproducible tip fabrication and cleaning for UHV STM, Ultramicroscopy 108 (2008) 873–877, http://dx.doi.org/10.1016/j.ultramic.2008.02.010.
[5] W. Chang, et. al. Method of electrochemical etching of tungsten tips with controllable profiles, Rev. Sci. Instrum. 83, 083704 (2012). doi: 10.1063/1.4745394
[6] J.P. Ibe, et al., On the electrochemical etching of tips for scanning tunneling microscopy, J. Vac. Sci. Technol. A 8 (4) (1990) 3570–3575.
[7] M.J. Fransen, Towards High-brightness, Monochromatic Electron Sources, Delft University of Technology, TU Delft, 1999.
[8] K. Yuasa, et. al. Modified Fowler – Nordheim field emission formulae from a nonplanar emitter model. Surf. Sci. 520 (2002) 18–28.
[9] E.W. Müller, J. Appl. Phys. 26 (1955) 732.
[10] A.S. Lucier, H. Mortensen, Y. Sun, P. Grütter, Phys. Rev. B - Condens. Matter Mater. Phys. 72 (1) (2005).
[11] A. Knapek, et al., Cold field-emission cathode noise analysis, Metrol. Meas. Syst. 19 (2) (2012) 417–422.
[12] R.G. Musket, et al., Preparation of atomically clean surfaces of elemental solids for UHV, Appl. Surf. Sci. 10 (1982) 143–207.

doi:10.1017/S1431927615013148 © Microscopy Society of America 2015

Simulation and optimization of a carbon nanotube electron source

Alexandr Knápek, Tomáš Radlička, Stanislav Krátký
Institute of Scientific Instruments of the ASCR, v.v.i., Královopolská 147, Brno,
612 64, Czech Republic, knapek@isibrno.cz

Abstract: This paper concerns the design and fabrication of a field-emission structure based on vertically aligned carbon nanotubes (CNT). A design concept for a fabrication method for a gate structure based on electron beam lithography is presented in the first part of the paper. A single carbon nanotube is grown by the PECVD method inside the gate structure. Calculations and simulations that help determine gate structure proportions in order to obtain the best possible electron reduced brightness and to predict the cathode's electric behavior are also essential parts of this study.

1. Introduction

Carbon nanotubes (CNT) are a quasi one-dimensional, non-metal structure meeting many of the requirements of field-emission (FE) applications that are unavailable in traditional emitter materials [1]. It is anticipated that a carbon nanotube electron source could perhaps replace the Schottky emitter for devices utilizing a focused electron beam, such as high-resolution scanning electron microscopes (SEMs) and scanning transmission electron microscopes (STEMs). Even though the field emission from carbon nanotubes was first reported in 1995 by Rinzler's group [2] and many concepts of CNT electron sources have been proposed in recent years [3, 4], there is still no field emitter commercially available for utilization in electron microscopy. CNTs have several advantages over field-emission sources made from sharp metal tips.

Firstly, since the CNT is not a metal but a highly ordered crystalline structure built by a covalent sp^2 (sigma) bond, the threshold for the removal of one atom is 17 eV, which is much higher than the activation energy for surface migration of a tungsten atom (3.2 eV), making the CNT much less sensitive for surface migration of the carbon atoms [5]. Additionally, carbon nanotubes have a larger Young's modulus, very high tensile strength and chemical inertness reacting only under extreme conditions or at high temperatures in the presence of oxygen or hydrogen. Moreover, carbon has a very low sputter coefficient so the current emitted from a CNT is considered stable compared with metal emitters that suffer from current fluctuations caused by the surface migration of atoms under a high electric field and by ion back sputtering. These properties make CNTs suitable candidates for an electron source [5]. Among the main advantageous parameters that could be achieved by a CNT-based emitter, the most important are very low energy width, typically 0.25 eV, high reduced brightness (up to 3×10^9 $A/m^2Sr.V$) and beam stability.

This paper presents a design and simulation of a new FE structure based on a multi-walled CNT source of electrons intended for electron microscopy.

2. Field-emission structure design

The proposed system is based on a triode configuration incorporating an extractor electrode which allows the field strength on the tip to be easily changed. The extraction voltage can be adjusted within a

range from zero to approx. 1 kV. The acceleration voltage can be set to as high as 5 kV. The radius of the CNT cathode is influenced mainly by the size of the iron particle from which it grows. The bore in the SiO_2 substrate bounds the region where the catalytic iron particles react during the plasmatic growth of the CNT. The length of the tube, determined by the PECVD process, will be higher than 0.5 µm so as to achieve a strong field at the tip of an order of magnitude of units of V/nm which is necessary for the field emission. As the molybdenum used for the extractor electrode has good chemical resistivity [6], it is possible to functionalize the MWCNT's surface using plasmatic or chemical methods. The bore diameter in the extractor is discussed further in the text based on a method published by Radlicka [7].

Techniques capable of very high resolution and precision are needed to create such small structures. Electron beam lithography and reactive ion etching (RIE) are more than suitable for this task [8, 9]. The described system, or more precisely the gate structure, is prepared using electron beam lithography by incorporating the following fifteen technological steps: firstly, a 300 nm layer of SiO_2 is evaporated in a vacuum onto the surface of a silicon wafer of a (100) orientation (see Fig. 1.a). Secondly, a molybdenum layer that is to be used as the extractor is Magnetron-sputtered on the oxide layer (see Fig. 1.b). The next step incorporates a 300 nm layer of *Poly(methyl methacrylate)*, abbreviated to PMMA, using the Spin-coating technique (see Fig. 1.c). As the PMMA layer is prepared, it is possible to exposure a pattern using a 100 keV e-beam writer (see Fig. 1.d). After the chemical development of the exposed pattern (see Fig. 1.e), the plasma developing of resist residues is performed by oxygen plasma (see Fig. 1.f). The molybdenum electrode is then etched by a mixture of SF_6 and O_2 (see Fig. 1.g), followed by removal of the resist layer (see Fig. 1.h).

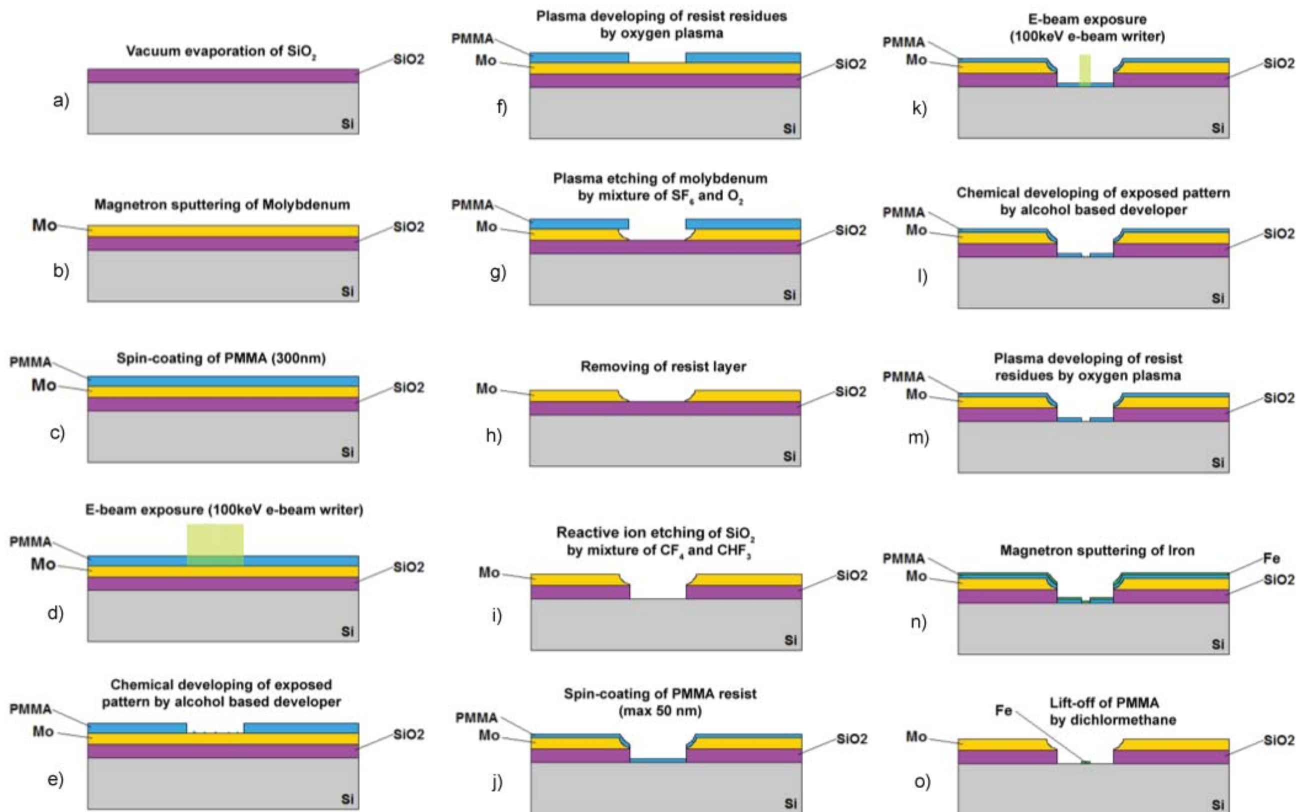

Figure 1. Fabrication technology of the gate structure: the fifteen basic steps (a-o).

At this moment, it is possible to etch the SiO_2 layer in order to prepare a space for CNT cathode growth. This is done using reactive ion etching with a mixture of CF_4 and CHF_3 (see Fig. 1.i). The usual lithography steps are performed to prepare the layer of catalytic iron particles: Spin-coating of PMMA resist (see Fig. 1.j), E-beam exposure of the pattern (see Fig. 1.k) and its chemical developing by an alcohol-based developer (see Fig. 1.l), followed by plasma developing of resist residues using oxygen plasma (see Fig. 1.m).

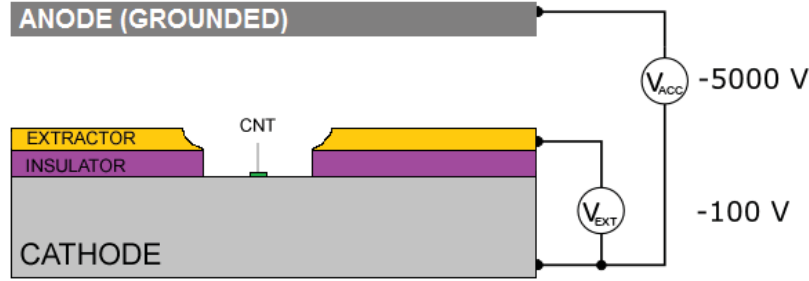

Figure 2. Fabricated gate structure after the PECVD process including an example of wiring.

A thin layer of catalytic particles is sputtered after the residues are developed (see Fig. 1.n), followed by the lift-off of the PMMA (see Fig. 1.o) and the PECVD process used for CNT growth (see Fig. 2).

1. Optimization and calculations

The CNT sources work at room temperature and a high field, so the emission is well described by the thermal-field emission model [7]. The emission current density can be calculated by the formula

$$j_{TF} = \frac{4\pi me}{h^3} d^2 \exp\left(-\frac{0.6\,W}{d}\right) \frac{\pi p}{\sin(\pi p)}$$

with m and e being the mass and the charge of the electron and h being the Planck constant. The work function for carbon $W = 4.8$ eV was used. The coefficient d is proportional to the field F on the cathode surface

$$d = \frac{e\hbar F}{2t(y_0)\sqrt{2mW}}$$

where $\hbar$ is reduced Planck constant, $t(y_0) = 1 + 0.1107 y_0^{1.33}$, and $y_0 = \Delta W/W$ with $\Delta W = \sqrt{e^3 F/4\pi\epsilon_0}$ is the decrease of the work function in the presence of a strong field on the cathode surface. The coefficient $p = kT/d$ describes the influence of the temperature on the emission mechanism.

The electrostatic field in the system was computed using the first order finite element method (FEM). We used a triangular mesh which is sufficiently dense in the vicinity of the CNT with a tip diameter of 20 nm and which expands in other parts of the system. The field calculation took about five minutes with a mesh consisting of about a million triangular elements. The emission was studied for several extractor bore diameters within a range from 0.5 to 2 μm. The typical potential in the vicinity of the cathode is plotted in Fig. 3. (left). The field on the cathode and the emission current are determined by the extraction voltage. The emission current can be computed as a function of the extraction voltage

using a thermal field emission model; Fig. 3 (right). Fig. 4 shows the typical field on the cathode and the emission current density.

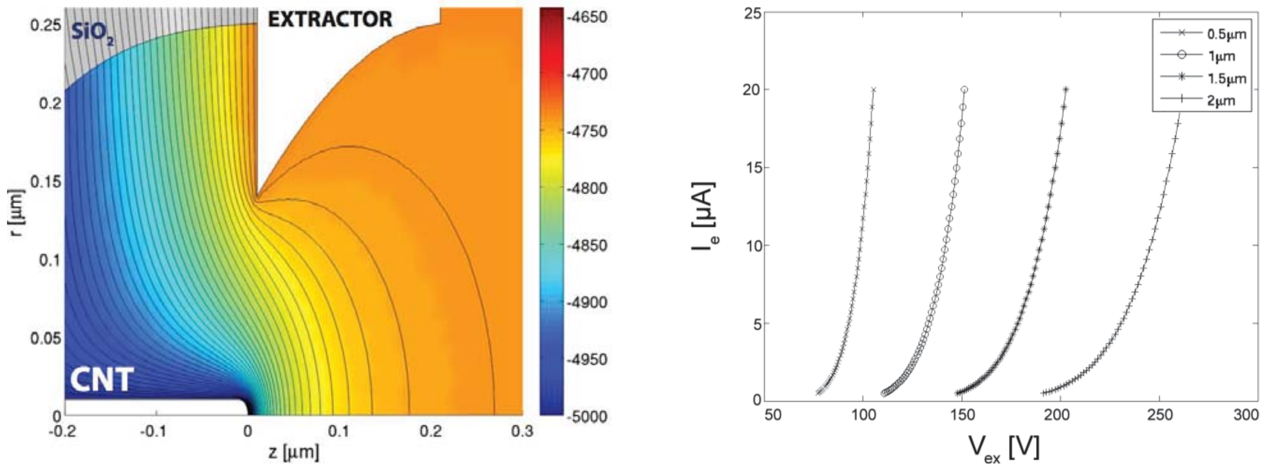

Figure 3. Potential in the vicinity of the cathode for a system with an extractor bore diameter of $250\ \mu$m computed by the FEM of the first order and the emission current as a function of the extraction voltage for several extractor bore diameters calculated by the thermal field emission model.

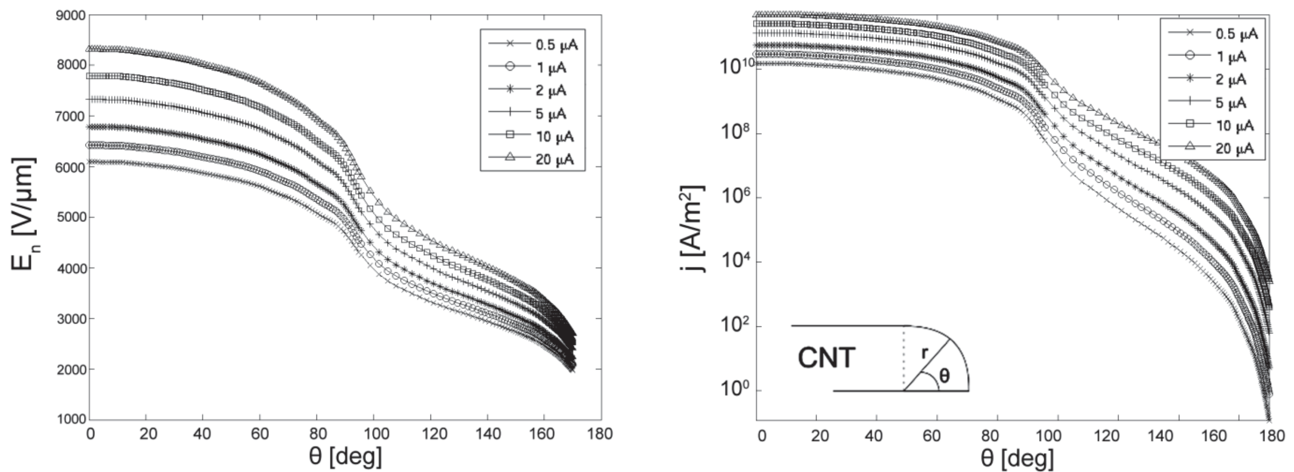

Figure 4. The field on the cathode (from Fig. 3) and the emission current density for several emission currents and an extractor bore radius of $250\ \mu$m. The emission outside the spherical tip of the cathode is almost negligible.

As the size of the CNT source is very small the energy distribution and brightness – the main optical parameters of the source – are strongly influenced by the stochastic Coulomb interactions (CI) in the beam. We simulated their effect using a Monte-Carlo simulation: (a) The initial conditions of emitted electrons were randomly generated to fulfill the theoretically computed current density j_{TF} and the energy distribution which can be approximated as $\rho(E) \approx \exp(E/d - E/kT)$ in the thermal field emission regime [8]. (b) The electrons were traced through the system field including the effect of the stochastic CI. We simulated a beam consisting of 20,000 electrons. For high efficiency, the beam was separated into sub-beams of 400 electrons bordered by 100 electrons on both ends to eliminate the effect

of beam separation [7]. The influence of the beam current on the global electrostatic field was ignored. Calculation of each beam took about four hours. (c) The resulting energy width and the reduced brightness were computed from the beam properties in the anode plane. The results for the brightness and energy width are presented for several emission currents and extractor bore diameters in Fig. 5.

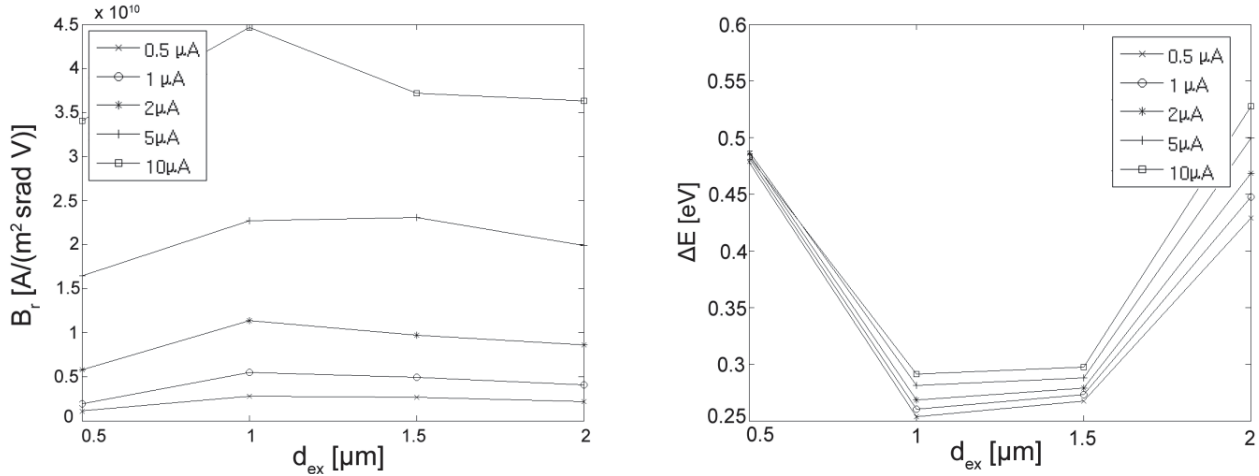

Figure 5. Reduced brightness and the energy width of the simulated CNT source.

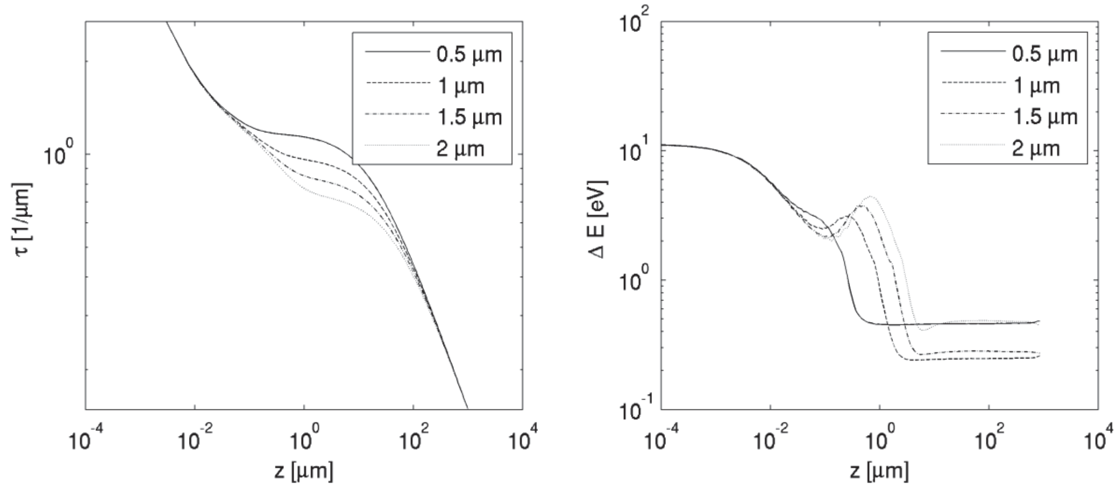

Figure 6. Linear electron density around the optical axis for several bore radii and the emission current 1 μA (left), energy width of the beam in planes perpendicular to the optical axis for several bore radii and emission current 1 μA (right).

The effect of the stochastic CI is proportional to the electron density in the vicinity of the cathode which decreases with increasing bore diameter; Fig. 6 (left). On the other hand, the equipotential lines are more curved with increasing bore radius which leads to higher energy width in each plane perpendicular to the axis; Fig. 6 (right). In the region close to the extractor plane the particles that are further from the axis are accelerated by different potential differences than particles near the axis. This increases the effect of

the stochastic CI. The results presented in Fig. 5 show that the optimal value of the bore diameter is between 1 and 1.5 micrometers, where the maximal brightness and the minimal energy width were achieved for all emission currents.

Conclusions

A design concept for a new field-emission microstructure based on a CNT cathode is presented. The proposed fabrication technology consists of two main parts: firstly, e-beam lithography for creating the gate structure, and secondly, a PECVD technique for growing the CNT cathode inside the pre-prepared structure.

The emission properties of the source were analyzed using the thermal-field emission model. The required extraction voltage was found for an emission current from 0.5 to 20 μA. The bore diameter in the extractor was optimized to achieve small energy width and high brightness using MC simulation of the emitted electron, including the effect of the stochastic CI. The optimal value was found to be between 1 and 1.5 micrometers.

References:

[1] NS Xu, S E Huq, Materials Science and Engineering: R: Reports, **48.2** (2005): 47-189.
[2] AG Rinzler, *et al*. Science, New Series, **269** (1995), pp. 1550-1553.
[3] C Li, *et al*. ACS nano, **6.4** (2012), pp. 3236-3242.
[4] Y Sun, *et al*. Small, **9.20** (2013), pp. 3385-3389.
[5] ND Jonge and JM Bonnard, Philos. Trans. R. Soc. London, Ser.A **362** (2004), p. 2239.
[6] K Balasubramanian and M Burghard. Small, **1.2** (2002), pp. 180-192.
[7] T Radlicka and B Lencova. Ultramicroscopy **108** (2008), pp. 445 – 454.
[8] Z Cui in "Nanofabrication Principles, Capabilities and Limits", (Springer, New York) p. 1-159.
[9] MA McCord, MJ Rooks in "Handbook of Microlithography, Micromachinning, and Microfabrication, Volume 1: Microlithography", ed. P Rai-Choudhury, (SPIE, Washington) p. 139-249.
[10] MJ Fransen, *et al*. Adv Imag El Opt **111** (1999), pp. 91.
[11] The authors acknowledge funding from the Ministry of Education, Youth and Sports of the Czech Republic (project number LO1212) and from Technology Agency of the Czech Republic (project number TE01020118)

Lithographic method of preparing a gating structure for a nanotube-based field mission source

D.Burda, A. Knápek
Institute of Scientific Instruments of the CAS, v. v. i.,
Královopolská 147, 612 64 Brno, Czech Republic
burda@isibrno.cz

Abstract

The gate structure is an integral part of the micro-scale field emission emitter serving for a two main purposes. Firstly, it is used as a substrate for the deposition of a nanotube and secondly, it is used as a basis of a triode system. There, an electric field is applied to the surface of the nanotube using an extraction electrode, which serves both to extract electrons from the facet of the nanotube's surface and also acting as the first (electrostatic) lens of created electron system [1]. Calculations based on the finite element method and the Monte Carlo method have been published in the past, leading to the determination of optimized dimensions of the structure with respect to the energy beam width and the beam brightness [2].

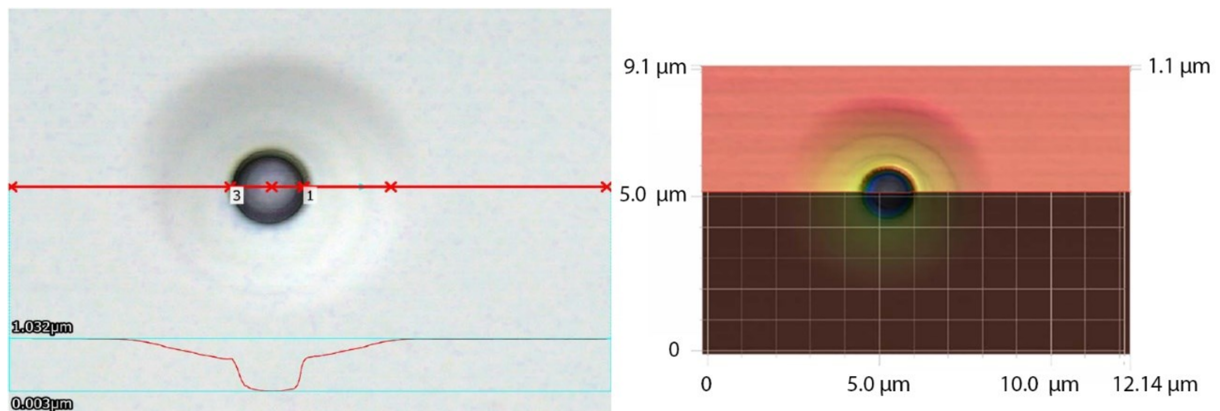

Fig. 1: Profile measurement of an example gate structure created by electron beam lithography; the overall image (left) and the 3D image of the structure (right).

As a feature of this structure, the extraction voltage can be adjusted within a range from zero to approx. 1 kV. The acceleration voltage is set to as high as 5 kV by default.

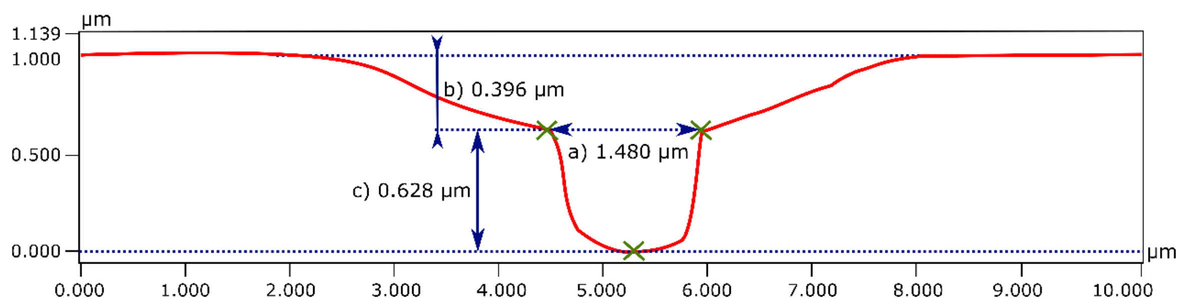

Fig. 2: Profile Measurement results: a) 1.480 μm; b) 0.396 μm; c) 0.628 μm.

The described gate structure is prepared using electron beam lithography and reactive ion-etching that are suitable for this task, as described in [1]. The topography

of the created are illustrated in Fig. 1, the profile measurements are in Fig 2. The imaging was performed using a confocal microscope branded Keyence VK-X series.

The bore in the SiO_2 substrate bounds the region where the nanotube is being growed. As the molybdenum used for the extractor electrode has good chemical resistivity, it is possible to functionalize the nanotube’s surface using plasmatic or chemical methods. The bore diameter in the extractor is calculated based on a method by Radlicka [2].

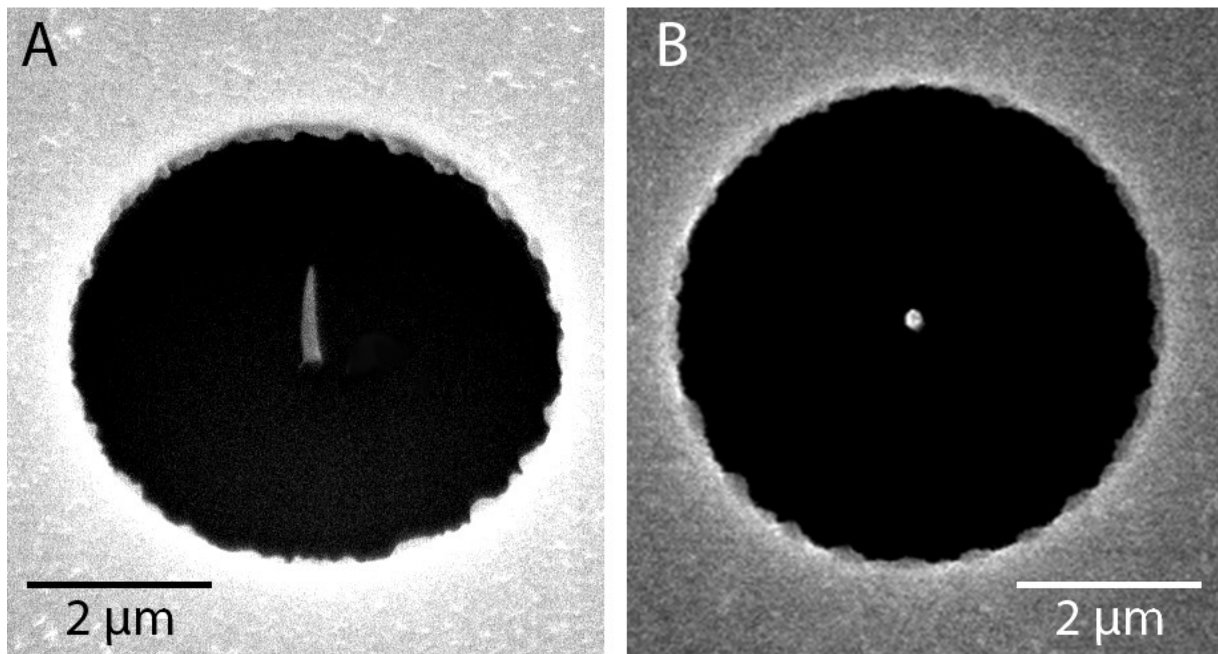

Fig. 3: SEM image obtained (mag. 10,000x) illustrating the side view of the Pt nanorod embedded into the gate structure (A) and the top view (B).

Figure 3 illustrates a model structure with an aperture size of 5 µm which is fitted with a platinum nanorod fabricated using electron beam assisted deposition [3]. The imaging was performed using a scanning electron microscopy branded JEOL JSM-7001F.

References

[1] KNÁPEK, A.; RADLIČKA, T.; KRÁTKÝ, S. Simulation and Optimization of a Carbon Nanotube Electron Source. *Microscopy and Microanalysis*, 2015, 21.S4: 60-65.

[2] RADLIČKA, T.; LENCOVÁ, B. Coulomb interactions in Ga LMIS, *Ultramicroscopy*, 2008, 108.5: 445-454.

[3] DE TERESA, J. M., et al. Origin of the difference in the resistivity of as-grown focused-ion-and focused-electron-beam-induced Pt nanodeposits. *Journal of Nanomaterials*, 2009.

Applied Surface Science 395 (2017) 157–161

Contents lists available at ScienceDirect

Applied Surface Science

journal homepage: www.elsevier.com/locate/apsusc

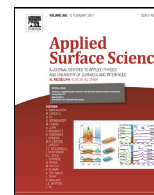

Field emission from the surface of highly ordered pyrolytic graphite

Alexandr Knápek [a,*], Dinara Sobola [b], Pavel Tománek [b], Zuzana Pokorná [a], Michal Urbánek [a]

[a] Institute of Scientific Instruments of the ASCR, v.v.i., Královopolská 147, Brno, Czech Republic
[b] Department of Physics, FEEC, Brno University of Technology, Technická 8, Brno, Czech republic

ARTICLE INFO

Article history:
Received 3 December 2015
Received in revised form 29 April 2016
Accepted 1 May 2016
Available online 3 May 2016

Keywords:
Field emission
HOPG
Scanning near-field optical microscopy
Scanning electron microscopy

ABSTRACT

This paper deals with the electrical characterization of highly ordered pyrolytic graphite (HOPG) surface based on field emission of electrons. The effect of field emission occurs only at disrupted surface, i.e. surface containing ripped and warped shreds of the uppermost layers of graphite. These deformations provide the necessary field gradients which are required for measuring tunneling current caused by field electron emission. Results of the field emission measurements are correlated with other surface characterization methods such as scanning near-field optical microscopy (SNOM) or atomic force microscopy.

© 2016 Elsevier B.V. All rights reserved.

1. Introduction

A simple method utilizing the field emission of electrons has been devised to characterize the sample surface. Electron and probe microscopies were used to determine the structure of both the bulk sample and the partially exfoliated shreds of the uppermost layers of graphite in locations where field emission is observed.

2. Experiment

We used a sample of highly ordered pyrolytic graphite (HOPG), ZYA grade, purchased from MaTecK GmbH. The upper layers of HOPG were mechanically exfoliated using 3 M adhesive tape and the freshly prepared sample was immediately placed via a vacuum feedthrough into a high vacuum chamber with a residual gas pressure of 10^{-7} Pa. This chamber allows for sample cleaning using electron bombardment heating and/or argon ion sputtering prior to electron microscopy observation in the adjacent ultra-high vacuum (10^{-8} Pa) chamber. In order to remove any possible contaminants that may have stuck to the surface, the HOPG slab was annealed to 900° Celsius for 20 min by means of electron bombardment heating.

After the cleaning procedure, the sample was moved via a feedthrough to the ultra-high vacuum chamber equipped for scanning low energy electron microscopy (SLEEM). [1] This technique makes use of the Cathode Lens [2], which is basically an electrostatic decelerating field between the negatively biased sample and a grounded electrode above it.

The sample was connected to a negative DC source providing the necessary extraction voltage. The emitted electrons were collected by a cerium-doped Yttrium Aluminum Garnet (YAG:Ce) scintillator, allowing to measure the emitted current. Additionally, the set-up can be extended to display spatial distribution of defects by adding a CCD chip in the vacuum chamber.

The negative voltage was continually increased until the YAG scintillator detected impinging electrons. A significant part of the total emission current was captured by the thin conductive Indium Tin Oxide layer covering the YAG scintillator, which allowed to measure basic current-voltage (*I-V*) characteristics. In the measurement, the inter-electrode distance was kept constant at 6 mm, which required rather high extractor voltage to gain sufficient electric field intensity *E*. Using a simple diode *I-V* measurement set-up, the current was measured by detector of backscattered electrons the following way: the electrons were converted to photons by the YAG scintillator, the resulting photons then converted back to electrons when entering a photo-multiplier where this current was multiplied by several orders of magnitude, the output was amplified by an amplifier, sampled and recorded in a computer. A schematic arrangement is illustrated in Fig. 1.

In order to interpret the *I-V* behavior, the standard Fowler-Nordheim (F-N) theory was used.

Fig. 2 illustrates the *I-V* characteristics showing a nearly exponential increase of the current, where I [A] = 2×10^{-12}

* Corresponding author.
E-mail address: knapek@isibrno.cz (A. Knápek).

http://dx.doi.org/10.1016/j.apsusc.2016.05.002
0169-4332/© 2016 Elsevier B.V. All rights reserved.

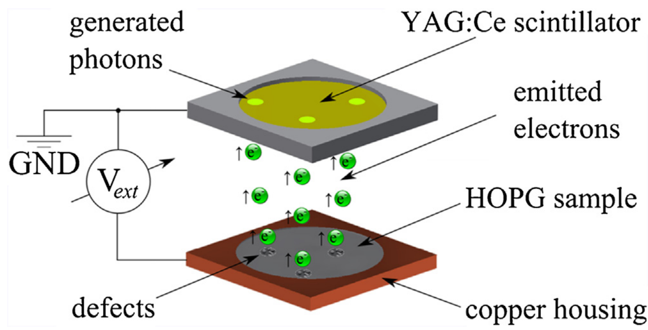

Fig. 1. Experimental setup; the HOPG sample is connected to the negative dc source and the YAG scintillator is grounded, serving as an extractor electrode.

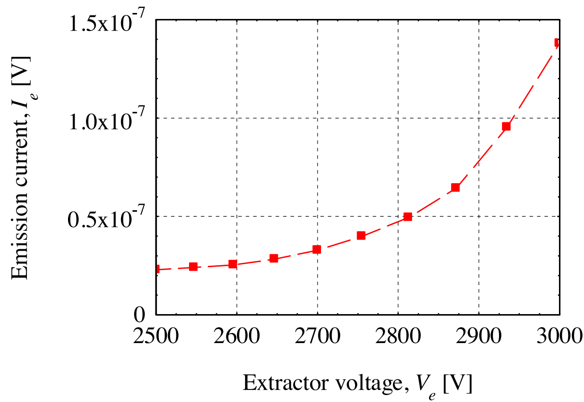

Fig. 2. *I-V* characterstics of the emission current as a function of applied voltage.

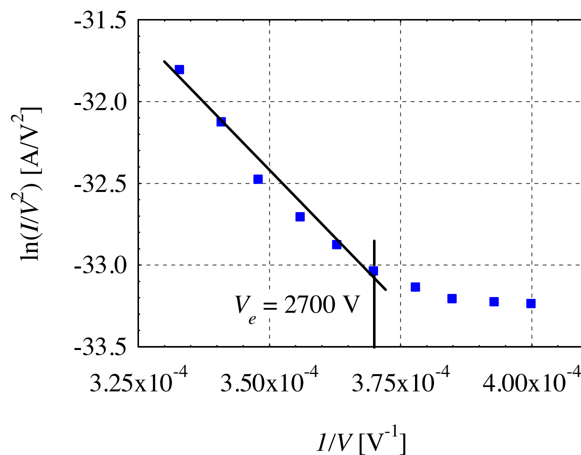

Fig. 3. Corresponding F-N plot for the *I-V* characteristics in Fig. 2.

exp(0.0036 V$_e$). Also the F-N plot (see Fig. 3) confirms the presence of electron tunneling because of the nearly linear plot.

As shown in Fig. 3, the non-linear behavior starts to appear at V_e = 2700 V suggesting the current contribution of larger defects, i.e. defects with lower field gradient. The nonlinearity of the plot can be explained by the presence of multiple microscopic electron sources. As each of them has a different geometry, the field gradient also differs, and with it the voltage necessary for the onset of field emission. This causes a gradual activation of particular sources making the *I-V* plot non-exponential [3].

For this reason it is also not possible to determine the exact work function and field enhancement factor β (the ratio of maximum electric field on the shred and the average electric field on the HOPG

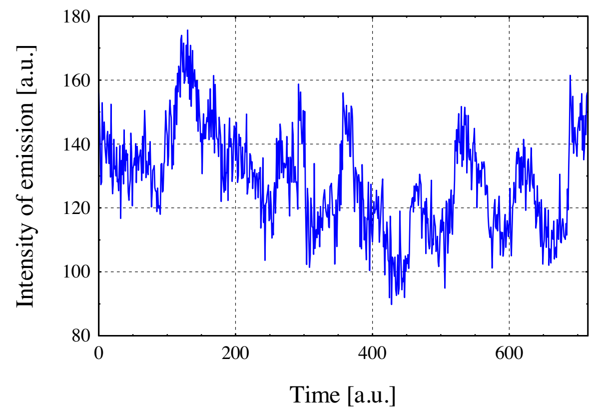

Fig. 4. Example of fluctuation of the total emission current of the HOPG slab at one particular voltage, V = 3010 [V].

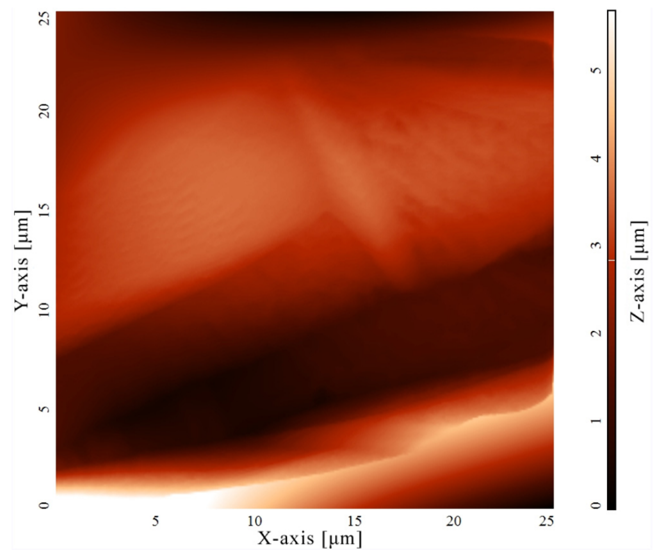

Fig. 5. Topography image of the HOPG surface, obtained by SNOM.

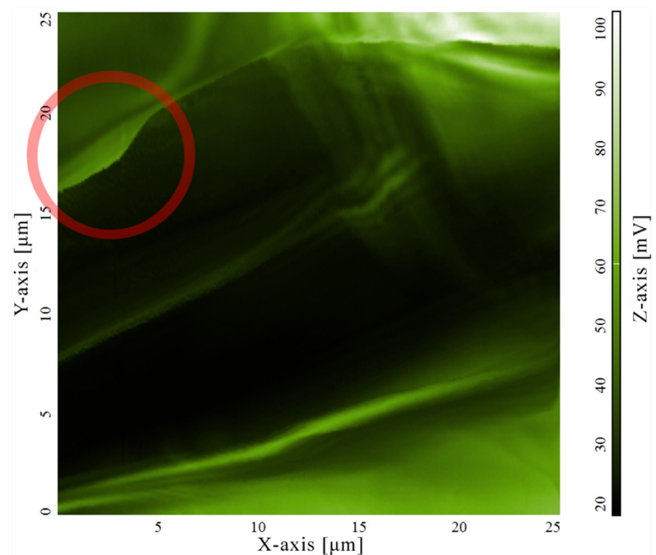

Fig. 6. Reflectance image from the same surface area as in Fig. 4, obtained by SNOM. The marked area shows a partly exfoliated shred of graphite surface. The milivolt scale denotes the photodetector signal intensity.

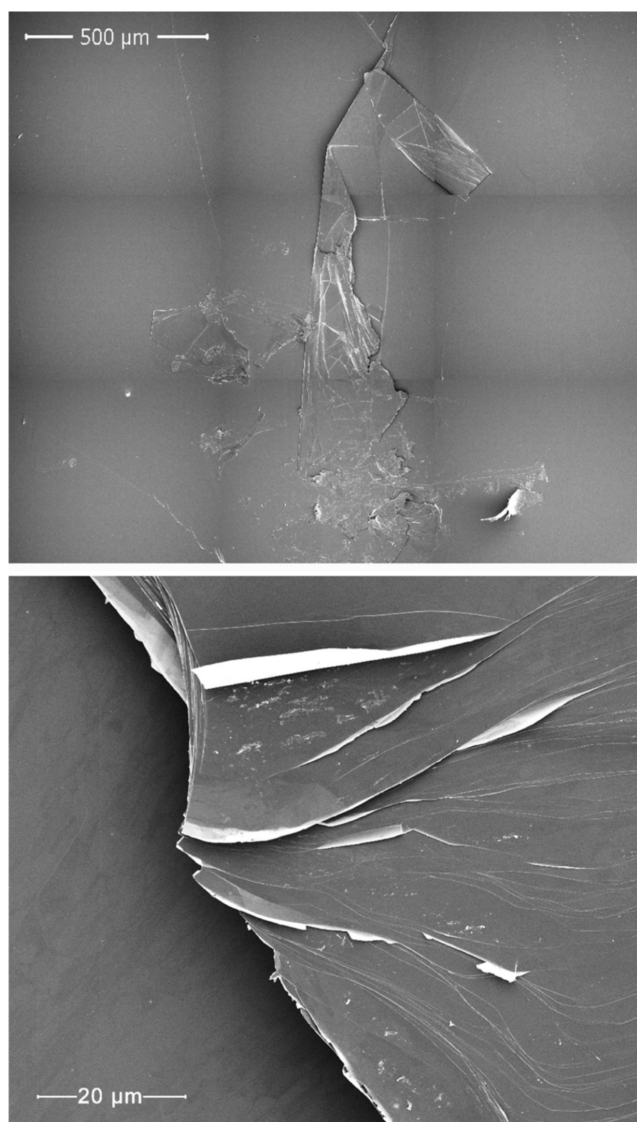

Fig. 7. SEM image of the HOPG surface. An overview of the sample surface (above) and typical example of ridge-like morphological structures with interspersed peak-like structures on the sample surface (image below).

slab), however it is possible to evaluate the compactness of the surface.

Fig. 4 shows fluctuations of the total emission current at one particular voltage. This can possibly be explained by the fact that the shreds are flailing as the surface charge distribution changes, causing the local field intensity to vary and influencing the onset of the electron emission.

3. Surface analysis methods

Scanning near-field optical microscopy (SNOM) belongs to the family of probe microscopies and allows a superior optical study of surface structures. SNOM is a non-destructive method for the characterization of surface features and defects. The optical properties of graphitic material strongly depend on the structure, and the reflectivity depends on the amount of layers [4].

The observed sample was illuminated by a green laser ($\lambda = 532$ nm) and the reflected signal was collected.

The partly exfoliated layers of graphite could be distinguished in the reflection mode. The tip of the SNOM probe is too large and the topographical resolution not as good as in other probe techniques, for example, semi-contact atomic force microscopy (AFM).

The SNOM topography image is shown in Fig. 5, and the contrast among layers of different thickness is observed in Fig. 6. For a homogeneous sample surface, the reflectance would have a uniform distribution. The marked area in Fig. 6 demonstrates the presence of a shred. The shreds are however not observed in the SNOM topography mode. Investigation of the surface imperfections shows that the defects did not involve the partly exfoliated topmost layer only, but they comprised of several layers.

Phase shift of coherent light coming through graphitic material increases linearly with its thickness [5]. Here, the phase shift of the SNOM reflection signal can be observed on shreds with heights up to 1 μm.

The morphology of the shred was characterized by atomic force microscopy (AFM) and scanning electron microscopy (SEM). Typical shreds found on the sample surface are shown in Fig. 7 (SEM) and Fig. 8 (AFM). SEM shows an otherwise smooth HOPG surface with some partly exfoliated shreds. The shreds exhibit a layered structure with folds and corrugations. The height of the surface

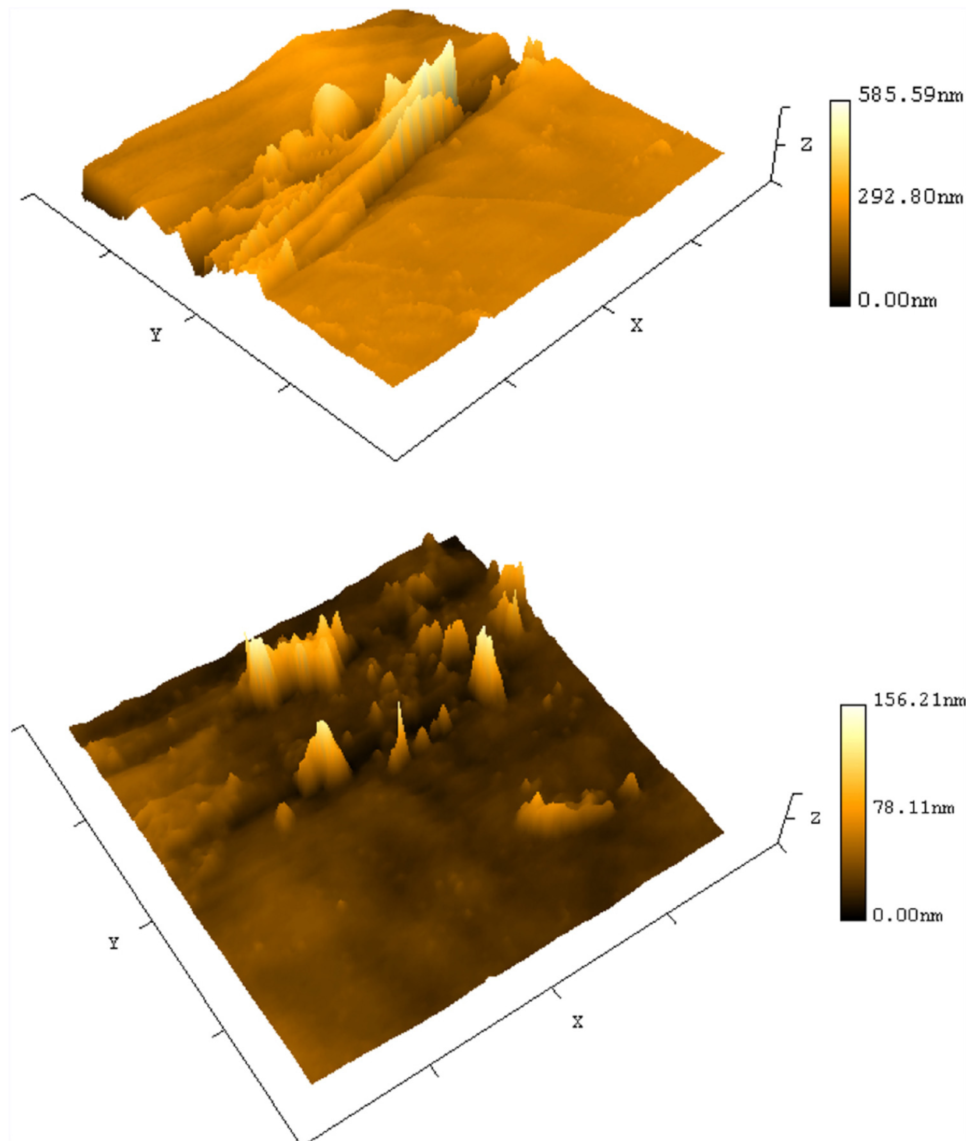

Fig. 8. AFM topography image of the HOPG surface showing the height of surface features. A typical example of ridge-like morphological structures on the sample surface (image above); and peak-like structures (below). In both cases, the field of view is 30 × 30 μm wide.

features was determined by AFM (Fig. 8). The maximum height of the scanned area is 586 nm.

4. Conclusions

Using various methods of surface characterization we obtained additional information about the properties of the Highly Ordered Pyrolytic Graphite exhibiting field emission. The morphology of the shreds on the HOPG surface was demonstrated by SEM. Precise information about the height of surface details was obtained by AFM. The presence of subwavelength structures in the near-surface area of the sample was confirmed by SNOM.

The comparison of the images taken using SNOM, SEM and AFM allowed us to characterize shreds of multi-layered graphite structure on the surface of HOPG.

In our method, the occurrence of the field emission of electrons acts as an indicator of disrupted HOPG surface. Since there are multiple electron sources with various sizes and threshold voltages, the Fowler-Nordheim plot is not linear and so the F-N theory cannot be applied in the entire voltage range. It can only serve for the confirmation of electron tunneling because of the initial linear part of the F-N plot. From Fig. 4 it can be concluded also that the HOPG shreds are flailing because of the inhomogeneous surface charge distribution.

Acknowledgment

The research was financially supported by the European Centre of Excellence CEITEC CZ.1.05/1.1.00/02.0068 and funding from the Technology Agency of Czech Republic project No. TE01020118.

The authors would also like to thank to Prof. Mohamed El-Gomati OBE for his invaluable contributions when discussing the subject, Mr. Jiri Sykora for his technical assistance with the ultra-high vacuum chamber, and Mr. Simon Siler for his kind cooperation during the I-V characteristics phase of the experiments.

References

[1] I. Mullerova, L. Frank, Scanning low-energy electron microscopy, Adv. Imaging Electron Phys. 128 (2003) 310–445.
[2] E. Bauer, Low energy electron microscopy, Rep. Prog. Phys. 57 (9) (1994) 895.

[3] R.G. Forbes, C.J. Edgcombe, U. Valdrè, Some comments on models for field enhancement, Ultramicroscopy 95 (2003) 57–65, http://dx.doi.org/10.1016/S0304-3991(02)00297-8.
[4] I.G. Ivanov, J.U. Hassan, T. Iakimov, A.A. Zakharov, R. Yakimova, E. Janzén, Layer-number determination in graphene on SiC by reflectance mapping, Carbon 77 (2014) 492–500, http://dx.doi.org/10.1016/j.carbon.2014.05.054.
[5] H.S. Skulason, P.E. Gaskell, T. Szkopek, Optical reflection and transmission properties of exfoliated graphite from a graphene monolayer to several hundred graphene layers, Nanotechnology 21 (2010) 295709, http://dx.doi.org/10.1088/0957-4484/21/29/295709.

Journal of Electron Spectroscopy and Related Phenomena 241 (2020) 146837

Contents lists available at ScienceDirect

Journal of Electron Spectroscopy and Related Phenomena

journal homepage: www.elsevier.com/locate/elspec

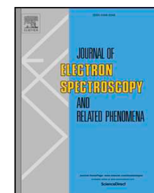

Field emission properties of single crystalline W_5O_{14} and $W_{18}O_{49}$ nanowires

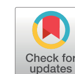

Muhammad Saqib[a], Janez Jelenc[a], Luka Pirker[a], Srečo D. Škapin[a], Lorenzo De Pietro[b], Urs Ramsperger[b], Alexandr Knápek[c], Ilona Müllerová[c], Maja Remškar[a,*]

[a] Jozef Stefan Institute, Condensed Matter Physics Department, Ljubljana, Slovenia
[b] ETH Zurich, Department of Physics, Zurich, Switzerland
[c] Institute of Scientific Instruments, Czech Academy of Sciences, Brno, Czech Republic

ARTICLE INFO

Keywords:
Nanowires
Tungsten oxides
Electron emitter
Field enhancement factor
Work function

ABSTRACT

Single crystalline tungsten oxides in a form of W_5O_{14} and $W_{18}O_{49}$ nanowires were synthesized by iodine transport method. The morphology, work functions and field emission properties of these nanowires were investigated. Work functions of the W_5O_{14} (4.20–4.34 eV) and $W_{18}O_{49}$ (4.55–4.57 eV) nanowires (NWs) have been measured by Kelvin probe force microscopy (KPFM) in ultra-high vacuum. Field emission (FE) measurements of individual nanowires were performed in ultra-high vacuum at microscopic and macroscopic distances between the emitter and electron collector. The obtained FE curves at microscopic distances were analyzed in the framework of the Fowler–Nordheim (F–N) theory. Field enhancement factors of W_5O_{14} at the emitter-collector distance of 2, 4 and 5 µm were calculated to be 110 ± 10, 180 ± 25 and 210 ± 30, respectively, and 125 ± 15 for W18O49 at 2 µm. At macroscopic distances, the F–N theory revealed unrealistic high field enhancement factors: for W_5O_{14} at 1 mm it was 17,000 ± 500, and for $W_{18}O_{49}$, the field enhancement factors were 5050 ± 30 and 6450 ± 30 at 600 µm and 800 µm emitter-collector distance, respectively. Therefore, more realistic model was discussed. The lower work function and typically smaller diameter of the W_5O_{14} nanowires in comparison with the $W_{18}O_{49}$ wires, range the W_5O_{14} nanowires to the promising sources of electrons in field emission devices.

1. Introduction

Metal oxides are the key components for the development of many advanced functional materials and smart devices. Among them are tungsten oxides, which belong to a family of transition metal oxides, and have various applications in photocatalysis [1], electrochemistry [2], energy conversion [2], gas sensors [3], and as recently found also in phototherapy [4]. Besides stoichiometric WO_3, which exists at different temperatures in several structures, such as monoclinic, triclinic, tetragonal, orthorhombic, cubic and hexagonal [5], oxygen reduced WO_{3-x} phases are also known, where tungsten oxidation state for some atoms changes from W^{6+} to W^{5+}. Among these phases, $W_{18}O_{49}$ is the most reduced stable phase. Less reduced W_5O_{14} crystals in needle like shape were reported as a homogeneous phase using iron in 1978 [6] and nickel in 2007 [7] as growth promoters. Oxygen vacancies in these sub-stoichiometric WO_{3-x} phases create donor states and strongly improve the electrical conductivity. Besides, these defects preferentially accumulate at the formed crystallographic shear planes. Here they change corner-shared octahedra WO_6 of stoichiometric WO_3 to edge-shared or face-shared WO_6 octahedra and bonds are formed between W^{+5} ions in edge sharing pairs [8]. In contrary with the stoichiometric WO_3 semiconductor with a band gap in the range of 2.5–3.2 eV [9] and electrical conductance from 10 to 10^4 Ωcm [10,11], the reduced W_5O_{14} phase growing as nanowires, revealed metallic conductivity with an electrical resistance of 25 µΩcm [7]. For comparison, electrical resistance of the most reduced $W_{18}O_{49}$ wires is 2750 µΩcm [12], i.e. more than two orders of magnitude larger with respect to W_5O_{14}.

Over the last few years, field emission (FE) studies have been performed with different phases of WO_{3-x}, mainly focused on $W_{18}O_{49}$ NWs [13,14] arrays, where FE properties with a low threshold field of 4.37 V/µm for an FE current density of 10 mA/cm^2 were measured, as well as a high time stability of FE current [14]. FE studies performed with thermally evaporated $W_{18}O_{49}$ NWs depended on temperature and anomalous changes in emission current were found in temperature range 300 K–723 K [13]. Decreasing of FE currents under the same applied electrical field with decreasing the temperature from RT to 143 K, was explained with the phonon-assisted tunnelling of electrons from defect states to the conduction band [15]. In a case of W_5O_{14} NWs, in-situ FE measurement was performed using FE-TEM holder, where a current as high as 35 µA was extracted from a single NW in parallel

* Corresponding author.
E-mail address: maja.remskar@ijs.si (M. Remškar).

https://doi.org/10.1016/j.elspec.2019.03.005
Received 13 August 2018; Received in revised form 18 February 2019; Accepted 12 March 2019
Available online 15 March 2019
0368-2048/ © 2019 Published by Elsevier B.V.

orientation to the electric field of 160 V/μm [16]. The second experiment was performed on a film composed of W_5O_{14} NWs that were oriented perpendicular to the electric field. The emitting current densities up to 6.4 mA/cm^2 have been obtained at a very low electric field of about 3 V/μm. The NWs were emitting for 100 h, with the emitting current stabilizing after 40 h at 2.4 μA [17].

In the present study, we report a comparative study of surface and field emission properties of W_5O_{14} and $W_{18}O_{49}$ NWs synthesized by a modified method using WO_3 and elemental tungsten as starting materials in the iodine transport reaction. Detailed structural and surface properties were revealed using X-ray-diffraction (XRD), scanning tunnelling microscopy (STM) and scanning electron microscopy (SEM). Work functions of single NWs were measured with Kelvin probe force microscopy (KPFM). The FE properties of individual NWs were measured at multiple distances that are orders of magnitude apart (2–5 μm and approx. 1 mm).

2. Materials and methods

The W_5O_{14} (O/W = 2.8) NWs were synthesized by iodine transport method [7] using nickel as a growth promoter and WO_3 as a source of tungsten and oxygen. The starting material consisted of 352.7 mg of WO_3 powder (Sigma Aldrich, 99.99%), 37.5 mg nickel (metal foil) and 567 mg iodine (1–3 mm beads, Sigma Aldrich, 99.7%). Adding a small quantity of tungsten powder (20 mg), growth of the $W_{18}O_{49}$ (O/W = 2.72) NWs was promoted. Evacuated (4×10^{-6} mbar) and sealed quartz ampoules were inserted into a two-zone furnace in such a way, that the material was transported from 860 °C to 736 °C. Transport reaction ran for 500 h and then the ampules were cooled with 70 °C/hour cooling rate. The transported materials of light (W_5O_{14}) and deep blue ($W_{18}O_{49}$) colour were obtained. Both W_5O_{14} and $W_{18}O_{49}$ consist of long, rigid NWs which tend to clump into bundles.

The crystalline structure of the NWs was examined by XRD at room temperature with D4 Endeavor diffractometer (Bruker AXS) using a quartz monochromatic Cu Kα1 radiation source (λ = 0.1541 nm) and a Sol-X dispersive detector. Morphology, surface structure and work functions of W_5O_{14} and $W_{18}O_{49}$ NWs were measured by scanning electron microscope (SEM) Supra 36 V P, Carl Zeiss, scanning tunneling microscope (STM), atomic force microscope (AFM), and Kelvin probe operating in ultra-high vacuum (Omicron VT-AFM).

The FE properties of individual W_5O_{14} NWs or $W_{18}O_{49}$ wires and NWs were measured in microscopic and macroscopic regimes. The NWs were attached on tungsten electrochemically etched tips by using OmniProbe Nano-manipulator in a Helios NanoLab 650 Focused Ion Beam-scanning electron microscope (FIB). At microscopic distances, the FE measurements were performed in ultra-high vacuum (Omicron VT-AFM) using a diode configuration, with a negatively biased WO_{3-x} wire as an electron source (cathode) and a freshly cleaved HOPG as an electron collector (anode). In the macroscopic regime, both nanowires were tested in slightly different configuration, which should not affect the results. While the FE testing of a W_5O_{14} NW was performed with positively biased electron extractor [18], the $W_{18}O_{49}$ NW was tested with negatively biased cathode and grounded anode [19].

3. Results

3.1. Morphology and crystal structure studies

Electron microscopy images (Fig. 1) of (a) W_5O_{14} and (b) $W_{18}O_{49}$ wires show that the length of both types of NWs exceeds several ten μm. The nanowires are very rigid and have a homogeneous diameter along their length. The mean diameter of the W_5O_{14} NWs is in the range of 100–200 nm, while majority of the $W_{18}O_{49}$ wires are thicker (up to 3 μm) with rare thinner ones.

The XRD spectra (Fig. 2) of (a) W_5O_{14} and (b) $W_{18}O_{49}$ match the tetragonal W_5O_{14} structure (JCPDS 71-0292) with lattice parameter: a = 23.33 Å and c = 3.78 Å, and monoclinic $W_{18}O_{49}$ phase with lattice parameters: a = 18.32 Å, b = 3.78 Å, c = 14.03 Å and β = 115.20° (JCPDS 036-0101) [20], respectively. Since the NWs have preferential orientation parallel with the substrate, the relative intensities differ from the ones in the database. In particular, the (001) peak of W_5O_{14} and the (010) peak of $W_{18}O_{49}$ which have the maximum intensity in the database, are relatively weak, while those attributed to the (hk0) interlayer distances are intensified. There are no indications of any other WO_{3-x} phase in the samples. The sharps peaks in the XRD pattern are clear evidence of high crystallinity of the materials.

High-resolution TEM images shown in the Fig. 3 reveal that both types of wires are single crystalline. While the W_5O_{14} NW (Fig. 3a) grows along [001], the $W_{18}O_{49}$ wire (Fig. 3b) grows along [010] direction [7,21]. Longitudinal axes of the growth are presented by arrows. A periodicity of 11.7 Å perpendicularly to the W_5O_{14} NW axis corresponds to the (200) planes, while periodicity along the axis reveals (001) planes. In the $W_{18}O_{49}$ wires, the spacing between the $(\bar{4}03)$ planes parallel with the longitudinal axis is 3.9 ± 0.1 Å and between the (010) planes is 3.9 ± 0.1 Å. Layers, where 3-layers blocks are shifted for a half of unit cell along [010] in the monoclinic $W_{18}O_{49}$ wires, is marked with horizontal black lines.

3.2. Scanning tunnelling microscopy

Scanning tunneling microscopy (STM) was used to study the surface corrugation of the NWs, and structure of their longitudinal ends (Fig. 4). Surface corrugations on a W_5O_{14} NW are typically several nm deep and have a periodicity of 20–30 nm (Fig. 4a). Compared to W_5O_{14}, the corrugations in $W_{18}O_{49}$ wires are shallower with a typical periodicity of around 10 nm (Fig. 4b). The longitudinal terminations of the wires consequently differ. While the W_5O_{14} NWs terminate with dome-shaped rods with a typical diameter of 20 nm and curvature radius below 10 nm (Fig. 4c), the ends of the $W_{18}O_{49}$ wires terminate more abruptly revealing a porous structure without protuberances (Fig. 4d).

3.3. Kelvin probe force microscopy (KPFM)

Kelvin probe force microscopy was used to measure the work functions of the wires at the nanoscale. The contact potential difference (CPD) measured between the AFM tip and the sample is defined as $V_{CPD} = (\phi_{tip} - \phi_{sample})/e$ [22], where ϕ_{tip} and ϕ_{sample} denote work functions (WF) of the tip and the sample, respectively. The topography and the Kelvin image based on CPD were obtained simultaneously. We used the frequency modulated KPFM where the frequency variation Δf_0 is approximately proportional to the force gradient, which can be written as $\Delta f_0 \propto -f_0\ (\partial F/\partial z)\ /\ 2k$ [23], where f_0 is the first resonance frequency of the cantilever (240 kHz) with an amplitude of approximately 10 nm, k is the cantilever spring constant (11.5 N/m) and F is the force acting on the cantilever. To measure the CPD separately from the topography, an alternating voltage $V = V_{DC} + V_{AC} \sin(\omega t)$ was applied between the tip and the sample with an amplitude $V_{AC} = 0.7$ V, and frequency $\omega = 2$ kHz. The topography is proportional to the part of the electrostatic force which is independent of ω, while the CPD is proportional to the frequency dependent electrostatic force $F_\omega \propto (V_{DC} - V_{CPD}) \sin(\omega t)$ which is detected by a lock-in amplifier. By tuning the V_{DC} in a way that F_ω is nullified, the value of the V_{CPD} is revealed. The WF of a tip strongly depends on the local tip conditions. By measuring V_{CPD} using the same AFM tip on the sample and on HOPG with a known WF value, 4.6 ± 0.05 eV [24], the influences of the tip WF variations were minimized.

Several measurements have been performed on different W_5O_{14} and $W_{18}O_{49}$ wires. The WF values obtained on W_5O_{14} single NW (Fig. 5a, b) were from 4.20 to 4.34 eV, i.e. for 260–400 meV lower than on HOPG. WF values from $W_{18}O_{49}$ wires were from 4.55 meV to 4.57 meV, only slightly lower (30–50 meV) than HOPG (Fig. 5c, d).

Work function was measured also as a function of surface

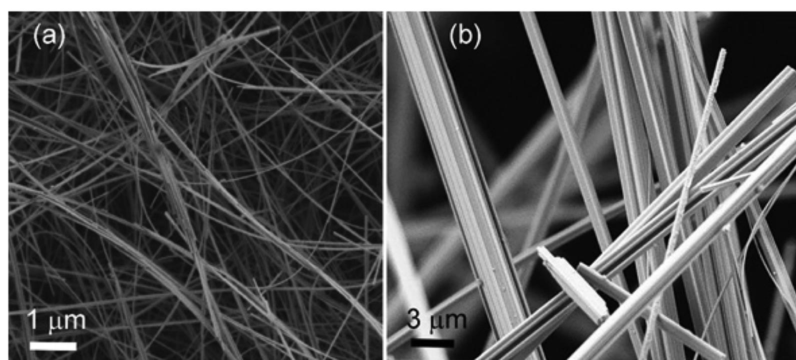

Fig. 1. SEM images of a) W_5O_{14} and b) $W_{18}O_{49}$ NWs.

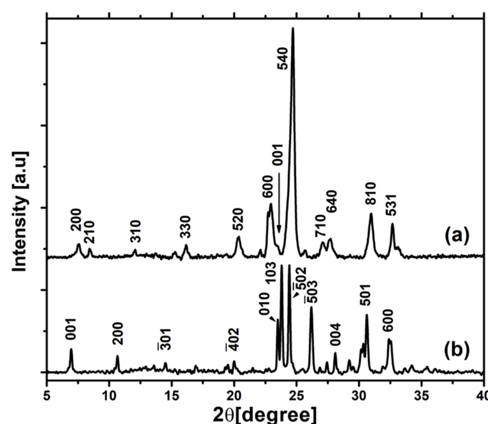

Fig. 2. The XRD spectra of a) W_5O_{14} nanowires; b) $W_{18}O_{49}$ wires.

corrugations. In the case of W_5O_{14} NWs with deep corrugations, the WF was found lower at bottom of the corrugation. In Fig. 6a, Kelvin image of a longitudinal termination of a W_5O_{14} NW is shown with two line profiles: A - perpendicular to the NW axis, and B - along the nanowire length. The minimum of the CPD in the profile A was found inside surface channels. It was 50 mV lower than on the peaks between them. At the very end of the NW, the CPD was 150 mV lower than inside the surface channels, and 400 mV lower than on HOPG (4.6 ± 0.05 eV [24]). The WF of the very end of the NW was only 4.2 eV. The reference CPD value for HOPG was taken at the ends of line profile A, where HOPG was free of any visible deformations like steps, cracks or folded layers of graphite.

Inhomogeneous electron density structure of a single W_5O_{14} NW was observed also through current enhancement in the contact-AFM current measurement (Fig. 7). Surface channels and end of the side strand (Fig. 7a) have a higher conductance than the rest of the NW (Fig. 7b). Knowing that oxygen vacancies improve electric conductivity of WO_{3-x} materials, one can conclude that they also lower the work function in the minima of the corrugations.

3.4. Field emission testing in microscopic regime

FE measurements with both kinds of wires were carried out in the STM chamber at the same distance (2 ± 0.2 µm) between a wire's apex and HOPG, which was used as an electron collector. The threshold voltages (onset voltages) for FE were determined from the minima of the corresponding Fowler–Nordheim (F–N) plots. After comparative testing, FE from a W_5O_{14} NW was studied also at a distance of 4 and 5 µm.

3.4.1. Comparative field emission studies of W_5O_{14} and $W_{18}O_{49}$ wires

The comparative FE studies were performed on two wires with very different diameters in the same FE configuration. A W_5O_{14} NW, 14 µm long and 109 nm in diameter, was attached on a tungsten wire using FIB (Fig. 8a). The NW terminated in a rectangular shape (Fig. 8b). Platinum contacts were deposited providing both a sufficient mechanical stability and electric conductance. The $W_{18}O_{49}$ wire, 247 µm in length and 4 µm in diameter, was attached on a Pt/Ir wire with silver epoxy paste (Fig. 8c). Then both tips were transferred into the UHV-STM chamber (7×10^{-10} mbar) and tested without any cleaning or annealing. A programmable voltage source (Keithley 2450) was used for applying a negative voltage onto the cathode (NW) in the range from 0 to 200 V through the field emission adapter of the Omicron STM system.

Firstly, the so-called activation process was studied, in which the FE tips were cleaned of adsorbents and/or impurities. Fig. 9 shows current-voltage (I–V) characteristics of the first (A) and the second (B) consecutive test and their corresponding F–N plots: a-b: W_5O_{14} NW, c-d: $W_{18}O_{49}$ wire. The measurements were performed at 2 µm. Significant changes have been noticed in the onset voltages in two consecutive FE measurements, which dropped for both wires in the second test. The onset voltage decreased from 63 V to 56 V for W_5O_{14} NW, and from 99 V to 74 V for $W_{18}O_{49}$ wire. A possible reason is the removal of adsorbates from the top end of the wires. Also the knees in the F–N plots of the first tests (Fig. 9a, b-A) can be explained with desorption of adsorbates under high electric fields [25]. Larger decrease of onset voltage in the case of $W_{18}O_{49}$ wire and very "noisy" FN plot for the first (A)

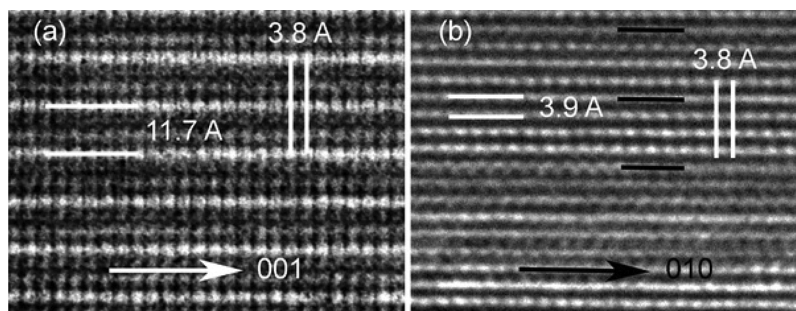

Fig. 3. High-resolution TEM: a) W_5O_{14} nanowires grown along [001] direction; b) $W_{18}O_{49}$ wires grown along [010] direction.

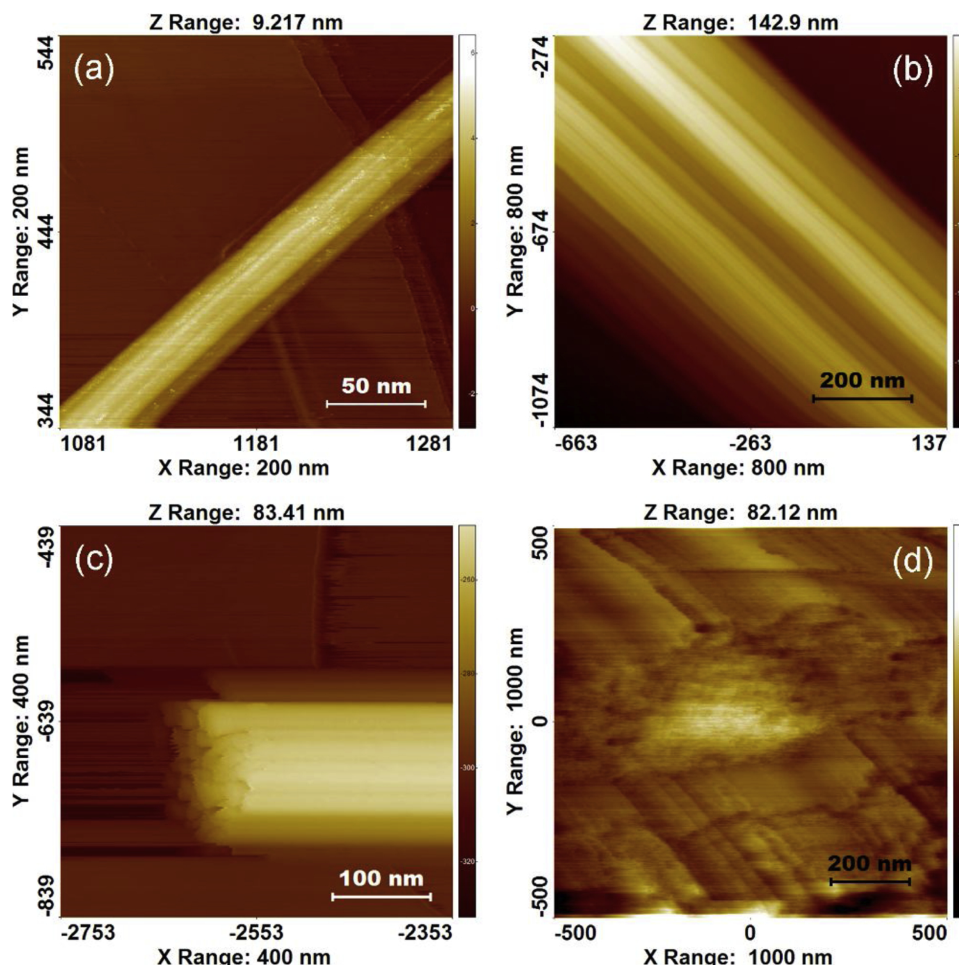

Fig. 4. STM microscopy (I = 0.3 nA; U = 0.5 V): a) single W_5O_{14} NW, 70 nm in diameter; b) a single $W_{18}O_{49}$ wire, 630 nm in diameter; c) termination of a W_5O_{14} NW, 145 nm in diameter and dome shaped protuberances; d) porous structure of a $W_{18}O_{49}$ wire.

experiment is explained with simultaneous cleaning/degradation process.

3.4.2. *Field emission from the W_5O_{14} nanowire as a function of distance and time*

In comparison to the $W_{18}O_{49}$ wire, the W_5O_{14} NW was found to be a more efficient field emitter because of its lower work function and lower onset voltage. Therefore, further FE tests were performed only on the W_5O_{14} NW and were carried out at three distances from HOPG: 2 µm, 4 µm and 5 µm. At each position, FE experiments were performed three times in order to confirm repeatability. No significant differences were detected when the voltage was ramped up or down. The FE current was limited to 160 nA with the aim to prevent damage of the nanowire. The onset voltages were 57 V, 67 V and 76 V at 2 µm, 4 µm and 5 µm, respectively. Fig. 10 shows the FE I–V characteristics (a) and their corresponding F–N plots (b).

In the F–N plot, a linear behaviour indicates the standard barrier-tunnelling mechanism of the field electron emission. The waviness of the F–N curves corresponding to the B (4 µm) and C (5 µm) positions cannot be explained by desorption of adsorbates, because the same FE emitter was used at all three positions and the plot A (the first test in this series) is practically linear. A possible reason for the deviation from the linearity is the electrical force which strengthens the emitter from a slightly curved shape (Fig. 8a). This effect might also be the origin of current instabilities observed during measurements of FE current over time (Fig. 11). Current over time was measured at 5 µm separation under 80 V and 85 V applied voltage in several sequences. The sample rate for the measurement illustrated in Fig. 11 was set to 10,000 readings/sec at 5½ digits and sent directly to the computer. In order to suppress the noise at the line frequency (50 Hz for most European countries), the NPLC (Number of Power Line Cycles) function was employed and set > 1, usually to 100 to achieve precise measurement accuracy. Typically, the current was stable for a certain period, then it suddenly jumped to a certain higher or lower value, which were not arbitrary. In Fig. 11a, a time stability test is shown. Four main values of the current over time are observed: 45 nA, 40 nA, 70 nA, 90 nA, and then again 40 nA, all with a standard deviation of 1 nA. Several FE current time stability measurements were recorded and fluctuations among similar values were found. A comparison of the I–V characteristics measured before and after ten current stability tests in total duration of 2.5 h (Fig. 11b), reveals a decrease of onset voltage after the stability test, from 75 V to 67 V. Deviations of the FE I–V curves from a typical exponential shape were observed only after time stability tests (Fig. 11b, curve 2). This effect indicates a structural or/and shape change of the NW. It is likely that high current densities, which for a short periods reached values up to 23 A/mm^2 (total cross section area of the NW was considered as the emission area), caused a local temperature increase, which affect the stoichiometry and accelerated the diffusion processes under the strong electric field. If comparing our results (Fig. 11a) to the previously published results illustrated by the Fig. 2 in [16], the waveform of the measured total emission current evince far stable behavior. The stability improvement is caused mainly by the decreased number of residual particles present in the ultra-high vacuum chamber comparing to the high vacuum ($P = 10^{-5}$ Pa) used in [16]. Based on equation of state, there are approx. 10^2 particles / cm^3 less in the ultra-high vacuum chamber comparing to the high vacuum

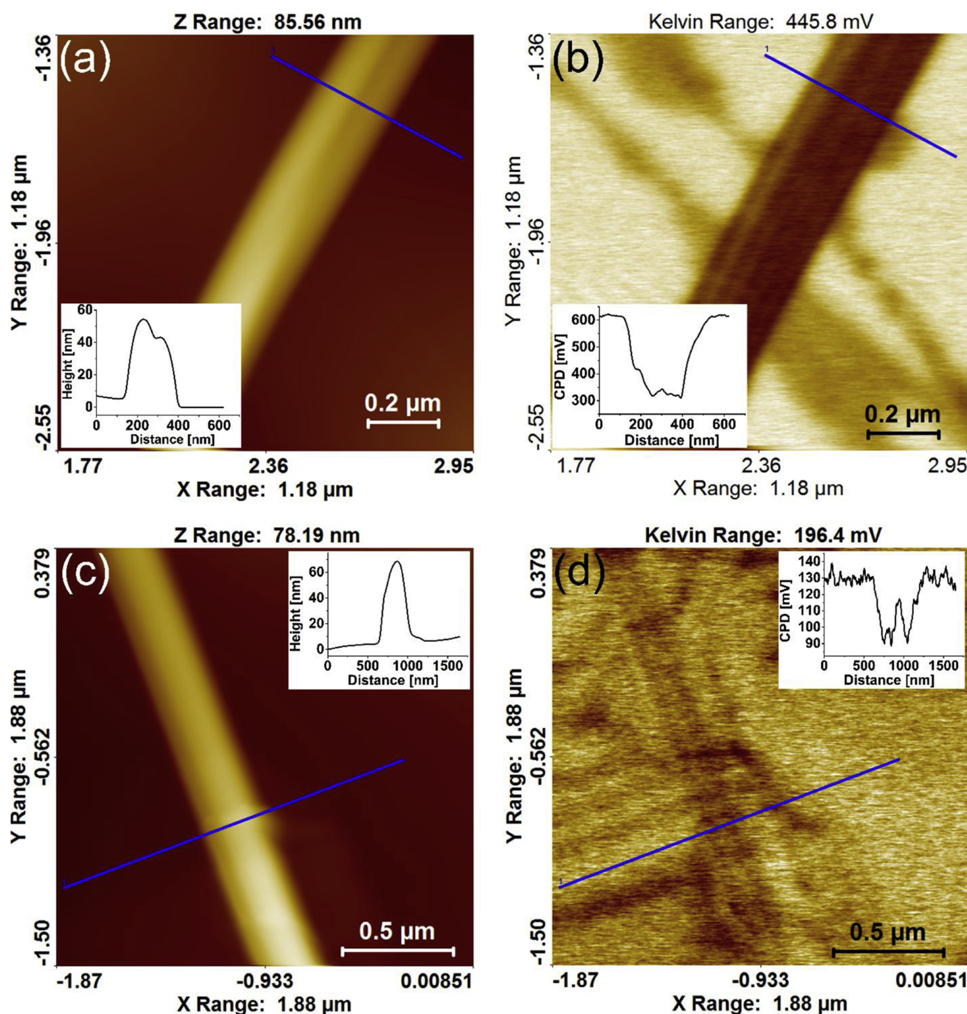

Fig. 5. AFM non contact images (df = 20 Hz) with corresponding Kelvin images: a-b: W_5O_{14}; c-d: $W_{18}O_{49}$. Line profiles marked with blue lines are shown in the insets.

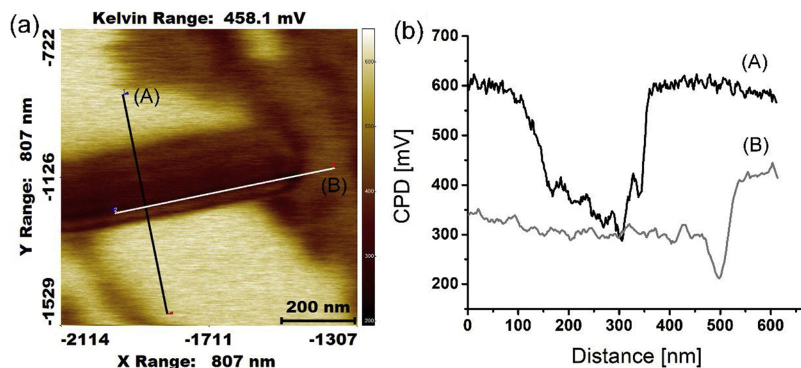

Fig. 6. Kelvin image of W_5O_{14} NW with two line profiles; b) CPD curves along A and B lines.

chamber, which reduces effects of the ions impinging on the cathode surface and hence causing ion bombardment [16]. These ions are attracted towards the cathode where they significantly influencing the thickness of the surface barrier and increasing the *1/f* and generation-recombination (g–r) noise component [18]. The effects of the ion bombardment were described by Sergeev in [32] where authors proved the relation between the ion bombardment of residual gas particles and decrease of the current noise density of the total emission current.

The local electric field at the emission point (apex) of the NWs could be much higher than the average applied field across the electrodes. As the first approximation, the field enhancement factor (β) of the local field at the apex of the NW tip was calculated using the F–N equation mimicking a parallel plate configuration and homogeneous electric field between the flat end of the nanoemitter and electron collector.

$$I = \left(A\alpha\beta^2V^2 \Big/ d^2\Phi \right) exp^{\frac{-B\Phi^{3/2}d}{\beta V}}, \quad (1)$$

where I is the emission current, $A = 1.56 \times 10^{-6}$ A V^{-2} eV and $B = 6.83 \times 10^9$ $eV^{-3/2}$ (Vm^{-1}) are F–N constants, α is the field emission area, β is the field enhancement factor, Φ is the WF, d is the distance

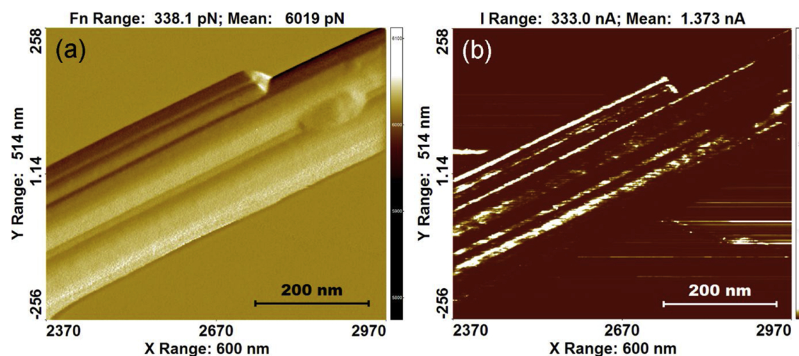

Fig. 7. Contact AFM observations of W_5O_{14} NW: a) topography image; b) current image.

between the anode and the apex of the NW and V is the applied voltage. The geometrical parameters mainly influencing the field enhancement factor are the ratio between the diameter and the length of the NW, the diameter of the nanowire, shape of the NW termination, the emitter-collector distance [26–28], etc.. Using Eq. 1, the field enhancement factor can be calculated from linear slope (k) of the F–N plot (log (I/V^2) vs. 1/V) [28]:

$$\beta = \frac{-Bd\Phi^{3/2}}{k}. \tag{2}$$

Considering an average work function of 4.3 eV for W_5O_{14} obtained from KPFM measurements, the apparent field enhancement factor for W_5O_{14} NW was 110 ± 10, 180 ± 25 and 210 ± 30 at 2, 4 and 5 µm, respectively. In comparison, the calculated field enhancement factor for $W_{18}O_{49}$ was 125 ± 15 at 2 µm, considering that the average WF is 4.56 eV. Larger field enhancement factor for $W_{18}O_{49}$ could be explained by protrusions (Fig. 8**b**-insert) or splinters (Fig. 4d) frequently observed at the ends of these NWs.

3.5. Field emission testing in macroscopic regime

The FE experiments at macroscopic distances (≈ 1 mm) were performed in two configurations: the $W_{18}O_{49}$ NW in a negatively biased cathode and grounded anode configuration [19], and W_5O_{14} NW in a positively biased electron extractor configuration [18].

3.5.1. Field emission from $W_{18}O_{49}$ wire

A $W_{18}O_{49}$ NW, 10 µm long and 180 nm in diameter, was attached on a tungsten electrochemically etched tip using FIB, as shown in the Fig. 12a. The I–V characteristics were measured with custom-made UHV system using a nanowire as an electron source and a Si wafer as an electron collector. The working pressure in the main chamber was 3.5×10^{-10} mbar.

Prior to field emission experiment, in-situ cleaning was performed by placing the tip in front of the first loop of a hot filament (˜1500 °C), which emitted electrons towards the positively biased tip (1 kV) shown in the Fig. 12b. The tip was annealed by the electron bombardment procedure for 15–20 min and flashed for 20 s. Typically, the annealing was performed at an emission current of 3–5 mA and flashing at a current of 20–30 mA.

After annealing, FE measurements of the $W_{18}O_{49}$ NW were carried out at two distances: 600 µm and 800 µm from the Si wafer. Fig. 13 shows the FE I–V characteristics for both distances and their corresponding F–N plots. At each position, FE experiments were performed three times in order to confirm repeatability. The FE currents were limited to 45 nA with the aim to prevent damage of the nanowire. The onset voltage of FE was 322 ± 1 V at 600 µm and 354 ± 1 V at 800 µm. The limit current was reached at 433 V and at 463 V, respectively (Fig. 13a). No significant differences were detected when the voltage was ramped up or down. In the F–N plots (Fig. 13b), the straight lines indicate the standard barrier-tunneling mechanism of the field electron emission. No degradation was observed.

The field enhancement factors were calculated according to the Fowler–Nordheim formalism for comparison with the relevant literature data. An average work function of $W_{18}O_{49}$ obtained from the KPFM measurements, i.e. 4.56 eV was considered. The field enhancement factors were 5050 ± 30 and 6450 ± 30 for 600 and 800 µm, respectively. These values were calculated using two parallel plates approximation, which is highly unrealistic for a nanowire emitter and flat electron collector at distances which, for several orders of magnitude, exceed the length of the nanowire. Therefore, a model developed for nanoemitters with an aspect ratio 1–500 and anode to cathode separation greater than three times the height of the emitter was used [29]:

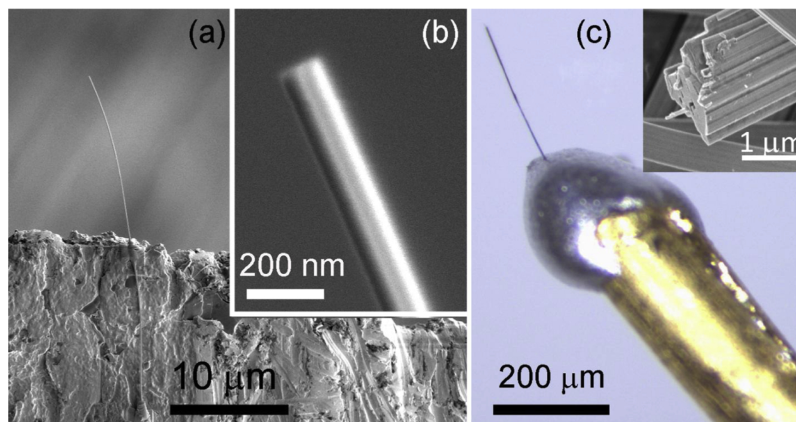

Fig. 8. SEM and optical images: a) W_5O_{14} nanowire on the W wire; b) rectangular termination of the W_5O_{14} NW; c) $W_{18}O_{49}$ wire on the Pt/Ir wire.

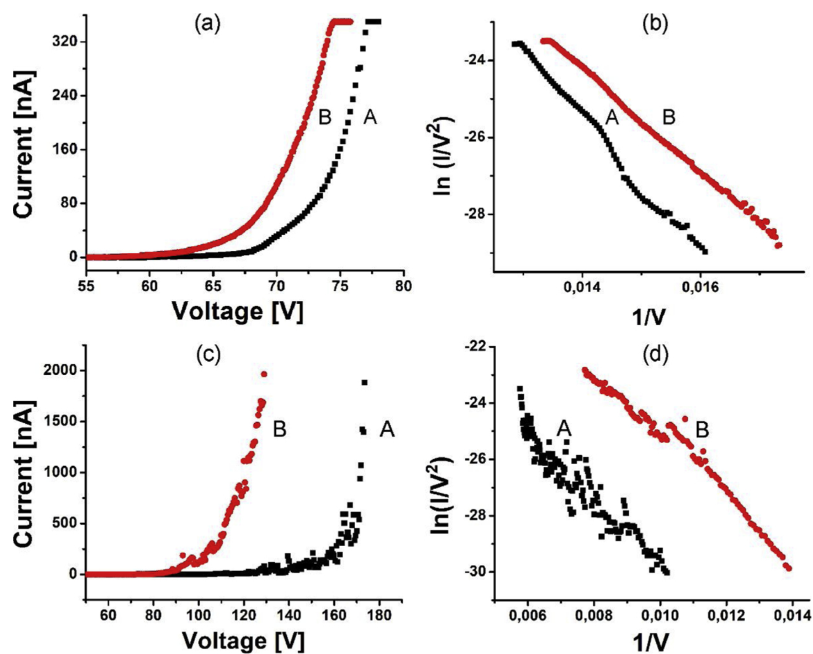

Fig. 9. I–V curves and corresponding F–N plots: a,b: W_5O_{14} NW ; c,d $W_{18}O_{49}$ wire. The first tests are labelled with A, and the second with B.

$$\beta = \left(1 + \sqrt{\frac{h}{\alpha r}}\right)^m \tag{3}$$

where h is length of the NW, r its radius, m = 1 and α = 2.

The field enhancement factor according to this model, which is independent on the anode location and is determined solely with length and diameter of an emitter, was 8 ± 0.5. Using this field enhancement factor, the onset fields for emission were 4.3 ± 0.3 V/μm and 3,5 ± 0.3 V/μm for 600 and 800 μm, respectively.

3.5.2. Field emission from W_5O_{14} nanowire

The W_5O_{14} NW used in the macroscopic FE regime measurement was 5 μm long, 148 nm in diameter (Fig. 14a) and mounted on an electrochemically etched tungsten wire by FIB. The experiment took place in an UHV chamber at 2×10^{-9} mbar with a separation of 1060 μm between the NW apex and the extractor plate.

Three relatively rough FE tests were performed. Voltage was manually increased step by step in 5 min intervals for the current to stabilize. In the first experiment, the voltage was increased to 990 V and the corresponding FE current reached 183 nA. The I–V curve (Fig. 14b) is exponential and relatively smooth. The second test revealed the maximum FE current of 1.2 μA at 890 V, while at higher voltages the current started to decrease. The FE current (990 nA) at 990 V was more than 5 times larger (Fig. 14c) than in the first test. In the third test, the maximum current of 1.063 μA was obtained at a higher voltage as in the second test, i.e. at 1063 V, while at 990 V the current was 1008 nA, i.e. again larger than in both previous tests (Fig. 14d). The explanation of the increase of FE current could be connected with the absence of cleaning of the emitters before FE testing. The subsequent tests gradually removed adsorbates from the NW, and the FE current consequently increased. Relatively high currents, which could cause diffusion of tungsten atoms and structural changes of the nanowire, could be the origin of degradation of the FE tip. While in the first test the maximum current was not reached, it decreased from the second to the third test for 12%. The onset voltages also increased gradually in subsequent tests, from 510 V, 535 V, to 551 V, respectively. Field enhancement factor from the F–N plot corresponding to the first test (Fig. 14e) was ≈ 17.000, while using the Eq. 3, it is 7 ± 0.5. The onset fields for three subsequent tests were 3.3 ± 0.3 V/μm, 3,4 ± 0.3 V/μ, and 3.5 ± 0.3 V/μm. The values match very well the onset field for emission from W_5O_{14} film [17].

4. Discussion

Two WO_{3-x} phases were studied, both in the shape of wires with a high aspect ratio. They differ in size, morphology, work function and field emission properties. In contrast with semiconducting WO_3 with a band gap in the range of 2.5–3.2 eV [9], the $W_{18}O_{49}$ and W_5O_{14} NWs are metallic with electrical resistance of 2750 μΩcm [12] and 25 μΩcm [7], respectively. The reason for improved electric conductance in these sub-stoichiometric WO_{3-x} phases are oxygen vacancies, which form

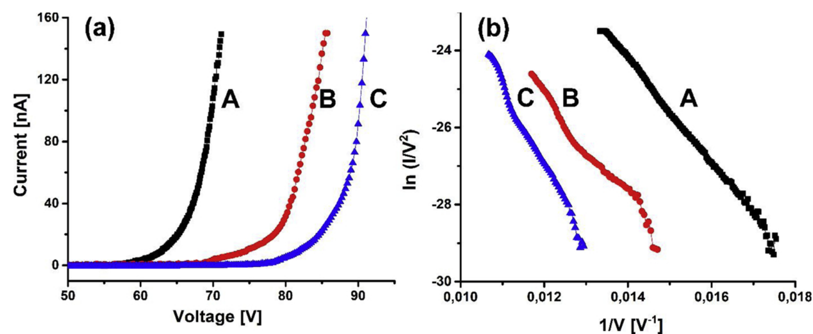

Fig. 10. I–V characteristics of a W_5O_{14} NW and the corresponding F–N plots. Distances between the NW tip and the electron collector: A - 2 μm; B - 4 μm; C - 5 μm.

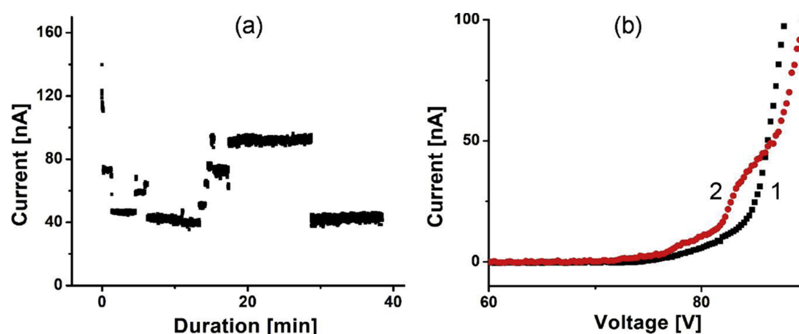

Fig. 11. a) FE current over time from a single W_5O_{14} NW, 5 µm away from electron collector, under 85 V of applied voltage; b) I–V curves before (1) and after (2) current time stability testing in total duration of 2,5 h under 80–85 V applied voltage.

donor states. Besides, these vacancies accumulate at the crystallographic shear planes, where they change the coordination number of tungsten ions from W^{+6} to W^{+5} [8] and cause structural changes like hexagonal or pentagonal tunnels in the structure oriented along the axis of the NWs [30]. Surface morphology of the NWs revealed by AFM and STM is not smooth, but wrinkled with undulations perpendicular to the NWs axis. These undulations can be understood as surface relaxation of the shear planes, which at the surface form undulated structure. The bottom parts of these undulations have the largest density of the oxygen vacancies, which is in accordance with the findings that they show the largest electric conductance in the current AFM image (Fig. 7) and the lowest work function (Figs. 5, 6). The same enhancement of electric conductance and decrease of work function was observed at longitudinal terminations of the NWs (Fig. 7), where the tunnels in the structure are exposed. Due to more than two orders of magnitude larger electric resistance of $W_{18}O_{49}$ NWs with respect to the W_5O_{14} NWs, and because of the diameter of W_5O_{14} is typically much smaller, the last ones were selected for detailed FE studies, and the former ones for comparison. While in-situ FE studies performed inside TEM from a single W_5O_{14} NW was reported with 35 µA extracted current [16], there is no report of FE studies on a single $W_{18}O_{49}$ NW, according to our knowledge. Our FE experiments were performed in ultra-high vacuum conditions at microscopic (2, 4, 5 µm) and macroscopic (600, 800, 1060 µm) distances between the tip of WO_{3-x} wires and the electron collectors. It was found, that at microscopic distances the field enhancement factors and onset voltages for FE increase with the distance, and two parallel plates model described by FN equation can be used. At 2 µm distance, there is no substantial difference in field enhancement factors between both types of the wires, i.e. 110 (W_5O_{14}) and 125 ($W_{18}O_{49}$), which could be explained with small splinters on otherwise wider $W_{18}O_{49}$ wires [30]. At the macroscopic distances, the FN equation revealed higher apparent field enhancement factors at the ends of W_5O_{14} NWs (17.000 at 1060 µm) than $W_{18}O_{49}$ NWs (5050 at 600 µm, and 6450 at 800 µm). This is explained with smaller diameter, deeper surface undulation, and the lower work function of W_5O_{14} NWs. The term “apparent” is used because the use of the FN equation in far field geometry is questionable and there is still an undergoing discussion, regarding the proper FE model in the far field geometry, within the scientific community. It represents an extreme ideal situation, which cannot be justified for our FE experiments done at macroscopic distances. Therefore, the other model [29] was utilized, which represent another extreme situation from the point that the field enhancement factor depends only on geometry of the emitter, i.e. its length and diameter. Using this model, the field enhancement factors are several orders of magnitude smaller than those calculated from FN equation. The values were: 8 ± 0.5 for $W_{18}O_{49}$ NW and 7 ± 0.5 for W_5O_{14} NW. This model predicts no dependency on cathode-anode distance, but our results do show the dependence of onset voltage and corresponding onset field on the distance between top of the emitter and electron collector. The onset fields for field emission (3–4 V/µm) match very well with the onset field for emission from W_5O_{14} film [17]. Nevertheless, it is worthy to note than neither of the above mentioned models cannot perfectly describe the results. It is known from other works, that the field enhancement factor increases by increasing the distance between the cathode and anode and by reducing the NW diameter [27,30]. In addition, the accurate emission area is not known. Reducing the diameter of the nanowires, the uncertainty of the emission area is also decreased, but special porous structure of the WO_x nanowires represents an additional challenge to find out, which part of the cross-section really emits. As it was shown in Fig. 6, the WF of the NW varies at the edge which could lead to field emission only from the part with the lowest WF. The apparent high field enhancement factors at macroscopic distances could be understood in a similar way as giant field enhancement up to 18 800 at carbon nanotubes grown on carbon cloth and explained by the multistage effect [31]. While the magnitude smaller nanotubes branching off the tips of bigger nanotubes were the

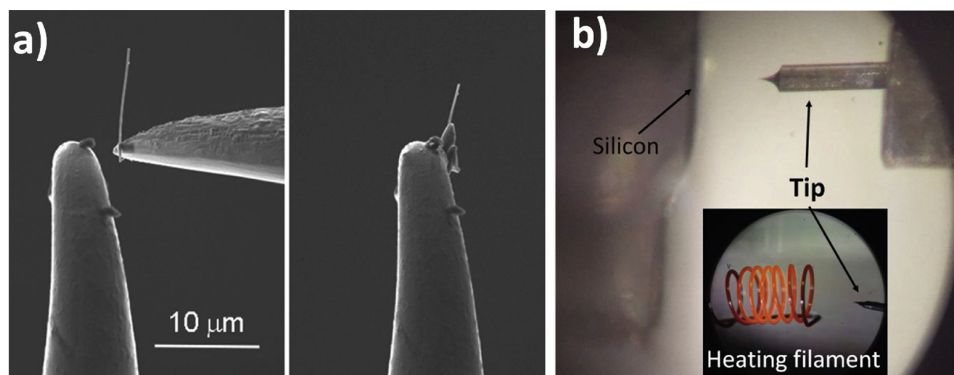

Fig. 12. a) SEM images showing the mounting of a single $W_{18}O_{49}$ NW; b) Optical image of the FE setup with the in-situ cleaning of the emitter by electron bombardment from heating filament.

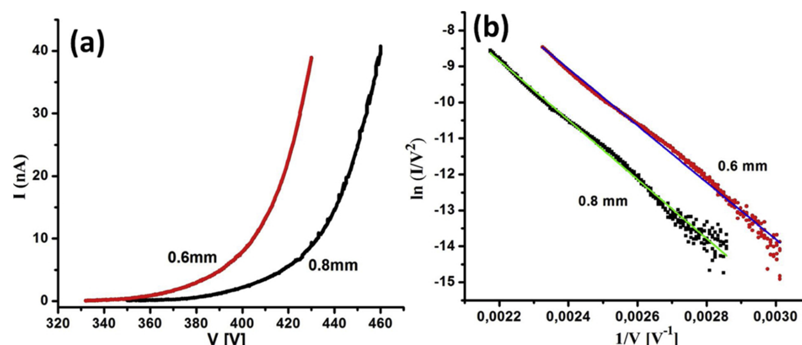

Fig. 13. FE testing of a $W_{18}O_{49}$ NW at two distances (600 µm and 800 µm): a) I–V characteristics; b) The corresponding F–N plots with linear fits.

origin of the field enhancement in carbon nanotubes case, the special porous structure of $W_{18}O_{49}$ wires and in particular W_5O_{14} NWs with deeper surface undulations could be the origin of the high field enhancement factors. One could assume that the areas around structural channels with concentrated oxygen vacancies and the bottom of the surface undulations with 50 mV lower work function than the average, represent the FE sites. Further research is needed to clarify this assumption.

5. Conclusion

In conclusion, field emission properties of single crystalline tungsten

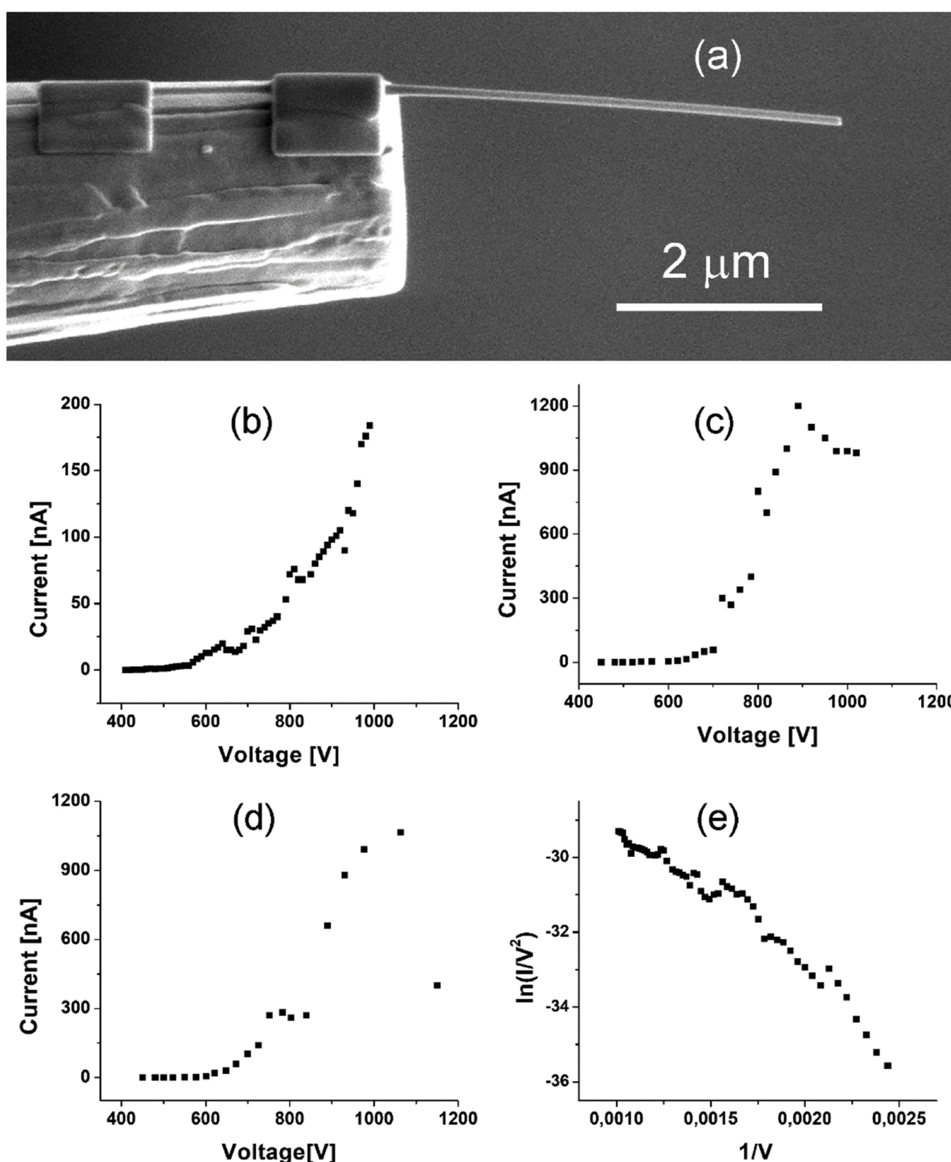

Fig. 14. a) SEM image of the W_5O_{14} NW mounted on tungsten wire; FE properties of a single W_5O_{14} NW in subsequent tests: b) the first test; c) the second test; d) the third test; e) F–N plot of the first test.

oxides W_5O_{14} and $W_{18}O_{49}$ wires were studied at microscopic and macroscopic distances between the nanowires and electron collectors. The work function of the NWs was determined by Kelvin probe force microscopy in non-contact AFM in ultrahigh vacuum. The average work function of W_5O_{14} NWs (4.3 eV) was found lower than $W_{18}O_{49}$ wires (4.56 eV), and the lowest, i.e. 4.2 eV inside surface corrugations of W_5O_{14}, where also enlarged electron conductance was observed with conductive AFM tip. The emitting characteristics of W_5O_{14} NWs situated at microscopic distances from electron collector follow the Fowler–Nordheim law with calculated field enhancement factors that are similar to the ones obtained from $W_{18}O_{49}$ NWs. It was found, that both the field enhancement factors and onset voltages increase with the distance between emitter and electron collector. At macroscopic distances, the Fowler–Nordheim formalism was used only for comparison with the literature data, while the results were explained with a model, which considers only the geometry of the nanowire in the calculation of the field enhancement factor. The onset fields were comparable for both kinds of the NWs. The obtained results open several perspectives in utilization of tungsten oxide nanowires as a source of low-energy electrons in different devices. In particular, the W_5O_{14} NWs are promising with larger electric conductance and typically smaller diameter than $W_{18}O_{49}$ NWs, as well as due to relatively high field enhancement factors they can be activated at relatively low electric fields.

Acknowledgment

This research was financially supported by the SIMDALEE2-Sources, Interaction with Matter, Detection, and Analysis of Low Energy Electrons, a Marie Curie Initial Training Network (Grant No. PITN 606988), financed by the European Commission. The first author (M.S.) is thankful for the financial support form ETH Zurich and to Prof. Danilo Pescia and his research group for help in experiments. We acknowledge Slovenian Research Agency for co-financing. The research was also funded by the Technology Agency of the Czech Republic, Project No. TE01020118.

References

[1] K. Gesheva, T. Ivanova, G. Bodurov, I.M. Szilágyi, N. Justh, O. Kéri, S. Boyadjiev, D. Nagy, M. Aleksandrova, Technologies for deposition of transition metal oxide thin films: application as functional layers in “Smart windows” and photocatalytic systems, J. Phys: Conf Ser. 682 (1) (2016) 012011 IOP Publishing.
[2] B. Gavanier, F.M. Michalak, J.R. Owen, Electrochemistry of WO 3 based smart windows: beliefs and facts, Ionics 3 (May (3-4)) (1997) 265–269.
[3] M. Ladouceur, J.P. Dodelet, G. Tourillon, L. Parent, S. Dallaire, Plasma-sprayed semiconductor electrodes: photoelectrochemical characterization and ammonia photoproduction by substoichiometric tungsten oxides, J. Phys. Chem. 94 (May (11)) (1990) 4579–4587.
[4] Z.F. Huang, J. Song, L. Pan, X. Zhang, L. Wang, J.J. Zou, Tungsten oxides for photocatalysis, electrochemistry, and phototherapy, Adv. Mater. 27 (September (36)) (2015) 5309–5327.
[5] K.R. Locherer, I.P. Swainson, E.K. Salje, Phase transitions in tungsten trioxide at high temperatures-a new look, J. Phys. Condens. Matter 11 (September (35)) (1999) 6737.
[6] I.J. McColm, R. Steadman, S.J. Wilson, Iron-promoted phases in the tungsten-oxygen system, J. Solid State Chem. 23 (January (1-2)) (1978) 33–42.
[7] M. Remškar, J. Kovac, M. Viršek, M. Mrak, A. Jesih, A. Seabaugh, W5O14 nanowires, Adv. Funct. Mater. 17 (August (12)) (2007) 1974–1978.
[8] M. Sundberg, R.J. Tilley, An electron microscope study of some nonstoichiometric tungsten oxides, J. Solid State Chem. 11 (October (2)) (1974) 150–160.
[9] F. Wang, C. Di Valentin, G. Pacchioni, Electronic and structural properties of WO3: a systematic hybrid DFT study, J. Phys. Chem. C 115 (April (16)) (2011) 8345–8353.
[10] T. Hirose, I. Kawano, M. Niino, Electrical conductivity of tungsten trioxide (WO3), J. Phys. Soc. Jpn. 33 (July (1)) (1972) 272.
[11] Z. Hu, Z. Ji, W.W. Lim, B. Mukherjee, C. Zhou, E.S. Tok, C.H. Sow, K-enriched WO3 nanobundles: high electrical conductivity and photocurrent with controlled polarity, ACS Appl. Mater. Interfaces 5 (May (11)) (2013) 4731–4738.
[12] K. Viswanathan, K. Brandt, E. Salje, Crystal structure and charge carrier concentration of W18O49, J. Solid State Chem. 36 (January (1)) (1981) 45–51.
[13] W.Q. Chen, R.Z. Zhan, S.Z. Deng, N.S. Xu, J. Chen, Anomalous temperature dependence of field emission from W18O49 nanowires caused by surface states and field penetration, J. Appl. Phys. 116 (January (13)) (2014) 133506.
[14] J. Zhou, L. Gong, S.Z. Deng, J. Chen, J.C. She, N.S. Xu, R. Yang, Z.L. Wang, Appl. Phys. Lett. 87 (November (22)) (2005) 223108.
[15] W.Q. Chen, C.X. Zhao, J.Q. Wu, S.Z. Deng, N.S. Xu, J. Chen, Phonon-assisted field emission from W18O49 nanowires, Appl. Phys. Lett. 103 (September (14)) (2013) 141915.
[16] M. Žumer, V. Nemanič, B. Zajec, M. Wang, J. Wang, Y. Liu, L.M. Peng, The field-emission and current− voltage characteristics of individual W5O14 nanowires, J. Phys. Chem. C 112 (April (14)) (2008) 5250–5253.
[17] G. Ulisse, C. Ciceroni, A.D. Carlo, F. Brunetti, J. Jelenc, M. Saqib, A. Varlec, M. Remskar, Synthesis and field emission characteristics of W5O14 nanowires film, Microelectron. Eng. 25 (February 170) (2017) 44–48.
[18] A. Knápek, L. Grmela, Methods of Preparation and Characterisation of Experimental Field-emission Cathodes, Vysoké učení technické, 2013.
[19] De Pietro L.G. Field Emission Scanning Tunnelling Microscopy with Spin Polarisation Analysis (Doctoral dissertation, ETH Zurich).
[20] J. Booth, T. Ekström, E. Iguchi, R.J. Tilley, Notes on phases occurring in the binary tungsten-oxygen system, J. Solid State Chem. 41 (March (3)) (1982) 293–307.
[21] Y. Li, Y. Bando, D. Golberg, Quasi-Aligned Single-Crystalline W18O49 Nanotubes and Nanowires, Adv. Mater. 15 (August (15)) (2003) 1294–1296.
[22] M. Nonnenmacher, M.P. o'Boyle, H.K. Wickramasinghe, Kelvin probe force microscopy, Appl. Phys. Lett. 58 (June (25)) (1991) 2921–2923.
[23] T. Glatzel, S. Sadewasser, M.C. Lux-Steiner, Amplitude or frequency modulation-detection in Kelvin probe force microscopy, Appl. Surf. Sci. 210 (March (1-2)) (2003) 84–89.
[24] F. Maeda, T. Takahashi, H. Ohsawa, S. Suzuki, H. Suematsu, Unoccupied-electronic-band structure of graphite studied by angle-resolved secondary-electron emission and inverse photoemission, Phys. Rev. B 37 (March (9)) (1988) 4482.
[25] K.A. Dean, B.R. Chalamala, Current saturation mechanisms in carbon nanotube field emitters, Appl. Phys. Lett. 76 (January (3)) (2000) 375–377.
[26] R.C. Smith, S.R. Silva, Interpretation of the field enhancement factor for electron emission from carbon nanotubes, J. Appl. Phys. 106 (July (1)) (2009) 014314.
[27] R.C. Smith, D.C. Cox, S.R. Silva, Electron field emission from a single carbon nanotube: effects of anode location, Appl. Phys. Lett. 87 (September (10)) (2005) 103112.
[28] H. Liu, S. Kato, Y. Saito, Effect of cathode-anode distance on field emission properties for carbon nanotube film emitters, Jpn. J. Appl. Phys. 20 (January 48) (2009) 015007.
[29] R.C. Smith, J.D. Carey, R.D. Forrest, S.R.P. Silva, Effect of aspect ratio and anode location on the field emission properties of a single tip based emitter, J. Vac. Sci. Technol. B 23 (2005) 632.
[30] G.L. Frey, A. Rothschild, J. Sloan, R. Rosentsveig, R. Popovitz-Biro, R. Tenne, Investigations of nonstoichiometric tungsten oxide nanoparticles, J. Solid State Chem. 162 (December (2)) (2001) 300–314.
[31] J.Y. Huang, K. Kempa, S.H. Jo, S. Chen, Z.F. Ren, Giant field enhancement at carbon nanotube tips induced by multistage effect, Appl. Phys. Lett. 87 (August (5)) (2005) 053110.
[32] E. Sergeev, et al., Noise diagnostic method of experimental cold field-emission cathodes, 2013 22nd International Conference on Noise and Fluctuations (ICNF) (2013) 1–4.

Metrol. Meas. Syst., Vol. 25 (2018) No. 3, pp. 451–458.

PAN
POLSKA AKADEMIA NAUK

METROLOGY AND MEASUREMENT SYSTEMS

Index 330930, ISSN 0860-8229
www.metrology.pg.gda.pl

M&MS

PREPARATION AND NOISE ANALYSIS OF POLYMER GRAPHITE CATHODE

Alexandr Knápek[1)], Miroslav Horáček[1)], Jana Chlumská[1)], Tomáš Kuparowitz[2)], Dinara Sobola[2)], Josef Šikula[2)]

1) *Institute of Scientific Instruments of the Czech Academy of Sciences, v. v. i., Královopolská 147, 612 64 Brno, Czech Republic* (✉ *knapek@isibrno.cz,* 420 541 514 258, *mih@isibrno.cz, jana.chlumska@isibrno.cz*)
2) *Brno University of Technology, Faculty of Electrical Engineering and Communication, Technická 8, 616 00, Brno, Czech Republic* (*xkupar01@stud.feec.vutbr.cz, sobola@vutbr.cz, josef.sikula@ceitec.vutbr.cz*)

Abstract

The paper deals with the preparation and measurement of an experimental polymer graphite cathode that seems to be a promising and cheap source of electrons utilizing cold field-emission in high- and ultra-high vacuum. Polymer graphite seems to be a proper material as it contains a large amount of hybridized carbon with a low degree of surface oxidation and *silicon monoxide* (SiO). Within the frame of this work, a special experimental method of tip preparation has been designed and tuned. This method is based on ion milling inside a dual-beam electron microscope enabling to obtain ultra-sharp tips of a diameter smaller than 100 nm with a predefined opening angle. The charge transport within experimental samples is evaluated based on results provided by the noise spectroscopy of the total emission current in the time and frequency domains.

Keywords: field emission, polymer graphite, noise analysis.

© 2018 Polish Academy of Sciences. All rights reserved

1. Introduction

Cathodes based on a pure field emission operating at room temperature ($\sim$ 300 K) are generally desirable for employing in electron optical devices working with a focused beam of electrons. As for pros, the most important include: high brightness (10^{13} A/m^{2}sr), high current density (10^{10} A/m^2), a small source size (< 0.01 μm), a high spatial coherence, and, last but not least, their small energy spread. As for cons, the most problematic seems now the stability of the total emission current which is negatively influenced by the tip cleanliness [1]. Since the tip is operated at room temperature, the active area of the emission is not being simultaneously cleansed by the effect of heating as it is known from thermally stimulated cathodes operating at high temperature ($\sim$ 2700 K). Contaminants which are present on the tip surface locally affect work function causing inhomogeneity of the quantum barrier affecting field emission performance in time [1]. Even though there are several papers describing certain stabilization using a controllable resistor in the high-voltage loop between the control electrode and the cathode [2], a physical solution for this issue has not been yet presented.

Carbon has recently been considered one of the essential elements in the latest attempts to create a stable, long-life and sufficiently bright source of free electrons. Carbon allotropes that are mostly used for field emission related experiments are *carbon nanotubes* (CNT), graphene

Article history: received on Jan. 22, 2018; accepted on Jun. 01, 2018; available online on Sep. 30, 2018, DOI: 10.24425/123895.

www.czasopisma.pan.pl PAN www.journals.pan.pl

and *highly ordered pyrolytic graphite* (HOPG). However, various kinds of graphite seem to be interesting for field emission experiments as well [3–5]. For our experiments, we have picked a special composite material based on graphite, the so called "polymer graphite", as mentioned before. The polymer graphite is easily disposable and provides high amount of sp^3 hybridized carbon (approx. 80%). This kind of graphite is mostly used as a pencil lead for modern micro pencils of various diameters (usually 0.3–0.8 mm). Our "polymer"-branded mechanical pencil lead is of a 0.3 mm diameter. Comparing with the classic wood-case lead pencil graphite containing a mixture of graphite and clay to provide desired hardness, the mechanical pencil leads contain a very resilient and elastic non-ceramic bonding which is achieved by a high-temperature carbonization of the graphite with high polymers of natural origin in an oxygen-free environment. Although there is a growing interest in polymer graphite as an electrode material for electroanalysis due to its high electron transfer rates [6], there is still no paper presenting this material as a cathode emitting free electrons into the vacuum.

2. Experimental

In the first part of this section, a method of preparation which is based on focused-ion beam milling is presented. The second part deals with the measurement set-up and electrical characterization of the tips. In the last part, noise measurements take place presenting the main physical sources of the current beam fluctuations.

2.1. Preparing ultra-sharp tip

An adequately small ultra-sharp tip with a diameter lower than 100 nm is required for obtaining a sufficiently large electric field that is additionally amplified by a field-enhancement factor. The field-enhancement factor depends on the radius of curvature which sets the equipotential surfaces and so the electric field, which corresponds to the gradient of the potential. As for the tip geometry: even though it is possible to form lead pencil graphite by means of precise electrochemical etching [7], it is still not possible to obtain a desired surface tension which would form the required taper angle and a sufficiently small tip diameter. For this reason, a method incorporating a *focused ion-beam* (FIB) was devised and implemented within a dual-beam electron microscope FEI Helios NanoLab 660 enabling to prepare nanostructures of a high lateral and axial resolution. The basic preparation steps are illustrated in Fig. 1.

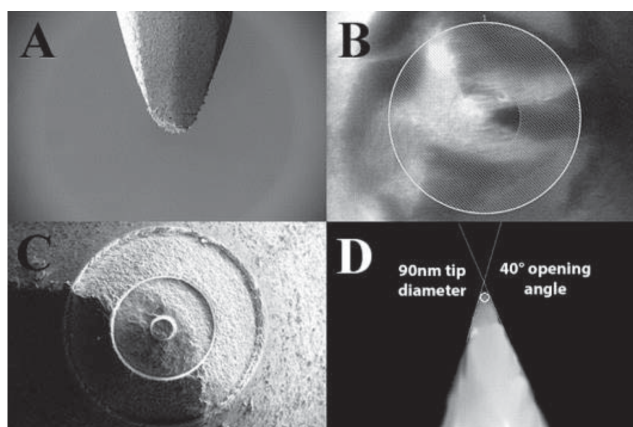

Fig. 1. Preparation of a sharp pencil lead tip by FIB: an SEM image of the preliminary shaped tip achieved by sanding (a); A view from above of the preliminary shaped tip with patterning (b); an FIB image of the stub with decreasing radius of the tip (c); an SEM image of the tip after final FIB milling (d).

An advantage of this approach is mainly the possibility of using the mechanically treated pencil lead which helps to avoid the use of chemicals and surface contamination in comparison with chemical wet etching. Hence, the preparation of a tip consists of two main steps: 1) sharpening mechanically the lead pencil graphite using sanding, and 2) FIB milling of the tip. To ensure the tip quality control, a high-resolution SEM is used to watch the tip geometry. A preliminary sharped stub (Fig. 1a) is inserted into a microscope vacuum chamber, followed by FIB milling which is done in a circular pattern directly at the tip end (Fig. 1b). The first patterning is carried out using a high FIB current (65 nA), followed by another patterning where the FIB current decreases (Fig. 1c). By choosing accurate milling currents and pattern sizes (the inner and the outer diameters), it is possible to control the shape of the tip. It is also possible to prepare a tip of any shape and sharpness. The result of the FIB process is a sharp tip with sizes smaller than 100 nm. This 3D surface modification of a lead pencil graphite rod is shown in Fig. 1d.

2.2. Measurement set-up

The measurement set-up used (Fig. 2) is based on a previous set-up presented in the papers [1, 7]. A field emission cathode is placed in an extractor electrode embedded in a vacuum chamber ($P \sim 10^{-7}$ Pa) aiming towards an anode which accelerates electrons by a high voltage (5 keV). The accelerated electrons are collected on the scintillator electrode made of Cerium-doped *Yttrium Aluminium Garnet* (YAG) coated with a conductive layer, which enables to display an emission pattern, and also to measure a particular number of electrons caught by the conductive layer (approx. 10%).

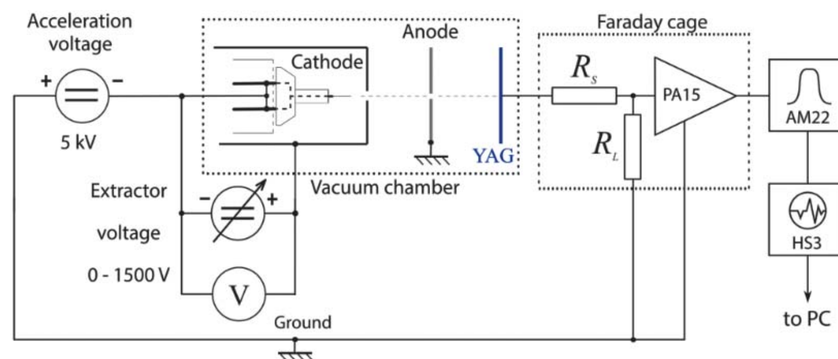

Fig. 2. The noise measurement set-up showing the connection of the electron gun and the noise measurement system located in a Faraday cage. A distance between the tip and the extraction cathode is usually 0.75–1 mm.

The measurement part of the set-up is placed outside the vacuum chamber in a Faraday cage shielding the measurement resistors R_S (491 kΩ), R_L (492 kΩ) and the preamplifier PA15 (20 dB) made by 3S Sedlak. The measurement amplifier AM22 is dynamically set based on the output signal level. The AM22 also serves as a filter providing a proper signal for the HS3 oscilloscopic card which samples the signal to the computer. Fig. 3 shows classical current-voltage characteristics based on the *Fowler–Nordheim* (FN) plot of the total emission current. It can be seen that the electron emission is based on the Fowler–Nordheim tunnelling process. The emission origin is thus considered to be caused predominantly by the field emission. A threshold of the applied voltage for the emission was above 240 V, usually up to 280 V, where the total emission current measured on a scintillator increases from 1 to 10 nA.

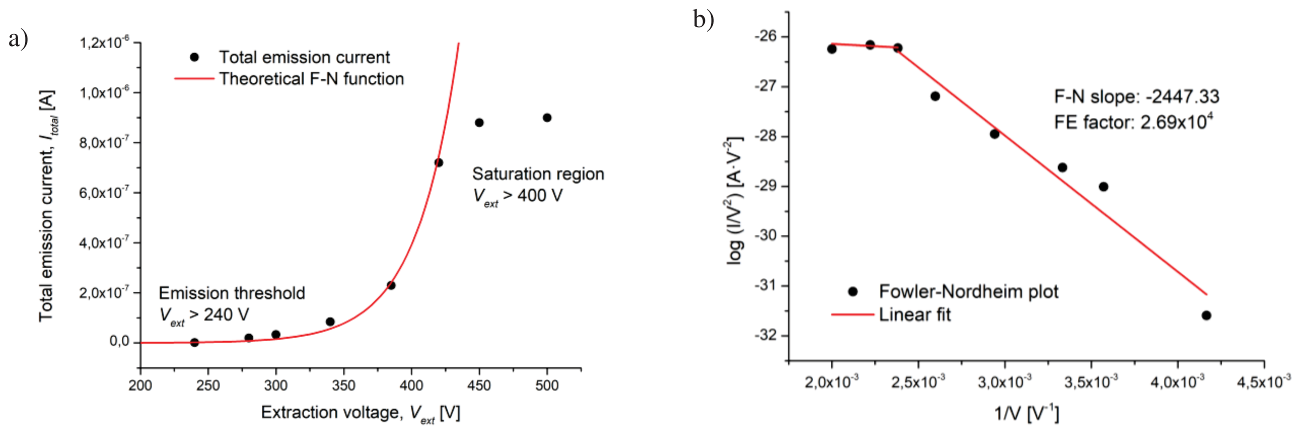

Fig. 3. The dependence of the total emission current (I_{total}) of graphite nanotip on the applied extraction voltage (V_{ext}) (a); the $\log(I/V^2)$ vs $1/V$ plot is shown: the black spots show the experimental data, and the red solid curves are the simulation results according to the FN equation (b).

2.3. Noise measurements

The current that is measured on the YAG scintillator in the time domain is transformed into the spectral domain and further analysed. It should be emphasized that the total emission current is lowered because of the collection efficiency of the YAG (approx. 10% of electrons are collected) and also because of the voltage divider which additionally lowers the current. An additional decrease of the signal intensity is due to the used resistor configuration, where only one half of the overall voltage is measured and therefore the obtained spectrum is decreased four times. Power spectral density is obtained by measuring particular frequency bands. Each band is determined by input and output cut-off frequency filters contained within the AM22 amplifier, which divides the spectrum into five parts. To avoid distortion caused by the filter characteristic, only a part of a spectral band is used, as it can be seen in Table 1. Before each measurement, the setup underwent an automated spectral calibration to achieve flat spectral sensitivity. The noise level of the inherent (background) noise of our setup, when shortened, equals 5×10^{-17} V^2/s, which is low enough to measure even the thermal noise level. Each measurement took 480 seconds and during this period 80,000 samples were recorded. In pursuance of meeting the signal quasi-stationarity requirement for power spectral density analysis, the ideal sampling time of a single run $t = f_s \times \mathrm{N} = 80 \times 103 \times 33.5 \times 106 = 418$ s has been empirically found. To reach a good frequency resolution at low frequencies, the sampled signal is processed by the *digital quadrature filter bank* (DQFB) of order $M = 4$, derived from the wavelet transformation algorithm.

Table 1. Bandwidths used to create the final spectrum.

Bands defined by filters	Frequency bands used
0.03 Hz – 300 Hz	0.1 Hz – 100 Hz
30 Hz – 3 kHz	100 Hz – 1 kHz
300 Hz – 30 kHz	1 kHz – 10 kHz
3 kHz – 300 kHz	10 kHz – 100 kHz
30 kHz – ...	100 kHz – 1 MHz

More detailed information about measurements of the low frequency noise and a description of particular problems that may be associated with such measurements is presented in [8]. In our measurement, the output of DQFB is a set of 16 band-limited fractional signals, where for

each sequence a fractional spectrum S_{yy}, evaluated by the Short-Time Discrete Fourier Transformation, is received. The resulting Power Spectral Density is calculated by the non-parametric Welch's method [1].

The results of noise measurements were obtained using two different extraction voltages representing two determined states of the field emission illustrated in Fig. 4 ($V_{ext} = 325$ V) and Fig. 5 ($V_{ext} = 525$ V). According to Fig. 3 (left), it can be seen that each voltage represents a different operation mode. For $V_{ext} = 325$, our cathode operates in a regular, unsaturated state and for $V_{ext} = 525$ V, the cathode operates in a saturation state, which means that for the increased extraction voltage the emission current does not increase anymore. For both extraction voltages, the thermal noise level is calculated, and its value is given by 4kTR, where T is temperature, R is resistance and k is the Boltzmann constant [9]. For our measurement, 4kTR equals 4.07×10^{-15} V^2s (or V^2/Hz).

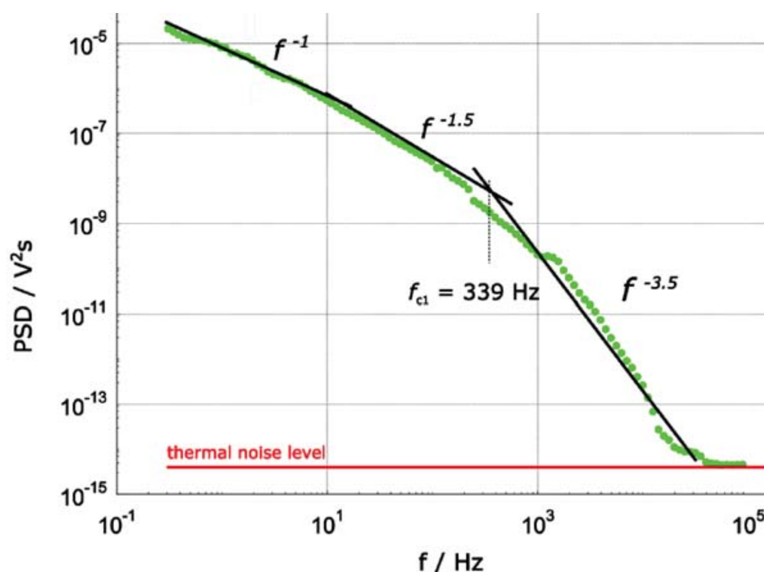

Fig. 4. Noise power spectral density for the total emission current measured at $V_{ext} = 325$ V at constant pressure and electron energy values. Plot colours are described in Table 1.

For $V_{ext} = 325$ V (Fig. 4), the $1/f$ noise which is also referred to as the "flickering" noise, dominates up to the cut-off frequency $f_{c1} = 339$ Hz. The $1/f$ noise is a process with such a frequency spectrum that the power spectral density is proportional to the reciprocal of the frequency and has been already studied in numerous papers [9–12]. As for the lower part of the spectrum where the $1/f^n$ noise is measured, the n parameter value is in a range $1.0 \leq n \leq 1.5$. The exact value of n is determined by the nature of recombination, the lifetime probability density function, and also by the trap density function. It has been already shown that the trap densities close to the conduction and valence band lead to higher values of n [13]. The cutting frequency is located near the region where the spectrum becomes steeper, which is caused by the superposition of particular $1/f$ and *generation-recombination* (G-R) processes. Such an effect may be explained by adsorption and desorption of various atoms present with some residual gas in the vacuum chamber, which happens on the tip surface. A precise model of adsorption-desorption has been formulated based on the Kolmogorov equation by Sergeev [14].

In the bulk, the volume diffusion (*i.e.* a diffusion within a single graphite flake) plays a more significant role, especially in the close vicinity of the emission tip, where temperature is increased due to electron tunnelling. For $V_{ext} = 525$ V, the spectrum slope shows such an influence, which is probably caused by increased temperature induced by a higher emission current. The diffusion

again takes place along with the *generation-recombination* process (G-R) caused by particle movement in the bulk towards the tip.The defects contained in the bulk – which are probably the "polymer" particles – behave like particle traps with an exponential energy distribution function. There are several cut-off frequencies associated with particular generation-recombination noise components; in particular: 8 Hz, 40 Hz, and 2 kHz.

Based on the presented data, our very first measurements show that the "polymer" pencil graphite may be used as a material for preparation of field emission cathodes when operating in a particular voltage regime. As for the setbacks which still prevent the cathode from working in a noiseless regime, it has been shown that the bulk defects, which are mostly cracks and inhomogeneity caused probably by the presence of higher polymers, behave like particle traps creating significant generation-recombination noise and hence the volume and surface diffusion which directly affects the number of emitted electrons. The correlation between the generation-recombination noise and the particle trapping/releasing was described in detail in our previous paper [1].

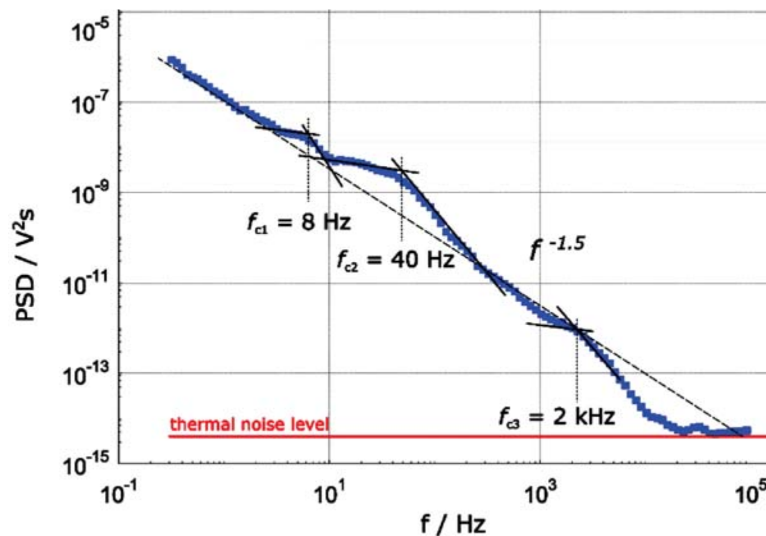

Fig. 5. Noise power spectral density for the total emission current measured at $V_{ext} = 525$ V at constant pressure and electron energy values. Plot colours are described in Table 1.

3. Results and discussion

3.1. Tip preparation using FIB milling

The classical approach to tip preparation is mostly based on electrochemical etching [7]. Since the surface tension is not constant in time as the tip elongates during the etching, it is not possible to prepare the tip with a predefined opening angle. FIB techniques do not suffer such setbacks. The local surface modification in combination with the topography control in nanoscale make this method reliable for preparation of tips from a cheap material source. For applications, where the surface cleanliness is not critical, the classical electrolytic etching [7] may be used instead of FIB.

3.2. Noise analysis

The total emission current measured on the YAG scintillator was further sampled and converted into a power spectrum density that has been subsequently worked with. Particular noise

components were determined in the obtained spectra based on different slopes of the fitting lines. Based on the present noise components, the charge transport in the bulk and at the tip of the cathode is described. The thermal noise component was neglected because of its low magnitude in comparison with the $1/f$ noise and G-R noise components which dominate the spectrum. For our case, the generation-recombination noise seems to be the most important factor influencing current stability: in the bulk of the cathode, the g-r noise originates from the particle movement in the bulk which is affected by structural inhomogeneity and defects contained in the bulk which were also reported by Navratil [6] who performed structural analysis of different "polymer"-branded leads. At the cathode tip, the G-R component is increased due to the electron attraction and release near the cathode surface, which is described in a previous paper [1]. The total emission current value is also decreased by the tip sputtering which continuously removes graphite flakes from the tip and hence blunts it. This results in discontinuous decreases in the total emission current. This phenomenon will be described in more detail in a separate paper.

4. Summary and conclusions

Noise measurements were performed on an entirely new polymer graphite cathode prepared by means of FIB in a dual-beam electron microscope, describing the charge transport and current stability of the total emission current showing the effect of bulk contaminants. Nevertheless, comparing this cathode with common metal FE cathodes, carbon exhibits many advantages; among them a low chemisorption rate of the CO and H_2 on a carbon surface compared with a metal surface. Another benefit that may make the cathode suitable for the use in focused electron beam devices is the fact that the extraction voltage can be kept low and thus limit the bombardment rate of the residual ions. To determine a specific application that should take advantage of the polymer graphite cathodes, the emitted *electron energy distribution spectra* (EEED) should be obtained in future.

Acknowledgements

This work was supported by EC and MEYS CR (project no. CZ.1.05/2.1.00/01.0017), and by the Technology Agency of the Czech Republic project no. TE01020118. This research was also subsidized by the Ministry of Education, Youth and Sports of the Czech Republic under the project CEITEC 2020 (LQ1601) and by the National Sustainability Program under the grant LO1401.

The authors would also like to thank Mr. Král, Mr. Hrubý and Mr. Sýkora for their support and assistance in the design of electrical and mechanical parts of the set-up.

References

[1] Knápek, A., *et al.* (2012). Cold field-emission cathode noise analysis. *Metrol. Meas. Syst.*, 19(4), 417–422.

[2] Harle, R. (1978). *Method for controlling the emission current of an electron source and an electron source having a control circuit for controlling the emission current*. U.S. Patent No 5, 808, 425.

[3] Houdellier, F., *et al.* (2012). New carbon cone nanotip for use in a highly coherent cold field emission electron microscope. *Carbon*, 50(5), 2037–2044.

[4] Khairnar, R.S., Dharmadhikari, C.V., Joag, D.S. (1989). Pencil lead tips: A field ion and field electron emission microscopic study. *Journal of Applied Physics*, 65(12), 4735–4738.

[5] Knápek, A., *et al.* (2017). Field emission from the surface of highly ordered pyrolytic graphite. *Applied Surface Science*, 395, 157–161.

[6] Navrátil, R., *et al*. (2016). Polymer lead pencil graphite as electrode material: Voltammetric, XPS and Raman study. *Journal of Electroanalytical Chemistry*, 783, 152–160.

[7] Knápek, A., *et al.* (2017). Programmable set-up for electrochemical preparation of STM tips and ultra-sharp field emission cathodes. *Microelectronic Engineering*, 173, 42–47.

[8] Kiwilszo, M., Smulko, J. (2009). Pitting corrosion characterization by electrochemical noise measurements on asymmetric electrodes. *Journal of Solid State Electrochemistry*, 13(11), 1681–1686.

[9] Šikula, J., Levinshtein, M. (2004). *Advanced experimental methods for noise research in nanoscale electronic devices*. Boston: Kluwer Academic Publishers, 271–278.

[10] Šikula, J., *et al.* (2007). RTS and 1/f Noise in Submicron MOSFETs. *AIP Conference Proceedings*, 71–76.

[11] Šikula, J., *et al.* (2007). Quantum 1/f Noise in Bio-Chemical Resonant ZnO Sensors. *AIP Conference Proceedings*, 339–342.

[12] Šikula, J., *et al.* (2003). Noise and non-linearity as reliability indicators of electronic devices. *Iinformacije Midem-Ljubljana*, 33(4), 213–221.

[13] Mohammadi, S., Pavilidis, D. (2000). A Nonfundamental Theory of Low-Frequency Noise in Semiconductor Devices. *IEEE Transactions on Electron Devices*, 47(11), 2009–2017.

[14] Sergeev, E., *et al.* (2013). Noise diagnostic method of experimental cold field-emission cathodes. *Noise and Fluctuations (ICNF), 2013 22nd International Conference IEEE*, 1–4.

nanomaterials

MDPI

Article

Field Emission Properties of Polymer Graphite Tips Prepared by Membrane Electrochemical Etching

Alexandr Knápek [1,*], Rashid Dallaev [2], Daniel Burda [1,2], Dinara Sobola [2,3], Mohammad M. Allaham [4], Miroslav Horáček [1], Pavel Kaspar [2], Milan Matějka [1] and Marwan S. Mousa [4]

1 Institute of Scientific Instruments of the Czech Academy of Sciences, Královopolská 147, 612 64 Brno, Czech Republic; burda@isibrno.cz (D.B.); mih@isibrno.cz (M.H.); mmatejka@isibrno.cz (M.M.)
2 Department of Physics, Faculty of Electrical Engineering and Communication, Brno University of Technology, Technická 2848/8, 616 00 Brno, Czech Republic; xdalla03@vutbr.cz (R.D.); sobola@vutbr.cz (D.S.); kasparp@feec.vutbr.cz (P.K.)
3 Central European Institute of Technology BUT, Purkyňova 123, 612 00 Brno, Czech Republic
4 Surface Physics and Materials Technology lab, Department of Physics, Mutah University, Al-Karak 61710, Jordan; quantum.master@live.com (M.M.A.); mmousa@mutah.edu.jo (M.S.M.)
* Correspondence: knapek@isibrno.cz; Tel.: +420541514258

Received: 11 June 2020; Accepted: 29 June 2020; Published: 1 July 2020

Abstract: This paper investigates field emission behavior from the surface of a tip that was prepared from polymer graphite nanocomposites subjected to electrochemical etching. The essence of the tip preparation is to create a membrane of etchant over an electrode metal ring. The graphite rod acts here as an anode and immerses into the membrane filled with alkali etchant. After the etching process, the tip is cleaned and analyzed by Raman spectroscopy, investigating the chemical composition of the tip. The topography information is obtained using the Scanning Electron Microscopy and by Field Emission Microscopy. The evaluation and characterization of field emission behavior is performed at ultra-high vacuum conditions using the Field Emission Microscopy where both the field electron emission pattern projected on the screen and current–voltage characteristics are recorded. The latter is an essential tool that is used both for the imaging of the tip surfaces by electrons that are emitted toward the screen, as well as a tool for measuring current–voltage characteristics that are the input to test field emission orthodoxy.

Keywords: polymer graphite tip; electrochemical etching; field emission microscopy

1. Introduction

Graphite materials find their applications in modern electronics with a rapidly increasing frequency [1–5]. They are employed in various sorts of batteries (e.g., graphene anodes), thermocouples, capacitors, transistors, electrical switches, as well as in ion-implantation that is a process that undergirds the production process of present microchips [6,7]. Graphite-based materials such as graphene are also capable of replacing conventional capacitors as its electrical characteristics 10–100 times exceed those of the currently used material—silicon (100 times thinner, 20 times more powerful, significantly superior electrical conductivity, etc.). Graphite-related carbon allotropes are also often incorporated as a source of field emission current in vacuum [8–10] or as a source of tunneling current operating both in vacuum and in atmospheric conditions [11].

Polymer graphite (PG) is a relatively young nanocomposite material that was invented mainly for micro-pencil refills containing a polymer-based binding agent and graphite flakes [11]. The electrochemical method that is used by us to obtain a sharp tip is one of the three previously used

methods enabling to form the PG rods [11]; however, for the PG, the method has not been studied in more detail yet. The PG has high conductivity and immunity against surface contamination, with a low price, which make it seem a highly suitable material for electrode manufacture in general [11–14]. Such pointed graphite rods may find various applications in analytical methods; for example, they can be used as a source of free electrons [15] or they can operate with a tunneling current in Scanning Probe Microscopy (SPM) conductive modes [11]. To conclude, it should be mentioned that graphite structures attract the attention of researchers from all over the world. Currently, according to the ScienceDirect, there are almost 1800 articles featuring graphite structures, which speaks in favor of the relevancy of our research.

This paper continues in this trend, putting as its main goal the characterization of the field emission properties of a PG in correlation to the electrochemical membrane etching method that is used for its preparation. As for the secondary targets, the first one is to provide a comprehensive analysis of a surface on the top of the tip apex achieved mainly by Scanning Electron Microscopy (SEM) and partly by Field Emission Microscopy (FEM). The second one is to describe the electrochemical preparation method and to examine the resultant tip by Raman Spectroscopy (RS). For the RS, the main task is to examine if the final tip is influenced by the type of the PG rod, by the type of etchant and its concentration, or by the etching voltage. To achieve this target, it has been experimented with pencils of different hardness, which is directly connected with the level of clay admixtures added to the graphite during the manufacture. The rods have been etched in alkali solutions—namely in potassium hydroxide (KOH) and sodium hydroxide (NaOH) of different concentrations.

As for the desirable result, we consider a conical-shaped graphite tip with a minimum amount of impurities, also containing multiple graphite flakes oriented perpendicularly to the tip surface. Therein lies the field emission properties that may appear even for a blunt tip. The number of particular FE sources is the main difference compared to the tip presented in [15], which has been formed by focused ion beam and behaves more similar to a single-source metallic emitter.

2. Materials and Methods

2.1. Materials

The graphite pencil rods have generally two main constituents: graphite itself and various clay minerals or rocks, which are finely ground (small amounts of wax or polymers are also present to serve as a binder) [11,14]. It was reported that polymer graphite contains usually from 30% up to 80% of sp^3 hybridized carbon which may shift its properties more toward those of diamond-like carbon (DLC) structures [11]. The macroscopic hardness of polymer graphite rod is determined by the graphite–clay ratio. An increase in the amount of clay will result in a harder rod that is therefore less smudgy when used on paper, whereas by reducing the amount of clay, a softer, more graphite-rich rod may be produced [16]. The conventional pencils are categorized by manufacturers in terms of hardness using different arbitrary grading scales. In this paper, we will be following the European system, which arranges the pencil graphite rods by their hardness in similar manner (from the hardest to the softest): 4H, 3H, 2H, H, F, HB, B, 2B, 3B, 4B, and 5B, etc. [17]. For our experiments, we have used Koh-i-Noor 0.5 micro-pencil leads (KOH-I-NOOR HARDTMUTH, Czech Republic).

2.2. Equipment and Methods of Analysis

Raman spectroscopy was utilized to investigate the chemical composition of the tips, whilst the topography of the etched PG tip was obtained using the Scanning Electron Microscopy (SEM) technique. The Raman measurements were obtained using the WITec confocal Raman imaging system utilizing green laser (532 nm, 30 mW) and the exposure of 10×10 s with a $50 \times$ objective. The Raman spectra were evaluated and fitted with Lorentzian peak shapes using Fityk 1.3.1 software (Marcin Wojdyr, Warsaw, Poland). The SEM measurements were carried out in Tescan Lyra3 scanning electron microscope with an in-built Aztec SSD detector (Oxford Instruments). For the etching, a

modified version of an NT-MDT Solver Nano etching device has been used. The field emission microscope (FEM) that was used to describe tip electrical properties is a custom-made device designed by Horáček and Knápek in the Institute of Scientific Instruments of the Czech Academy of Sciences.

Raman Spectroscopy

To obtain additional information about the composition of etched polymer graphite tips, broad range spectra from 100 cm^{-1} to 3500 cm^{-1} have been recorded. Raman spectroscopy is a powerful analytic tool that has been widely used in geosciences. Raman spectra of clay minerals are well documented, and the main peaks usually lie in the 3750–3550 cm^{-1} region attributed to various OH group stretching modes (such as Al-OH, Mg-OH), and in the 0–1200 cm^{-1} region, they are attributed mainly to O–Si–O and O–A1–O, Si–O–Si groups and various OH group bending modes [18,19]. The mass fraction of clay content in polymer graphite rods is generally high; looking at other polymer graphite manufacturers, it is around 20% and 50% for grade 2B and H hardness, respectively [20]. Despite the high mass fraction of clays in the final polymer graphite rods, the Raman bands from the region of 0–1200 cm^{-1}, which are attributed to the presence of clays and clay minerals in samples, were not visible in any of the recorded spectra.

Unsurprisingly, the main carbon Raman peaks are well visible. It can be seen that the two most intensive Raman peaks in our scenario occur in the region between 1000 and 1600 cm^{-1}. The first peak at 1345–1350 cm^{-1} is associated with breathing modes and disorders of graphene sp^2 rings (D-band). The peak at 1575–1580 cm^{-1} belongs to the G-band, which is associated with the stretching of all pairs of sp^2 atoms [21]. The second region 2400–3300 cm^{-1} contains a 2D band at 2710 cm^{-1} and a less intensive G*-band at 2445 cm^{-1} and 2D′-band at 3240 cm^{-1}. Among these, the 2D-band at around 2700 cm^{-1} gives information about the turbostraticity of graphite; it is undivided in the case of highly oriented graphite, but in the case of structured graphite or amorphous carbon, the 2D-band is significantly broader.

Raman spectra of etched polymer graphite rods in the graphite range can be seen in Figure 1. The spectra are normalized by dividing each of them by the intensity value at the maximum of its G-band. Three sets of measurements have been carried out with both NaOH and KOH etching solutions. When comparing etchants of the same concentration between each other, the overall peak shapes and positions vary only slightly, with the exception of the first sets with 5 g/40 mL concentration (marked blue). Those sets were analyzed with Raman spectroscopy just two days after the etching, whereas the rest of the etched tips were analyzed later, after one week (red and green lines). The spectra measured after 1 week also do not seem to be influenced by the choice of KOH versus NaOH. Even when comparing spectra by the hardness from the same set, there are just slight differences. Based on the Raman spectra, those samples can be categorized as macroscopic-size graphite flakes.

Only the tips analyzed after two days seem to be unlike others, namely 2B, HB, F, H from 5 g NaOH/40 mL. The D-band of those samples is significantly more intensive; also, the presence of a G-band leg toward higher wavenumbers indicates an increase of defects or the presence of unstable compounds on the etched surface formed during or after the amorphization of graphite during the etching. We suppose this may be a temporary effect, as these features were not visible when measuring the one-week-old etched tips. The absence of a G-band leg in the spectra of samples measured after one week may be related to the degradation or evaporation processes of unstable compounds during the one-week period.

It was found out that the spectra taken at the etched tips of polymer graphite show more crystalline graphite than the unetched side layers of the rods. The amorphization of the side layer graphite flakes most likely happens during the extrusion step of the manufacture of polymer graphite rods. During the tip preparation, the side layer is locally etched away, and more crystalline graphite flakes at the tip are uncovered.

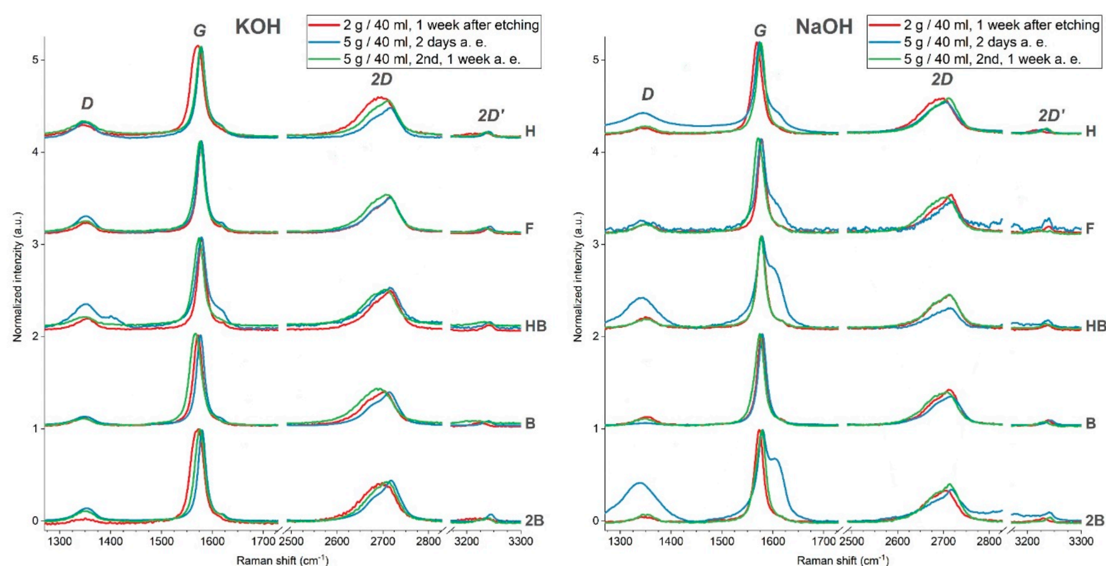

Figure 1. Comparison of Raman spectra of polymer graphite rods of different hardness etched: in 2 g/40 mL (one set) and 5 g/40 mL KOH solution; two sets of experiments (**left**) and secondly (**right**), they were etched in 2 g/40 mL (one set) and 5 g/40 mL NaOH solution. Raman spectra were captured two days or one week after etching, as indicated.

It can be noted that during the etching, the amorphous side layer of the polymer graphite pencil rod, which is probably formed during the extrusion step of manufacture, is etched away, and thus, more crystalline bulk graphite is uncovered after the etching.

The efforts on the subject considering the material composition of various polymer graphite rods and noise analyses of prepared field electron emitters were published earlier [11,15]. The SPM probes and field electron emitters prepared from polymer graphite pencil leads of various hardness values and from different manufacturers are greatly dissimilar in terms of the tip radius and the performance. The admixtures, which are among the main affecting factors, were shown to be rather complex [11].

2.3. Electrochemical Membrane-Etching Method

The membrane-etching method that has been used for a sample preparation shares same electronic configuration as a tip-etching method that takes place in the filled cylinder, which was published earlier [22]. Instead of the cylinder, we are working with a thin membrane contained inside the ring cathode illustrated in Figure 2. Left. In addition, the membrane-etching method is based on the well-known drop-off method of etching that was developed to be used originally for single-crystalline tungsten field-emission tips production. The electrochemical method of tip preparation and sharpening provides good reproducibility of the tip shape and sharpness, as it was reported in the same paper [22].

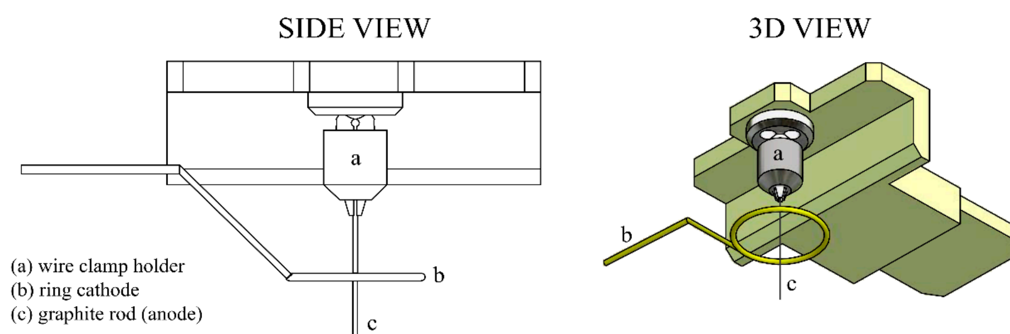

Figure 2. A precise clamp holder extension intended for 0.2–0.4 mm diameter wires' perpendicular fixation toward the electrolyte surface.

The type and concentration of hydroxide (NaOH, KOH) along with the voltage of the etching current allows controlling the tip-etching rate and thus the tip quality. Qualitative parameters are discussed further in the text in more detail.

The potential between the etched rod (anode) and ring that creates a membrane with the alkali electrolyte (cathode) is usually set from 5 to 12 Volts DC. The etching voltage affects the etching speed and linearity of the etching current. This means that for voltages higher than 5 V, the bubbles generation during the etching (on cathode) is more noticeable, resulting in etching current fluctuations and thus affecting the resulting tip regularity and hence the tip reproducibility. The current fluctuations of the etching current are also dependent on the composition of the PG rod. Even for the same brand, each production series has slightly different chemical composition (based on our previous experiences, the difference in composition could be up to 5%).

In order to provide a precise cone-shaped tip and hence to increase production repeatability, it is desirable to work with 5 V voltage despite the etching time being longer in proportion to the increased etching voltage.

As for the mechanical part of the etching set-up, an etching station for probe production made originally by NT-MDT Company (NT-MDT Spectrum Instruments, Moscow, Russia) was used and partially modified by adding a precise clamp-holder to fix the graphite rod during etching. This allowed a precisely perpendicular attachment of the tip toward the electrolyte surface, as it is illustrated in Figure 2, and hence increasing the symmetry of the produced tip. During the etching, one of the graphite rod's ends passes through a conducting diaphragm that keeps a drop of alkali solution, providing the necessary surface tension that cuts the rod as follows. As the bottom part falls off due to its own weight, the electric circuit providing the etching current switches off. The main requirement for adjustment of the existing setup for etching and the sharpening of graphite probes was the positioning of the pencil lead perpendicular to the ring electrode.

3. Results and Discussion

3.1. Description of the Electrochemical Etching

It is not a trivial task to fully represent the whole range of chemical reactions that take place during the electrochemical etching of a graphite pencil lead due to its multicomponent nature. It has been reported [23] that clay minerals are chemically attacked by NaOH, which results in portions of SiO_2, Al_2O_3, MgO, and Fe_2O_3, which they contain, to be etched away. Based on our previous ICP-MS analysis of PG rods, the clay minerals may be from a kaolinite group such as kaolinite or illite. However, chemical reactions of clay with hydroxide are very slow [23] compared to the hydroxide etching of graphite. However, we can be quite certain that at a least part of the graphite undergoes the following reactions illustrated by Equations (1)–(6) in a different proportion, since we were able to observe quite an intense emission of gas throughout the process.

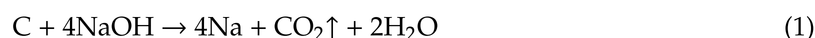

$$C + 4NaOH \rightarrow 4Na + CO_2\uparrow + 2H_2O \quad (1)$$

$$C + 4KOH \rightarrow 4K + CO_2\uparrow + 2H_2O \quad (2)$$

$$C + 2NaOH \rightarrow 2Na + CO\uparrow + H_2O \quad (3)$$

$$C + 2KOH \rightarrow 2K + CO\uparrow + H_2O \quad (4)$$

$$C + NaOH + H_2O \rightarrow H_2\uparrow + Na_2CO_3 \quad (5)$$

$$C + KOH + H_2O \rightarrow H_2\uparrow + K_2CO_3 \quad (6)$$

The bulk of the graphite rod most likely remains unreacted and precipitates on the metal ring in the form of flakes. The gas generation is illustrated in Figure 3 by etching current waveforms.

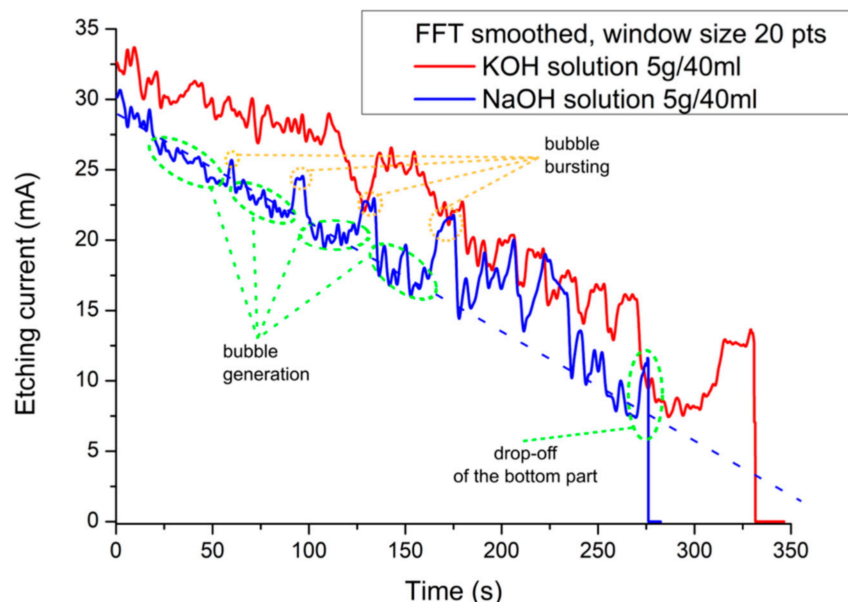

Figure 3. The etching current of a polymer graphite rod using two different etchants.

There are two different waveforms for two different solutions etched by the same etching voltage (5 V) showing a quasiperiodic occurrence of peaks that are connected to the generation of bubbles. When a bubble is generated near the etched tip, the surface that is in connection with the etchant starts to be reduced, and hence the etching current starts decreasing. When the equilibrium between the air pressure and the surface tension of the bubble is broken, the bubble pops whilst increasing the wetted area of the etched rod and, in this way, it increases the etching current. This effect also appears quasiperiodically. The slope of the etching current versus time is usually linear depending on the conductivity of the bulk.

The end of the etching is initiated by a drop-off of the bottom part of the rod steeply decreasing the etching current, which can be identified by a differential detector [22]. Recently, this technique proved to be very effective as an indicator of the drop-off moment for the etching in a volume of electrolyte (oppositely to the membrane etching), where it is more crucial to disconnect the etching current in time in order to prevent tip blunting [22].

3.2. Scanning Electron Microscopy Analysis

The initial analysis of the polymer graphite tip, providing basic tip geometry and topography, was obtained by classical Scanning Electron Microscopy. The SEM measurements were done using 5 keV primary beam energy and the Everhart-Thornley Secondary Electrons detector [11]. Those observations have been done on Koh-i-Noor PG rods of various hardnesses going from H, F, HB, B, to 2B etched by KOH and NaOH etchants, as it is illustrated in Figure 4. The top row within the Figure 4 illustrates tips that were created using KOH. The bottom row of the same figure illustrates the NaOH-etched tips. Both lines are divided into five rows showing one hardness. It is shown that that the tips are, from the point of view of geometry, rather blunt (the diameter is in the micrometer-scale rather than nano-scale); however, they contain multiple sharp tips that are more or less oriented perpendicularly against the tip surface plane. These images also demonstrate that the reproducibility of the tip's surface structure is very low. It can be seen that some of the flakes may have a sufficient field gradient when connected to the negative power supply in the vacuum chamber of the FEM and act as a partial electron source. For this reason, the whole tip is considered more like a Large Area Field Emitter (LAFE) composed of non-homogeneously distributed tips of different sharpness and hence different field enhancement. According to the SEM measurements illustrated in Figure 4, it seems that the surface of the etched rods becomes more sharp for the rods with hardnesses H, F, and partly HB.

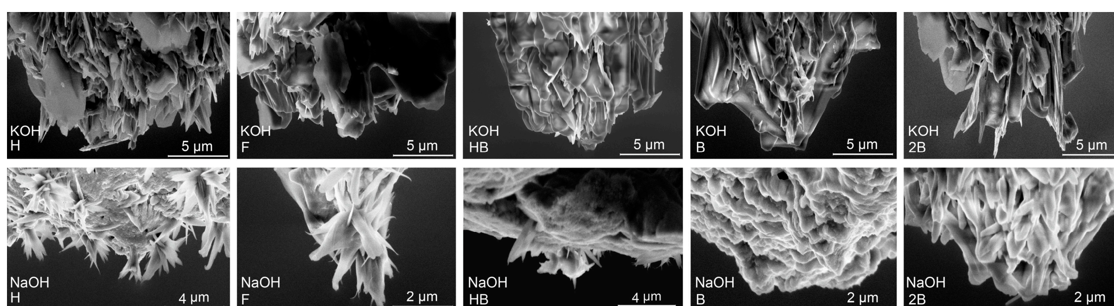

Figure 4. SEM image of the tips of various hardnesses (H, F, HB, B, and 2B) that were produced by electrochemical etching using KOH (**top row**) and NaOH (**bottom row**). The material used for these tips is Koh-i-Noor PG [22].

Due to the charging effects and beam interaction of the surface, the analysis provided by SEM is limited, even at very low energies (incorporating so-called "breaking voltage") and a very low primary electron beam current. In addition, this fact made us use the Field Emission Microscopy technique that proved to be an ideal tool to evaluate field emission properties in general.

3.3. Field Emission Microscopy Analysis

The Field Emission Microscopy (FEM) was originally invented by Erwin W. Müller, creating an analytical technique suitable for use in materials science to investigate molecular surface structures and their electronic properties [24]. In the last five decades, the methods of interpretation of the current–voltage data provided by measuring the total emission current in FEM have been considerable improved and extended mainly by Richard G. Forbes [25], on whose work we base our interpretation of the experimentally obtained I-V data. With consideration to our recent work [11], where polymer graphite tips were suggested to be used as a cheap STM probe, the use of the FEM for tip analysis makes here very good sense, making use of the field emission properties of the materials.

The structure located on the surface has been put in a FEM, inside a strong electric field, whose electric potential was set above the threshold voltage (V > 650 Volts), where the total emission current collected by a scintillator started following the Fowler–Nordheim principles, and so the PG etched tip behaved similar to a field-emission cathode. Experimental data have been obtained in the field emission region that is located above the tunneling current region, and the potential was therefore set approximately above 1000 Volts and measured in steps of 25 V up to 2000 Volts. The effect of the limiting resistor, which is connected serially to protect the cathode tip, started to be apparent approximately above 1700 Volts where the current that was measured by a conductive aluminum layer on the Cerium doped Yttrium aluminum garnet (YAG: Ce) showed currents higher than 5 microamperes. It should not be omitted that the collection efficiency of the scintillator used is approximately 80% comparing to a Faraday cage. Therefore, this setback introduces a systematic error where all our values are measured lower than they really are. Figure 5 presents the I-V characteristics of a polymer graphite electron emitter in diode configuration that was measured in the field electron microscope equipped with a pair of Varian Vaclon Plus 55 Starcell ion pumps.

The emission current between the emitter and Al-coated scintillator was measured by a precise Agilent 33410a digital multimeter enabling extended measurement functions. In order to compensate for the current fluctuations, for each measurement located in between 1 and 2 kV, an integration feature was used. The threshold voltage was found out to be 1050 V. By further increasing the applied voltage, the emission current increases and starts to fluctuate. This behavior is believed to be directly attributed to the degradation of the graphite structure—to be more specific, the ripping and formation of graphite flakes where the electrons do really escape. To assure the optimal pressure needed for the measurement, the setup has to be conditioned first. The FEM setup was pumped down by an ion pump and baked at 150 °C for 8 h, then left to cool, while still being continuously pumped down. This way, the lower range of the ultra-high vacuum was achieved (10^{-7} Pa) prior to the actual measurement.

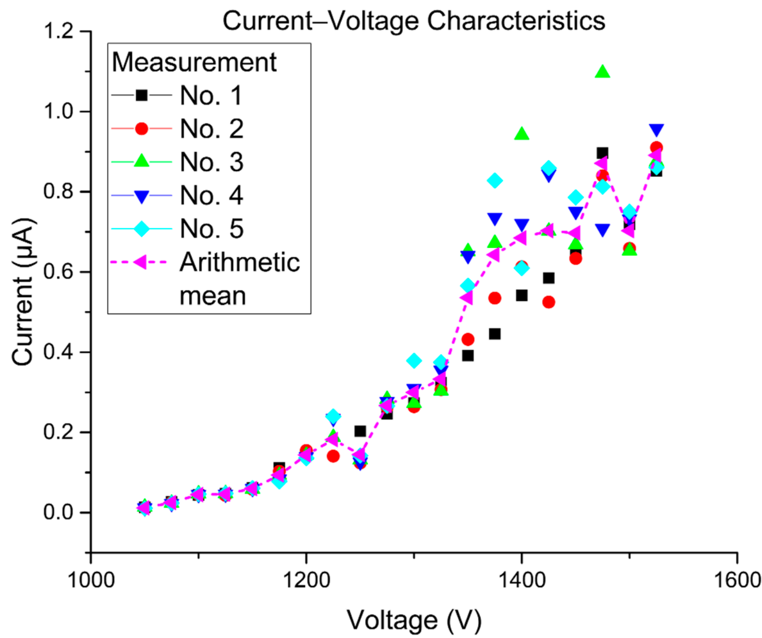

Figure 5. Current–voltage characteristics were recorded for 5 cycles.

Figure 6 presents the FEM pattern image which describes the emission total current and its fluctuations. As shown in the figure, the pattern contains bright small dots that describe multiple locations for the orthogonal to the tip surface that provide a higher number of electrons to reach the scintillator screen; these electrons are believed to have higher energies than other electrons, since they were emitted directly to the screen.

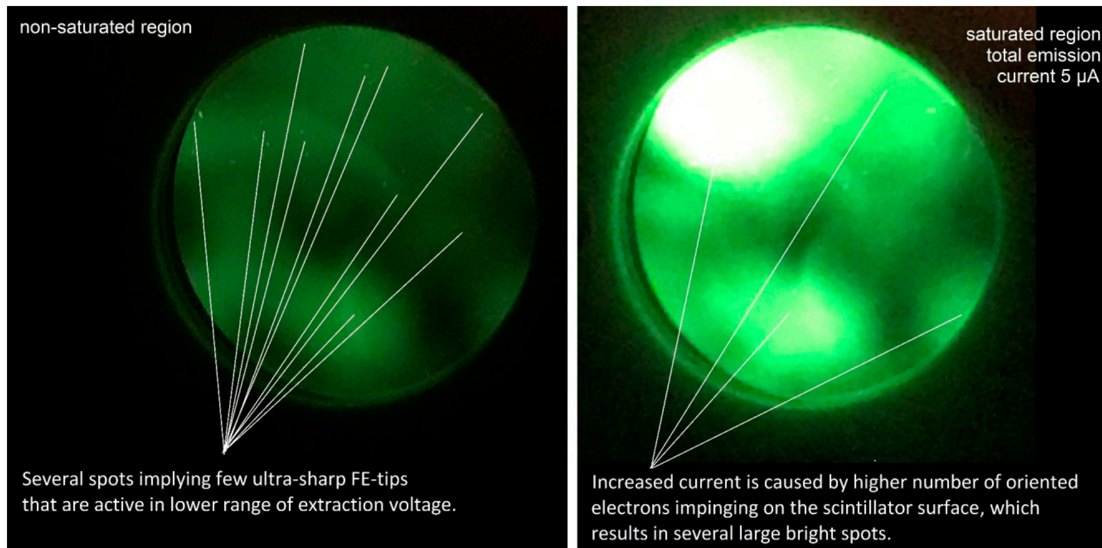

Figure 6. Field Emission Microscope Pattern Images for non-saturated (**left**) and saturated (**right**) region of the I-V plot. The diameter of the scintillator plane here is 31.5 mm.

As mentioned earlier, the surface of the tip is considered to be a Large Area Field Emitter (LAFE), and to completely analyze this type of emitter, we need to extract two important characterization parameters which are the Macroscopic Field Enhancement Factor M – FEF (γ_M) and the Formal Area Efficiency (α_f^{SN}) for Schottky–Nordheim (SN) as a potential barrier. In order to do these analyses, the Murphy–Good plots [25] are used to analyze the obtained data and to extract the characterization parameters for the emitter.

These plots take the form of ln(I/V$^{\kappa}$) versus 1/V, where κ is a function of the work function (φ) for the used material (κ =1.22719212 for φ = 4.5 eV). Figure 7 presents the analysis plots for the 5 periods for the tested tip, and Table 1 presents the extracted data from these plots. Table 1 illustrates the extracted parameters of the emitter from the Murphy–Good plots. Here, the R is the apex radius of the emitter, $\left\{A_f^{SN}\right\}^{extr}$ is the extracted formal emission area, ξ_C^{extr} is the extracted characteristic voltage conversion length that describes the effective range of the local electrostatic field at the surface of the tip, $\left\{\alpha_f^{SN}\right\}^{extr}\left[= \left\{A_f^{SN}\right\}^{extr}/A_M\right]$ is the extracted formal area efficiency, which describes as the ration between the effective emission area and the real macroscopic area of the effective surface, $\gamma_M^{extr}\left[= d_M/\xi_C^{extr}\right]$ is the macroscopic field enhancement factor with $d_M = 1$ mm being the system distance used to define the field enhancement factor, and $A_M = 1590$ µm^2 is the large area field emitter macroscopic area. The macroscopic area was calculated by integrating the surface area element of the sphere that is presented in Figure 8, where:

$$A_M = R^2 \int_0^{\pi/3} Sin[\theta] d\theta \int_0^{2\pi} d\varphi.$$

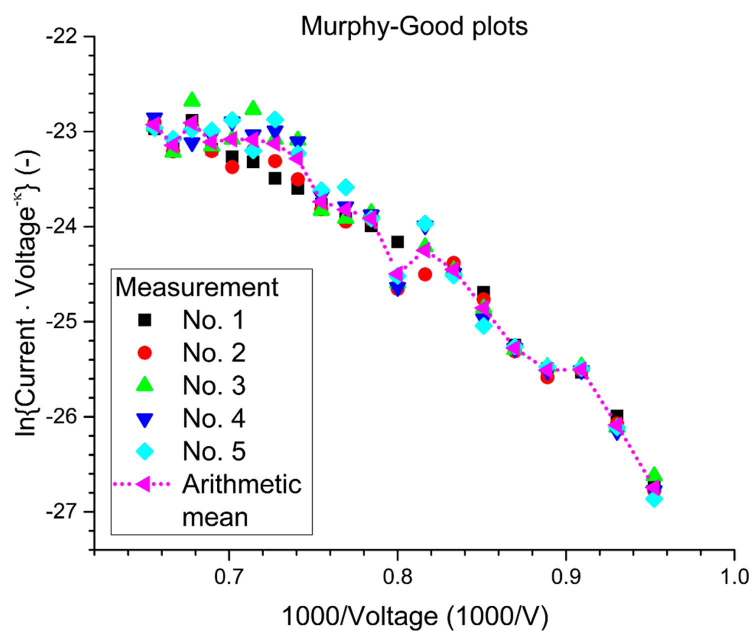

Figure 7. The analysis plots for the five cycles of the tested tip.

Table 1. Extracted emitter's parameters were obtained from the Murphy–Good plots.

Measure n.	Fitting Points x [V^{-1}]	Fitting Points y [Np]	R [µm]	Φ [eV]	Slope [Np.V]	$\{A_f^{SN}\}^{extr}$ [nm^2]	ξ_C^{extr} [nm]	$\{\alpha_f^{SN}\}^{extr}\times10^{-10}$	$\gamma_M^{extr}\times10^3$
1	0.0007 0.0009	−22.1 −25.5	22.5	4.5	−17000	1.0350	260.71	6.509625	3.8357
2	0.0007 0.0009	−22.9 −25.5	22.5	4.5	−13000	0.9096	199.36	5.720596	5.0159
3	0.0007 0.0009	−22.7 −25.5	22.5	4.5	−14000	1.6424	214.70	10.32977	4.6577
4	0.0007 0.0009	−23.1 −25.5	22.5	4.5	−12000	1.6112	184.03	10.13346	5.4339
5	0.0007 0.0009	−23 −25.5	22.5	4.5	−12500	1.7456	191.70	10.97855	5.2166
Mean	0.0007 0.0009	−23 −25.5	22.5	4.5	−12500	1.2932	191.70	8.133221	5.2166

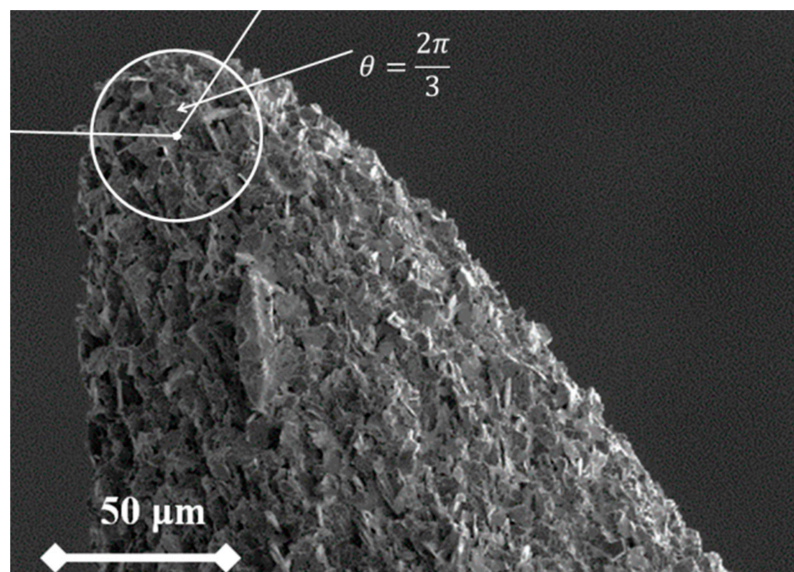

Figure 8. Calculation of the macroscopic area. For the illustration, the HB polymer graphite (PG) rod image was used.

4. Conclusions

This paper presents the field emission behavior of field emission tips containing multiple graphite flakes that are behaving similar to particular electron sources on a single tip. To obtain a sample, we have adapted a device using a well-established method of electrochemical etching to create a tip from a composite material based on graphite flakes in a membrane of alkali etchant. The electrochemical setup has been described along with particular chemical processes taking place during the process of PG etching.

Before the analysis of the field emission properties, it was necessary to describe the effect of the electrochemical etching and to evaluate multiple PG nanocomposites that are currently commercially available. The Raman spectroscopy that was used for the evaluation proved that after the etching, there may be a temporal change of surface properties indicated by a strong increase of D-bands and the presence of a G-band leg, which changes after a longer period of one week. Other than that, Raman spectra of graphite of etched tips do not show any conspicuous differences in peak shapes and positions. The Raman spectroscopy bands related to clay minerals are not visible. The topographic information of the tip surface was provided by Scanning Electron Microscopy and Field Emission Microscopy. The SEM showed multiple graphite flakes originated from the PG rod and oriented perpendicularly toward the rod, which has been lately put in a correlation to the bright spots on the FEM screen showing the areas containing particularly emitting surface of the PG tip.

The field emission analysis is based on a finding presented in our previous work [11] reporting favorable properties' tunneling behavior. For our analysis, we have increased the current density and inter-electrode distance, transferring the work mode to the field emission region, where it is possible to take advantage of the recent methodology developed by Forbes [25–27] and hence to fully characterize the tip as for the field-emission point of view.

In order to analyze the field emission properties, the FEM was used to examine the tip surface and to describe the field-emission behavior of graphite flakes present on the tip apex. The analysis is based on current–voltage data measured in the classical FEM using a recent methodology based on Forbes' Field Emission Orthodoxy Test, which has been used to prove the quantum-tunneling nature of the measured current. This analysis also implied the existence of multiple sources (sharp tips) that are sufficiently sharp to achieve a field gradient strong enough to provide the field emission current. From Table 1, the values of the formal emission area efficiency are in the range of ($\times 10^{-10}$). So, the total effective emission area was much lower than the real macroscopic area, which is in agreement with

the hypothesis that the effective emission was from the flakes' apexes as shown by the bright dots in Figure 6. This is in perfect agreement with the topographical analysis provided by the SEM showing multiple flakes oriented perpendicularly toward the tip surface. The latter arrangement behaves similarly to general LAFE providing extended tunneling capabilities even for a tip of a relatively blunt diameter.

Author Contributions: Conceptualization, A.K. and D.S.; Formal analysis, R.D., D.B. and M.M.A.; Investigation, A.K., R.D., D.B., M.H., P.K. and M.M.; Methodology, A.K. and D.S.; Validation, D.S.; Writing—original draft, A.K. and D.S.; Writing—review and editing, D.B., P.K. and M.S.M. All authors have read and agreed to the published version of the manuscript.

Funding: We acknowledge the Ministry of Education, Youth and Sports of the Czech Republic under the project CEITEC 2020 (LQ1601), the Internal Grant Agency of Brno University of Technology, grant No. FEKT-S-20-6352, the CAS (RVO:68081731), the Ministry of the Interior of the Czech Republic (project. No. VI20192022147) and CEITEC Nano Research Infrastructure supported by MEYS CR (LM2018110).

Conflicts of Interest: The authors declare no conflict of interest. The funders had no role in the design of the study; in the collection, analyses, or interpretation of data; in the writing of the manuscript, or in the decision to publish the results.

References

1. Vishnu, N.; Gopalakrishnan, A.; Badhulika, S. Impact of intrinsic iron on electrochemical oxidation of pencil graphite and its application as supercapacitors. *Electrochim. Acta* **2018**, *269*, 274–281. [CrossRef]
2. Torrinha, A.; Amorim, C.G.; Montenegro, M.; Araujo, A.N. Biosensing based on pencil graphite electrodes. *Talanta* **2018**, *190*, 235–247. [CrossRef]
3. Azadmehr, F.; Zarei, K. Ultrasensitive determination of ceftizoxime using pencil graphite electrode modified by hollow gold nanoparticles/reduced graphene oxide. *Arab. J. Chem.* **2020**, *13*, 1890–1900. [CrossRef]
4. Kaspar, P.; Sobola, D.; Dallaev, R.; Ramazanov, S.; Nebojsa, A.; Rezaee, S.; Grmela, L. Characterization of Fe_2O_3 thin film on highly oriented pyrolytic graphite by AFM, Ellipsometry and XPS. *Appl. Surf. Sci.* **2019**, *493*, 673–678. [CrossRef]
5. Purushothama, H.T.; Nayaka, Y.A.; Vinay, M.M.; Manjunatha, P.; Yathisha, R.O.; Basavarajappa, K.V. Pencil graphite electrode as an electrochemical sensor for the voltammetric determination of chlorpromazine. *J. Sci. Adv. Mater. Devices* **2018**, *3*, 161–166. [CrossRef]
6. Jin, J.; Peng, X.; Jiang, J.; Meng, X.; Zhao, W. Frictional characteristics of impregnated graphite with different graphitization degree versus chromium stainless steel under varying PV values. *Tribol. Int.* **2019**. [CrossRef]
7. Urban, F.; Lupina, G.; Grillo, A.; Martucciello, N.; Di Bartolomeo, A. Contact resistance and mobility in back-gate graphene transistors. *Nano Express* **2020**, *1*, 010001. [CrossRef]
8. Di Bartolomeo, A.; Giubileo, F.; Iemmo, L.; Romeo, F.; Russo, S.; Unal, S.; Passacantando, M.; Grossi, V.; Cucolo, A.M. Leakage and field emission in side-gate graphene field effect transistors. *Appl. Phys. Lett.* **2016**, *109*, 023510. [CrossRef]
9. Shao, X.; Srinivasan, A.; Ang, W.K.; Khursheed, A. A high-brightness large-diameter graphene coated point cathode field emission electron source. *Nat. Commun.* **2018**, *9*, 1–8. [CrossRef]
10. Mousa, M.S.; Daradkeh, S.I.; Ali, E.S.B. Comparative Study of Field Electron Emission from Single-Walled Carbon Nanotube and Multi-Walled Carbon Nanotube Mounted on Tungsten. *Jordan J. Phys.* **2019**, *12*, 7–15.
11. Knapek, A.; Sobola, D.; Burda, D.; Danhel, A.; Mousa, M.; Kolarik, V. Polymer Graphite Pencil Lead as a Cheap Alternative for Classic Conductive SPM Probes. *Nanomaterials* **2019**, *9*, 1756. [CrossRef] [PubMed]
12. Purushothama, H.T.; Arthoba Nayaka, Y. Pencil graphite electrode based electrochemical system for the investigation of antihypertensive drug hydrochlorothiazide: An electrochemical study. *Chem. Phys. Lett.* **2019**, *734*. [CrossRef]
13. Riman, D.; Prodromidis, M.I.; Jirovsky, D.; Hrbac, J. Low-cost pencil graphite-based electrochemical detector for HPLC with near-coulometric efficiency. *Sens. Actuators B Chem.* **2019**, *296*, 126618. [CrossRef]
14. Navratil, R.; Kotzianova, A.; Halouzka, V.; Opletal, T.; Triskova, I.; Trnkova, L.; Hrbac, J. Polymer lead pencil graphite as electrode material: Voltammetric, XPS and Raman study. *J. Electroanal. Chem.* **2016**, *783*, 152–160. [CrossRef]

15. Knapek, A.; Horacek, M.; Chlumska, J.; Kuparowitz, T.; Sobola, J.; Sikula, J. Preparation and noise analysis of polymer graphite cathode. *Metrol. Meas. Syst.* **2018**, *25*, 451–458. [CrossRef]
16. Nagarajan, S.; Vairamuthu, R.; Angamuthu, R.; Venkatachalam, G. Electrochemical fabrication of reusable pencil graphite electrodes for highly sensitive, selective and simultaneous determination of hydroquinone and catechol. *J. Electroanal. Chem.* **2019**, *846*, 113156. [CrossRef]
17. Kim, Y.; Sung, A.; Seo, Y.; Hwang, S.; Kim, H. Measurement of hardness and friction properties of pencil leads for quantification of pencil hardness test. *Adv. Appl. Ceram.* **2016**, *115*, 443–448. [CrossRef]
18. Sakia, B.J.; Parthasarathy, G.; Borah, R.R.; Borthakur, R. Raman and FTIR Spectroscopic Evaluation of Clay Minerals and Estimation of Metal Contaminations in Natural Deposition of Surface Sediments from Brahmaputra River. *Int. J. Geosci.* **2007**, *7*, 873–883. [CrossRef]
19. Kloprogge, J.T. Raman Spectroscopy of Clay Minerals. *Infrared Raman Spectrosc. Clay Miner.* **2017**, 150–199. [CrossRef]
20. Chen, K.; Xue, D. From graphite-clay composites to graphene electrode materials: In-situ electrochemical oxidation and functionalization. *Mater. Res. Bull.* **2017**, *96*, 281–285. [CrossRef]
21. Naemura, K.; Ikuta, D.; Kagi, H.; Odake, S.; Ueda, T.; Ohi, S.; Kobayashi, T.; Svojtka, M.; Hirajima, T. Diamond and Other Possible Ultradeep Evidence Discovered in the Orogenic Spinel-Garnet Peridotite from the Moldanubian Zone of the Bohemian Massif, Czech Republic. *Ultrah. Press. Metamorph.* 2011. [CrossRef]
22. Knápek, A.; Sýkora, J.; Chlumská, J.; Sobola, D. Programmable set-up for electrochemical preparation of STM tips and ultra-sharp field emission cathodes. *Microelectron. Eng.* **2017**, *173*, 42–47. [CrossRef]
23. Carroll, D.; Starkey, H.C. Reactivity of Clay Minerals with Acids and Alkalies. *Clays Clay Miner.* **1971**, *19*, 321–333. [CrossRef]
24. Drechsler, M. Erwin Müller and the early development of field emission microscopy. *Surf. Sci.* **1978**, *70*, 1–18. [CrossRef]
25. Forbes, R.G. The Murphy–Good plot: A better method of analysing field emission data. *R. Soc. Open Sci.* **2019**, *12*, 190912. [CrossRef]
26. Allaham, M.M.; Forbes, R.G.; Knapek, A.; Mousa, M.S. Implementation of the orthodoxy test as a validity check on experimental field emission data. *J. Electr. Eng. Slovak* **2020**, *71*, 37–42. [CrossRef]
27. Allaham, M.M.; Forbes, R.G.; Mousa, M.S. Applying the Field Emission Orthodoxy Test to Murphy-Good Plots. *Jordan J. Phys.* **2020**, *13*, 101–111.

© 2020 by the authors. Licensee MDPI, Basel, Switzerland. This article is an open access article distributed under the terms and conditions of the Creative Commons Attribution (CC BY) license (http://creativecommons.org/licenses/by/4.0/).

nanomaterials

MDPI

Article

Polymer Graphite Pencil Lead as a Cheap Alternative for Classic Conductive SPM Probes

Alexandr Knápek [1,*], Dinara Sobola [2,3], Daniel Burda [1,2], Aleš Daňhel [4], Marwan Mousa [5] and Vladimír Kolařík [1]

1 Institute of Scientific Instruments of the Czech Academy of Sciences, Královopolská 147, 612 64 Brno, Czech Republic; burda@isibrno.cz (D.B.); kolariq@isibrno.cz (V.K.)
2 Department of Physics, Faculty of Electrical Engineering and Communication, Brno University of Technology, Technická 8, 616 00 Brno, Czech Republic; sobola@vutbr.cz
3 Central European Institute of Technology, Brno University of Technology, Technická 10, 616 00 Brno, Czech Republic
4 Institute of Biophysics of the Czech Academy of Sciences, Královopolská 135, 612 65 Brno, Czech Republic; danhel@ibp.cz
5 Department of Physics, Mu'tah University, Al-Karak 61710, Jordan; mmousa@mutah.edu.jo
* Correspondence: knapek@isibrno.cz; Tel.: +420-5415-142-58

Received: 13 November 2019; Accepted: 6 December 2019; Published: 10 December 2019

Abstract: This paper presents polymer graphite (PG) as a novel material for the scanning tunneling microscopy (STM) probe. Conductive PG is a relatively modern nanocomposite material used for micro-pencil refills containing a polymer-based binding agent and graphite flakes. Its high conductivity and immunity against surface contamination, with a low price, make it seem like a highly suitable material for electrode manufacturing in general. For the tip production, three methods were developed and are further described in the paper. For the production, three commercially available polymer graphite rods were used. Each has been discussed in terms of performance within the tunneling microscope and within other potential applications.

Keywords: scanning tunneling microscopy; sharp tip formation; graphite

1. Introduction

Graphite is a natural mineral and one of carbon's allotropes that possesses a layered structure. It's soft, malleable, and greasy to the touch [1]. Several unique properties make graphite a widely used material: production of electrodes, lubricants, fillers of plastics, neutron moderators in nuclear reactors, and many other applications [2,3]. Graphite is also used in the production of aluminum, synthetic diamonds, and in thermal protection of warheads of ballistic missiles and space modules. Classical pencil leads are made from a mixture of white clay (kaolinite) and graphite [4].

The classical pencil lead in its modern form was invented in 1794 by Nicolas Jacques Conte, a talented French scientist and inventor. Conte developed a recipe for mixing graphite with white clay and produced high-quality rods from these materials. Strength was achieved by heat treatment, at which the clay hardens [4]. Varying the proportion of the mixture made it possible to make rods of different hardness. The composition of modern leads includes polymers, which make it possible to achieve the desired combination of hardness, strength, and elasticity. Carbon itself as well as polymer graphite (PG) also show field-emission behavior as it was described in previous papers [5–7]. Main characteristics of polymer graphite which could be convenient for usage in scanning probe microscopy (SPM) are: heat resistance, considerable durability, resistance to mechanical and hydraulic stress, and, last but not least, corrosion resistance [8]. Also, it has been previously reported that polymer graphite

contains up to 80% of sp^3 hybridized carbon, moving its properties more towards graphene-based structure [9,10].

For our study, we have chosen a scanning tunneling microscopy (STM) to demonstrate the use of pencil lead in conductive SPM techniques [8]. Whether it's a study of topography or electrical characteristics, the scanning probe microscopy is an integral part of modern research [11,12]. Possibilities of SPM are defined by both set-up configuration and sample-tip interface [13]. In order to achieve maximum resolution by STM, it is necessary to obtain an extremely sharp conductive tip serving as a probe scanning over a sample surface. The STM probes, which are currently used, are made traditionally of platinum-iridium alloy in proportions of 90:10 or 70:30 (Pt:Ir). This composition benefits from the chemical stability of platinum and an increased hardness. The main disadvantage of this material is its high price.

Another commonly used material is tungsten (W) which is used mainly for its high melting point, good conductivity, and a relatively easy way of creating the sharp tip. This is done mostly by incorporating an electrochemical etching method, where the etched tungsten wires dissolute in an alkaline electrolyte yielding a sharp tip by the increased tension of the electrolyte near its surface [14]. Tungsten is still quite an expensive material compared to the graphite pencil lead, even when working with the polycrystalline wire. Tungsten also tends to create surface oxide which blunts the tip and hence decreases the scanning resolution. From the above mentioned factors, the development of new probes is important for surface science because STM is a high-accuracy method for characterization of micromorphology and nanomorphology of surface, defects and fractures of surface, measurements of nano-scaled structures, and, last but not least, understanding mechanisms on the surface [15].

2. Materials and Methods

2.1. Materials

The market of pencil leads consists of several popular brands of mechanical pencils (e.g., Pilot, Erich Krause, Proff, Parker, Koh-i-Noor Hardtmuth, Stabilo, Pentel, Staedtler, Faber-Castell, Rotring, Bic, Conte, Index, Lamy, Constructor, and many others). The production of carbon pencils is spread over the world and each product is based on a special fabrication technology. For our experiments, we have used three different brands of polymer graphite rod, in particular: Koh-i-Noor, Staedtler, and Pentel Hi-polymer E.

2.2. Equipment and Methods of Analysis

For the analysis, several analytical methods were used, providing information based on different physical principles. Such a complementary approach allows for achieving reliable conclusions on the pencil lead's chemical composition.

Raman spectroscopy was carried out in the inVia Spectrometer (Renishaw, Wotton-under-Edge, UK) utilizing green laser (DPSS 532 nm, P = 30 mW) and the exposure of 10 × 10 s with a 50× objective. The Raman spectra were evaluated and fitted with Lorentzian peak shapes using Fityk 1.3.1 software (Marcin Wojdyr, Warsaw, Poland). X-ray photoelectron spectroscopy (XPS) measurements were carried out with Kratos Supra with monochromatic Al-Kα source and photon energy of 1486.7 eV. The survey scans were measured within the binding energy range of 0–1200 eV with the step of 1.0 eV. The spectra that were referenced were evaluated in CasaXPS 2.3.22PR1 software (Casa Software Ltd., London, UK) which allows calculation of atomic percent and many different parameters like Full width at half maximum (FWHM), deconvolution for the peak.

The Scanning electron microscopy (SEM) and Energy Dispersive X-Ray Analysis (EDX) measurements were carried out in Tescan Lyra3 scanning electron microscope with an in-built Aztec SSD detector (Oxford Instruments, Abingdon-on-Thames, UK). The EDX spectra were obtained with accelerating voltage of 15 kV at a working distance of 9 mm, view the field of 20 μm, and spot size of 5.5 nm. The ICP-MS measurements were carried out in Agilent 7900 (Santa Clara, CA, USA) that is a

quadrupole system offering high matrix tolerance, wide dynamic range, and an effective interference removal for trace elements across most typical applications.

2.2.1. Raman Spectroscopy

The Raman spectra of pencil leads show peaks common in polycrystalline graphite. The G peak was observed at 1580 cm^{-1}, which arises from the bond stretching of all pairs of sp^2 hybridized atoms; the D peak is around 1360 cm^{-1}, which becomes visible in relation with the defects in sp^2 graphite sheets, in polycrystalline graphite, and graphite-like materials with crystalline defect; the D peak overtone called 2D peak is observed at around 2690 cm^{-1}, which on polycrystalline graphite samples splits into two components: $2D_1$ and $2D_2$ [16]. The above-mentioned measurements are illustrated in Figure 1.

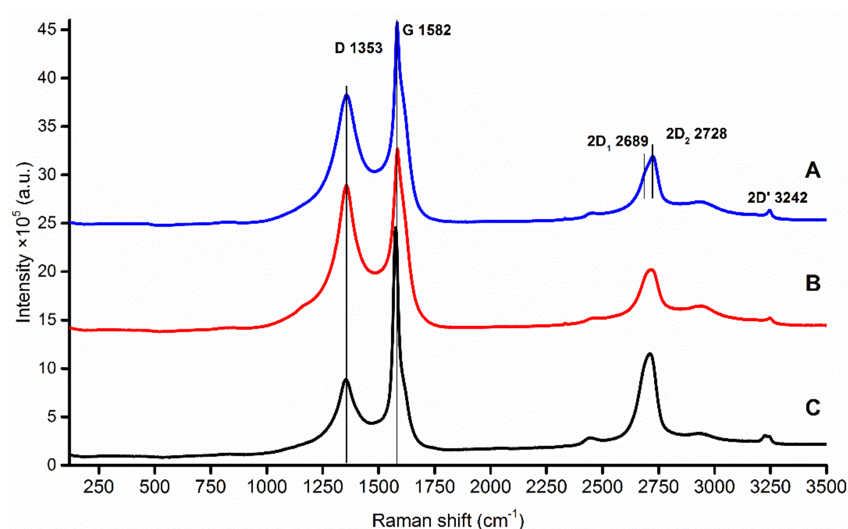

Figure 1. Stacked Raman spectra of each sample: (**A**) Pentel Hi-Polymer E (blue); (**B**) Koh-i-Noor (red); (**C**) STAEDTLER (black).

D/G and $2D_1/2D_2$ intensity ratios give information about the estimated size and turbostraticity of layers of polycrystalline graphite flakes, which may play a significant role in the fabrication of sharp STM tip. Properties of analysed pencil leads include Raman I_D/I_G intensity ratio, calculated crystallite size, and relative atomic concentration (derived from XPS measurements) are illustrated in Table 1.

Table 1. Properties of analysed pencil leads, Raman I_D/I_G intensity ratio, calculated crystallite size, and relative atomic concentration derived from XPS measurements.

	Raman		EDX Contaminants		XPS [Atomic %]				
Sample	**I_D/I_G**	**Crystallite Size [nm]**	**Side Surface**	**Spot at the Rod Axis**	**C**	**O**	**Si**	**Fe**	**F**
Pentel	0.60	63	O, Na, Si, P, Fe	O, Na, Si, P, Zn	65.3	23.4	8.8	0.6	1.3
Koh-i-Noor	0.36	101	O, Na, Mg, Al, Si, P, S, Cl, K, Ca, Fe	O, Na, Mg, Al, Si, P, S, Cl, K, Ca, Fe	67.2	23.9	8.0	0.7	-
Staedtler	0.35	102	O, Na, Mg, Al, Si, S, Cl, Ca	O, Na, Si, S, Cl, Ca	48.2	24.1	15.6	0.8	1.3

2.2.2. EDX and XPS Analysis

The pencil leads were also thoroughly investigated using EDX and XPS with the aim to obtain complex information about both the surface and the bulk properties. Compositional analysis of different carbon leads was presented originally by Kariuki [17] and Navratil et al. [10].

Here, we compare XPS spectra of each tip by measuring in the area where the lead has been etched in a hydroxide solution versus in the unprocessed area of the lead, yielding several double spectra for each sample presented in Figure 2. The background for the all etched areas tends to be higher than for the unprocessed areas. It was observed that Koh-i-Noor pencil leads are more stable against wet etching since the spectra before and after etching show more similarities to each other (small background for etched area, the same shape of peaks) compared to Staedtler and Pentel Hi-Polymer E leads. Furthermore, XPS analysis revealed iron contamination present at the side surface of the pencil leads, most likely due to the specific method of fabrication of those pencil leads.

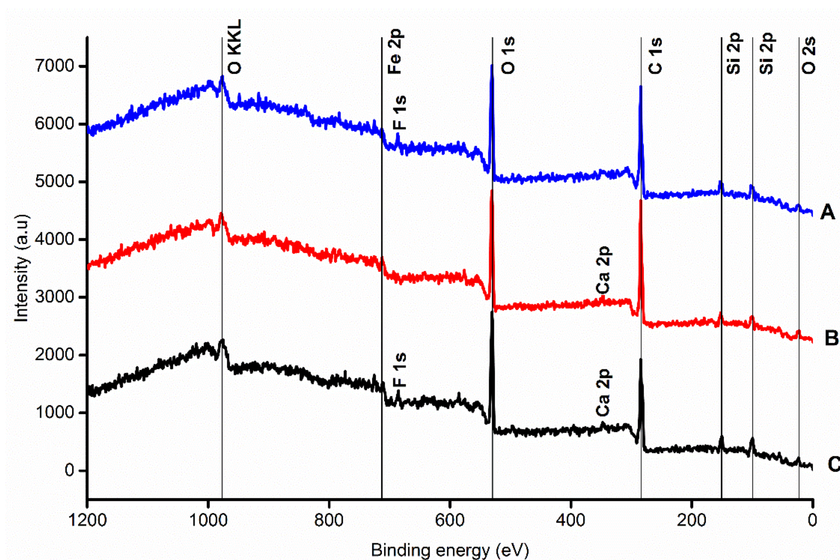

Figure 2. XPS spectra of each sample: (**A**) Pentel Hi-Polymer E (blue); (**B**) Koh-i-Noor (red); (**C**) Staedtler (black).

The EDX spectra were obtained from two different spots for each type of pencil lead, from the side surface of the rod and from the rod axis after breaking off a small piece of it. These measurements give valuable information about the surface and bulk; the measurements taken at the rod axis are illustrated in Figure 3. Quantitatively, Pentel Hi-Polymer E pencil lead elemental composition significantly differs from Koh-i-Noor and Staedtler leads, which both use clay-like binder containing sulfur. These findings are in good agreement with the results presented in [10].

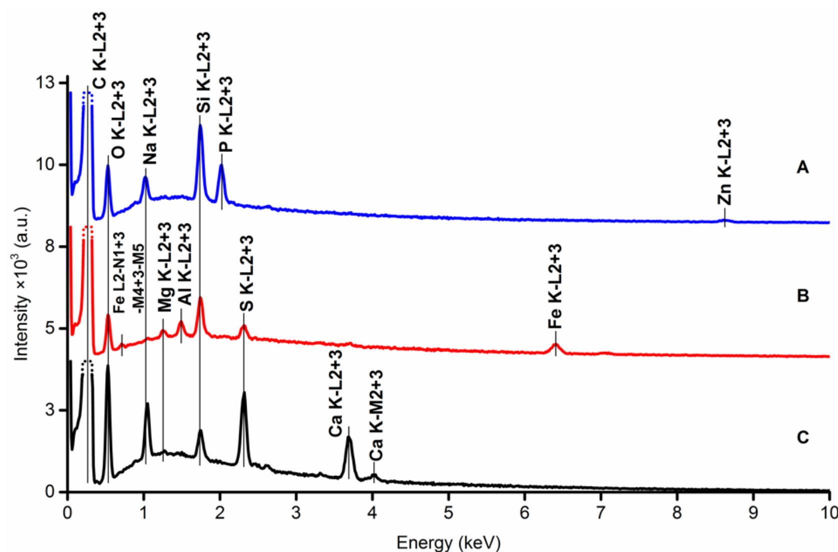

Figure 3. EDX measurements from the spot at the rod axis of Pentel Hi-Polymer E (**A**); Koh-i-Noor (**B**); STAEDTLER (**C**) pencil leads.

2.2.3. ICP-MS Analysis

The preparation of a sample for ICP-MS analysis was done firstly by grinding of micro-pencil rods obtaining fine-grained powder. Following this, 10 milligrams of the powder was placed in a 2.5 mL of polypropylene in an Eppendorf micro tube along with: 250 microliters of concentrated sulfuric acid (96%) containing V_2O_5 serving as a catalytic converter, and concentrated perchloric acid (71%), both practical grade chemicals. These suspensions were sonicated for 10 min in a laboratory ultrasound sonicator, then heated to 90 °C and shaken at 700 rpm for 30 min using an Eppendorf ThermoMixer (Eppendorf AG, Hamburg, Germany). After this procedure, the sample was diluted with 10 mL of distilled water and poured into a 20 mL syringe equipped with a nylon membrane filter (0.45 µm) from which it was injected into a 50 mL volumetric flask. After that, 3.85 mL of concentrated nitric acid (65%) was added to the volumetric flask in order to obtain a 5% solution after adding a particular volume of distilled water. Three 3 Ml samples were taken away from the solution and used for Inductively coupled plasma mass spectrometry (ICP-MS) analysis yielding 3 sets of results that were averaged. From these measurements, the arithmetic mean value and the standard deviation were calculated. The results are illustrated in Table 2.

The obtained results illustrated in the Table 2 are in agreement with the results provided by the EDX and XPS analyses. Elements like C, Cl, S, and O cannot be detected using ICP-MS. Also, phosphorus (P) and silicon (Si) also cannot be detected in our setup due the absence of particular measurement standards. Between particular brands, there is a significant difference in chemical composition of the contents, in particular the elements: Na, Li, Mg, Fe, and Zn, which is, in our opinion, caused by a specific composition of a bonding agent for each brand.

From the electrochemical point of view, Staedtler seems to be most suitable since the majority of the components are more electrochemically inert; in particular, we are referring to the elements: Na, Mg, Ca, and Fein opposition to the Koh-i-Noor brand that contains a high amount of heavy metals (Al, Ti, Cr, Mn, Co, Ni, Cu, As, and Bi) which are often more electrochemically active (i.e., whose cations are reducible at low potentials, starting at 0–1.2 V).

Table 2. Results of quantitative determination of 26 elements contained in micro-pencil rods by the means of chemical dilution using acids and an additional analysis of ICP-MS.

ppm = ng·mg^{-1}	Staedtler		Koh-i-Noor		Pentel Hi-Polymer E	
Element	**Average (ppm)**	**SD**	**Average (ppm)**	**SD**	**Average (ppm)**	**SD**
Li	<0.000	N/A	<0.000	N/A	404.331	5.519
Be	<0.000	N/A	<0.000	N/A	<0.000	N/A
B	<0.000	N/A	<0.000	N/A	<0.000	N/A
Na	2604.058	425.603	<0.000	N/A	<0.000	N/A
Mg	126.655	32.525	256.163	9.741	<0.000	N/A
Al	<0.000	N/A	302.484	20.995	33.291	7.363
K	<0.000	N/A	<0.000	N/A	<0.000	N/A
Ca	296.026	53.874	79.924	34.929	<0.000	N/A
Ti	2.810	0.929	49.382	5.577	3.685	1.313
V	<0.000	N/A	262.205	41.036	<0.000	N/A
Cr	7.240	0.751	5.273	0.209	5.571	0.857
Mn	10.734	1.252	43.852	0.869	2.166	1.112
Fe	168.076	48.795	4186.431	30.789	346.161	36.538
Co	<0.000	N/A	5.192	0.065	<0.000	N/A
Ni	3.978	1.266	11.485	0.380	3.979	1.023
Cu	<0.000	N/A	46.328	3.203	<0.000	N/A
Zn	<0.000	N/A	<0.000	N/A	2945.454	38.845
As	<0.000	N/A	1.079	0.144	<0.000	N/A
Se	<0.000	N/A	<0.000	N/A	<0.000	N/A
Sr	2.475	0.967	1.326	0.669	1.938	1.542
Mo	0.563	0.097	34.617	0.430	2.689	0.096
Cd	<0.000	N/A	<0.000	N/A	<0.000	N/A
Ba	3.594	1.925	6.339	1.544	73.393	2.737
Tl	<0.000	N/A	<0.000	N/A	<0.000	N/A
Pb	<0.000	N/A	<0.000	N/A	<0.000	N/A
Bi	0.451	0.033	2.405	0.026	45.076	0.585

2.3. Tip Aroduction

2.3.1. Electrochemical Etching

The basic method that has been tested for preparation of the graphite sharp tip is based on electrochemical etching, as it was published earlier [14]. This method is well known and also used for field-emission microscope production. The electrochemical method of tip preparation and sharpening provides good reproducibility of the tip shape and sharpness. Type and concentration of hydroxide (NaOH, KOH) allow to control the tip quality. An electrochemical etching station for probe production of NT-MDT Company (Moscow, Russia) was used. The device was partially modified by adding a precise clamp-holder to fix the graphite rod during etching. The potential between two electrodes (one is a graphite rod and the other is a metal ring) is 12 V with alternative current.

This allows a precisely perpendicular attachment of the tip towards the electrolyte surface, as illustrated in Figure 4, and hence increases the symmetry of the produced tip. During the etching, one of the graphite rod ends passes through a conducting diaphragm that keeps a drop of alkali solution, providing necessary surface tension cutting the rod as follows. As the bottom part falls down due to its own weight, the electric circuit providing the etching current switches off. The main requirement for adjustment of the existing setup for etching and sharping of graphite probes was the positioning of the pencil lead perpendicular to the ring electrode.

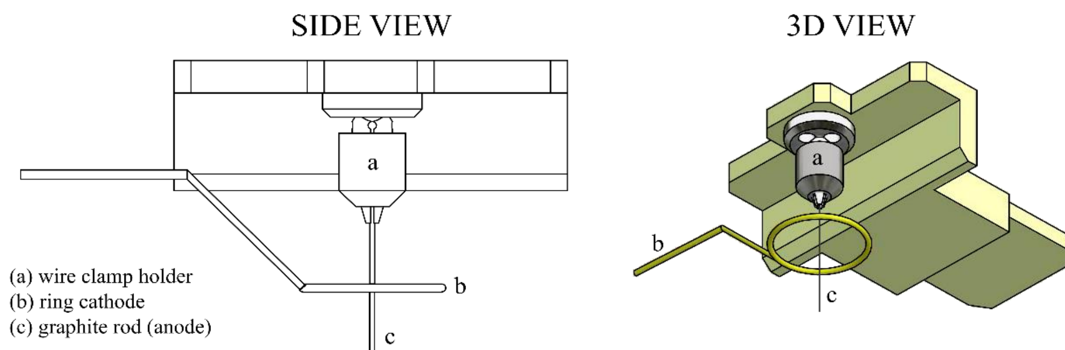

Figure 4. Precise clamp holder extension intended for 0.2–0.4 mm diameter wires providing precisely perpendicular fixation towards the electrolyte surface.

From the following figures, it can be seen that for each material the produced tip is of a different shape based on different materials of the used rod. The tips were made of three different micropencil brands: Pentel Hi-Polymer 0.3 HB (Figure 5), Koh-i-Noor 0.3 HB (Figure 6), and Staedtler 0.3 HB (Figure 7). In the left part of each figure, the overall view of the tip is shown. The surface detail is illustrated in a right part of image.

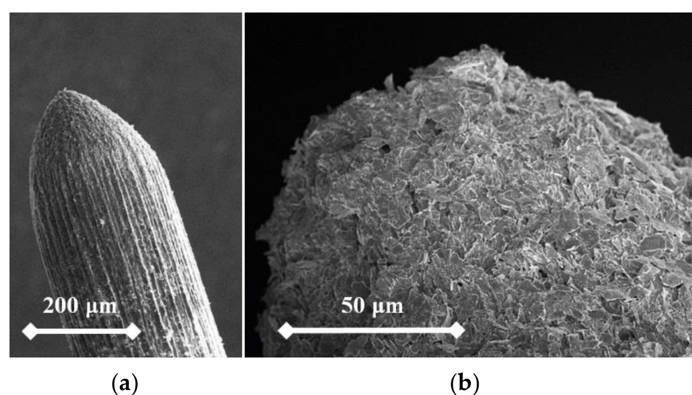

(**a**) (**b**)

Figure 5. SEM image of the tip produced by electrochemical etching (**a**) and the tip surface detail (**b**) showing graphite flakes. Material used for this tip is Pentel Hi-Polymer 0.3 HB.

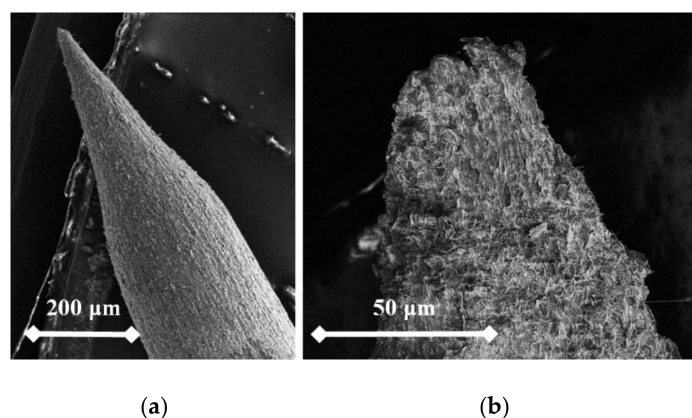

(**a**) (**b**)

Figure 6. SEM image of the produced tip by electrochemical etching (**a**) and the tip surface detail (**b**) showing graphite flakes. Material used for this tip is Koh-i-Noor 0.3 HB.

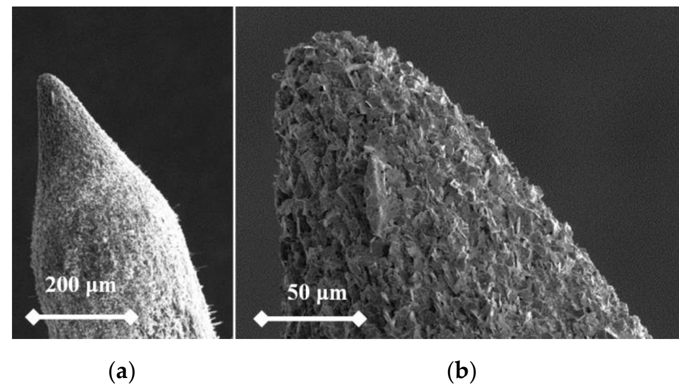

(**a**) (**b**)

Figure 7. SEM image of the tip produced by electrochemical etching (**a**) and the tip surface detail (**b**) showing graphite flakes. Material used for this tip is Koh-i-Noor 0.3 HB.

2.3.2. Mechanical Sharping

Mechanical sharping achieved by sanding is the simplest method. The only disadvantage is the low reproduciblity of the probe's shape and the absence of a tip-sharping control (Figure 8); however, the tip sharpness may be sufficient for measurements performed in atmospheric pressure and just for preliminary control of large area samples with a large range of heights and valleys. The sharping could be carried out by grinding, for example, on sandpaper or by forming with a sharpener.

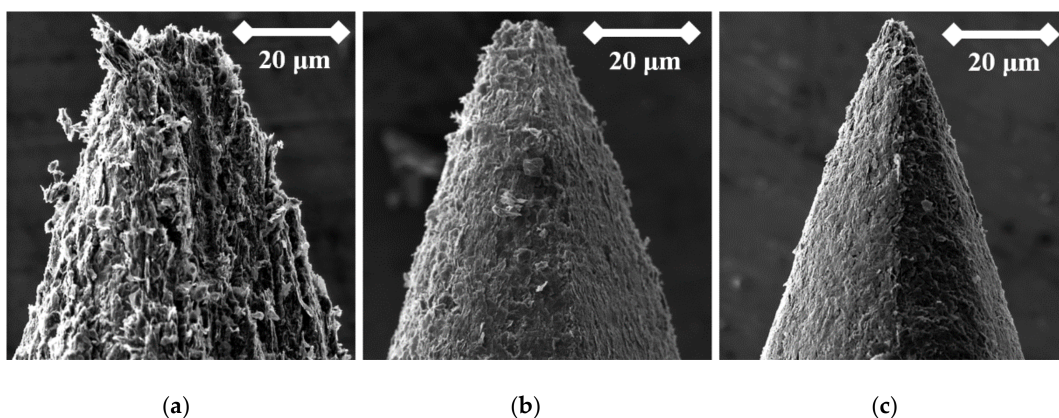

(**a**) (**b**) (**c**)

Figure 8. SEM image of the tip produced by mechanical sharping from the Hi-Polymer rod (**a**); by the mechanical sharping from Koh-i-Noor rod (**b**); and the mechanical sharping from Staedtler rod (**c**).

2.3.3. Focused Ion Beam Milling

The probes were prepared by Focused Ion Beam (FIB) at microscope Helios (FEI production, Hillsboro, OR, USA). The advantage of this microscope is the possibility of the automation of tip sharpening and the preparation of tips with desired shape. FIB processing provides control of shape and sharpness of the probes (Figures 9–11). The disadvantage of this process is a high price of the final product. We used preliminarily mechanically sharpened probes to decrease the time of milling.

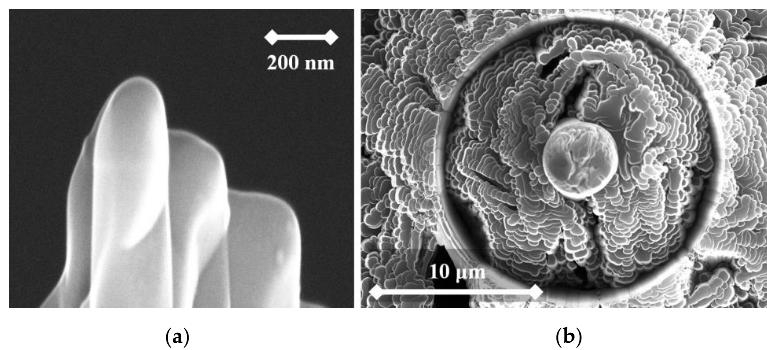

(**a**) (**b**)

Figure 9. SEM image of the tip produced by FIB milling (**a**) and the tip surface detail (**b**) showing graphite flakes from top. Material used for this tip is Pentel Hi-Polymer 0.3 HB.

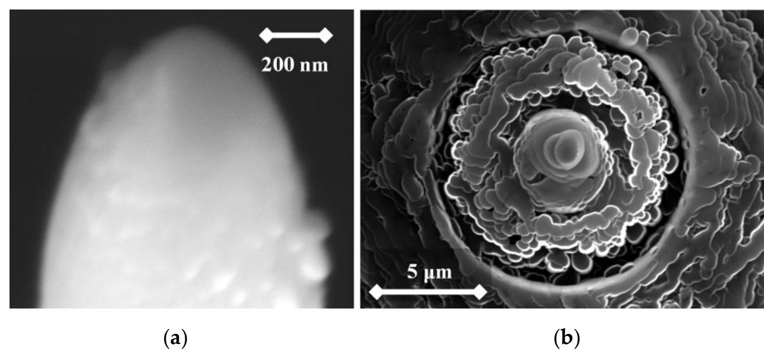

(**a**) (**b**)

Figure 10. SEM image of the tip produced by FIB milling (**a**) and the tip surface detail (**b**) showing graphite flakes from top. Material used for this tip is Koh-i-Noor 0.3 HB.

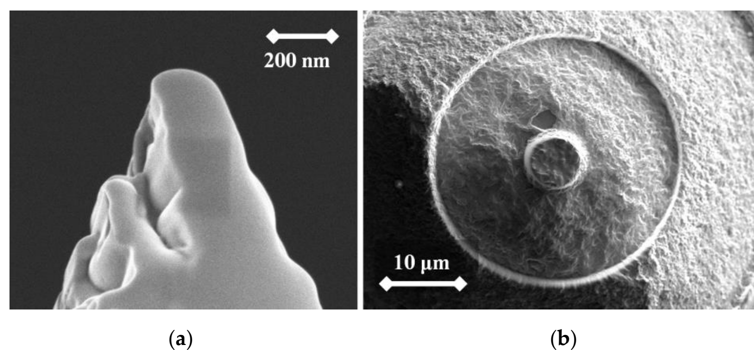

(**a**) (**b**)

Figure 11. SEM image of the produced by FIB milling (**a**) and tip surface detail (**b**) showing graphite flakes from top before milling. Material used for this tip is STAEDTLER 0.3 HB.

3. Results and Discussion

The results published in this paper are partially based on preliminary results that were obtained in our previous paper which discusses field emission behavior of an ultra-sharp polymer-graphite tip [7]. Electrical measurements proved that the graphite flakes behave like metallic conductors while the bonding agent used for bonding the graphite flakes within the polymer-graphite compound behaves more like an electron trap affecting current stability of the total emission current. However, in the region of tunneling currents, the emission showed quasi-stable behavior.

To test functionality, three types of probes for SPM measurements were used: the tips prepared by electrochemical etching (Figures 5–7), the tips prepared by mechanical sharping (Figure 8), and the tips prepared by FIB milling (Figures 9–11). Each of the tips were successfully used for SPM images acquisition. The sharpness of all our tips proved to be sufficient; however, the sharpness depended strongly on the brand of the chosen pencil lead. The lowest sharpness was obtained with

Pentel HiPolymer rod. Koh-i-Noor and Stadler allow preparation of tips with small cultivate radius. FIB processing and chemical etching of the tips ensure reliable obtaining of the tips with demand geometry. Nevertheless, even the mechanical sharping proved to be sufficient during STM in air when sub-nanometer resolution is not demanded. The probes are also stable against oxidation and can be repeatedly sharpened for continuous measurement in a simple sharping procedures. The shape of the tip apex is usually created by a single flake of graphite and determines the output quality of SPM, while the precise shape of the tip does not play a significant role.

In order to demonstrate the simplicity of working with PG probes, all the results presented were obtained using mechanically sharpened tips that can be prepared almost effortlessly just by sharpening a PG rod using sandpaper of high granularity (>1600 grains·cm^{-2}). The probes were tested within an SPM NT-MDT Nanoeducator II (Moscow, Russia). As a reference sample for estimation of our probes, a surface of a compact disc (CD) and highly oriented pyrolytic graphite (HOPG) were chosen (Figure 12a). The HOPG surface (Figure 12b) was used as a reference sample for different types of electrical characterization in probe microscopy [8].

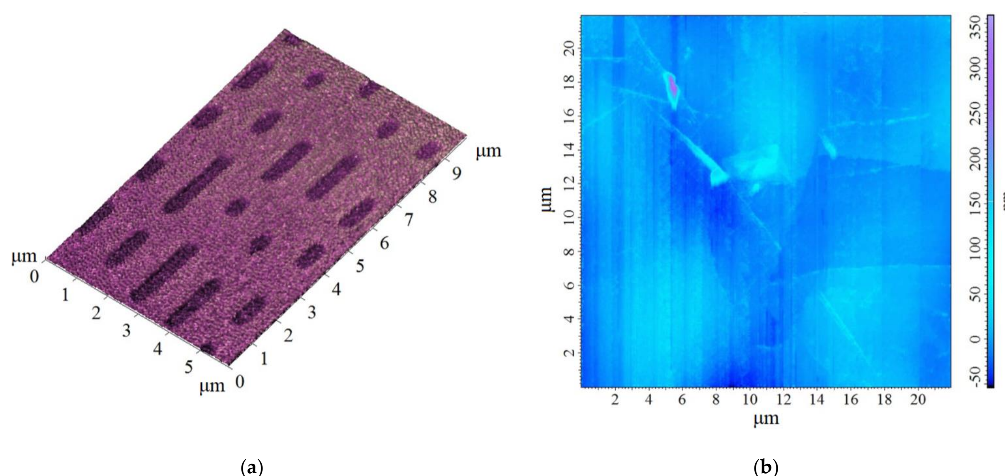

(**a**) (**b**)

Figure 12. Scanning probe microscopy (SPM) image of the reference sample obtained by polymer graphite (PG) tip: (**a**) the surface of a compact disc; (**b**) the surface of a highly oriented pyrolytic graphite (HOPG).

In order to demonstrate the tip's performance on a regular-structured surface, a special calibration sample that is prepared by electron-beam lithography and intended for testing a scanning electron microscope's resolution was used. The calibration sample, which is illustrated in Figure 13, contains grids of various sizes. For our measurements, we have used a 10, 5, and 2.5 µm grids to demonstrate tip's resolution.

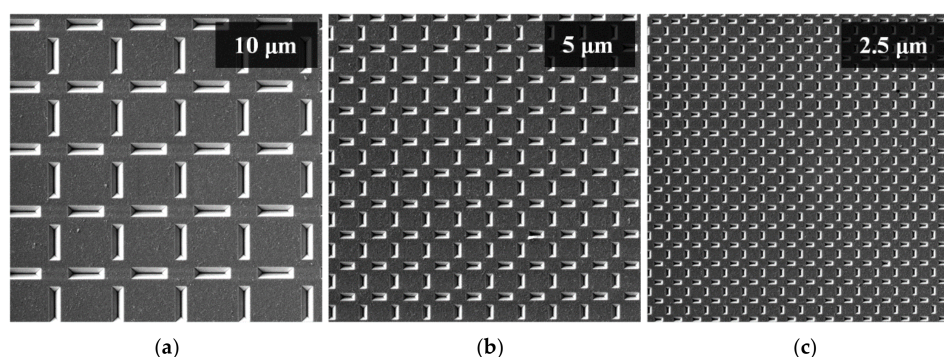

(**a**) (**b**) (**c**)

Figure 13. SEM image of the special calibration sample showing various grid sizes: (**a**) 10 µm grid; (**b**) 5 µm grid; (**c**) 2.5 µm grid.

The results of the measurements are illustrated in the Figure 14 showing the three different grid sizes presented above. It can be seen that in all the grids used, the probe was able to follow the surface details precisely and also to cover a broader area without a change of the spatial sensitivity.

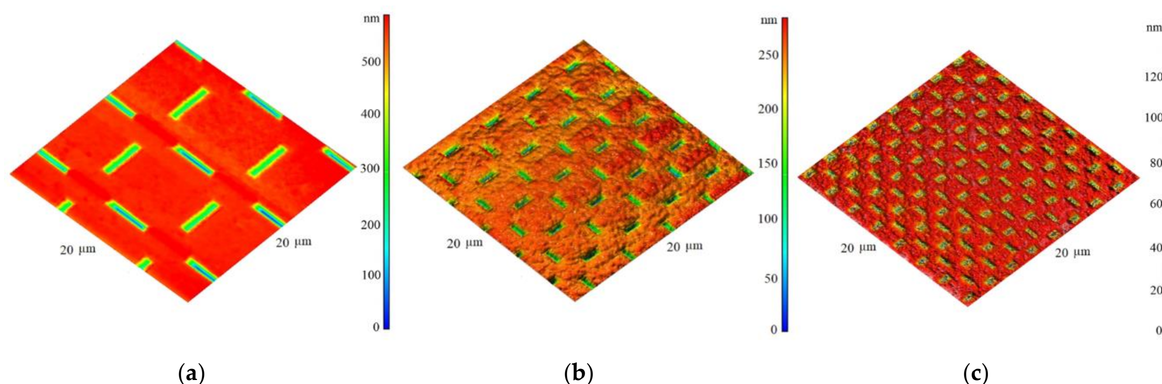

Figure 14. SPM image of the special calibration grid showing tip performance and spatial resolution: grid. (**a**) 10 µm grid; (**b**) 5 µm grid; (**c**) 2.5 µm

4. Conclusions

The aim of this study was to introduce different pencil lead probes for both surface visualization and modification by SPM conductive techniques. SPM is continuously developing and the methods of probe preparation and shaping are at the center of interest. Pencil lead is a cheap solution as an SPM probe for inspection of surface and its modification.

Here, we demonstrate that mechanically polished pencil leads are suitable for fast and low-resolution SPM measurements. These probes proved to be reliable for routine characterization of the samples by SPM in air, with low resolution of surface features. The cost-effective, easy preparations make them useful within the education process in laboratory SPM classes. Generally, a tip made of PG can find application in the education process in the area of scanning probe microscopy techniques or in the area of topography estimation of conductive samples with high roughness at low resolution of texture details. Electrochemical etching and FIB milling allow the preparation of probes for imaging of nanoscale surface features. Besides the introduced STM lithography by pencil lead, the probes have a potential for application at nano-grafting at atomic force microscopy techniques. The mechanical properties of flexible pencil lead could be also used for preparation in SPM techniques.

Author Contributions: Conceptualization, A.K. and D.S.; formal analysis, A.K., D.S., D.B. and A.D.; investigation, D.S. and A.D.; methodology, A.K.; supervision, V.K.; validation, D.S.; writing-original draft, A.K.; writing-review and editing, M.M.

Funding: The research was supported by the Ministry of Industry and Trade of the Czech Republic, MPO-TRIO project FV10618. The research was also financially supported by the Ministry of Education, Youth and Sports of the Czech Republic under the project CEITEC 2020 (LQ1601), Grant Agency of Czech Republic under project No. 19-17457S. A part of the work was carried out with the support of CEITEC Nano Research Infrastructure (ID LM2015041, MEYS CR, 2016–2019), CEITEC Brno University of Technology.

Acknowledgments: We also gratefully acknowledge the contribution of the late Prof. Pavel Tománek to this paper and the contribution of Mr. Jiří Sýkora for the design of the micro-clamp holder.

Conflicts of Interest: The authors declare no conflict of interest. The funders had no role in the design of the study; in the collection, analyses, or interpretation of data; in the writing of the manuscript, or in the decision to publish the results.

References

1. Kelly, B.T. *Physics of Graphite*, 1st ed.; Springer: London, UK, 1981; pp. 17–39.
2. Wissler, M. Graphite and carbon powders for electrochemical applications. *J. Power Sources* **2006**, *156*, 142–150. [CrossRef]

3. Bannov, A.G.; Prášek, J.; Jašek, O.; Shibaev, A.A.; Zajíčková, L. Investigation of Ammonia Gas Sensing Properties of Graphite Oxide. *Procedia Eng.* **2016**, *168*, 231–234. [CrossRef]
4. Encke, F.L. The chemistry and manufacturing of the lead pencil. *J. Chem. Educ.* **1970**, *47*, 575. [CrossRef]
5. Mousa, M.S. Electron emission from carbon fibre tips. *Appl. Surf. Sci.* **1996**, *94*, 129–135. [CrossRef]
6. Mousa, M.S.; Kelly, T.F. Characteristics of carbon-fibre cold field emission tips with a dielectric coating. *Surf. Interface Anal.* **2004**, *36*, 444–448. [CrossRef]
7. Knápek, A.; Horáček, M.; Chlumská, J.; Kuparowitz, T.; Sobola, D.; Šikula, J. Preparation and noise analysis of polymer graphite cathode. *Metrol. Meas. Syst.* **2018**, *25*, 451–458.
8. Loos, J. The Art of SPM: Scanning Probe Microscopy. *Sci. Adv. Matter* **2005**, *17*, 1821–1833. [CrossRef]
9. Janowska, I.; Vigneron, F.; Bégin, D.; Ersen, O.; Bernhardt, P.; Romero, T.; Ledoux, M.J.; Pham-Huu, C. Mechanical thinning to make few-layer graphene from pencil lead. *Carbon* **2012**, *50*, 3092–3116. [CrossRef]
10. Navrátil, R.; Kotzianová, A.; Halouzka, V.; Opletal, T.; Třísková, I.; Trnková, L.; Hrbáč, J. Polymer lead pencil graphite as electrode material: Voltammetric, XPS and Raman study. *J. Electroanal. Chem.* **2016**, *783*, 152–160. [CrossRef]
11. Ţălu, Ş.; Nikola, P.; Sobola, D.; Achour, A.; Solaymani, S. Micromorphology investigation of GaAs solar cells: Case study on statistical surface roughness parameters. *J. Mater. Sci. Mater. Electron.* **2017**, *28*, 15370–15379. [CrossRef]
12. Ţălu, Ş.; Yadav, R.P.; Arman, A.; Korpi, A.G.; Sobola, D.; Ţălu, M.; Rezaee, S.; Achour, A.; Jurečka, S.; Mardani, M. Analyzing the fractal feature of nickel thin films surfaces modified by low energy nitrogen ion: Determination of micro-morphologies by atomic force microscopy (AFM). *Vak. Forsch. Prax.* **2019**, *31*, 30–35. [CrossRef]
13. Sobola, D.; Ţălu, Ş.; Solaymani, S.; Grmela, L. Influence of scanning rate on quality of AFM image: Study of surface statistical metrics. *Microsc. Res. Tech.* **2017**, *80*, 1328–1336. [CrossRef] [PubMed]
14. Knápek, A.; Sýkora, J.; Chlumská, J.; Sobola, D. Programmable set-up for electrochemical preparation of STM tips and ultra-sharp field emission cathodes. *Microelectron. Eng.* **2017**, *173*, 42–47. [CrossRef]
15. Bai, C. *Scanning Tunneling Microscopy and Its Application*, 2nd ed.; Springer Science & Business Media: New York, NY, USA, 2000; pp. 243–279.
16. Ferrari, A.C. Raman spectroscopy of graphene and graphite: Disorder, electron-phonon coupling, doping and nonadiabatic effects. *Solid State Commun.* **2007**, *143*, 47–57. [CrossRef]
17. Kariuki, J.K. An Electrochemical and Spectroscopic Characterization of Pencil Graphite Electrodes. *J. Electrochem. Soc.* **2012**, *159*, 747–751. [CrossRef]

© 2019 by the authors. Licensee MDPI, Basel, Switzerland. This article is an open access article distributed under the terms and conditions of the Creative Commons Attribution (CC BY) license (http://creativecommons.org/licenses/by/4.0/).

Ultramicroscopy 204 (2019) 49–54

Contents lists available at ScienceDirect

Ultramicroscopy

journal homepage: www.elsevier.com/locate/ultramic

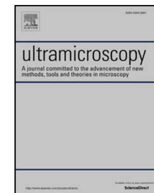

Fluctuations of focused electron beam in a conventional SEM

Alexandr Knápek[a,*], Josef Šikula[b], Milada Bartlová[c]

[a] Institute of Scientific Instruments of the ASCR, v.v.i., Královopolská 147, Brno, Czech Republic
[b] Brno University of Technology, Central European Institute of Technology, Technická 10, CZ-61600 Brno, Czech Republic
[c] Brno University of Technology, FEEC, Dept. of Physics, Technická 8, 616 00, Brno, Czech Republic

ARTICLE INFO

Keywords:
Thermal electron emission
Electronic noise
Low-energy electron beam

ABSTRACT

Noise diagnostics was performed on a tungsten hairpin cathode that was used in conventional scanning electron microscope (SEM) which operates in a high vacuum. The focused beam was firstly measured and its power spectrum obtained in order to characterize its slope in the lower frequencies which are connected with the events occurring on the cathode surface during the emission of electrons. Further experiments involved additional noise measurements which evaluated electron beam with altering beam energy, in particular at 5 kV, 10 kV and 20 kV up to 30 kV; with and without electron beam scanning involved and with different levels of cathode heating. Obtained results were evaluated in relation to a $1/f$ type noise component, generation-recombination process on the cathode surface, on the shot noise and on the velocity fluctuations caused by the ion oscillations. Achieved results were discussed.

1. Introduction

Analysis of current fluctuations of low-energy electron beam for focused electron optics is presented. Anticipated electronic noise sources are: (1) **the electron random velocity**, (2) **the rate of electron emission from the cathode**, (3) **partition noise on extractor electrode**, (4) **the non-uniformity of electron emission velocity across the cathode area**, (5) **secondary-emission noise** and (6) **ion-oscillation noise**.

The randomness in the density and velocity of the emitted electrons causes random currents and voltages to appear at the output. The electrons are usually accelerated in the gun region and then continue to move with an essentially constant velocity in the drift space. The electrons generally form a high current density, well-defined beam [1–7, 12]. The "switching-on" phenomenon, which proves itself as a steep increase of a total emission current from zero emission current to a highly stable high current density electron beam was already described in several papers [13, 14].

Despite the electron microscope operates in high vacuum ($3{\cdot}10^{-3}$ Pa), it is necessary to take into account ions impinging on the cathode, which creates spikes like RTS noise. Mathematical description is based on method of moments of the charge density distribution function for multi-velocity electron beam [2, 3]. The zero-, first-, and second- order moments of the Boltzmann equation with respect to the velocity variable yields macroscopic equations that express the conservation of charge, momentum, and energy.

Emitted electrons possess random emission velocities. The velocity fluctuations cause initial velocity modulation on the electron beam. The emitted electrons move toward the potential minimum, those of lowest velocity are sorted out and pulled back to the cathode. Based on the probability distribution function for electron emission velocities (Maxwell distribution for temperature T_C of the cathode) the average velocity of the electrons moving away from the cathode at the point between the cathode and the potential minimum where the potential relative to the cathode is V can be calculated [11]

$$\bar{u} = \sqrt{\frac{\pi k T_C}{2m}} \tag{1}$$

It is constant independent of the potential V, and also of the potential difference between the cathode and the potential minimum. The average velocity is an average taken over a sufficiently long length of time. At any particular time, the average electron velocity may be slightly higher or lower. The mean square fluctuation of the average velocity at the potential minimum is [11]

$$\overline{u_A^2} = \frac{ekT_C\Delta f}{mI_{a0}}(4-\pi) \tag{2}$$

I_{a0} is the dc anode current. Δf is the band-with over which the noise is measured. The dc anode voltage V_a then accelerates the electrons and the mean-square velocity fluctuation is

* Corresponding author.
E-mail address: knapek@isibrno.cz (A. Knápek).

https://doi.org/10.1016/j.ultramic.2019.05.008
Received 27 February 2019; Received in revised form 9 May 2019; Accepted 19 May 2019
Available online 20 May 2019
0304-3991/ © 2019 Elsevier B.V. All rights reserved.

$$\bar{v}^2 = \frac{2m}{e}V_a\bar{u}_A^2 = 2kT_C\frac{V_a}{I_{a0}}\Delta f(4-\pi) \tag{3}$$

For studying of the effect of the velocity fluctuations in the electron beam, the space-charge wave theory should be considered [11]. The theory concerns the propagation of small, sinusoidal perturbations on an electron beam. It describes well the noise perturbation because instantaneous current and velocity fluctuations are measured as a function of time over a finite time interval. These fluctuations may be analyzed by means of Fourier integral to obtain an equivalent sinusoidal current and velocity for a frequency interval Δf. The propagation of noise perturbations may be determined from the propagation of the equivalent sinusoidal quantities.

Electrons in the primary beam collide with residual gas molecules resulting in the production of positive ions and secondary electrons. The secondary electrons give rise to more ionization. Two contributions of ions to the observed noise are expected. Firstly, the positive ions oscillate transversely in the space charge of the beam (plasma oscillations) [7]. The oscillations depend on the beam current and ionization cross-sections of neutral atoms. Another effect can be explained by the trapping of ions in the space charge of the beam. The positive ions are attracted to regions of negative potential. The ions collect along the beam potential depression due to electron space charge, filling the potential wells until a critical value is reached and the ions can drain into the cathode. A small ion current continuously bombards the center of the cathode [8–11]. The escaped ions are replaced by new ionization. The process then repeats, giving the relaxation type of these ion oscillations.

The trapped positive ions often oscillate at a low frequency, and the resulting fields defect the electron beam causing undesirable modulations. Positive ions oscillations can be best avoided by maintaining as good a vacuum as possible. Experiments proved that the thermal and shot noise components are less about by 2 orders comparing to the achieved experimental values.

There is no single theory. The usual approach is to seek solutions separately in the different regions of the electron flow and then apply the right initial and boundary conditions, or at least useful approximations thereof. The solutions for the lowest mode of a finite beam, with an axial magnetic field in the drift space, predicted an infinite noise-current standing wave.

2. Experiment

Noise diagnostics was performed on a classical tungsten hairpin cathode operating in a high vacuum. The cathode worked in thermal electron emission mode at several temperatures based on the level of heating (weak, middle, strong and extra). Power source consists of a DC source of the SEM connected in triode mode (cathode, control electrode and anode). In this measurement, several acceleration voltages have been used starting at 5 kV, 10 kV and 20 kV up to 30 kV, giving the primary beam energies of 5 to 30 keV.

2.1. Electron optical system

Tested cathode is placed in a column of an older but still frequently used commercial scanning electron microscope branded TESCAN Vega-1 (SEM) marked simply as a laboratory sample SEM1. Emitted current goes through a column consisting of two condenser lenses, the auxiliary centering lenses and stigmators and a pair of scanning coils. The beam then continues through objective out of the column as illustrated in Fig. 1. There are two apertures cropping the electron beam and reducing the total emission current approximately thousand times.

The electron beam is focused into a Faraday cage through narrow aperture on the top of the cage that was placed under the objective collecting all impinging electrons within.

In order to reduce a deflection of the beam, the following configuration was set: the beam has been focused to the edge of the Faraday cage and then magnified inside the cage to obtain as smallest field of view. At the highest magnification the area of scanning was minimized to a square covering 5 nm^2, which almost suppressed the beam scanning. By reducing the scanning speed (s) to level $s = 12$, the dwell time (i.e. the period of time that a beam remains in a same position) for a single pixel is equal to 2.36 ms, therefore, the area of 5 nm^2 (17 squared pixels) is scanned periodically every 0.68 s obtaining continual output current.

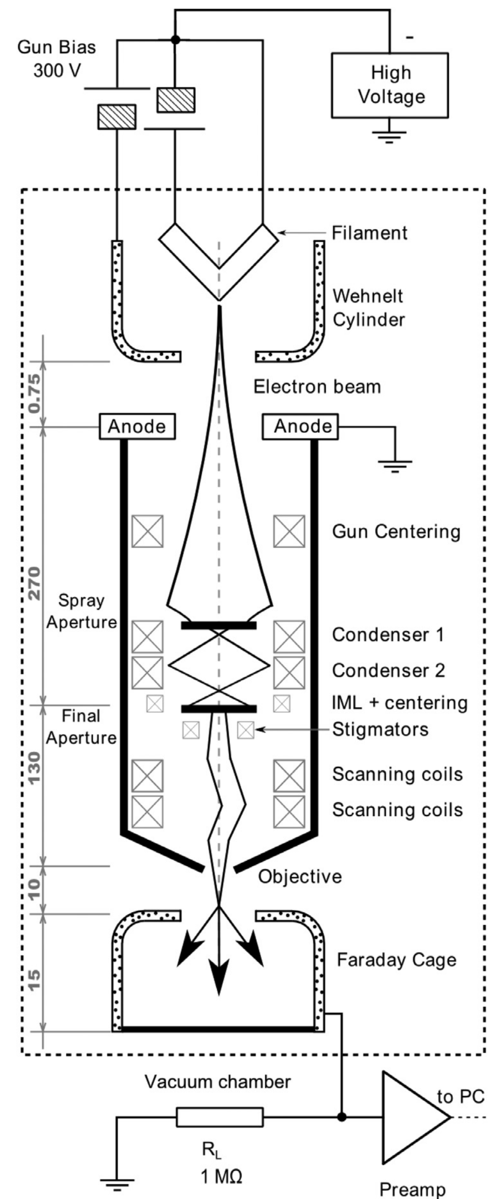

Fig. 1. Schematic representation of the cathode and optical elements of the laboratory scanning electron microscope where left are distances in mm.

Output current of the Faraday cage has been grounded through a 1 MΩ resistor on which the voltage fluctuations have been measured. After the voltage on the load resistor stabilizes, the voltage is measured, sampled and recorded. In order to meet the signal in quasi-stationary state for power spectral density analysis, it has been empirically found the ideal sampling time of a single realization

$$t = f_s \cdot N = 418\text{s}, \tag{4}$$

where f_s is sampling frequency and N is number of samples. The second measurement setup was performed without electron beam scanning in

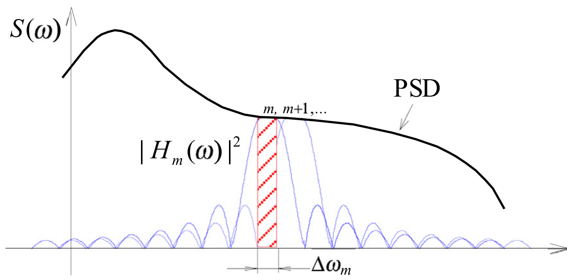

Fig. 2. The final composition of a power spectral density (PSD) of all fractional spectra.

order to avoid unwanted signal from scanning. Both setups were compared from the point of view of the noise spectral density value. To reach good frequency resolution at low frequencies, the sampled signal was processed using a digital quadrature-filter-bank (DQFB) of the order $M = 4$, derived from the wavelet transformation algorithm. The output of the DQFB is a set of 16 band-limited fractional signals as is shown in Fig. 2.

From each sequence, a fractional spectrum S_{yy}, evaluated using the Short-Time Discrete Fourier Transformation, is obtained. The resulting noise spectral density is calculated using the non-parametric version of Welch's method [1]:

$$S(\omega) = \sum_{m=0}^{M-1} S_{yy}(\omega_{m-1} - \omega_m) \tag{5}$$

2.2. Noise spectral density of the emitted beam

Low frequency noise spectral density of the emitted beam depends on the value of accelerated voltage, cathode heating temperature, scanning frequency and time interval of electron beam on dwell time which is determined by the scanning speed setting. Within our measurements, the average life-time of a cathode is from 120–150 h of operation. After this period, the total emission current starts to decrease and sudden current fluctuations (up to 10%) starts to appear. The first measurement was performed on a cathode that was stored for a long-time at the room temperature. In this case the cathode surface was initially covered by thin film of tungsten trioxide that is created during cathode cooling from previous operation. The presence of the surface oxide-layer on a cathode samples was confirmed using an FEI Quanta 3D FEG DualBeam scanning electron microscope (SEM). Cross-section analysis of the oxide layer thickness was obtained using a focused ion beam (FIB). Voltage noise spectral density S_u as a function of frequency is shown in Fig. 3. The measurement resistor R operates at room

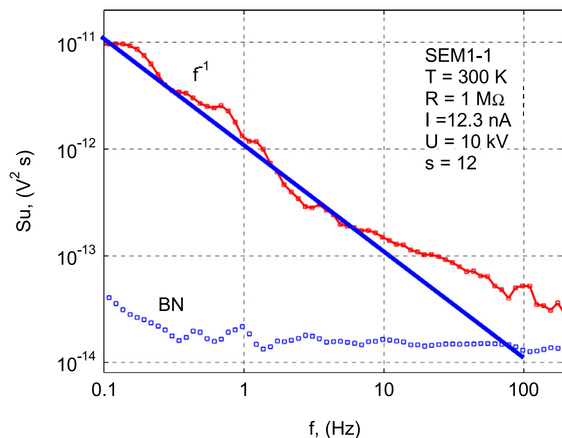

Fig. 3. Voltage noise spectral density for sample SEM 1 configuration SEM1-1 measured for $s = 12$.

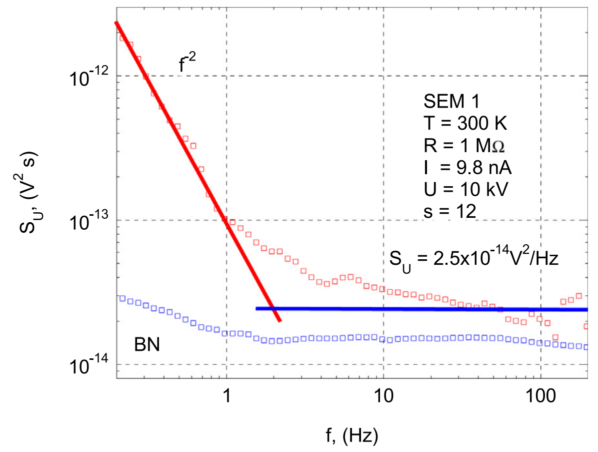

Fig. 4. Voltage noise spectral density for sample SEM 1 configuration SEM1-1 measured for $s = 12$ after 1000s.

temperature

$T = 300$ K yielding background noise level (BN) equal to 4kTR, as it is plotted in the Fig. 3.

At the frequency range from 0.1 up to 10 Hz is noise spectral density *1/f* type. Low frequency component is changed from $1/f$ spectrum to $1/f^2$ due to a progressive accumulation of emitted carriers near the cathode surface. These carriers don't have sufficient energy to leave the surface and move towards the anode. For the period of

$t = 1000$ s the voltage noise spectral density is decreasing as is shown in Fig. 4.

This phenomena was explained by Sergeev [12], who suppose that the one part of that the generation-recombination noise results from the electron movement which takes place near the surface of the cathode. Presuming, that one part of electrons is being evaporated out of the cathode surface, the second part is being attracted and caught back on the surface. Considering these interactions between two reservoirs, Sergeev proposed a model of adsorption-desorption noise that was formulated on the basis of the Kolmogorov equation. An equation determining the noise power spectral density (NPSD) of captured electrons was derived by using Wiener/Khinchin theorem [12]

$$S_{\delta N} = 4\int_{0}^{+\infty} \sigma^2 e^{-|t|/\tau}\cos\omega t dt = \frac{4\sigma^2\tau}{1+\omega^2\tau}, \tag{6}$$

where σ^2 denotes the mean square value of δ_N, which is the dependence of the fluctuation $\delta_N(t)$ around the value N_0 at the emission/capture equilibrium on the cathode surface solved in [15]; t stands for the time for which a single electron remains in the higher energy state and τ is the characteristic time which is inversely proportional to the transition probability density μ [12]. Based on Eq. (6), it may be concluded that the shift of generation-recombination noise is caused by the increase of amount of electrons passing between the surface of the cathode, which corresponds to the decrease of the surface barrier that also show itself with an increased variation of current fluctuations.

For electron beam with a current of $I_{eb} = 9.8$ nA, the current noise spectral density $S_i = 3.14 \cdot 10^{-27}$ A^2/Hz as a result of the shot noise was found. Shot noise may be dominant when the finite number of charged carriers is sufficiently small so that uncertainties due to the Poisson distribution, which describes the occurrence of independent random events, are of significance. In our measurements, the shot noise component is about one order below the mean the obtained current noise spectral and for this reason, the effects of a shot noise were neglected.

2.3. Influence of the accelerating voltage

The second experiment (SEM1-2) was performed with various accelerating voltages starting from 5 to 20 kV as it is illustrated by Fig. 5.

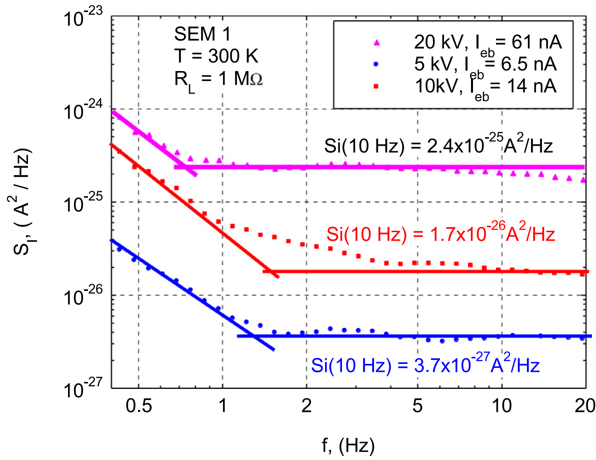

Fig. 5. Current noise spectral density S_I at applied voltage 5 to 20 kV for sample SEM 1 in configuration SEM1-2.

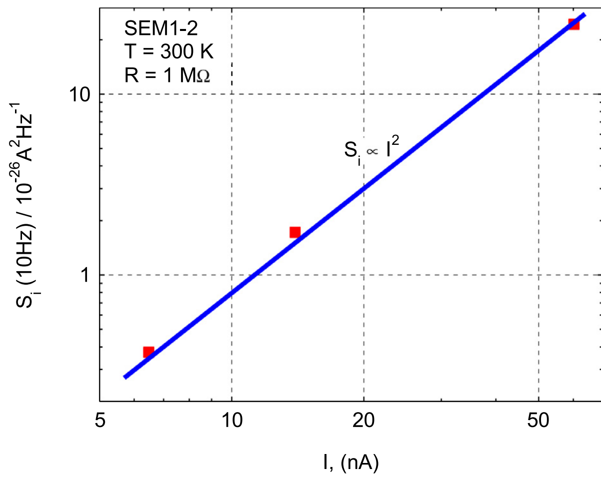

Fig. 6. Current noise spectral density vs. electron beam current for sample SEM 2.

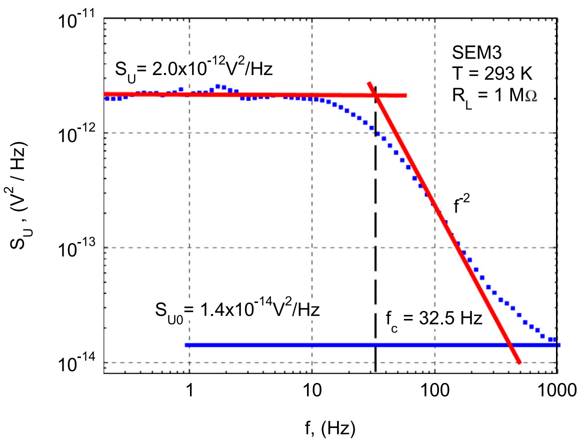

Fig. 7. Voltage noise spectral density for sample SEM 1 configuration SEM1-3 measured for $s = 0$.

Low frequency noise measured was located in scale from 0.3 to 1 Hz and was of $1/f^n$ type where n varies from 1 to 2.

In the frequency band from 2 to 20 Hz the current noise spectral density can be described by the generation-recombination noise in the sense as it was discussed before (Section 2.2). In this particular case, the current noise spectral density was influenced (and increased) by the

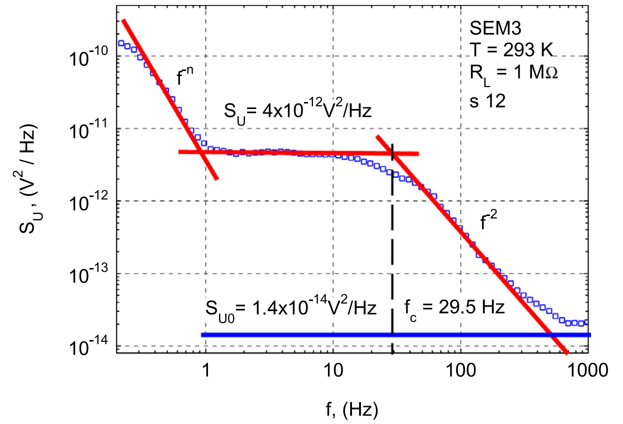

Fig. 8. Voltage noise spectral density for sample SEM 1 configuration SEM1-3 measured for $s = 12$.

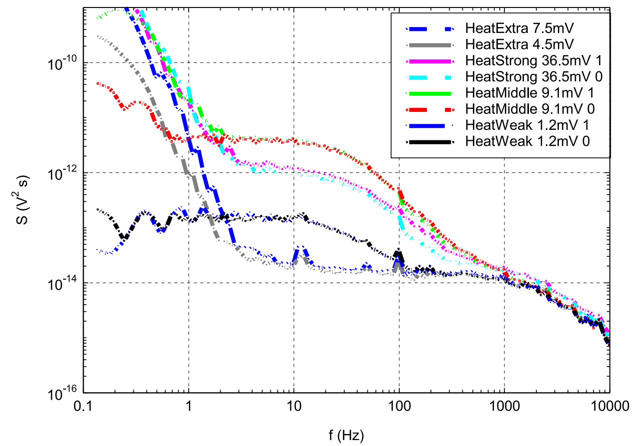

Fig. 9. Voltage noise spectral density of 30 keV primary electron beam at various cathode heating levels (measured twice for two different 1MΩ resistors at each heating level), mean levels are measured for $f = 10$ Hz.

increased accelerating voltage. This noise component is also partially contributed by the effect of velocity fluctuation as described by Eq. (3). Based on the equation, it can be seen that the function of the mean square velocity fluctuation vs beam energy is decreasing along with the increasing accelerating voltage, which can be regressed by a power function.

From the measurement illustrated in Fig. 5, it can be concluded that the current noise spectral density at frequency 10 Hz increased with increasing electron beam current as it is shown in Fig. 6. The current noise spectral density increased with a square of current also confirming a supposition that the noise is of a generation-recombination type [12, 15] (see Fig. 6).

2.4. Influence of the scanning speed

Third experiment was performed with accelerating voltage 30 kV and special values of voltages on condensers and stigmators. This configuration is described as SEM1-3.

Measured voltage noise spectral density for scanning speed $s = 0$ is g-r type as is shown in Fig. 7. The cut-off frequency in this case is $f_c = 32.5$ Hz and voltage noise spectral density at 1 Hz S_u equal to 2×10^{-12} V^2/Hz, as it is illustrated by Fig. 7. It is supposed that this particular g-r noise component originates from the electron optics and relates to the electric field distribution among anode, condensers, stigmators and objective as it is illustrated in Fig. 1.

Beam deflectors which are used to scan the electron beam across the specimen consist basically of two scanning coils: one is for horizontal

Table 1
Voltage noise power spectral density (NPSD) for at various heating levels vs. working regime of the cathode.

Heating	"weak"	"middle"	"strong"	"extra"
Voltage NPSD	$1.5 \cdot 10^{-12}$ [V^2s]	$4 \cdot 10^{-10}$ [V^2s]	$1 \cdot 10^{-11}$ [V^2s]	$2 \cdot 10^{-13}$ [V^2s]
Working regime	Non-saturated region	Non-saturated region	Particularly saturated region	Saturated region
Noise mean level	Increase	increase	decrease	decrease

deflection and second one for vertical deflection. Since both operate on particular frequencies whose overall speed may be set by end-user, the effect of beam deflection has been considered as a possible source of unwanted fluctuations and was further examined.

Effect of scanning frequency is shown in Fig. 8 where $f_c = 29.5$ Hz, which is slightly lower than for the scanning frequency where $s = 0$. Moreover, in the frequency band below 1 Hz, a new source of noise appears. This particular noise component is related to the electric field distribution between anode and objective and is dependent on the scanning frequency.

2.5. Influence of the filament heating

Accelerating voltage source also contains a current source for the heating of the cathode filament on the accelerating voltage potential as illustrated in Fig. 1. After each cathode exchange, cathode heating intensity is increased till the saturation, i.e. to the zone where the further heating current increasing does not increase the total emission current. When the procedure is finished, the cathode is left for couple of minutes to stabilize the beam before the measurement. The level of the filament heating can be simply chosen from a four different presets which are marked as: "weak", "middle", "strong" and "extra" offering four levels of a cathode heating. The increase of the heating intensity also increases the total emission current. For each heating level, two spectral measurements were done as it is illustrated in Fig. 9. From the spectral density measurements, it can be seen that the heat increase is not directly proportional to the mean value and also to the shape of the spectral curve (or spectral components distribution) is not constant.

The explanation is rather straightforward and may be explained in few steps. In Fig. 9, it can be seen that the lowest noise mean level belongs to the "extra heat" option. In this case, the cathode working point is located in the region of current saturation, which means that all the available electrons are used for charge transport and any current increase would not increase the emission. This also positively influences the electron emission probability, which means that vast part of electrons emitted has sufficient momentum energy to leave the surface and move towards the anode, hence, the effect of superposed generation-recombination noise is rather minor.

For the mean value of the noise spectrum by the "middle heat" option, it can be seen that this particular value is the highest value which means, that in this case, the working point of the cathode is located in between the regions of saturation and partial saturation. When the heat is further increased (by choosing the "strong heat" option), the noise mean value is increased as it reaches the boundary of the saturated region.

As it was mentioned above, the heating intensity is determined by the automated procedure that is executed every time after a cathode is changed. For this reason, the mean level of the spectra at one of the particular heat settings is different for each particular cathode and in present state of the software, it cannot be determined precisely.

Conclusions

Main sources of noise and fluctuations were described in the theoretical part and further discussed in relation to the measured spectra. It should be emphasized that electron microscope rather complicated device with several noise components that should be evaluated based on their final product since there are surface effects and plasma-related effects affecting the out-coming beam stability. From the point of view of end-user, the Tescan Vega 1 electron microscope may be considered as a very reliable and immune device from the point of view of its own fluctuations as the added noise originating from the cathode and electron-optical system is rather minor comparing to outcome signal and may be even lowered by setting suitable working regime.

In the experimental part, current- and voltage-noise spectroscopy were conducted in order to describe noise properties of the electron beam in SEM in relation to acceleration voltage (i.e. electron energy), scanning speed and to temperature of the cathode.

The electron beam was characterized firstly at the frequency range from 0.1 up to 10 Hz, where the noise spectral density obtained was of $1/f$ type for a cathode with thin film of tungsten oxides. In many experiments the, noise was of $1/f^{\,n}$ type with n in the range 1 to 2. The shot noise in this case was neglected as its mean value was located about one order below the current noise spectral density.

From the point of view of accelerating voltage influence, at the voltages 5 kV to 20 kV, the noise in the frequency band from 2 to 20 Hz was described by the model of a generation-recombination noise and discussed on the basis of existing theory. In this case, the current noise spectral density increased with a square of a beam current. At accelerating voltage 30 kV a new g-r noise component appeared. It is supposed that the source of this noise is related to electric field distribution among the electron-optical components located in the chamber.

From the point of view of scanning speed influence, it has been concluded that the scanning frequency has minor effect on the noise current density by moving its cut-off frequency almost 4 Hz lower, which influences the final composition of spectral components implicating relation to the scanning frequency due to the altered electric field distribution between anode and objective.

Another source of electric noise is the filament heating. The mean level of the spectra is related to the working point of the cathode since in the saturation regime, the cathode behaves more stable. Spectra measured in Fig. 9 are concluded in Table 1.

Acknowledgment

Author would like to express his gratitude to Mr. Tomáš Kuparowitz (BUT) and Filip Mika (ISI) for technical assistance during the measurement.

Research was financially supported by the Technology Agency of Czech Republic project No. TE01020118 and by institutional support RVO:68081731. This research has been financially also supported by the Ministry of Education, Youth and Sports of the Czech Republic under the project CEITEC 2020 (LQ1601) and under the project No. CZ.02.1.01/0.0/0.0/16_013/0001638 (CVVOZE Power Laboratories-Modernization of Research Infrastructure).

Supplementary materials

Supplementary material associated with this article can be found, in the online version, at doi:10.1016/j.ultramic.2019.05.008.

References

[1] A. Knapek, et al., Cold field- emission cathode noise analysis, Metrol. Meas. Syst.

2012 (iss. 2) (2012) 417–422 ISSN: 0860- 8229.
[2] H.C. Hsieh, Hydrodynamic analysis of noise in a finite temperature electron beam, J. Appl. Phys. 36 (8) (1965) 2414–2421.
[3] J.R. Pierce, A theorem concerning noise in electron streams, J. Appl. Phys. 25 (1954) 931.
[4] S. Ramo, Space charge and field waves in an electron beam, Phys. Rev. 56 (1939) 276–283.
[5] L. Brillouin, A theorem of Larmor and its importance for electrons in magnetic fields, Phys. Rev. 67 (1945) 260–266.
[6] C.C. Cutler, C.F. Quate, Experimental verification of space charge and transit time re-duction of noise in electron beams, Phys. Rev. 80 (1950) 875–878.
[7] T.G. Milhran, Positive ion oscillations in long electron beams, IRE Trans. Electron Dev. Vol. 3 (1956) 117–121.
[8] C.C. Cutler, Spurious modulation of electron beams, Proc. IRE 44 (1956) 61–64.
[9] E.W. McCune, Ion oscillation considerations for pulsed klystron amplifiers, IEDM 83 (1983) 148–150.
[10] W.M. Manheimr, On the theory of ion noise in microwave tubes, NRL/MR/ 6707—99-8323 (1999), 1–49.
[11] J.W. Gewartowski, H.A. Watson, Principles of Electron Tubes. Chapter 13, Noise. D Van Nortrand Comp., Inc., Princeton, 1956.
[12] E. Sergeev, et al., Noise diagnostic method of experimental cold field-emission cathodes, Noise and Fluctuations (ICNF), 2013 22nd International Conference on, IEEE, 2013, pp. 1–4.
[13] R.V. Latham, M.S. Mousa, Hot electron emission from composite metal-insulator micropoint cathodes, J. Phys. D: Appl. Phys. 19 (4) (1986) 699.
[14] M. Mousa, et al., Switch-on'phenomena in field-electron and field-ion microscopy, Vacuum 45 (2–3) (1994) 249–254.
[15] P. Sedlák, et al., Adsorption-desorption noise in QCM gas sensors, Sens. Actuat. B Chem. 166-167 (2012) 264–268 ISSN 09254005.

Journal of ELECTRICAL ENGINEERING, VOL 71 (2020), NO1, 37–42

sciendo

PAPERS

Implementation of the orthodoxy test as a validity check on experimental field emission data

Mohammad M. Allaham[1], Richard G. Forbes[2], Alexandr Knápek[3], Marwan S. Mousa[1]

In field electron emission (FE) studies, it is important to check and analyse the quality and validity of experimental current-voltage data, which is usually plotted in one of a small number of standard forms. These include the so-called Fowler-Nordheim (FN), Millikan-Lauritsen (ML) and Murphy-Good (MG) plots. The Field emission orthodoxy test is a simple quantitative test that aims to check for the reasonableness of the values of the parameter "scaled field" that can be extracted from these plots. This is done in order to establish whether characterization parameters extracted from the plot will be reliable or, alternatively, likely to be spurious. This paper summarises the theory behind the orthodoxy test, for each of the plot forms, and confirms that it is easy to apply it to the newly developed MG plot. A simple, new, accessible web application has been developed that extracts scaled-field values from any of these three plot forms, and tests for lack of field emission orthodoxy.

Keywords: field electron emission, field emission orthodoxy test, Fowler-Nordheim plots, Millikan-Lauritsen plots, Murphy-Good plots, field enhancement factor, emitter characterization parameters

1 Introduction

This paper discusses a simple new methodology for processing measured current-voltage $I(V)$ data from devices or systems that involve the process of field electron emission (FE) [1–5]. Note that in this paper the symbols I and V always denote the measured quantities that in some recent papers (*eg* [6]) have been denoted by I_m and V_m. The symbols I and V do not denote the so-called "emission" quantities I_e and V_e.

In FE literature, two types of plot have been used to analyze $I(V)$ data, namely Fowler-Nordheim (FN) plots [6-8] and Millikan-Lauritsen (ML) plots [9, 10]. A third plot form, the Murphy-Good (MG) plot, has recently been proposed [11]. If the FE device/system is orthodox, as defined below, then all these plots present the $I(V)$ data as a nearly straight line that can be subjected to mathematical analysis, in order to extract emitter characterization parameters.

An FE device/system is defined as "ideal" if its $I(V)$ characteristics are determined only by the combination of (a) – unchanging total system geometry (including emitter shape) and (b) – the emission process. It is further described as "orthodox" if it is an adequately valid approximation to assume that tunnelling takes place through a Schottky-Nordheim (SN) ("planar image-rounded") barrier, and that there is no significant voltage dependence in the emission area or in the local work-function. If a device/system is not orthodox, then data plots as discussed above may be defective, and extracted characterization-parameter values may be spurious.

There exists an "Orthodoxy test" [12], developed in the context of FN and ML plots, that can be applied to an experimental FE $I(V)$ data-set, in order to establish whether or not the related FE device/system is orthodox, and hence whether extracted characterization-parameter values would be reliable. For example, there is some evidence [12] that many published field-enhancement-factor values may be spuriously large.

The present work describes a simple web application that can apply the orthodoxy test to any of the above plots, including the new MG plot. Relevant theory has been discussed elsewhere [8, 12, 13] and is summarised below. The orthodoxy test and web application are then described and applied to illustrative examples of $I(V)$ data.

A motivation for this work has been to enhance the procedures available for testing field electron sources under development for possible use in electron microscopes and other electron beam instruments.

This paper uses the common "electron emission convention", whereby fields, currents, and current densities are treated as positive, even though they would be negative in classical electromagnetism. Where values of uni-

[1] Surface Physics and Materials Technology lab, Department of Physics, Mutah University, Al-Karak 61710, Jordan, [2] Advanced Technology Institute & Department of Electrical and Electronic Engineering, Faculty of Engineering & Physical Sciences, University of Surrey, Guildford, Surrey GU2 7XH, UK, [3] Institute of Scientific Instruments of the CAS, Kálovopolská 147, 612 64 Brno, Czech Republic, Corresponding author: mmousa@mutah.edu.jo

DOI: 10.2478/jee-2020–0005, Print (till 2015) ISSN 1335-3632, On-line ISSN 1339-309X

© This is an open access article licensed under the Creative Commons Attribution-NonCommercial-NoDerivs License (http://creativecommons.org/licenses/by-nc-nd/3.0/).

versal constants are given, numerical values are specified to seven significant figures.

2 Theory of extracting scaled-field values

2.1 Basic field electron emission theory

For an orthodox FE device/system, the measured emission current I can be given, in terms of the local work function ϕ and the characteristic local barrier field f_{C}, by the extended Murphy-Good (EMG) equation, see [11], (2.2). It is better here to employ a "scaled" form that uses the dimensionless characteristic scaled field $f_{\mathrm{C}} = c_S^2\phi^{-2}F_{\mathrm{C}}$, where c_{S} is the Schottky constant (see Appendix). For orthodox systems, f_{C} can be related to the measured voltage V by

$$f_{\mathrm{C}} = V/V_R \tag{1}$$

where V_R is a (constant) reference measured voltage [11] needed to pull the top of a characteristic SN barrier, of zero-field height ϕ, down to the emitter Fermi level. The EMG equation for $I(V)$ can thus be written, [11]

$$I(V) = A\theta(V/V_R)^2\exp\Big(-v_F\eta V_R/V\Big). \tag{2}$$

where A is a parameter called the *formal emission area for the SN barrier* (denoted by $A_{\mathrm{f}}^{\mathrm{SN}}$ in [11]), θ and η are $\phi-$dependent scaling parameters defined in [11], with $\eta \cong 9.836239(\mathrm{eV}/\phi)^{1/2}$, and v_F is the appropriate value of a special mathematical function $v(x)$, [14]. It can be shown that $v_F = v(x = f_{\mathrm{C}})$.

A simple good approximation exists [15] namely: $v_F \approx 1-f_{\mathrm{C}}+(f_{\mathrm{C}}/6)\ln(f_{\mathrm{C}})$. Substituting into (2), and using (1) again, yields, after some re-arrangement, the alternative format

$$I(V) = \{A(\theta\exp\eta)V_{\mathrm{R}}^{-\kappa}\}V^{\kappa}\exp(-\eta V_{\mathrm{R}}/V), \tag{3}$$

where, for this SN-barrier case, $\kappa = 2 - \eta/6$.

In general terms, what the orthodoxy test does is to deduce, using the slope of a given plot form, the range of f_{C}-values that corresponds to the range of measured-voltage used in the experiments. As discussed below, this extracted range of f_{C}-values is then compared with the known range of f_{C}-values within which (tungsten) emitters normally operate.

Theory relating to the plot slopes is now given. In what follows, subscripts such as "FN" label the plot type, and the notation $\ln\{Q\}$ means (see [16]) "take the natural logarithm of the numerical value of the quantity Q, when this quantity is measured in SI units" (here amperes, and volts to an appropriate power).

2.2 The Fowler-Nordheim (FN) plot slope

With (2), on dividing both sides by V^2 and taking natural logarithms, we obtain

$$L_{\mathrm{FN}} = \ln\{I/V^2\} = \ln\{A\theta V_{\mathrm{R}}^{-2}\} - v_{\mathrm{F}}\eta V_{\mathrm{R}}V^{-1}$$

This is a theoretical equation for a Fowler-Nordheim (FN) plot. Its slope is given by

$$S_{\mathrm{FN}}(V^{-1}) = \mathrm{d}L_{\mathrm{FN}}/\mathrm{d}(V^{-1}) = -\eta V_{\mathrm{R}}\mathrm{d}(v_{\mathrm{F}}V^{-1})/\mathrm{d}(V^{-1})$$

A standard result [15] is that $\mathrm{d}(v_{\mathrm{F}}V^{-1})\mathrm{d}(V^{-1}) = s(f_{\mathrm{C}})$, where $s(f_{\mathrm{C}})$ is the slope correction function for a SN barrier, and f_{C} corresponds to V. Hence, the FN-plot slope is

$$S_{\mathrm{FN}}(V^{-1}) = -s(f_{\mathrm{C}})\eta V_{\mathrm{R}} \tag{4}$$

In FN-plot analysis, the slope is (in principle) taken at the "fitting value" where the tangent to the theoretical plot is parallel to the line fitted to the experimental results [15]. This fitted line has slope $S_{\mathrm{FN}}^{\mathrm{fit}}$, and the fitting value of $s(f_{\mathrm{C}})$ is denoted by s_t. It follows from (4) that the extracted V_{R}-value is $\{V_{\mathrm{R}}\}^{\mathrm{extr}} = -S_{\mathrm{FN}}^{\mathrm{fit}}/s_t\eta$, and hence the extracted f_{C}-value corresponding to measured voltage V is

$$\{f_{\mathrm{C}}\}^{\mathrm{extr}} = -(s_{\mathrm{t}}\eta/S_{\mathrm{FN}}^{\mathrm{fit}})V = -(s_t\eta/S_{\mathrm{FN}}^{\mathrm{fit}})/V^{-1} \tag{5}$$

Since $s(f_{\mathrm{C}})$ varies only weakly with f_{C}, it is normally adequate to take $s_t = 0.95$.

2.3 The Millikan-Lauritsen (ML) plot slope

Using (2) and taking natural logarithms of both sides, yields

$$L_{\mathrm{ML}}(V^{-1}) \equiv \ln\{I\} = \ln\{A\theta V_{\mathrm{R}}^{-2}\} - 2\ln\{V^{-1}\} - v_{\mathrm{F}}\eta V_{\mathrm{R}}V^{-1}$$

This is the theoretical equation for a Millikan-Lauritsen (ML) plot. Its slope is

$$S_{\mathrm{ML}}(V^{-1}) = \mathrm{d}L_{\mathrm{ML}}/\mathrm{d}(V^{-1}) =$$
$$= -2V - \eta V_{\mathrm{R}}\mathrm{d}(v_{\mathrm{F}}V^{-1})/\mathrm{d}(V^{-1}) = S_{\mathrm{FN}}(V^{-1}) - 2V$$

Let V_{mid}^{-1} be the midpoint of the range of values of V^{-1} used in an experimental ML plot. It follows that the slope $S_{\mathrm{FN}}^{\mathrm{eff}}$ of the corresponding FN plot is given approximately by

$$S_{\mathrm{FN}}^{\mathrm{eff}} \approx S_{\mathrm{ML}}^{\mathrm{fit}} + 2V_{\mathrm{mid}}.$$

Values of scaled field can be extracted by using (5), with $S_{\mathrm{FN}}^{\mathrm{fit}}$ replaced by $S_{\mathrm{FN}}^{\mathrm{eff}}$.

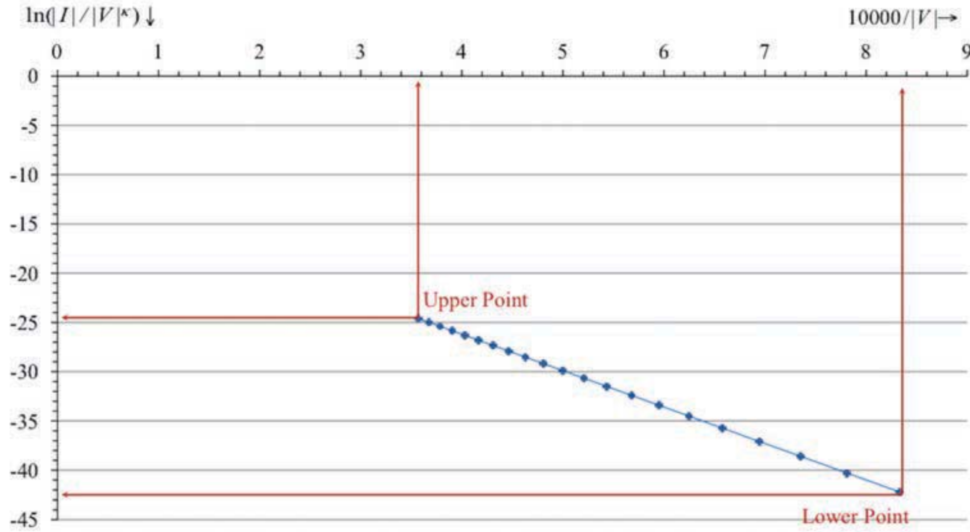

Fig. 1. Simulated MG plot showing the upper-left and lower-right data points that need to be extracted and entered. The symbols |V| and |I| denote the numerical values of measured voltage and current when recorded in volts and amperes, respectively. The plotted points are selected points in the voltage range 1.2 to 2.8 kV

Table 1. General criteria for the orthodoxy test

Condition	Result	Explanation
$f_{\rm low}^{\rm A} \le f_{\rm low}^{\rm extr}$ *AND* $f_{\rm up}^{\rm extr} \le f_{\rm up}$	Pass	Reasonable range
$f_{\rm low}^{\rm extr} \le f_{\rm low}^{\rm NA}$ *OR* $f_{\rm up}^{\rm NA} \le f_{\rm up}^{\rm extr}$	Fail	Clearly unreasonable range
$f_{\rm low}^{\rm NA} \le f_{\rm low}^{\rm extr} \le f_{\rm low}^{\rm A}$ *OR* $f_{\rm up}^{\rm A} \le f_{\rm up}^{\rm extr} \le f_{\rm up}^{\rm NA}$	Inconclusive	More investigation is needed

Table 2. Range limits for the orthodoxy test, as a function of work function ϕ. (Symbol meanings as defined in the text.)

$\phi(eV)$	$f_{\rm low}^{\rm NA}$	$f_{\rm low}^{\rm A}$	$f_{\rm up}^{\rm A}$	$f_{\rm up}^{\rm NA}$
5.50	0.09	0.14	0.41	0.69
5.00	0.095	0.14	0.43	0.71
4.50	0.10	0.15	0.45	0.75
4.00	0.105	0.16	0.48	0.79
3.50	0.11	0.17	0.51	0.85
3.00	0.12	0.18	0.54	0.91
2.50	0.13	0.20	0.59	0.98

2.4 The Murphy-Good (MG) plot slope

Dividing both sides of (3) by V^κ, and taking natural logarithms, yields

$$L_{\rm MG}(V^{-1}) \cong \ln\{I/V^\kappa\} \approx \ln\{A(\theta \exp\eta)V_{\rm R}^{-\kappa}\} - \eta V_{\rm R} V^{-1}$$

This is the equation for a theoretical Murphy-Good (MG) plot. Its slope is [11]

$$S_{\rm MG}(V^{-1}) = -\eta V_{\rm R}$$

Using (1), the extracted $f_{\rm C}$-value corresponding to a given V-value is

$$\{f_{\rm C}^{\rm extr}\} = -(\eta/S_{\rm MG}^{\rm fit})/V^{-1} \qquad (6)$$

As compared with (5), the factor s_t is not present.

For the extraction of other characteristic parameters see [6, 8].

3 Applying test criteria

For new data plots, use of the Murphy-Good (MG) plot [11] is recommended, because this method of extracting formal emission areas is more precise. However, all three experimental plot types will be approximately straight for an orthodox emitter. A straight line can be fitted either manually (this is usually good enough), or by a regression calculation.

To apply the orthodoxy test, the web tool will first calculate the slope of the fitted line from entered values of the plot's upper left ("up") and lower right ("low") ends. Figure 1 shows an example [13] of a MG plot with the required points to apply the test marked.

After calculating the plot slope, the $f_{\rm C}$-values corresponding to the ends of the range of voltages measured are extracted, using (5) or (6) as appropriate, depending on the plot type. The web tool will then apply the

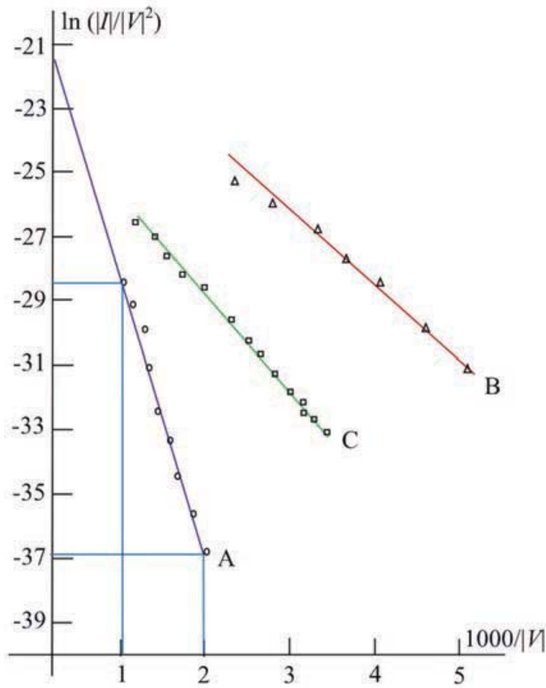

Fig. 2. Curve A shows a Fowler-Nordheim plot taken from an uncoated tungsten emitter [19]. The symbols |V| and |I| denote the numerical values of measured voltage and current when recorded in volts and amperes, respectively.

test criteria shown in Tab. 1 [12,13]. Here: A/NA indicates the allowed/not-allowed limits for f_C; the parameter $\{f_{low}\}^{extr}$ is the extracted f_C value for the lower-right point, and $\{f_{up}\}^{extr}$ is the extracted f_C value for the upper-left point. Table 2 shows how the A/NA limits vary as a function of local work function ϕ (interpolation can be used if needed).

The physical meanings of the "not allowed" limits for the lower and upper points are as follows. The lower limit corresponds to the value where the field is too low to emit a current that can be measured or detected in a normal experiment. The upper limit corresponds to the value where the emitter will electroform or self-destruct. In both cases, if any extracted f_C-value is on the "not-allowed" side of the limit, then it can be concluded that the FE device/system is not orthodox, and that extracted values of emitter characterisation parameters may be spurious [12].

4 Results and examples

During the project reported in this paper, the orthodoxy test was applied to many experimental and simulated data plots, using the web application [17] in its state as currently developed. Data relating to the orthodoxy test is displaying correctly. Our plan is to extend this application in order to extract characterisation parameters from plots that pass the orthodoxy text, but this aspect of the application is still under development and related "boxes" may either be blank or may not be displaying meaningful data.

4.1 Murphy-Good(MG)plot analysis

Figure 1 shows a simulated MG plot. Extracted input data for the orthodoxy test, and output results, as associated with the web tool [17], are recorded in Tab. 3 and 4. As expected with simulated data, the result is "PASS".

4.2 Millikan-Lauritsen plot analysis

The spreadsheet originally developed in connection with the orthodoxy test (see Electronic Supplementary Material to [12]) has been extensively used to test ML plots. We therefore confirm here, for one example only, that the new web application generates the same result as the original 2013 spreadsheet. The chosen example is emitter X89 (Fig. 4) in the well-known paper by Dyke and Trolan [17]. The relevant data (relating to the "direct-current" voltage range) are re-entered in Tables 3 and 4. It has been confirmed that the present web application gives the same extracted f_C-values as the original spreadsheet.

4.3 Fowler-Nordheim (FN) plot analysis

With FN-plot analysis we we show an example of an "inconclusive" outcome. Curve A in Fig. 2 shows a FN plot for an "uncoated" tungsten emitter. Relevant data is shown in Tables 3 and 4. Although the FN plot is a good straight line, the orthodoxy test reports that the outcome is inconclusive. The most likely explanation is that the emitter was being operated up to higher fields than is usually the case – possibly up to higher fields than would usually be advisable.

Many examples of FN plots that fail the orthodoxy test are given in [12].

4.4 Outcomes and discussion

For convenience, the outcomes from the above illustrative tests are shown together in Tables 3 and 4.

It needs to be remembered that this test is an "engineering triage test", with somewhat arbitrary boundaries for the three categories of "pass", "fail", and "inconclusive". The "pass" and "fail" categories have been set so that outcomes in these categories are reasonably certain. The "inconclusive" category can therefore cover both situations that are "nearly normal" and and others that are "definitely not normal", as illustrated here.

5 Summary and conclusions

This paper has set out in a concise form the theory behind the orthodoxy test, and has shown that, in addition to its current use with Millikan-Lauritsen plots and Fowler-Nordheim plots, it can also easily be applied to Murphy-Good plots.

Table 3. Input data for orthodoxy test. Note that the Neper (Np) is a unit of natural logarithmic difference (here relative to $Y = 0$).

Plot type	Source	Figure here	Upper (Left) Point		Lower (Right) Point	
			X (1/V)	Y (Np)	X (1/V)	Y (Np)
MG	simulated	Fig. 1	3.6×10^{-4}	-24.6	7.8×10^{-4}	-40.4
ML	[18], Fig. 2 (X89)	na	2.45×10^{-4}	-9.0	4.15×10^{-4}	-19.0
FN	[19], Fig. 8	Fig. 3	1.0×10^{-4}	-28.5	2.0×10^{-4}	-36.9

Table 4. Output data from orthodoxy test

Plot type	Figure here	$\{f_{\mathrm{low}}\}^{\mathrm{extr}}$	$\{f_{\mathrm{up}}\}^{\mathrm{extr}}$	Result
MG	Fig. 1	0.16	0.36	PASS
ML	na	0.20	0.34	PASS
FN	Fig. 2	0.26	0.52	INCONCLUSIVE

It has been argued elsewhere [11] that MG plots provide a better methodology of FE current-voltage data analysis than do FN plots, because for ideal FE devices/systems they lead to the more precise extraction of information about formal emission area. The work in this paper confirms that, in addition, MG plots can be subject to the orthodoxy test that is the necessary preliminary to meaningful data analysis.

We have also reported the initial development of a prototype web tool that can carry out the orthodoxy test for all three types of $I(V)$ data plot. Further development of this web tool is in progress, in order to allow the extraction of characterization parameters from plots that pass the test. Our intention is that, in future work on carbon field emitters at Mu'tah University, Murphy-Good plots and the related form of orthodoxy test will be used. It is also our intention to develop a downloadable spreadsheet version of the web application.

Appendix: The Schottky constant

The "Schottky constant" is the modern equivalent of the numerical constant that appeared in equation (6) of the 1914 paper [20] that first put the theory of the Schottky effect (see Wikipedia) onto a quantitative basis. Since the term "Schottky constant" may be unfamiliar to many people, relevant background information is presented here.

A classical point electron escaping from a surface to which a high negative field (of magnitude F) is applied experiences forces due to both its electrical image in the surface and the external electrostatic field. As a consequence, as compared with the classical potential energy (PE) barrier that would be seen by the electron when $F = 0$, the escaping electron experiences a classical PE barrier with a maximum height that has been reduced by an energy Δ_{S} given by

$$\Delta_{\mathrm{S}} = c_{\mathrm{S}} F^{1/2}.$$

This is the well-known classical Schottky effect, in fact first suggested as an electron emission mechanism by J. J. Thomson in 1903 [20]. The parameter c_{S} is a universal constant that has now been called the *Schottky constant*.

In terms of the fundamental physical constants, c_{S} is given by [15]

$$c_{\mathrm{S}} = (e^3/4\pi\varepsilon_0)^{1/2}$$

where e is the elementary charge and ε_0 is the vacuum electric permittivity. In the units now often used in field emission, c_{S} has the value $1.199985\,\mathrm{eV}^2(\mathrm{V/nm})^{-1}$.

As already noted, the Schottky effect was first put on a quantitative basis in Schottky's 1914 paper [21]. If fields are measured in V/cm, as often done before the SI system was introduced, then the modern parameter c_{S} has the value $3.794686 \times 10^{-4}\,\mathrm{eV}\,(\mathrm{V/cm})^{-1/2}$. The corresponding numerical value, approximated as 3.8×10^{-4}, appears in equation (6) of [20]. This is the origin of the name "Schottky constant" for c_{S}. In one form or another, the physics of the Schottky constant has been in use for over 100 years, but only recently has c_{S} been explicitly given this name.

Acknowledgements

The authors would like to thank the Deanship of Academic Research at Mu'tah University for supporting this work through research project number 241/19/120. The research was also supported by the Ministry of Industry and Trade of the Czech Republic, MPO-TRIO project FV10618, and by the University of Surrey, UK.

References

[1] A. Modinos, *Field, Thermionic, Secondary Electron Emission Spectroscopy*, New York, Plenum, 1984.

[2] G. N. Fursey, *Field Emission in Vacuum Microelectronics*, New York: Kluwer, 2005.

[3] S.-D. Liang, *Quantum Tunneling Field Electron Emission Theories*, World Scientific: Singapore, 2014.

[4] A. Evtukh, H. Hartnagel, O. Yilmazoglu, H. Mimura, and D. Pavlidis, *Vacuum Nanoelectronic Devices*, Chichester, UK, Wiley, 2015.

[5] K. L. Jensen, *Introduction to the Physics of Electron Emission*, Chichester, UK: Wiley, 2018.

[6] R. G. Forbes, "Why Converting Field Emission Voltages to Macroscopic Fields before Making a Fowler-Nordheim Plot Has Often Led to Spurious Characterization Results", *Journal of Vacuum Science Technology B*, vol. 37, p. 051802, 2019.

[7] T. E. Stern, B. S. Gossling, and R. H. Fowler, "Further Studies in the Emission of Electrons from Cold Metals", *Proceedings of the Royal Society of London Series A*, vol. 124, pp. 699–723, 1929.

[8] R. G. Forbes, J. H. B. Deane, A. Fischer, and M. S. Mousa, "Fowler-Nordheim Plot Analysis: A Progress Report", *Jordan Journal of Physics*, vol. 8, pp. 125–147, 2015.

[9] R. A. Millikan and C. C. Lauritsen, "Relations of Field-Currents to Thermionic Currents", *Proceedings of the National Academy of Sciences*, vol. 14, pp. 45–49, 1928.

[10] R. G. Forbes, "Use of Millikan-Lauritsen Plots, Rather than Fowler-Nordheim Plots", *Journal of Applied Physics*, vol. 105, p. 114313, 2009.

[11] R. G. Forbes, "The Murphy-Good plot: A Better Method of Analysing Field Emission Data", *Royal Society Open Science*, vol. 6, 190912, 2019.

[12] R. G. Forbes, "Development of a Simple Quantitative Test for Lack of Field Emission Orthodoxy", *Proceedings of the Royal Society of London* Series A, vol. 469, p. 20133027, 2013.

[13] M. M. Allaham, R. G. Forbes, and M. S. Mousa, "Applying the Field Emission Orthodoxy Test to Murphy-Good plots", *Jordan Journal of Physics*, in press, March 2020.

[14] J. H. B. Deane and R. G. Forbes, "The Formal Derivation of an Exact Series Expansion for the Principal Schottky-Nordheim Barrier Function v", *Journal of Physics A: Mathematical Theoretical* vol. 41, p. 395301, 2008.

[15] R. G. Forbes and J. H. B. Deane, "Transmission Coefficients for the Exact Triangular Barrier: an Exact General Analytical Theory that can Replace Fowler & Nordheim's 1928 Theory", *Proceedings of the Royal Society of London* Series A, vol. 467, pp. 2927–2947, 2011, See Electronic Supplementary Material for information about universal constants used in field emission.

[16] International Standards Organization (ISO) *International Standard ISO 80000-1:2009 Quantities and Units Part 1: General*, Geneva: ISO, 2009, Section 6.

[17] http://fieldemissionanalysis.weebly.com/.

[18] W. P. Dyke and J. K. Trolan, "Field Emission: Large Current Densities", *Physical Review* vol. 89, pp. 799–808, 1953.

[19] M. S. Mousa, "Influence of a Dielectric Coating on Field Electron Emission from Micro-Point Electron Sources", *Surface Interface Analysis*, vol. 39, pp. 102–110, 1986.

[20] W. Schottky, "Über den Einfluss von Strukturwirkungen, besonders der Thomsonschen Bildkraft, auf die Elektronenemission der Metale", *Physikalische Zeitschrift*, vol. 15, pp. 872–878, 1914.

[21] J. J. Thomson, *Conduction of Electricity through Gases*, 1st ed, Cambridge University Press, page 386, 1903.

Received 18 November 2019

Mohammad Allaham (student) was born in 1986 in Amman, Jordan. He is currently an MSc student in Mutah University, Al-Karak, Jordan and a part of a research team led by Prof. Marwan S. Mousa. The team investigates development of new experimental electron sources along with a theoretically oriented team which analyses data obtained from the experiments.

Richard G. Forbes (DSc), studied at Trinity College, Cambridge, where he received a Tripos Prize, a Senior Scholarship and a Research Scholarship. After a first degree in Physics (Theoretical option), he did PhD research in the Department of Metallurgy and Materials Science in Cambridge. He did postdoctoral work at Aston University, subsequently becoming a Lecturer in Physics. He moved to Surrey University in 1983, and retired as Reader in Applied Electrophysics. He continues to be active in research, as a Visiting Reader, and is well known internationally for work in high-electric-field nanoscience and in field electron emission.

Alexandr Knápek (PhD) was born in 1983 in Brno, Czech Republic. He received his PhD from Brno University of Technology in Brno in 2013 where he also continued to lecture Physics to bachelor students till 2017. Currently, he works as a researcher at the Institute of Scientific Instruments of the Czech Academy of Sciences within the Electron-beam Lithography Group. There, he deals mainly with experimental research of field emission emitters and other topics within the field of physical electronics.

Marwan S. Mousa (Prof, PhD) is affiliated to the Department of Physics, Mu'tah University, where he has been working since 1985. He has authored and co-authored more than 150 national and international publications. His research interests focus mainly on field emission of electrons from composite electron sources and has an active association with different societies and academies around the world, leaving his mark in the scientific community. He became a full professor in Physics and Materials Technology in May 1996, and has received several awards for contributions to the scientific community. In October 2019, he was appointed Vice-President of Mu'tah University.

User-friendly method for testing field electron emission data: Technical report

Mohammad M. Allaham[1, 2*], Alexandr Knápek[1], Marwan S. Mousa[3], and Richard G. Forbes[4]
[1]*Institute of Scientific Instruments of CAS, Královopolská 147, 612 64 Brno, Czech Republic*
[2] *Central European Institute of Technology, Brno University of Technology, Purkyňova 123, 612 00 Brno, Czech Republic*
[3]*Physics Department, Mu'tah University, Al-Karak 6170, Jordan*
[4]*Advanced Technology Institute & Department of Electrical and Electronic Eng., University of Surrey, Guildford, Surrey GU27XH, UK.*
*Contact: allaham@isibrno.cz, Phone +420 541 514 318

Abstract—**In field electron emission (FE) studies, the current/voltage or the macroscopic current-density/field characteristics of single tip or large area field emitters can be expressed in a nearly linear form using one of a small number of standard data-analysis plots. Usually, the chosen plot is a Fowler-Nordheim plot, a Murphy-Good plot or a Millikan-Lauritsen plot. The FE orthodoxy test can be applied to any of the three types of plots, to test the reasonability of the obtained experimental data. A difficulty of using the orthodoxy test is that there is no technical procedure or simple platform that can be used to apply the test to the experimental data. This report describes a simple web-tool that is designed to apply the FE orthodoxy test to any of these data-analysis plots, and then to use the test results to extract the emitter characterization parameters if the data passes the orthodoxy test. The web-tool is used by specifying the nature of the plot, the emitter's local work function, relevant system macroscopic parameters, and the coordinates of two "end-of-range" points on a line fitted to the data-analysis plot. The web-tool simplifies the data processing related to FE studies and experiments by: determining the value of the pre-exponential voltage/field exponent κ for Murphy-Good plots; evaluating the scaled-field parameters in FE theory that correspond to the ends of the working range; determining the status of the tested data before publishing it; determining the status of the emitter or experiments. Hopefully, the web-tool can help to develop basic understanding of the different behaviors of emitters.**

Keywords—Fowler-Nordheim plot, Murphy-Good plot, orthodoxy test, characterization parameter, data-analysis web-tool.

I. INTRODUCTION

In field electron emission (FE) theory, Fowler-Nordheim (FN), Murphy-Good (MG) and Millikan-Lauritsen (ML) data-analysis plots are methods for presenting measured current/voltage $I_m(V_m)$ or the macroscopic current-density/field $J_M(F_M)$ characteristics of FE experiments in a nearly linear form. Advantages of using Murphy-Good plots are that they are predicted to be "very nearly straight" [1], and that there are fewer correction factors in the mathematics of the data-analysis process.

A web-tool has been developed that allows researchers to easily test and analyze experimental results by first applying the so-called orthodoxy test and then (if the test is passed) extracting characterization parameters for the emitter used.

The three types of plots can be presented in the general form $\ln(Y/X^\kappa)$ vs X^{-1}. Here, Y is either the measured total emission current I_m or the macroscopic current density J_M, X is either the measured voltage V_m or the macroscopic electrostatic field intensity F_M, and κ is the pre-exponential voltage exponent in the *empirical FE equation*

$$I_m = C V_m^{\kappa} \exp[-B/V_m], \quad (1)$$

where B can be treated as a constant and C can often be approximated as a constant.

In the expanded form of the Murphy-Good FE equation, κ is given by $2-\eta/6$, where η is the scaling parameter for the Schottky-Nordheim (SN) barrier and is given by $\eta(\phi) = bc_S^2\phi^{-1/2}$, where b is the second FN constant, c_S is the Schottky constant and ϕ is the local work function [2]. Thus, κ=2 for FN plots, 0 for ML plots, and $(2-\eta/6)$ for MG plots [2].

The field emission orthodoxy test is a quantitative test that can be applied to any of the data-analysis plots and to any geometrical emitter shape for which MG FE theory is an adequate approximation. The test is based on extracting values of a specific and important parameter in FE theory. This parameter is the *characteristic scaled field* $f_C = c_S^2\phi^{-2}F_C = c_S^2\phi^{-2}\zeta_C^{-1}V_m$, where F_C is the local electrostatic field at a characteristic location on the emitter surface (usually taken as its apex), and ζ_C [$\equiv V_m/F_C$] is the related *characteristic voltage conversion length (VCL)*. The extracted f_C-values are then compared to a set of internal analyzed historical data, taken from metal emitters between 1926 and 1972. These data provide the orthodoxy test criteria as listed in [3].

The test is an "engineering triage" test and provides three results. (1) Pass: the data are reasonable. (2) Fail: the data are unreasonable, and the extracted parameters are likely to be spurious. (3) Inconclusive; the data need more study and analysis. If the orthodoxy test is passed, then the characterization parameters of the emitter can validly be extracted. Typically, these are: the formal emission area (for a Schottky-Nordheim barrier) A_f^{SN}, and the related formal area

efficiency α_f^{SN}; and the VCL ζ_C, and the related characteristic field enhancement factor (FEF) γ_C [2].

II. Methodology

The FE analysis web-tool [4] had been developed for the purpose of applying the orthodoxy test. It does this by making precise calculations for the parameter-extraction process from any of the three types of data-analysis plot. It is necessary to precisely calculate the values of the FE theory scaled parameters and (for MG plots) the κ value as defined in [1]. The main tool requires only the plot form, the assumed value of ϕ, and the coordinates of the upper and lower limits for the line fitted to the data. To extract values for γ_C and α_f^{SN}, where relevant-usually only for large area field electron emitters (LAFEs)-further macroscopic system parameters are needed, namely a cathode-anode macroscopic distance d_M (there are several types) and the macroscopic area A_M of the LAFE.

To test the performance of the web-tool, simulated current-voltage data plots were generated, for each of the three types of plot, using the input parameter-values: ϕ=4.65 eV, A_f^{SN}=100 nm^2, ζ_C=180 nm, d_M=100 µm, A_M=100 mm^2, with the tested range set to be $0.17 \leq f_C \leq 0.43$ (which is chosen to pass the orthodoxy test).

III. Results and Discussion

The simulated data are presented in Fig. 1. For the MG plot, the value of κ has been calculated using the formula given earlier, which yields κ=1.2398. With each of the plots, a line fitted to the plot would have slope S^{fit} and intercept $\ln(R^{fit})$ on the vertical (1000/V_m=0) axis. Both these values can in fact be obtained from the coordinates that correspond to the range of the fitted lines. The resulting values of S^{fit} and $\ln(R^{fit})$, as evaluated by the web-tool, are shown in Table I. [Note that the Neper (Np) is the SI recognised unit of natural logarithmic difference, for amplitude-type quantities].

The range of f_C-values extracted from ea ch of the plots, using the relevant formula in [3], coincides with the chosen input range, thereby demonstrating consistency.

Table I also shows values of extracted characterization parameters, except that no reliable theory currently exists for extracting area-like quantities from a ML plot.

All the data-analysis plots have "nearly straightline behavior", but each plot is slightly curved in a different way. This leads to a noticeable variation and percentage error in the extracted values of the characterization parameters but does not significantly affect the results of the orthodoxy test.

With this set of chosen data the FN plot appears to work slightly better than the MG plot, but our general impression is that for extracting area-like quantities the MG plot is expected to be more reliable and easier to use.

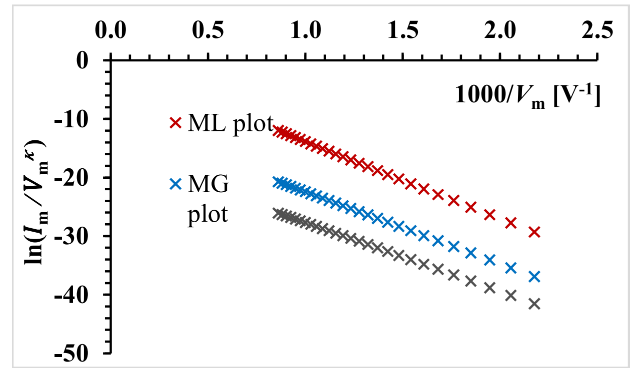

Fig. 1. Simulated data-analysis plots for the three plot types shown, for ϕ=4.65 eV, A_f^{SN}=100 nm^2, ζ_C=180 nm, and $0.17 \leq f_C \leq 0.43$.

IV. Conclusions

There is a need for a user-friendly tool that can apply the field emission orthodoxy test to experimental data, and (if appropriate) easily extract characterization parameters. Information of this kind is useful in the research and development of electron sources, in our case improved electron microscope sources and hybrid-design sources involving dielectric layers on metal point sources, but more generally sources based on large area field electron emitters. Our web-tool [4], now in its final stages of development, seeks to provide this facility, for all the forms of data-analysis plot commonly used.

Notwithstanding this, our strong recommendation is that best engineering and scientific practice is to *always* plot the *raw measured current/voltage data* [5], to use a Murphy-Good plot rather than a Fowler-Nordheim plot, and to apply the orthodoxy test before attempting to extract characterization parameters.

Acknowledgment

The research described in this paper was financially supported by the Ministry of the Interior of the Czech Republic (project. No. VI20192022147)

References

[1] R. G. Forbes, R. Soc. Open Sci. 6, 190912 (2019).
[2] M. M. Allaham, R. G. Forbes, A. Knápek, and M. S. Mousa, J. Electr. Eng. Slovak 71, 37 (2020).
[3] R.G. Forbes, Proc. R. Soc. Lond. A 469, 20130271 (2013).
[4] M. M. Allaham, R. G. FORBES, A. Knápek, and M. S. MOUSA. Field emission analysis software [online]. Mu'tah University [cit. 2021-6-11]. Available from: https://fieldemissionanalysis.weebly.com.
[5] R. G. Forbes, "Using the parameter 'formal area efficiency (α_f^{SN})' to analyze current-voltage measurements on large-area field electron emitters, 34th IVNC, Poster/Paper this conference.

TABLE I
The Extraction Results for Each of the Fig. 1 Data-Analysis Plots

Plot type	S^{fit} [Np V]	$\ln(R^{fit})$ Np	f_C	ζ_C nm	γ_C	A_f^{SN} nm^2	α_f^{SN}
FN	–11720	–16.00	0.17 – 0.43	180.11	555.21	94.21	9.42×10^{-7}
MG	–12258	–10.18	0.17 – 0.43	178.96	558.79	94.72	9.47×10^{-7}
ML	–11813	–0.68	0.17 – 0.43	181.54	550.83	-	-
Simulation Input	-	-	0.17 – 0.43	180.00	555.56	100	10^{-6}

UŽITNÝ VZOR

(11) Číslo dokumentu:
33 278

(13) Druh dokumentu: **U1**

(51) Int. Cl.:

C25F 3/14	(2006.01)
C25F 3/16	(2006.01)
C25F 7/00	(2006.01)
G01R 17/02	(2006.01)

(19) ČESKÁ REPUBLIKA

ÚŘAD PRŮMYSLOVÉHO VLASTNICTVÍ

(21) Číslo přihlášky: **2019-36443**
(22) Přihlášeno: **26.07.2019**
(47) Zapsáno: **07.10.2019**

(73) Majitel:
Ústav přístrojové techniky AV ČR, v.v.i., Brno, Královo Pole, CZ

(72) Původce:
Ing. Alexandr Knápek, Ph.D., Brno, Žabovřesky, CZ
Pavel Klein, Vojkovice, CZ
prof. Ing. Armin Delong, Dr.Sc., Brno, Stránice, CZ

(74) Zástupce:
KANIA, SEDLÁK, SMOLA, s.r.o., Mendlovo náměstí 907/1a, 603 00 Brno, Staré Brno

(54) Název užitného vzoru:
Zařízení pro opakovatelnou výrobu ostrých hrotů

CZ 33278 U1

Úřad průmyslového vlastnictví v zápisném řízení nezjišťuje, zda předmět užitného vzoru splňuje podmínky způsobilosti k ochraně podle § 1 zák. č. 478/1992 Sb.

Zařízení pro opakovatelnou výrobu ostrých hrotů

Oblast techniky

Technické řešení se týká plně automatizovaného zařízení pro opakovatelnou výrobu ostrých hrotů elektrochemickou cestou, kdy je v zásaditém elektrolytu metodou anodického rozpouštění vytvořen ostrý hrot s průměrem řádově v desítkách nanometrů. Zařízení slouží pro výrobu ostrých autoemisních katod, dále pro výrobu sond pro sondovou rastrovací tunelovou mikroskopii (STM) a také pro hroty nanomanipulátorů. Technické řešení sestává z mechanické a elektronické (řídicí) části, která zahrnuje speciální řídicí algoritmus založený na vyhodnocování gradientu leptacího proudu v reálném čase.

Dosavadní stav techniky

Stávající zařízení, která v principu využívají pro tvorbu hrotů obecný princip anodického rozpouštění, který je známý z elektrochemie, obvykle fungují na čistě manuálním principu. Konkrétně se jedná:

1) o manuální manipulaci s leptaným materiálem (jeho zanořování do elektrolytu) a dále

2) o manuální odepínání leptacího proudu.

Ad 1) Přesné vynořování a zanořování je zcela zásadní pro dosažení přesného, osově symetrického hrotu. Pokud je leptaný materiál zanořen s jiným než pravým úhlem vůči hladině, dojde k osově nesymetrickému rozložení povrchového napětí a tím pádem i nehomogenní rychlosti leptání na povrchu smáčeném elektrolytem.

Ad 2) Určení přesného okamžiku, kdy má dojít k odepnutí leptacího proudu, a dále jeho odepnutí jsou kritické fáze výroby ostrého hrotu, protože sebemenší prodleva zapříčiní přeleptání a tedy ztupění leptaného hrotu. Naopak předčasné odepnutí má za následek nedokončení leptání, kdy neodpadne spodní část menisku.

Obě tyto nevýhody, v kombinaci s neideální strukturou leptaného kovu, kdy je rychlost leptání na celé ploše neuniformní (vlivem nestejné krystalové orientace), vedou k nedokonalostem geometrie takto vytvořeného hrotu.

Podstata technického řešení

Výše uvedené nedostatky dosavadního stavu techniky jsou eliminovány zařízením pro opakovatelnou výrobu ostrých hrotů, které zahrnuje:

- kleštinu pro upnutí drátku,
- pohon, který je propojený s kleštinou a uzpůsobený pro přemísťování kleštiny pohybem ve vertikálním směru,
- svorku pro připojení katody pro elektrolytické leptání a leštění,
- zdroj stejnosměrného proudu, který je propojený se svorkou pro připojení katody, a
- elektronickou řídicí jednotku, která je pro řízení pohybu kleštiny propojená s pohonem a pro řízení stejnosměrného proudu přiváděného do katody je propojená se zdrojem

stejnosměrného proudu.

Ve výhodném provedení zařízení pohon zahrnuje

- krokový motorek,
- převodový mechanizmus, pro převod točivého pohybu na translační, a
- pístový vodicí mechanismus,

které jsou navzájem propojeny pro realizaci lineárního pohybu kleštiny.

Výhodné provedení zařízení dále zahrnuje

- stolek pro uložení misky s elektrolytem,
- nosič, na kterém je uspořádán pohon, a
- stojinu, která je jedním koncem upevněna ke stolku, zatímco k jejímu druhému konci je upevněn nosič.

Ve zvlášť výhodném provedení je stolek opatřen šroubovatelnými nožkami pro ustavování stolku do vodorovné polohy, přičemž pohon je uzpůsobený pro přemísťování kleštiny pohybem ve směru kolmém ke stolku.

Rovněž je výhodné, když zařízení dále zahrnuje zdroj střídavého proudu, který je propojený se svorkou pro připojení katody, a současně je pro řízení střídavého proudu přiváděného do katody propojený s elektronickou řídicí jednotkou.

Zařízení dále s výhodou zahrnuje měřič pro měření proudu vedeného ze zdroje stejnosměrného proudu a měřič pro měření proudu vedeného ze zdroje střídavého proudu, přičemž měřiče jsou propojené s elektronickou řídicí jednotkou. Elektronická řídicí jednotka pak přednostně zahrnuje mikročip s pamětí, ve které jsou uloženy tabulky mezních hodnot a software pro zpracovávání údajů z měřičů a jejich porovnávání s uloženými mezními hodnotami a pro řízení činnosti zdroje stejnosměrného proudu a zdroje střídavého proudu na základě výsledků zpracování a porovnání.

Další výhodné provedení zařízení zahrnuje dorazové spínače s kontakty pro vymezení mezních poloh převodového mechanizmu pro převod točivého pohybu na translační.

Za provozu zařízení dále zahrnuje prstencovou katodu pro elektrolytické leptání a leštění, přičemž prstencová katoda je opatřena upínacím ramenem pro vsazení do svorky.

A rovněž je výhodné, když zařízení dále zahrnuje komunikační rozhraní propojené s řídicí jednotkou a uzpůsobené pro zadávání pokynů do zařízení a zobrazování informací o stavu zařízení.

Objasnění výkresů

Technické řešení je ilustrováno na přiložených výkresech, kde na obr. 1 je schematicky znázorněno příkladné provedení zařízení pro opakovatelnou výrobu ostrých hrotů, na obr. 2 je blokové schéma zapojení zařízení z obr. 1 a na obr. 3 je blokové schéma řídicího algoritmu, který je implementován v čipu elektronické řídicí jednotky zařízení z obr. 1.

Příklad uskutečnění technického řešení

Na obr. 1 je vyobrazena mechanická část zařízení, která obsahuje stolek 5, stojinu 10, která je svým dolním koncem upevněná ke stolku 5, a nosič 11, který je upevněný k hornímu konci stojiny 10.

V alternativním provedení lze stojinu 10 s nosičem 11 nahradit obecně nosným rámem.

Na nosiči 11 je uspořádaný krokový motorek 1, který je přes mechanizmus 2, pro převod točivého pohybu na translační, propojen s pístovým vodicím mechanismem 3.

Na distálním konci pístového vedení je uspořádána kleština 9 pro upnutí zpracovávaného dílce, konkrétně pro upnutí drátku 90. Pístový vodicí mechanismus 3 je přitom uzpůsoben pro přemísťování kleštiny 9 obecně ve směru svislém, konkrétně v tomto provedení ve směru kolmém na stolek 5.

Alternativně lze použít místo krokového motorku 1 jiný typ pohonu a/nebo místo pístového vodicího mechanismu 3 jiný typ lineárního vedení.

A v ještě dalším provedení lze sestavu motorku 1, převodového mechanizmu 2 a pístového vodicího mechanismu 3 nahradit jiným vhodným pohonem lineárního pohybu kleštiny 9.

Pod kleštinou 9 je na stolku 5 ustavena miska 7 na elektrolyt. V misce 7 je uspořádána prstencová katoda 80, která je vyrobená z platinového plechu a je vodivě pomocí připojovacího ramena připojená ke svorce, resp. ke svorkovnici 8.

Zařízení je dále opatřeno kontakty 4.a, 4.b dorazových spínačů, které jsou rovněž propojeny přes řadič a svorkovnici 8 s řídicí jednotkou 20. Kontakty 4.a, 4.b fungují tak, že při dosažení krajní polohy u mechanizmu 2 pro převod točivého pohybu na translační dojde k sepnutí příslušného spínače a k okamžitému zastavení pohybu.

Svorkovnice 8 je propojena s neznázorněným konektorem (například typu CANNON-15) pro připojení elektronické jednotky.

Stolek 5 je opatřen vodováhou 6 a trojicí šroubovatelných nožek 5.a, 5.b, 5.c pro vyrovnáván celého zařízení za pomoci vodováhy 6 tak, aby byl stolek 5 vodorovný a díky tomu pohyb kleštiny 9 svislý, resp. kolmý na hladinu elektrolytu v misce 7.

Obr. 2 ilustruje blokové zapojení zařízení znázorněného na obr. 1. Zařízení zahrnuje elektronickou řídicí jednotku 20, která je propojena přes konektor svorkovnice 8 a řadič 21 s krokovým motorkem 1 a s dorazovými tlačítky 4.a, 4.b a je uzpůsobena pro řízení krokového motorku 1, zejména pro jeho zapínání/vypínání, nastavení směru pohybu, nastavení počtu kroků a případně i resetování polohy k dorazu.

Současně je elektronická řídicí jednotka 20 propojená s prstencovou katodou 80 volitelně přes zdroj 22 stejnosměrného proudu (o velikosti např. 50 mA a s napětím například 6,9 V), určený pro leptání, a přes zdroj 23 střídavého proudu (o velikosti např. 50 mA a s napětím například 3 V a frekvencí 50 Hz), určený pro elektrolytické leštění. Elektronická řídicí jednotka 20 je přitom uzpůsobena pro řízení zapínání a vypínání zdrojů 22, 23 a pro měření a vyhodnocování hodnot leptacího, případně lešticího proudu přiváděného do prstencové katody 80.

Elektronická řídicí jednotka 20 je rovněž propojena s měřičem 26 pro měření proudu vedeného ze zdroje 22 stejnosměrného proudu do prstencové katody 80 a měřičem 27 pro měření proudu vedeného ze zdroje 23 střídavého proudu do prstencové katody 80.

V některých případech nemusí být elektrolytické leštění před samotným leptání vyžadováno, proto zdroj 23 střídavého proudu a jeho měřič 27 nemusí být přítomny.

Elektronická řídicí jednotka 20 je dále propojena se zobrazovací jednotkou 24, v tomto
5 příkladném provedení ve formě LCD displeje, pro zobrazování stavových informací o zařízení.

Dále je elektronická řídicí jednotka 20 propojena s ovládacím rozhraním 25, v tomto příkladném provedení ve formě ovládacích tlačítek.

10 Elektronická řídicí jednotka 20 zahrnuje procesorovou jednotku, která je realizována jednočipem (například mikročipem typu RISC od firmy ATMEL) s příslušnou pamětí pro uložení programu a případně mezních hodnot jednotlivých kroků pracovního procesu a dále napájecí zdroje pro komunikační rozhraní představované v tomto příkladném provedení zobrazovací jednotkou 24 a ovládacím rozhraním 25.
15
Obr. 3 ilustruje řídicí algoritmus, který je implementován v procesorové jednotce elektronické řídicí jednotky 20. Jedná se o sekvenční algoritmus, který je založený na vyhodnocování hodnot leptacího proudu a výpočtu druhé diskrétní derivace proudu, která slouží k určení přesného okamžiku odepnutí leptacího zdroje a ukončení celého procesu, a to zcela automaticky, bez
20 jakéhokoliv zásahu ze strany uživatele.

Pracovní proces z obr. 3 je zahájen inicializací komponent.

Krokovým motorkem 1 se spustí kleština 9 dolů do vnitřního prostoru misky 7 s elektrolytem
25 a zapne se zdroj 22 stejnosměrného proudu. Následně se měří leptací proud. Pokud je jeho hodnota pod 1 µA, vyhodnotí se, že se hrot drátku 90 ještě nedotkl hladiny elektrolytu a spouštění kleštiny 9 stále pokračuje. Pokud je hodnota změřeného proudu alespoň 1 µA, vypne se zdroj 22 stejnosměrného proudu, pohyb způsobený krokovým motorkem 1 je ukončen a přenastaví se pozice drátku 90 za účelem nastavení povrchového napětí v požadovaném místě leptaného drátku
30 90.

Poté následuje elektrolytické leštění, při kterém se zapne zdroj 23 střídavého proudu na stanovený časový interval, například 180 sekund. Poté se vypne zdroj 23 střídavého proudu a přenastaví se pozice drátku 90 opět na hladinu, aby bylo možno pokračovat dalším
35 technologickým krokem.

Následně se provede opět zanoření drátku do elektrolytu v misce 7, zapne se zdroj 22 stejnosměrného proudu a měří se jeho velikost. Pokud je alespoň 1 µA, zahájí se první leptací fáze, při které se nejprve přenastaví pozice drátku 90, poté se drátek 90 zanoří do elektrolytu
40 a měří se velikost leptacího proudu. Když velikost leptacího proudu klesne pod 1 µA, zahájí se druhá leptací fáze tím, že se nastaví pozice drátku tak, aby do elektrolytu zasahovalo pouze již vytvořené zúžení drátku 90. Když velikost měřeného stejnosměrného proudu klesne pod 6,5 µA inicializuje se gradientní detektor, tedy zahájí se průběžné propočítávání gradientu aktuálního proudu a v okamžiku, kdy hodnota druhé diskrétní derivace překročí nastavený práh, v tomto
45 příkladu 10^{-3}, se zdroj 22 stejnosměrného proudu vypne a drátek 90 se vytáhne z elektrolytu.

Přesně kolmé nastavení pozice i pohybu leptaného drátku 90 vůči hladině elektrolytu je tedy v tomto technickém řešení zajištěno jednak možností přesně vodorovného ustavení stolku 5 za pomoci trojice nastavitelných nožiček 5.a, 5.b, 5.c stolku 5, což je indikováno vodováhou 6
50 umístěnou v rovině stolku 5, a jednak zajištěním přesně kolmého upnutí drátku 90 v kleštině 9 a přesně kolmého vedení jeho pohybu vzhledem ke stolku 5.

Řízení leptacího proudu, konkrétně jeho rychlé odepínání, je realizováno za pomoci algoritmu druhé diskrétní derivace, kdy je v reálném čase měřen leptací proudu a ve chvíli, když hodnota
55 jeho druhé diskrétní derivace překročí nastavený práh, je leptání ukončeno, zdroj leptacího

proudu odepnut a vyleptaný hrot je vynořen z elektrolytu.

Mezi ostatní výhody patří programovatelná paměť elektronické jednotky, kam je možno uložit prahy (ať už proudové, či časové) jednotlivých kroků výrobního procesu, díky čemuž je dosaženo maximální opakovatelnosti výroby.

Ačkoli byla popsána zvlášť výhodná příkladná provedení, je zřejmé, že odborník z dané oblasti snadno nalezne další možné alternativy k těmto provedením. Proto rozsah ochrany není omezen na tato příkladná provedení, ale spíše je dán definicí přiložených nároků na ochranu.

NÁROKY NA OCHRANU

1. Zařízení pro opakovatelnou výrobu ostrých hrotů, **vyznačující se tím**, že zahrnuje:

- kleštinu (9) pro upnutí drátku (90),

- pohon, který je propojený s kleštinou (9) a uzpůsobený pro přemísťování kleštiny (9) pohybem ve vertikálním směru,

- svorku pro připojení katody (80) pro elektrolytické leptání a leštění,

- zdroj (22) stejnosměrného proudu, který je propojený se svorkou pro připojení katody (80), a

- elektronickou řídicí jednotku (20), která je pro řízení pohybu kleštiny (9) propojená s pohonem a pro řízení stejnosměrného proudu přiváděného do katody (80) je propojena se zdrojem (22) stejnosměrného proudu.

2. Zařízení podle nároku 1, **vyznačující se tím**, že pohon zahrnuje

- krokový motorek (1),

- převodový mechanizmus (2), pro převod točivého pohybu na translační, a

- pístový vodicí mechanismus (3),

které jsou navzájem propojeny pro realizaci lineárního pohybu kleštiny (9).

3. Zařízení podle kteréhokoli z předcházejících nároků, **vyznačující se tím**, že dále zahrnuje

- stolek (5) pro uložení misky (7) s elektrolytem,

- nosič (11), na kterém je uspořádán pohon, a

- stojinu (10), která je jedním koncem upevněna ke stolku (5), zatímco k jejímu druhému konci je upevněn nosič (11).

4. Zařízení podle nároku 3, **vyznačující se tím**, že stolek (5) je opatřen šroubovatelnými nožkami (5.a, 5.b, 5.c) pro ustavování stolku (5) do vodorovné polohy.

5. Zařízení podle kteréhokoli z předcházejících nároků, **vyznačující se tím**, že dále zahrnuje zdroj (23) střídavého proudu, který je propojený se svorkou pro připojení katody (80), a současně je pro řízení střídavého proudu přiváděného do katody (80) propojený s elektronickou řídicí jednotkou (20).

6. Zařízení podle nároku 5, **vyznačující se tím**, že dále zahrnuje měřič (26) pro měření proudu vedeného ze zdroje (22) stejnosměrného proudu a měřič (27) pro měření proudu vedeného

5 ze zdroje (23) střídavého proudu, přičemž měřiče (26, 27) jsou propojené s elektronickou řídicí jednotkou (20).

7. Zařízení podle nároku 6, **vyznačující se tím**, že elektronická řídicí jednotka (20) zahrnuje mikročip s pamětí pro uložení tabulek mezních hodnot a software pro zpracovávání údajů
10 z měřičů (22, 23) a jejich porovnávání s uloženými mezními hodnotami a pro řízení činnosti zdroje (22) stejnosměrného proudu a zdroje (23) střídavého proudu na základě výsledků zpracování a porovnání.

8. Zařízení podle kteréhokoli z předcházejících nároků, **vyznačující se tím**, že dále zahrnuje
15 dorazové spínače s kontakty (4.a, 4.b) pro vymezení mezních poloh převodového mechanizmu (2) pro převod točivého pohybu na translační.

9. Zařízení podle kteréhokoli z předcházejících nároků, **vyznačující se tím**, že dále zahrnuje prstencovou katodu (80) pro elektrolytické leptání a leštění, přičemž prstencová katoda (80) je
20 opatřena upínacím ramenem pro vsazení do svorky.

10. Zařízení podle kteréhokoli z předcházejících nároků, **vyznačující se tím**, že dále zahrnuje komunikační rozhraní, propojené s řídicí jednotkou (20) a uzpůsobené pro zadávání pokynů do zařízení a zobrazování informací o stavu zařízení.

25

3 výkresy

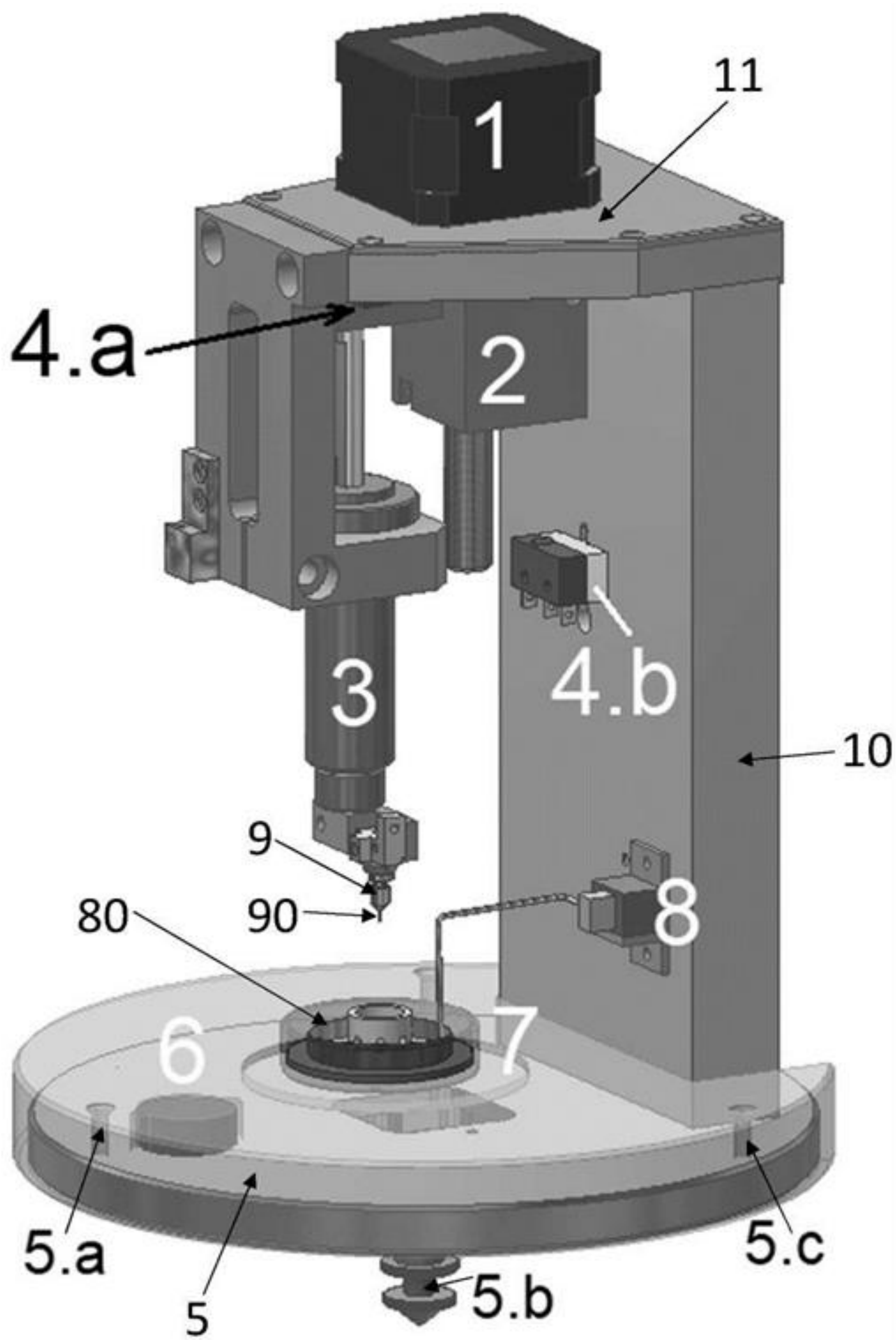

Obr. 1

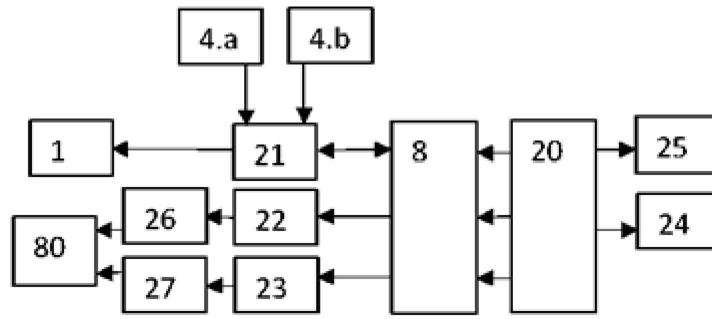

Obr. 2

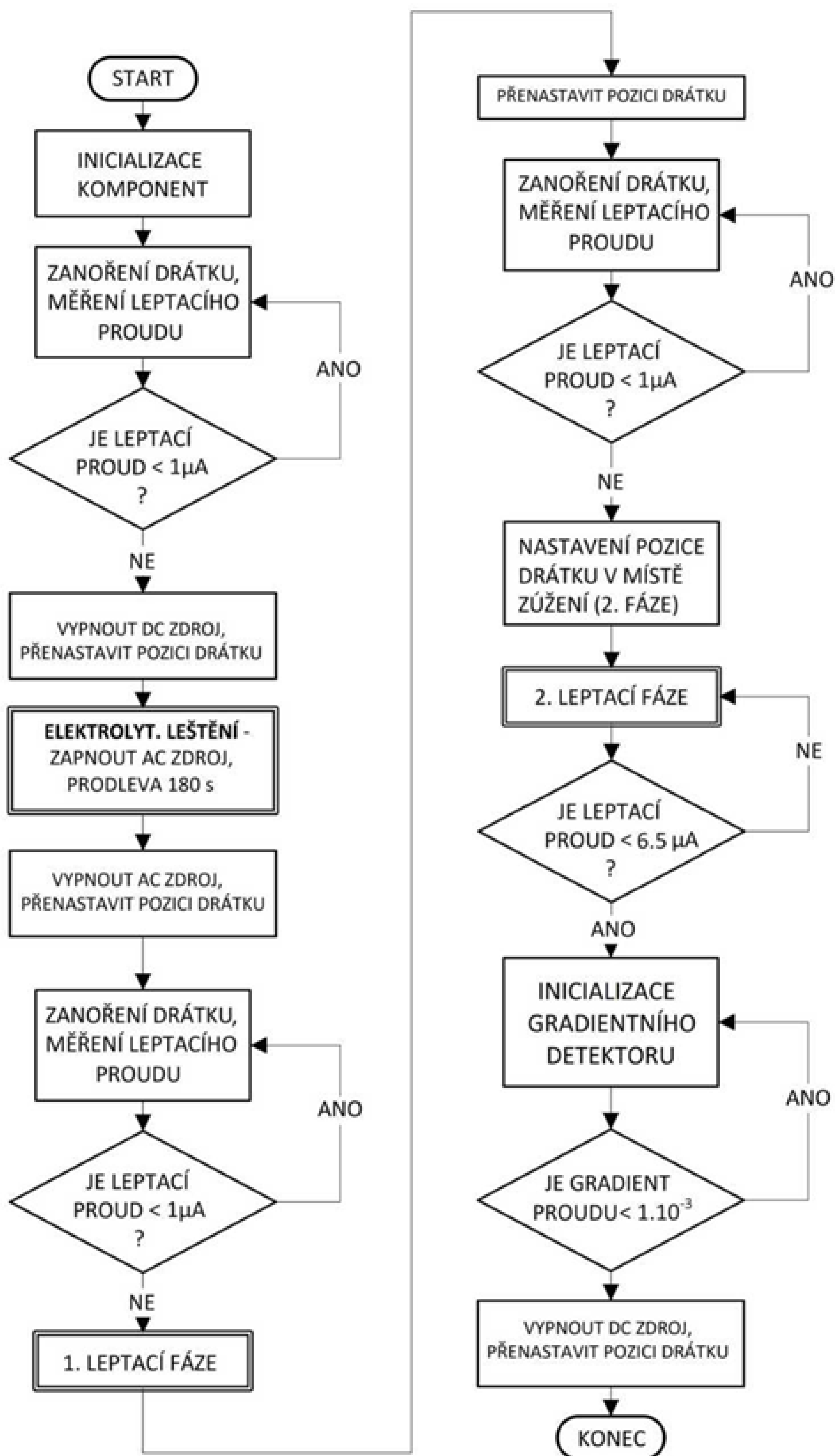

Obr. 3